UNIVERSITÀ DEGLI STUDI DI MILANO

FACOLTÀ DI SCIENZE E TECNOLOGIE

DOCTORATE IN PHYSICS, ASTROPHYSICS AND APPLIED PHYSICS
XXXIV CYCLE

The Astrophysical Gravitational Wave Background: impacts of primary and secondary anisotropies on the GW-LSS cross-correlation

Candidate:
Mrunali Mansukhbhai Gaijan

Supervisor: Dr. Carmelita Carbone
Co-supervisor: Dr. Matteo Calabrese
Internal Tutor: Prof. Luigi Guzzo

Milano, May 2022

Sometime the hardest part of the journey is believing you're worthy of the trip.

Glenn Beck

To my MummaPappa

Contents

Acknowledgements

Main laaga uss ek se, ek bhaya sab maahin,
Sab mera main saban ka, tihan doosara naahin.
(I am attached with the one, that primordial one who is with all,
When everyone is mine, and I am everyone's, there ends all duality.)

Kabir

This is the moment I had been waiting for so long and would cherish forever! Finally, a moment has arrived when I can say 'thank you' to every single one who has contributed directly or indirectly in this beautiful journey.

I would like to sincerely thank my Ph.D. advisor, Dr. Carmelita Carbone for being an amazing guide, mentor, a collaborator and above all, a wonderful human being. Thank you for always being generous with your time and kind to guide me in countless situations. You made my living in Italy safe and the most memorable one, it was truly honour to be your Ph.D. student! I also thank my co-supervisor Dr. Matteo Calabrese for being available to help in many of the simulation parts and guiding through the technicalities.

Thank you so much to the University of Milan, Physics Department, a special thanks to Prof. Luigi Guzzo, Prof. Claudio Grillo, Prof. Marco Lombardi, Prof. Francesco Vissani, Prof. Matteo Paris, Prof. Stefano Forte and Prof. Aniello Mennella. I would like to thank sincerely Prof. Guzzo for providing a profound background of understanding physics of the cosmic structure formation in the simplest and easiest way possible and also funding my many academic visits.

It has been privilege to collaborate with Prof. Mairi Sakellariadou and Dr. Alexander Jenkins, Kings College London who have kindly showed interest in this project and provided much needed input for the thesis. I am truly grateful for the productive collaboration and fruitful discussions.

I heartily acknowledge the funding provided by the Department of Physics, University of Milan under 34th Ph.D. School in Physics, Astrophysics and Applied Physics. I earnestly thank Dr. Petra Dell'Arme and Dr. Andrea Zanzani for being always cooperative and patient to help. I thank each and every staff member of the Physics Department of the University of Milan and also to the INAF, Institute of Space Astrophysics and Cosmic Physics Milano for being generous to offer offices and providing

the very simulating academic environment. I was fortunate to make few true friends for the life- Dr. Claudia Tocci and to-be Dr. Elisabetta Carella, you made my stay in Italy a memorable one. I cannot forget the happy strolls we had in the evenings in the Duomo and every hours we spent together in our offices, classrooms and during our outings in Milan.

Finally, words are failing to make justice to thank my parents- Daxa Damodra and Mansukh Gaijan. Thanks Mumma for your unconditional love and for always being there, this has been the strongest support in my entire journey. Thanks Pappa for always believing in me, even when I did not believe myself. You both deserve the most and the best, thank you so much MummaPappa for making my dream a reality, I could never reach this point without your support.

Finally, I thank the medical staff and frontline workers who have been constantly working globally to make the world a better and safer place after the COVID-19 pandemic.

I am honoured to be a part of the wonderful journey that started from a small town University in India from- M. K. Bhavnagar University in my hometown for graduation, then shifted to Pondicherry University for my master's degree and lead me the the University of Milan. I thank specially to my M.Sc. thesis supervisor Dr. G. Sakthivel and summer internship advisor Prof. R. Rangarajan. They helped me a lot in every academic endeavours.

Thank you so much Alps, Duomo and Milano!

Introduction

> Between every two pine trees
> there is a door leading to a new
> way of life.
>
> *John Muir*

Direct detection of Gravitational Waves (GWs) from the binary black hole merger-GW150914 [1] opened a completely new window to unveil the mysteries of those parts of Universe which remained inaccessible via electromagnetic waves. GWs are the perturbations of the *spatial* subspace of the 4D spacetime which travel at the speed of light and are generated from accelerating masses, in particular from the time variation of the mass quadrupole moment. GWs prove themselves as the messengers of the early Universe, especially belonging to the pre-recombination era which remains hidden by means of electromagnetic astronomy.

The so-called Standard Model of Cosmology (SMC) or the ΛCDM model, is framed within the mathematical language of General Relativity (GR) and is constantly evolving due to ongoing astonishing revelations. In this model, the luminous part of the Universe is only about 4% of the total matter density and the rest is made of dark or weakly/gravitationally interacting particles/fields commonly categorized as dark components which includes Dark Matter and Dark Energy with the latter in the form of a cosmological constant Λ. According to the current observations, the Universe on the larger scales is spatially flat, homogeneous and isotropic which resulted from tiny, inhomogeneous primordial density perturbations interacting gravitationally. These density perturbations merged and grew to form the Large Scale Structure (LSS) of the observable Universe. Prior to this large scale structure formation, perturbations had been stretched in the primordial era known as the inflationary expansion which provided the initial conditions for the density fluctuations and the so-called tensor perturbations.

Such tensor perturbations, i.e. GWs of primordial origin are important tool to understand the dark Universe. First, Primordial Gravitational Waves (PGWs) are supposed to have been produced during the inflationary era and therefore upon their detection, they could provide us glimpse of the early Universe. In addition, the large scale cosmological structure which includes galaxies, galaxy clusters, voids, filaments and so on, could actually act as "lens" to deviate the original path of the GWs propagating to the observer. This phenomenon, known as gravitational lensing, is very much similar to lensing in optics. Detecting lensed GWs would provide us information about the large scale distribution of dark matter regardless its particle nature. These discoveries upon reaching their enough detection sensitivity would indeed be remarkable for the next centuries in the scientific history.

When considered as the superposition of many events, these GWs form a Stochas-

tic Gravitational Wave Background (SGWB) which based upon their sources can be classified as Cosmological Gravitational Wave Background (CGWB) and Astrophysical Gravitational Wave Background (AGWB). The sources of CGWB are on the other hand much primordial; they include inflationary expansion, cosmological phase transition, primordial magneto-hydrodynamics, GWs emitted by cosmic strings and even from the Big Bang itself. Apart from the louder, individual events detected by the LIGO, VIRGO and KAGRA scientific collaborations, there are many events which are too far and faint to be detected individually. GWs produced by many weak, quiet, independent and unresolved sources constitute the SGWB. The sources of AGWB include binary coalescence of black holes, neutron stars, black hole-neutron star merger, magnetars, first stars or supernovae (SNe) explosions. Future experiments such as LISA, ET, PTA, etc. would be able to test gravitational wave theory to the low frequency limits where they are expected to be able to detect and possibly distinguish different kinds of stochastic backgrounds. This makes it crucial to study sources and properties of SGWB and distinguishing their origin to fathom many mysteries of the Universe.

This thesis is dedicated to understand cross-correlation of the SGWB produced by GWs of astrophysical sources with LSS and CMB and effects of gravitational lensing on them. When GWs emitted by astrophysical sources are received at the detector, prior to their detection, they undergo lensing effect due to intervening matter present between the source and the detector which includes visible cosmological large scale structure and yet unseen dark matter. Matter present in the space deforms the original geodesic of GWs and hence, mutual interactions between GWs and matter leave imprint on their energy density distribution. Since GR predicts non-zero spatial correlation between SGWB and CMB due to sharing common origin of geodesic deviation, lensing of GWs can be treated in similar way as lensing of CMB within the geometric optics approximation. Assuming this, we provide the cross-correlation of simulated AGWB signals with different simulated cosmological probes which include Weak Lensing (WL) convergence maps, CMB lensing convergence maps, Galaxy number counts and CMB Integrated Sachs-Wolfe (ISW)/Rees-Schiama (RS) effect using the cosmological N-body simulation suite- the "Dark Energy and Massive Neutrino Universe" (DEMNUni). We then produce mock lensed AGWB maps to check the imprints of gravitational lenses on the AGWB intensity anisotropies. We present our work here within the framework of standard ΛCDM scenario.

This thesis is organised as follows.

In Chapter 1, we first present in brief the SMC and its basic concepts.

In Chapter 2, we describe the thermal history of the Universe. This chapter deals with problems posed by the SMC, how inflation can solve these problems and how with the help of primordial power spectra we can read the earliest evolutionary phases of the Universe.

Chapter 3 describes how due to primordial inflationary era, the large scale structure of the Universe was formed and what are the current constraints on cosmological parameters. In this chapter, we provide detailed physics of gravitational lensing and report the mathematical framework needed for the following chapters.

In Chapter 4, the journey of relic photons forming CMB is described including CMB primary and secondary anisotropies. Since we implement lensing of GWs in similar manner to CMB lensing, this chapter includes a thorough description of weak lensing of CMB photons.

Chapter 5 presents physics of GWs starting from mathematical description of GW propagation, geometric optics approximation, sources and spectrum of GWs to physics of PGWs generated in the inflationary era. As we previously described, detection of such PGWs would give us hints of the physics very close to the Big Bang. Finally, this chapter presents how using GWs as standard sirens (GWSS), ongoing Hubble tension in cosmography can be eased.

In Chapter 6 we describe the physic of SGWB including GW sources, distribution, characterisation, analysis and how inhomogeneous spatial distribution of astrophysical GW sources leads to anisotropic energy density of the AGWB. Here, we describe the current mathematics for the angular power spectrum of anisotropic AGWB and motivate our work by presenting arguments how GW anisotropies can be numerically analysed in similar way to the CMB anisotropies. In this Chapter, we propose for the first time in literature, the terms- *primary anisotropies in the AGWB intensity* and *secondary anisotropies in the AGWB intensity* which are classified based on the source of the anisotropy, i.e. at the GW source level or at GW propagation level. Here we also present the mathematical framework needed to motivate how AGWB intensity anisotropies can be cross-correlated with various cosmological probes.

Chapter 7 is dedicated to GW detectors- both Earth-based and Space-based. We present overview of almost all current and upcoming missions, their detection sensitivities and how they can be helpful for the forthcoming new era of GWSS.

Finally, in Chapter 8 we provide our results on simulated AGWB maps, their cross-correlations signals with mock- WL convergence, CMB convergence, ISW/RS and galaxy distribution simulated from DEMNUni. We also describe the map-making procedure for weak lensing of SGWB via the DEMNUni simulations, and present the resulting lensed AGWB angular power spectrum.

We conclude by presenting briefly our main results and future prospects in the Conclusions.

If all you can do is crawl,
start crawling.

Rumi

Chapter 1

The standard model of cosmology

> There is nothing bigger or older than the Universe.
>
> *Stephen Hawking*

Cosmology is probably the most ancient branch of science which aims to understand the physics of the Universe as a whole and describes its evolution and structure on the very large scales. The Universe has always been an open platform offering infinite curiosities, possibilities and mysteries. Though our understanding of the Universe has always been challenged from time to time, starting from silent astounding sky gaze to being armed with giant space telescopes today, mankind has seeming come so far attempting to know the cosmos in a better and a deeper way. The Universe has always attracted wise men from age to age- starting from pure philosophical point of view to precise scientific perspective. From early idea of Plato-no human being is of serious importance to Copernican principle which denies the specific location of the Earth in the Universe, thanks to ardently questing cosmologists, we hope to attempt unfolding few mysteries of the Universe in future.

In this chapter, we present the current mathematical language which so far has been proven correct to describe the Universe on large scales. Thanks to Einstein's revolutionary *General Theory of Relativity* (GR) and contributions by many pioneers, we can try to study the Universe by a simple model encapsulated within mathematical language of GR and six cosmological parameters.

The evolution of the Universe is well described by the Standard Model of Cosmology which is also known as the *Hot Big Bang model*. The SMC is parametrized through the so-called ΛCDM model where Λ stands for elusive dark energy which is responsible for the late time accelerated expansion of the Universe. CDM is the abbreviation of *Cold Dark Matter* which is the prominent component responsible for the large scale structure formation in the Universe and provides extra mass density accounting for gravitational lensing. The SMC within the language of GR attempts to predict how the Universe evolved from initial singularity having infinite temperature, density and pressure and has been evolving for approximately 14 billion years resulting into what we see today as the observable Universe. According to the SMC, the Universe consist of 68% dark energy, 25% dark matter, 5% baryonic matter and 0.1% amount of radiation. The remarkable success of the *Hot Big Bang model* is that it is surprisingly a simple model using only six fundamental parameters to describe evolution and possible future

of the Universe. The SMC assumes *homogeneity* and *isotropy* on the larger scales ($\sim$ 100 Mpc). Thanks to this feature, the Universe generously allows us to make observations from any point of view which represents the Universe as a whole and can therefore be used to test different cosmological models. This assumption of large scale homogeneity and isotropy is known as the *Cosmological Principle* (i.e. absence of any privileged reference point) but this perception of smoothness changes when we observe the Universe on smaller scales. Universe is abundantly inhomogeneous on small scales in form of galaxies, clusters of galaxies and superclusters, etc. and we need to consider perturbations in the geometry describing the smooth Universe. The observable patch of the universe is $\approx$ 3000Mpc and the Universe continues to be homogeneous and isotropic over distances beyond the scale of observable patch. However it is tremendously inhomogeneous when observed on scales much larger than 3000Mpc.

The crucial evidence in favor of the Big Bang model comes from the detection of Cosmic Microwave Background (CMB) radiation which is uniformly distributed field of thermal radiation left over from the time of recombination. CMB being the primordial light in the Universe was originated when the photon energy reduced enough to become smaller than the electron binding energy in the hydrogen nucleus. Recombination indicates the earliest era of the Universe when the electrons and protons started to bound together in order to form hydrogen atoms; before this era the Compton scattering of electrons and high energy photons prevented those stable bounds which resulted into continuous scattering of photons. The newly formed lighter elements- mainly hydrogen and helium with traces of lithium reached their ground state by releasing photons (by a process called *photon decoupling*) which we see today as the uniformly distributed Cosmic Microwave Background. We present further details about CMB and its observable anisotropies in Chapter 2.

In addition to CMB, the SMC finds observational support in form of Hubble diagram indicating expansion of the Universe and light element abundance which is in accord with the Big Bang Nucleosynthesis (BBN). With the help of such experimental aids, we can constrain cosmological models and infer cosmological parameters; this include Baryonic Acoustic Oscillations (BAO) which can be used to constrain models using geometrical methods, Hubble parameter using redshift-distance relation through the observation of supernovae which helps us to determine expansion rate today, power spectrum of matter fluctuations for the late time matter distribution and the cluster counts and detection of weak lensing through cosmic shear may shed light on matter distribution on large scale.

In this Chapter we present the journey of the Universe for almost 13.8 billion years [2] assuming that *the Universe is homogeneous and isotropic on large scales* and we use *Einstein equations* based on his famous GR published in the paper "Cosmological Considerations of the General Theory of Relativity" [3] which describes the evolution of the system under the influence of gravity. In this thesis we will work with units ($c = h = 1$). Since Chapter 1 describes the fundamentals of SMC, we focus only on equations governing the dynamics and expansion of the Universe without developing full calculations, for further reading we request, e.g. Ref. [4], [5] and [6].

1.1 Homogeneity and isotropy

In this section, we discus one of the fundamental concepts on which the model of cosmology is built- the so-called *Cosmological principle*. This section is based on Ref.[5]. Entire standard model of cosmology is based on Cosmological Principle which states that when the Universe is observed on large scales ($\geq$100 Mpc) it demonstrates homogeneity and isotropy, indicating the absence of any specific location and any preferred direction in the Universe. *Homogeneity* mentions that the Universe looks the same at each point i.e. it is *translationally invariant* and by *isotropy*, the Universe mentions the property of *rotational invariance* i.e. it looks the same in all directions. A space which is everywhere isotropic is necessarily homogeneous, but the converse is not always true. Since the Universe is highly symmetric when observed on large scales, if the Universe appears isotropic about one location in the space, it would appear isotropic to other locations as well. Hence, the term isotropic may refer to isotropy about all locations. Hoyle, Bondi and Gold proposed the *perfect cosmological principle* in which the Universe apart from local fluctuations, was homogeneous in space and time both making the Universe appear the same to all observers at all times. This supports the fact why the Hubble parameter is constant and the Universe has exponential expansion [6]. Homogeneity is used to model the matter content of the Universe as a perfect fluid with no shear stresses, viscosity or heat conduction, and therefore fully characterized by two parameter only- its mass density ρ and pressure p.

Einstein made an assumption of isotropy and homogeneity in order to simplify mathematical calculations to describe evolution of the Universe. However this assumption shows experimental support too. To list a few, isotropy of the observed Universe finds evidence from uniformity of the temperature of the CMB, i.e. the intensity of CMB temperature is the same whichever direction we observe. Although motion of Earth relative to the cosmic rest frame results into dipole anisotropies, the temperature difference is very minute. The striking uniformity of the CMB is a clear indication that at the epoch of the last scattering, the CMB was extremely isotropic and homogeneous. In addition to CMB, isotropy of the Universe also gets evidence from isotropic X-ray radiation background due to distribution of radio sources and galaxies. Therefore, the observed higher degree of isotropy provides strong evidence for the present level of large-scale homogeneity and isotropy of our Hubble-volume.

Evidences for homogeneity of the Universe include galaxy count surveys and determination of peculiar velocity field of the Universe. Here, the term peculiar velocity refers to the motion of a cosmological object (the four velocity u^μ) with respect to the cosmic rest frame which is defined by the rest frame of the CMB. However it is worthy to mention that assumption of homogeneity and isotropy made by Einstein is just for the sake of simplicity of mathematical treatment which changes to very complex inhomogeneous metric structure when dealt with nearby scales. Observations of CMB aniostropies suggest that the presence of primordial fluctuations which grew during inflation, lead to the formation of large scale structure thanks to their mutual gravitational attraction. Inflation provides the much needed way to generate primordial perturbations that broke the ideal homogeneity and isotropy allowing the structures to form. To study this structures we must introduce perturbations using the *cosmological perturbation theory* in the metric defining geometry of the spacetime by carrying out Fourier expansion in comoving wavenumber k. The inverse wavenumber defines

a length scale corresponding to a particular mode of inhomogeneities. Since this thesis deals with late time Universe- accessing effects of stochastic background generated by GWs emitted from astrophysical sources and lensing phenomena they experience while traveling on large distances before reaching us, we will not mention details of perturbation theory and focus mainly assuming large scale flatness of the Universe.

In brief, it is observed experimentally that the distribution of the galaxies is homogeneous and isotropic on scales larger than 100 Mpc [7] and thanks to Planck collaboration, intensity of the CMB radiation is astonishingly homogeneous and isotropic with anisotropies being of the order of $\Delta T/T \simeq 10^{-5}$ (2013 [8], 2015 [9] and 2018 [2]). Hence, the cosmological principle is not exact, at least when observed on the nearby scales; it is actually a global property of the Universe, breaking down when observed locally.

1.2 Geometry and dynamics of the Universe

The dynamics of the expanding Universe are characterised by the expansion rate given by the Hubble parameter and the spatial curvature which is determined by the different matter content in the Universe [10]. The SMC is formulated in terms of spacetime metric which is also called the Friedmann–Lemaître–Robertson–Walker (FLRW) metric. In GR, the spacelike hypersurface of constant time t define the *slicing* to the four dimensional spacetime and the timelike worldlines of constant X define *threading*. The FLRW threading corresponds to motion of comoving observers who see zero momentum density at their location. FLRW metric is the exact solution of Einstein Field Equations (EFEs) assuming the validity of cosmological principle. If the FLRW metric equations are assumed to be valid to all the way back to the beginning of the Universe, they lead us to a point where distances between objects in the Universe were infinitesimally small. Hence FLRW metric going backward leads us to the Big Bang singularity and extending forward provides us a model of the Universe that matches current observations in close approximation. In this section we will present vital mathematical treatment needed to obtain theoretical predictions from the SMC.

1.2.1 The Friedmann–Lemaître–Robertson–Walker metric

Entire ΛCDM model is built on the base of GR valid on the cosmological scales $r \gg 10h^{-1}Mpc$, which gives birth to a branch called the *Relativistic cosmology* [11]. One of the fundamental ideas of GR is the equivalence of free-fall of reference frames which lead Einstein to conclude that gravitation is actually not a force, instead it is the curvature of spacetime which is related closely with the mass-energy. If we consider a particle in a free-fall state whose trajectory in spacetime is defined by *geodesic* and if gravitational field due to mass locally curves the spacetime (and remains flat in the absence of it), its geometry is formulated in terms of a metric tensor denoted by $g_{\mu\nu}$. This metric tensor characterizes the invariant line element ds^2 for a local 4-space coordinates of non-Euclidean geometry as follows:

$$ds^2 = g_{\mu\nu}dx^\mu dx^\nu \tag{1.1}$$

where, $x^\mu = (x^0, x^i)$ is a set of coordinates with $x^0 = t$ is the time coordinate and x^i are three spacial coordinates. The metric describes the connection between

spacetime events and all geometrical and causal structures of spacetime. In our sign convention, we follow Lorentzian sign convention following $(-,+,+,+)$, repeated indices being summed over and Greek letter indices span four dimensional spacetime indices $\mu, \nu, ... = 0, 1, 2, 3$ and Latin letter $i, j, ... = 1, 2, 3$ for the space coordinates. ds^2 is the distance between two points and $g_{\mu\nu}$ is the metric describing the geometric properties of the spacetime. The spacetime metric defined in Eq.1.1 is invariant under coordinate transformation, this phenomena is known as *diffeomorphism invariance* and it shows that all observers in different inertial frames will measure the same interval. The invariant interval ds^2 defines boundary of the causal structure of the spacetime. This spacetime interval can be positive, negative or zero: when $ds^2 < 0$ it defines *time-like* interval ($\sqrt{ds^2}$ defining proper time), $ds^2 = 0$ defines the *lightlike* or *null* interval and $ds^2 > 0$ defines the *spacelike* interval. The inverse metric is denoted with upper indices following property: $g^{\mu\alpha} g_{\mu\beta} = \delta^{\alpha}_{\beta}$, where δ^{α}_{β} is the Kronecker delta function. Since the metric $g_{\mu\nu}$ is a tensor, it has specific transformation properties under change of coordinates:

$$g_{\mu\nu} = \frac{\partial x^{\mu'}}{\partial x^{\mu}} \frac{\partial x^{\nu'}}{\partial x^{\nu}} g_{\mu'\nu'} \tag{1.2}$$

Thus the behaviour of this metric tensor depends on the mass-energy of the test particle summarised in form of EFEs as follows:

$$G_{\mu\nu}(x) = 8\pi G T_{\mu\nu}(x) \tag{1.3}$$

Here, $G_{\mu\nu}$ is the *Einstein tensor* quantifying the behaviour of the metric tensor $g_{\mu\nu}$, $T_{\mu\nu}$ is the *energy-momentum tensor* representing the energy, momentum density, shear and pressure [11], G is the Newton's gravitational constant related to Planck mass by $M_P = 1/\sqrt{8\pi G}$ and c is the speed of light in vacuum. The left hand side describes the curvature of the spacetime in the Einstein tensor $G_{\mu\nu}$ and, the right hand side describes the distribution of matter and energy in form of the energy-momentum tensor $T_{\mu\nu}$[12]. This equation is the covariant generalization of the Poisson equation for the Newtonian gravitational potential. The energy-momentum tensor in component form can be written as [13],

$$T_{\mu\nu} = \begin{pmatrix} T_{00} & T_{01} & T_{02} & T_{03} \\ T_{10} & T_{11} & T_{12} & T_{13} \\ T_{20} & T_{21} & T_{22} & T_{23} \\ T_{30} & T_{31} & T_{32} & T_{33} \end{pmatrix} \tag{1.4}$$

where,
T_{00} = energy density,
T_{i0} = momentum density,
T_{0i} = energy flux,
T_{ij} = pressure and,
$T_{ij}|_{i\neq j}$ = shear forces.

Hence, $T_{\mu\nu}$ depends only on the content of the Universe. Left hand side of Eq.(1.3) is geometrical while right hand side is describing the physical content of the Universe [13]. Local conservation of mass and momentum can be expressed using energy-momentum tensor,

$$T^{\mu\nu}_{;\nu} = 0 \tag{1.5}$$

where, $;\nu$ denotes the covariant derivative of $T_{\mu\nu}$ with respect to ν. If we assume perfect fluid description of the Universe (absence of shear stress, energy or momentum flux), the energy-momentum tensor would be,

$$T_{\mu\nu} = (\rho + p)u_\mu u_\nu + p g_{\mu\nu} \tag{1.6}$$

where, ρ is the mass density, p is the pressure of the perfect fluid, u_μ is the 4-velocity of the fluid ($u^\mu = (1, 0, 0, 0)$) and $g_{\mu\nu}$ is the spacetime metric. Eq.(1.6) is the most compatible form of the stress-energy tensor with the homogeneity and isotropy and this stress-energy tensor becomes diagonal for a perfect fluid [14]:

$$T^\mu_\nu = (-\rho, p, p, p) \tag{1.7}$$

The stress-energy tensor of the perfect fluid in Eq.(1.6) will have the trace: $T = T^\mu_\mu = -\rho + 3p$.

In a comoving orthonormal basis, the energy-momentum tensor becomes [13],

$$T_{\hat{\mu}\hat{\nu}} = \begin{pmatrix} \rho & 0 & 0 & 0 \\ 0 & p & 0 & 0 \\ 0 & 0 & p & 0 \\ 0 & 0 & 0 & p \end{pmatrix} \tag{1.8}$$

where, hat in Eq.(1.8) stands for orthonormal comoving basis. For the barotropic fluid (i.e. the pressure of each fluid can be expressed as a function of its density alone), using the *Equation of State* (EoS), we can relate pressure (p) and density (ρ) of the cosmic fluid by assuming a linear relation,

$$p = w\rho \tag{1.9}$$

where w is called the equation of state parameter which depends on the nature of the fluid.

Now, the metric $g_{\mu\nu}$ must be symmetric 4×4 tensor having 4 diagonal and 6 off-diagonal independent components. Friedmann showed that using the cosmological principle, one can build a coordinate system to solve Einstein equations for a dynamical model that describe a homogeneous, isotropic and expanding Universe. Cosmological principle restricts various possibilities for such a metric: due to homogeneity, we can define a metric with radial dependence and use a parameter, lets say k to mention possible variations in the spatial curvature (*curvature of the spacetime*) and isotropy restricts us to define a spatial metric through the infinitesimal 4-line element ds such that it is independent of the spatial curvature. Since metric describes the Universe, it must obey homogeneity and isotropy by remaining rotational and transitional invariant. In order to mention possible time dependence of space component of the metric, we use an arbitrary function $a(t)$ known as *the Robertson-Walker scale factor* having dimension of length. This scale factor is associated with the expansion of the Universe and, increasing value of $a(t)$ indicates decreasing number densities of matter or radiation for particular comoving coordinate system. For convenience we consider spherical coordinates and using gauge freedom to arbitrarily fixing some terms of the metric

($g_{00} = 1$ and $g_{0i} = 0$) the metric for a space with homogeneous and isotropic spatial sections is the maximally-symmetric *FLRW metric* given as,

$$ds^2 = -dt^2 + a^2(t)\left[\frac{1}{1-kr^2}dr^2 + r^2(d\theta^2 + \sin^2\theta d\phi^2)\right] \tag{1.10}$$

Here, $k = 0$ stands for flat and infinite Universe, $k = +1$ denotes spherical and finite (closed) Universe and $k = -1$ denotes hyperbolic and infinite (open) Universe respectively. This metric corresponds to a specific gauge, i.e. a choice of coordinates in which the Universe appears spatially isotropic and homogeneous, defined by $x^\mu = (t, r, \theta, \phi)$ which is known as *comoving coordinates*. An object at rest with respect to comoving coordinates will remain at rest with time, it keeps moving the expansion of the Universe. If an object has velocity w.r.t. the comoving coordinates due to gravitational interactions, then the object is said to have the *peculiar velocity* which is important when considering Hubble's law. In the FLRW metric, the spatial term is modulated by the *scale factor* denoting the expansion of the Universe whose present value is denoted by $a(t_0) = 1$. The angular distance depends on the radial function $f_k(r)$ which is either a trigonometric, hyperbolic or a linear function of r depending on whether the curvature is positive, negative or zero respectively:

$$f_k(r) = \begin{cases} k^{-1/2}\sin(\sqrt{k}x) & k > 0 \\ r & k = 0 \\ (-k)^{-1/2}\sinh[(\sqrt{-k})x] & k < 0 \end{cases} \tag{1.11}$$

If considered local observer, GR can be approximated with the theory of special relativity described by the Minkowsky spacetime metric $\eta_{\mu\nu} = diag(-1, +1, +1, +1)$. The FLRW metric $g_{\mu\nu}$ can be approximated by Minkowsky metric only locally $\eta_{\mu\nu}$ ($g_{\mu\nu} \approx \eta_{\mu\nu}$). From the isotropy of the Universe, the off-diagonal terms $g_{\mu\nu}$ with $\mu \neq \nu$ must vanish and from the property of homogeneity, $g_{\mu\nu}$ in Cartesian coordinates must be independent on the spatial coordinates. For a flat Universe, the metric can be written as,

$$g_{\mu\nu} = \begin{pmatrix} -1 & 0 & 0 & 0 \\ 0 & a^2(t) & 0 & 0 \\ 0 & 0 & a^2(t) & 0 \\ 0 & 0 & 0 & a^2(t) \end{pmatrix} \tag{1.12}$$

hence, Eq.(1.10) becomes,

$$ds^2 = -dt^2 + a^2(t)\delta_{ij}dx^i dx^j \tag{1.13}$$

where, $\delta_{i,j} = \text{diag}(+1, +1, +1)$ is the Kronecker delta in Euclidean space.

Having known $g_{\mu\nu}$, we can study particle trajectory in the spacetime, for this it is worth to obtain the *Christoffel symbol* which is symmetric in indices μ and ν:

$$\Gamma^\rho_{\mu\nu} \equiv \frac{g^{\rho\tau}}{2}(\partial_\mu g_{\nu\tau} + \partial_\nu g_{\mu\tau} - \partial_\tau g_{\mu\nu}) \tag{1.14}$$

where, notation is $\partial_\mu g_{\nu\tau} = \frac{\partial g_{\nu\tau}}{\partial x^\mu}$.

The geodesic defines particle trajectory in the spacetime in the absence of any forces (a straight line), Christoffel symbols are used in determining such a particle trajectory [15]:

$$\frac{d^2x^\mu}{d\lambda^2} = -\Gamma^\mu_{\alpha\beta}\frac{dx^\alpha}{d\lambda}\frac{dx^\beta}{d\lambda} \tag{1.15}$$

where, λ can be any scalar parameter describing position on the geodesic which we can consider analogous to conformal time. We need to compute components of Christoffel symbol from metric $g_{\mu\nu}$ using definition of Eq.(1.14) and insert them in Eq.(1.15). For a flat Universe having the FLRW metric written in Cartesian coordinate system, most of the derivatives of $g_{\mu\nu}$ and most of the components of $\Gamma^\rho_{\mu\nu}$ vanish, so we get:

$$\Gamma^0_{0\mu} = \Gamma^0_{\mu 0} = 0 \tag{1.16}$$

$$\Gamma^0_{ij} = \delta_{ij}\dot{a}a \tag{1.17}$$

$$\Gamma^i_{0j} = \Gamma^i_{j0} = \delta_{ij}\frac{\dot{a}}{a} \tag{1.18}$$

$$\Gamma^i_{\alpha\beta} = 0 \tag{1.19}$$

With the help of Christoffel symbols we can define *Ricci tensor* which is symmetric in the indices μ and ν:

$$R_{\mu\nu} \equiv \partial_\alpha\Gamma^\alpha_{\mu\nu} - \partial_\nu\Gamma^\alpha_{\mu\alpha} + \Gamma^\alpha_{\beta\alpha}\Gamma^\beta_{\mu\nu} - \Gamma^\alpha_{\beta\nu}\Gamma^\beta_{\mu\alpha} \tag{1.20}$$

The trace of the Ricci tensor is called the *Ricci scalar*:

$$\mathcal{R} \equiv R^\mu_\mu = g^{\mu\nu}R_{\mu\nu} \tag{1.21}$$

where $g^{\mu\nu} = diag(-1, a^{-1}, a^{-1}, a^{-1})$ is the inverse of $g_{\mu\nu}$.

The Ricci tensor is diagonal with components given by:

$$R_{00} = -3\frac{\ddot{a}}{a} \tag{1.22}$$

$$R_{ij} = \delta_{ij}(2\dot{a}^2 + a\ddot{a}) \tag{1.23}$$

While the Ricci scalar is simply the trace of the Ricci tensor given by:

$$\mathcal{R} = 6\left(\frac{\ddot{a}}{a} + \frac{\dot{a}^2}{a^2}\right) \tag{1.24}$$

The Riemann tensor has many symmetry properties in permutations of its indices. Bianchi identities is a differential identity which is an important consequence of symmetry:

$$\nabla_\lambda R_{\rho\sigma\mu\nu} + \nabla_\rho R_{\sigma\lambda\mu\nu} + \nabla_\sigma R_{\lambda\rho\mu\nu} = 0 \tag{1.25}$$

These quantities- Christoffel symbols and its components, Ricci tensor and Ricci scalar are used in Einstein equations, which we shall discuss in the next section.

1.2.2 Einstein Field Equations

Einstein equations can be used to derive evolution of the Universe with time,

$$G_{\mu\nu} = 8\pi G T_{\mu\nu} \tag{1.26}$$

where,

$$G_{\mu\nu} \equiv R_{\mu\nu} - \frac{1}{2}\mathcal{R}g_{\mu\nu} \tag{1.27}$$

is the Einstein tensor and $G = 6.67 \times 10^{-11} m^3 s^{-2} K g^{-1}$ is the Newton's constant. The twice contracted Bianchi identity implies conservation of the Einstein tensor:

$$\nabla^{\mu} G_{\mu\nu} = 0 \tag{1.28}$$

The Einstein equations are reduced from 10 independent sets of equations to only 2 (the time-time component and the space-space component) as follows:

$$G_{00} = 8\pi G\rho \tag{1.29}$$

$$G_{ii} = 8\pi G p \tag{1.30}$$

Calculating the tensors G_{00} and G_{ij} using the FLRW metric, we can obtain the Friedmann equations which we should see in the next subsection. Since stress-energy tensor $T_{\mu\nu}$ contains all information about the energy content of the Universe, for a homogeneous and isotropic fluid it can be written as:

$$T_{\mu\nu} = diag(\rho, p, p, p) \tag{1.31}$$

where, ρ and p are the energy density and pressure of the fluid respectively. We can define ρ and p using momentum distribution function [15] by denoting momentum by P and degeneracy of the spices by g:

$$\rho = g \int \frac{d^3P}{(2\pi)^3} f(P) E(P) \tag{1.32}$$

$$p = g \int \frac{d^3P}{(2\pi)^3} f(P) \frac{P^2}{3E(P)} \tag{1.33}$$

Due to conservation laws, the covariant derivatives of stress-energy tensor must vanish:

$$D_{\mu} T^{\mu}_{\nu} \equiv \partial_{\mu} T^{\mu}_{\nu} + \Gamma^{\mu}_{\alpha\mu} T^{\alpha}_{\nu} - \Gamma^{\alpha}_{\mu\nu} T^{\mu}_{\alpha} = 0 \tag{1.34}$$

This is the general relativity equivalent of the continuity equation. For a perfect fluid with the stress-energy tensor in Eq.(1.31), the $\nu = 0$ component of Eq.(1.34) is

$$\dot{\rho} + 3\frac{\dot{a}}{a}(\rho + p) = \dot{\rho} + 3\frac{\dot{a}}{a}(1 + w)\rho = 0 \tag{1.35}$$

$$\dot{\rho} + 3\frac{\dot{a}}{a}(\rho + P) = a^{-3}\frac{\partial(\rho a^{3(1+w)})}{\partial t} = 0 \tag{1.36}$$

where, we have used the equation of state $p = w\rho$

Using the Hubble parameter $H = \dot{a}/a$ and conservation of the stress-energy tensor ($\nabla_\mu T_{\mu\nu} = 0$) we can obtain the *energy conservation law for fluid components* within the cosmological context:

$$\dot{\rho} = -3H(\rho + p) \tag{1.37}$$

For a generic fluid, w, the solution of Eq.(1.37) would be the density evolution given as:

$$\rho(t) = \rho_0 a^{-3(w+1)} \tag{1.38}$$

The matter content of the Universe includes contribution from non-relativistic baryonic matter and cold dark matter following $p << \rho c^2$ in good approximation. As a result the matter is called pressure-less that is assumed to follow $w = 0$. The components including relativistic photons and neutrinos have pressure components following $p = \rho c^2/3$. Since equations of state would be different for different fluids, the scaling of the energy density would be different during expansion:

$$w_r = 1/3, \quad \rho_r \propto a^{-4}(t), \tag{1.39}$$

$$w_m = 0, \quad \rho_m \propto a^{-3}(t), \tag{1.40}$$

where, subscripts r and m denotes radiation/relativistic particles and non-relativistic matter respectively. Thus it is clear from above equations that the radiation energy density drops more quickly with time than matter energy density. When the scale factor was small, the densities were necessarily higher [4]. Though in the present Universe these contributions are less dominant compared to the early Universe.

Our Universe is not composed of single perfect fluid, rather it has a combination of different components with different density, the energy density of different component evolves differently indicating different phase in the thermal history of the Universe.

According to the ΛCDM model, the Universe was initially dominated by radiation having all relativistic species of particles and later in the evolutionary stage, reached to non-relativistic matter dominated phase where total energy-density diminishes slower than radiation energy density. In the current stage when the Universe experiences acceleration due to enigmatic *dark energy*, it is necessary to introduce a *cosmological constant* Λ having negative pressure. The current phase of accelerated expansion cannot be a radiation or matter dominated phase as these components do not give accelerated expansion. Introducing Λ, the corresponding equation of state is $w = -1$ and ρ_Λ is constant over time following Eq. (1.37). We can include Λ in the stress-energy tensor and it can be considered as a new fluid.

If the Universe is accelerating in the current time, then it must be in Λ-dominated phase, which can be seen from the solution of the time-time component of the Einstein equation described in next sub-section. The current measurements of the CMB supports late time expansion of the Universe dominated by energy following equation of state: $w = -1$ [2].

1.2.3 The Friedmann's equations

Once metric is established- Eq.(1.2), we can calculate the equations describing motion and evolution for the Universe. If we insert Eq.(1.27) into Eq.(1.23) with Ricci tensor and Ricci scalar as defined in Eq.(1.20), Eq.(1.21) and Eq.(1.24) we obtain two different independent differential equations- the so-called Friedmann equations corresponding to the 00 (time-time) and ii (space-space) components:

$$\boxed{H^2 = \left(\frac{\dot{a}}{a}\right)^2 = \frac{8\pi G}{3}\rho} \tag{1.41}$$

This is known as the *first Friedmann equation* and H is known as the Hubble parameter which describes *the rate of expansion of the Universe.*

$$H(t) \equiv \frac{\dot{a}}{a} \tag{1.42}$$

where dot denotes derivative with respect to time, i.e. $\dot{a} = da/dt$. The Hubble parameter has units of inverse time and is positive for an expanding Universe. The Hubble parameter for today H_0 is called *Hubble constant* which is measured about $70 kms^{-1}Mpc^{-1}$. The reciprocal of the Hubble constant is known as the *Hubble time* $t_H \equiv H^{-1}$ which represents the time galaxies could have taken to attain their present separation starting from a condition of infinite compaction [16]. The Hubble parameter is the defining parameter for distance measurements on the cosmological scale as it sets the characteristic time-scale of the homogeneous Universe in form of Hubble time scaling the age of the Universe, and characteristic length-scale in form of *Hubble length* which sets the size of the observable Universe.

It gives the connection between the density of the Universe and its geometry.

And,

$$\boxed{\dot{H} + H^2 = \frac{\ddot{a}}{a} = -\frac{4\pi G}{3}(\rho + 3p)} \tag{1.43}$$

where, $\rho = \Sigma\rho_i$ and $p = \Sigma p_i$ are the total energy density and pressure of the Universe respectively which include contribution from all the existing spices: baryons, photons, neutrino, dark matter and cosmological constant. Eq.(1.42) is known as the *second Friedmann equation* or the *Raychaudhari equation* describing the *acceleration of the scale factor.*

The combination of these two Friedmann equations along with conservation law, supplemented with equation of state forms a system of equations that determines the the unknown functions $a(t)$ and $\rho(t)$.

The contribution of these species is different at different evolutionary stages of the Universe- relativistic components (photons, baryons and neutrinos before non-relativistic transition) contribute at the early stages known as the *radiation dominated era* (RD) and non-relativistic components (baryons and neutrinos after the non-relativistic transition and dark matter) contributing to the *matter dominated era* (MD).

However, Einstein before discovery of Hubble's law introduced a cosmological constant Λ in his equations in order to maintain static Universe which he later famously called as his biggest blunder. Introducing Λ, Eq.(1.26) becomes:

$$G_{\mu\nu} + \Lambda_{\mu\nu} = 8\pi G T_{\mu\nu} \tag{1.44}$$

For this Einstein equation, the Friedmann solution would be:

$$\left(\frac{\dot{a}}{a}\right)^2 = \frac{8\pi G}{3}\rho - \frac{k}{a^2} + \frac{\Lambda}{3} \tag{1.45}$$

$$\frac{\ddot{a}}{a} = -\frac{4\pi G}{3}\Big(\rho + 3p\Big) + \frac{\Lambda}{3} \tag{1.46}$$

The presence of ρ which shows mass-energy prevents the acceleration of the Universe, on the other hand, the Λ term with opposite sign changes the dynamics of the Universe due to its opposite sign. Therefore if the value of Λ term dominates other terms, it can make the Universe to expand with positive acceleration of the scale factor. The energy density due to the cosmological constant remains constant in time which using Eq.(1.38) implies,

$$-3(w_\Lambda + 1) = 0, \implies w_\Lambda = -1 \implies p_\Lambda = -\rho_\Lambda \tag{1.47}$$

Therefore, the cosmological constant has negative pressure. If this term is dominant then from Eq.(1.46) and (1.45), we obtain an expanding and accelerating Universe. So, when the Universe has very small scale factor, it denotes the radiation domination era and it was in matter dominated phase until the curvature density becames the leading term in total energy density. Finally it is the cosmological constant term dominating in the later evolutionary stages of the Universe when it enters accelerated expansion phase.

The cosmological constant ($w = -1$) can be described by some unknown species that contribute with negative pressure. In this case the component that substitutes the cosmological constant is known as dark energy and can have generic $w < -1/3$ required to have an accelerated expansion, with a possible dependence $w(t)$ [15].

Critical energy density of the Universe is defined as:

$$\rho_c(t) \equiv \frac{3H(t)^2}{8\pi G} \quad \text{and} \quad \rho_{c,0} = 1.88h^2 \times 10^{-29} g cm^{-3} \tag{1.48}$$

Fig.1.1 shows evolution of energy density of different cosmic components[1] normalized to critical density today as a function of scale factor:

Critical energy density defines the total energy density of the flat Universe at a given time in the absence of a cosmological constant. A Universe with $\rho > \rho_c$ will be spatially closed and the one with $\rho < \rho_c$ will be spatially open. $\rho_{c,0}$ defines the value of critical energy density today which depends on the current value of Hubble parameter H_0. Using the ρ_c we can define the *density parameter* which is the ratio of the absolute energy density ρ to the critical energy density ρ_c corresponding to each different spices:

$$\Omega_i \equiv \frac{\rho_i}{\rho_c} = \frac{8\pi G}{3H^2}\rho_i \tag{1.49}$$

here we can use different subscripts e.g. $i = \Lambda, k, m, r$ corresponding to the cosmological constant, curvature, matter and radiation respectively. Since ρ and H are

[1] General Relativity, Black Holes, and Cosmology by Andrew J. S. Hamilton

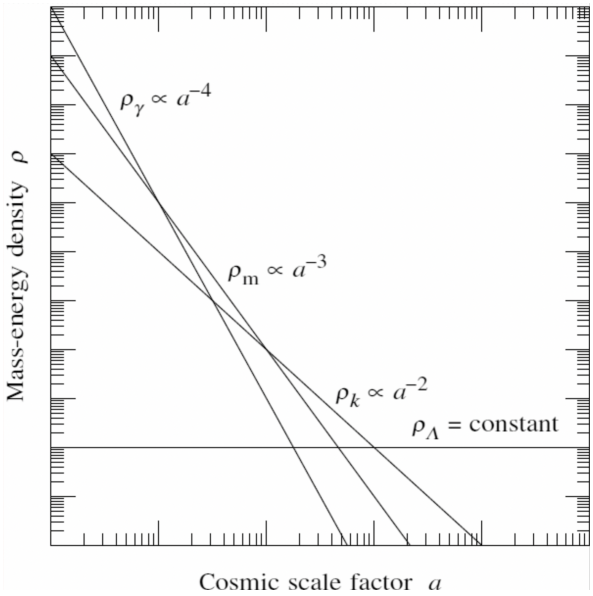

Figure 1.1: The evolution of scale factor related with energy densities for different components (matter, radiation, curvature and cosmological constant).

both time dependent, Eq.(1.48) defines an epoch-dependent density parameter and its present value is denoted by ρ_0 expressed as [6]:

$$\rho_0 = 1.88 \times 10^{-26} \Omega h^2 kgm^{-3} = 2.78 \times 10^{11} \Omega h^2 M_\odot Mpc^{-3} \tag{1.50}$$

Considering contribution from different above mentioned components, the first Friedmann equation becomes:

$$H^2(t) = \frac{8\pi G\rho(t)}{3} = H_0(t)^2(\Omega_\Lambda^0 + \Omega_k^0 a^{-2} + \Omega_m^0 a^{-3} + \Omega_r^0 a^{-4}) \tag{1.51}$$

This equation suggests that the evolution of the Universe depends on the relative amount of energy density corresponding to each fluid. At different cosmic times, one of the contributors in Eq.(1.51) is dominant and the evolution rate $H = \dot{a}/a$ has a different behaviour. If we consider $a = 1$ in Eq.(1.50), we obtain following relation between all density parameters:

$$\Omega_\Lambda^0 + \Omega_k^0 + \Omega_m^0 + \Omega_r^0 = 1 \tag{1.52}$$

where the density parameter of the curvature, cosmological constant, matter and radiation are defined by,

$$\Omega_k(t) \equiv -\frac{k}{a^2(t)H^2(t)} \tag{1.53}$$

$$\Omega_\Lambda(t) \equiv \frac{\Lambda}{3H_0^2} \tag{1.54}$$

$$\Omega_m(t) \equiv \frac{\rho_m}{\rho_c} \tag{1.55}$$

$$\Omega_r(t) \equiv \frac{\rho_r}{\rho_c} \tag{1.56}$$

Evolution of various contributions to $H(a)$ is shown in Fig.1.2:

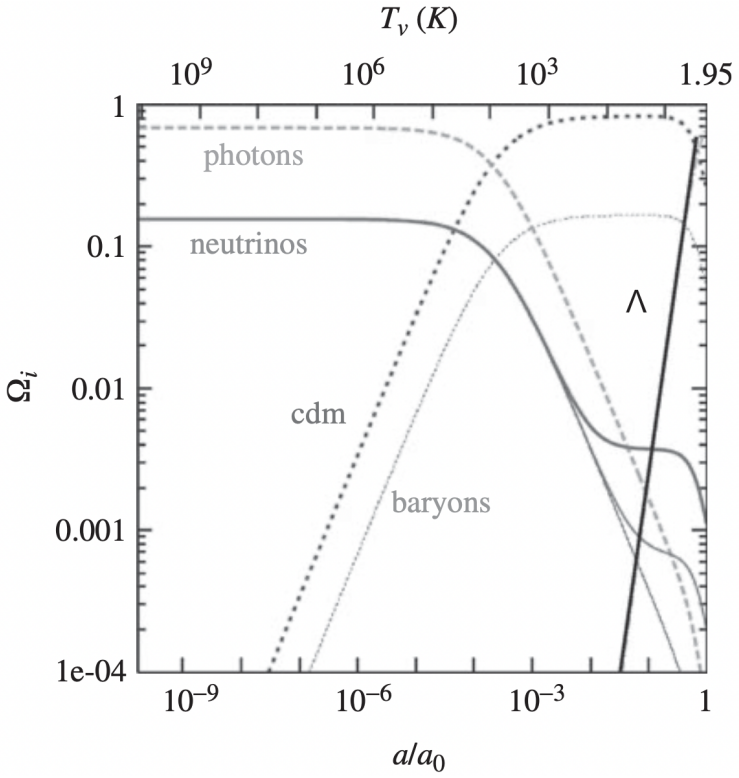

Figure 1.2: Evolution of the fractional energy density Ω of photons, three massive neutrinos ($m_\nu = 0, 0.05, 0.009$eV), CDM, baryons and Λ as a function of scale factor a/a_0 or of the neutrino temperature T_ν. There is the change in the behaviour of two massive neutrino contributions when they become non-relativistic particles as seen from the plot [17].

For $\Omega_r(t)$ it is useful to express the quantity as a function of the frequency of the source of radiation. In logarithmic scale,

$$\Omega_r(t) = \int \Omega_r(f) d\ln f \tag{1.57}$$

where,

$$\boxed{\Omega_r(f) \equiv \frac{1}{\rho_c}\frac{d\rho_r}{d\ln f}} \tag{1.58}$$

which is widely used in analysing GWs.

Considering the equation of state $p_i = w_i\rho_i$ of the different components, it is possible to obtain the relation between density and scale factor which indicates what kind of energy density would be dominant for a particular interval of time defining *cosmological era*. Restating Eq.(1.38) as

$$\rho \propto a^{-n_i} \tag{1.59}$$

where, $n_i = 3(1 + w_i)$. Following table 1.1 gives various values of energy densities:

component	w_i	n_i	$\rho(a)$	$a(t)$	$a(\tau)$	τ_i
matter	0	3	a^{-3}	$t^{2/3}$	τ^2	0
radiation	1/3	4	a^{-4}	$t^{1/2}$	τ	0
vacuum	-1	0	a^0	e^{Ht}	$-\tau^{-1}$	$-\infty$

Table 1.1: Values of w_i, evolution power of energy densities, FLRW solutions for a flat Universe dominated by matter, radiation and a cosmological constant.

1.3 Expansion of the Universe and the Hubble law

Expansion of the Universe is a fact that finds many observational supports like Hubble's law derived from receding galaxies and observational data from Supernovae Type Ia (SNIa). Figure 1.3 shows the original plot by Hubble showing receding galaxies with their recessional velocity in linear proportion to their distance and Figure 1.4 shows the Hubble diagram from Type Ia supernovae respectively:

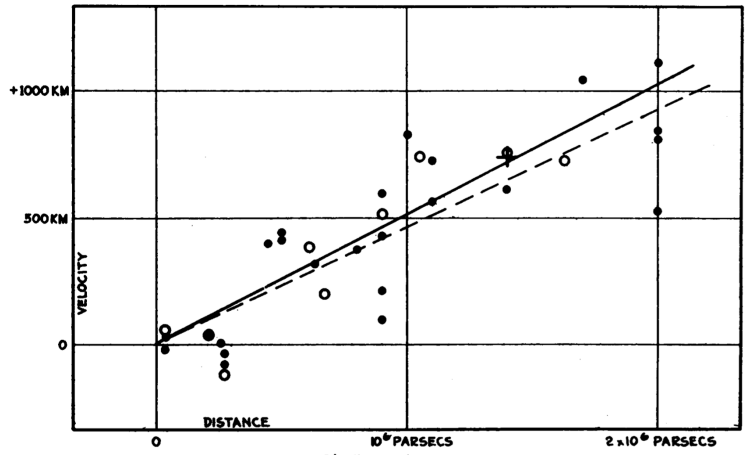

Figure 1.3: Velocity-distance relation among extra-galactic nebulae showing a clear evidence of expansion of the Universe, original plot reproduced from [18].

The expansion of the Universe can be explained by introducing scale factor $a = a(t)$ whose present value is $a_0 = a_0(t) = 1$. Using the scale factor we can define the *comoving distance* which is the physical distance in terms of the scale factor. If two particles are at rest during the expansion of the Universe then their comoving distance remains constant. Whereas *physical distance* evolves with time as it is proportional to the scale factor. The *comoving frame* is a reference frame where the coordinates of an observer at rest remains unchanged under evolution (expansion) of the Universe and comoving distance is used to measure distance between two points in such frame. Therefore an observer at rest has constant comoving coordinates but the physical coordinates do evolve with time scaling with scale factor a. The mathematical relation between comoving distances (d_C) and physical distance (d_P) is given by $d_P(t) = a(t)d_C$. So in general the expansion of the Universe means that the proper physical distance between a pair of well-separated galaxies increases with time, that is the galaxies are receding from each other.

Current understanding enriched by observations suggests that Universe experiences

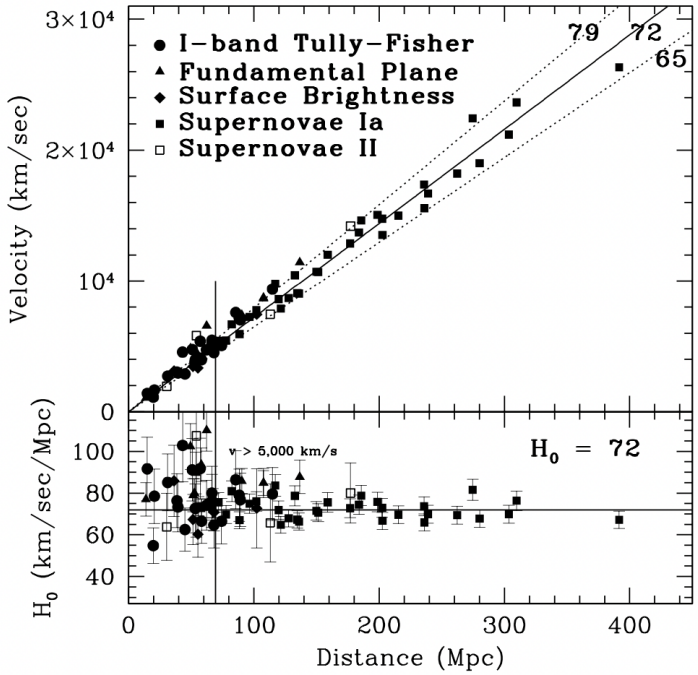

Figure 1.4: Hubble diagram using different measurements of distance as mentioned in the plot (Tully-Fisher, fundamental plane, surface brightness, SN Ia and SN II) with the bottom panel showing H_0 vs distance with the horizontal line equal to the best fit value of $72 kms^{-1}Mpc^{-1}$. The bottom panel shows the residuals in the H_0 as a function of velocity. Original diagram is taken from [19].

expansion due to repulsive *Dark Energy* capable enough to overcome attractive gravity. This acceleration could also be due to presence of *cosmological constant* Λ term present in the Einstein equations. Einstein introduced cosmological constant in order to achieve the static Universe which later on by discovery of Hubble's law was abandoned. However, a positive and sufficiently large Λ can overcome the gravitational attractive force to provide repulsion leading to acceleration o the Universe [20].

Another factor important to understand expanding Universe is through geometry of the Universe. As discussed previously there are three possibilities for the spacetime geometry: *flat, open* and *closed* Universe. In flat Universe, geometry follow Euclidean treatment where initially parallel trajectories remain parallel. Whereas in open/closed Universe, the trajectories will diverge/converge during their motion if they travel on parallel trajectories initially. A flat, open or closed Universe respectively has zero, negative or positive curvature or in other words, positive, negative or zero spatial curvature respectively corresponds to spatially closed, open or flat Universe. Fig.1.5 show geometry of the Universe in these three cases:

If in the comoving frames, the peculiar velocities of the objects (e.g. galaxies) is absent i.e. $\dot{r} = 0$, the relative velocities between the objects depends on their distance:

$$v \equiv \dot{d_p} = \dot{a(t)}r = H(t)d_p \tag{1.60}$$

Hubble, in 1929 observed the linear relation between distance and redshift based

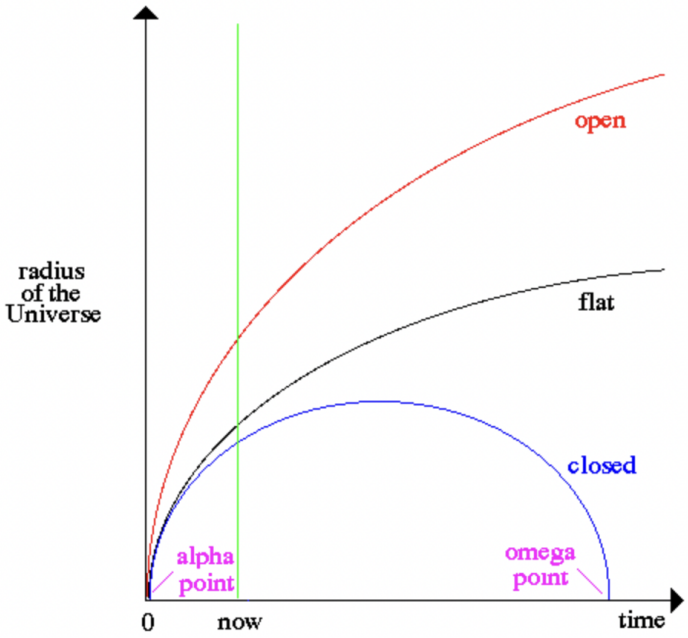

Figure 1.5: Different cases for evolution of the Universe based on the geometry of the spacetime: if the actual density of the Universe is greater than the critical energy density, the Universe would be closed and in future it would be contracting leading to a big crunch. If the energy density is equal to the critical one, it should lead to an open Universe where cosmological constant would be responsible for accelerated expansion of the matter. In an open Universe scenario, the Universe keeps expanding at an ever-increasing rate whereas in a flat Universe, it keeps expanding but as it grows bigger, the rate of expansion slows.

on individual distance measurements of about twenty-four relatively bright galaxies at redshifts $v = cz \leq 1000 kms^{-1}$ [21] and discovered that distant galaxies were receding away from Earth and the receding velocity was found proportional to the relative distance between them. This result of his study is known as the *Hubble diagram* and the linear relation between distance to a galaxy and its observed redshift is known as the *Hubble law*,

$$v = H_0 d \tag{1.61}$$

where, v is the velocity of the receding object, $H_0 = 100h\text{kmsec}^{-1}\text{Mpc}^{-1}$ is the present value of Hubble constant and d is the distance between receding galaxies. Since we assumed that the Universe is homogeneous, the linear relation of Hubble's law remains the same for all comoving observers (moving with the mean galaxy flow). This supports the cosmological principle which states that there is no specific point to measure the expansion of the Universe. Similarly dimensionless Hubble constant $h \cong 0.7$ is defined as $h \equiv H_0/(100 kms^{-1} Mpc^{-1})$.

From Hubble's law we can obtain a physical quantity known as *Hubble's radius* which is defined as the radius at which an object reaches the recessional velocity equal to that of light:

$$R_H = \frac{c}{H} \tag{1.62}$$

Physical objects farther than this radius have $v > c$, making it impossible to observe such objects.

The direct consequence of Hubble's law is that the relative velocity for distant objects is higher and is direct indication that the Universe is expanding. To measure the Hubble parameter H_0 we should obtain the distance and velocity which can be related to the redshift z. The *redshift parameter* is defined as the fractional shift in wavelength of a photon emitted by a distant galaxy z_e and that observed on the Earth today z_0 as:

$$z = \frac{\lambda_0 - \lambda_e}{\lambda_e} \tag{1.63}$$

An object gets blue-shifted while moving towards the detector and it is red-shifted while moving away. Change in wavelength of the emitted light is related to the redshift by,

$$1 + z \equiv \frac{\lambda_o}{\lambda_e} \tag{1.64}$$

And in terms of frequency at small separations, the recessional velocities gives the Doppler shift:

$$\frac{\nu_e}{\nu_o} = 1 + z \cong 1 + \frac{v}{\mathrm{c}} \tag{1.65}$$

Here subscripts o and e denotes observer and emitter respectively. If $a(t)$ is increasing, it is redshifted denoting decrease in frequency by an expansion factor $a(t_e)/a(t_0)$ which is equivalent to an increase in wavelength by a factor conventionally denoted by,

$$1 + z = \frac{a(t_0)}{a(t_e)} \tag{1.66}$$

Astronomers observe today that the distant galaxies show redshifts and hence we can conclude that the Universe is expanding. Since the redshift is related to the scale factor $a_e = a(t_e)$ at the emission time and by using the relation $a(t_0) = 1$,

$$1 + z = a^{-1} \tag{1.67}$$

Alternatively, if $a(t)$ is decreasing, then we have blueshift which denotes decrease in wavelength given by factor shown in Eq.(1.64) with z negative. For increasing or decreasing cosmological scale factor the proper distance to any comoving source of light (for example a galaxy) increases or decreases with time. This affects such light source to look receding from us or approaching to us resulting into cosmological redshift or blueshift.

Chapter 2

The Early Universe

> Nature does not hurry, yet
> everything is accomplished.
>
> *Lao Tzu*

In this chapter we describe in detail the early evolutionary phases of the Universe- its thermal history, inflationary era and how the first ever snapshot of the Universe captured the images of primeval inhomogeneities which later turned out the seeds of everything- from stars and galaxies to life on our planet.

2.1 Evolution of the Universe

Within the framework of SMC, the Universe began from an initial singularity which is conventionally taken as $t = 0$ [22] which is known as the *Big Bang*- a term coined by Fred Hoyle [23]. The phase from $t = 0$ till 10^{-43} seconds after the Big Bang includes the Planck epoch when all fundamental forces were unified and our current laws of physics break down to explain them. The four fundamental forces of the nature were combined and were probably a unified singular force during the Planckian epoch. The initial phases of the Universe are still obscure as we need a theory of quantum gravity to understand interactions at such extreme energy scales. After the expansion and eventual cooling of the Universe between around 10^{-43} seconds to 10^{-36} seconds, the Universe experienced phase transition during which fundamental forces separated from each other. This phase transition in the fundamental forces is believed to be caused by symmetry breaking and this cosmic epoch is known as the *Grand Unification Epoch*. The properties of the Universe are completely different before and after every phase transitions due to variation in energies and temperature. Vast scientific community believe that assuming validity of "Grand Unified Theory" (GUT), gravity separated first from the universally combined gauge force causing to separate gravity and electrostrong interactions. Later, with the second phase transition electrostrong interactions separated from gravity which resulted into two separate interactions- strong and electroweak interaction. The electroweak interaction, between about 10^{-36} seconds to 10^{-32} seconds divided into electromagnetic and weak interactions. In this stages of evolution, the temperature and energies were extremely high, however it is still unclear when exactly electrostrong symmetry was broken.

After the Big Bang singularity, in the time between 10^{-33} and 10^{-32} seconds, exponential expansion of very hot Universe resulted into tiny ripples or *primordial fluctuations* which are believed to be the seeds of large scale cosmological structures that we can see today. This expansion era is known as *cosmological inflation* which is a promising theory to explain many cosmological conundrums such as isotropy and flatness of the Universe, nonexistence of magnetic monopole and explains why CMB is evenly distributed across the space. The primordial gravitational waves (which are yet not detected) put an upper bound of 10^{16}GeV on inflationary energy scale. During inflation, the scale factor grows as $a(t) = \exp(Ht)$. Inflation is generally modelled with introduction of a scalar field ϕ known as *inflaton* which behaves as the cosmological constant when rolling down a slowly varying potential $V(\phi)$. This inflaton field settled into its lowest state and generated the repulsive force that lead the exponential expansion of the metric defining the Universe. Due to this expansion, elementary particles remaining from the grand unification epoch could be distributed across the Universe.

Reheating is the phase when inflation ends and scalar field decays into another particles with a consequent energy transfer to the primordial plasma. This resulted into raised temperature of the plasma of coupled particles and raised their energy too. Reheating is the phase during which known particles of Standard Model of Particle physics (from now SMP) were produced with a smooth transition to a radiation dominated Universe. We will present in detail physics of inflation in section 2.2.

After the end of inflationary era and due to the reheating effect, the Universe was filled with a hot quark-gluon plasma. Due to expansion, temperature of the Universe continued to decrease, as a result, the kinematics of the processes occurring in the particle abundance and process of plasma changes of early Universe could not be produced at later times. For stable particles this means that those particles disappeared due to production and decay processes being out of equilibrium. At the same time, some of the symmetries that hold in the very early Universe began to break spontaneously. Around 10^{-12} seconds after the Big Bang, the third symmetry- electroweak symmetry was broken and the four fundamental forces took their form familiar to us. But still temperature was too high to allow formation of any atoms we can see today. Between 10^{-12} seconds and 10^{-6} seconds after the Big Bang, the Universe was in its earliest evolutionary stages when electroweak symmetry was broken and gravitation, electromagnetism, strong and weak interactions had already taken their separate forms but the temperature was high enough forbidding quarks to bind together to form hadrons. This phase is known as the *quark epoch* and Universe in that epoch was filled with a dense, hot plasma of quarks, gluons, leptons and their antiparticles. The quarks released in this phase were highly energetic to be confined in hadrons. However as the temperature of the Universe stared to decrease, the kinetic energy of these quarks reduced and they could finally confine making the Universe to enter into the so-called *hadron epoch* which was approximated between 10^{-6} seconds to 1 second. The majority of hadrons and anti-hadrons annihilated with each other at the end of the hadron epoch. This left Universe dominating with the pairs of leptons and anti-lepton forming the *lepton epoch*. In the similar way as the hadron epoch, in this phase initially leptons and anti-leptons were produced but after the temperature reduced to a point constraining formation of new pairs of leptons and anti-leptons, their quick annihilation resulted into pair formation of high energy photons and minor residue of non annihilated leptons.

It is approximated that in the early phase after the Big Bang, the Universe experi-

enced *Barogenesis*- a phenomena which indicates presence of more number of baryons than antibaryons. It is expected that there could be equal number of baryons and antibaryon formed, however in the present Universe there seems to have no antibaryons. This is still a mystery open for revelations. There were several epochs of phase transitions in the early Universe at each of which the background equation of state changed drastically within a short time compared with the expansion rate of the Universe [24].

Before hadron epoch, there have been speculations about possible *Dark Matter decoupling*, in this phenomena DM particles depending on their mass and interaction rates could decouple. When the DM particles could possibly annihilate but could not be produced because of kinematic interactions, their energy density diluted with the evolution and they stopped interacting. This is called the *dark matter freeze-out*; freeze-out is the inability of annihilations to keep the particle in equilibrium [4]. The annihilation rate depends on the squared number density and it decreases due to expansion of the Universe.

All physical reactions which took place about 1TeV energy scale can be probed by physics of the high energy, but energy scales much higher than 1TeV are far beyond reach of mankind. Due to lack of experimental data in this high energy regime, the physics responsible for the very early phase of the Big Bang is unfathomable.

At approximately 1 second after the Big Bang and about 1 Mev temperature, the equilibrium of neutrino-electron interactions was broken and neutrinos decoupled from rest of the plasma forming the *Cosmic Neutrino Background(CNB)* or $C\nu B$ identical to *Cosmic Microwave Background* (CMB) formed by relic photons. Helium abundance from the Big Bang nucleosynthesis and anisotropies in the CMB are the strong supporting evidences that $C\nu B$ exists. These relic neutrinos might have left some very precise imprints on the CMB. Neutrinos being extremely weakly interacting makes very low possibilities of detecting experimentally the $C\nu B$ or even their imprints on the CMB. If $C\nu B$ could ever be detected, the anisotropies in $C\nu B$ could give us the glimpse of the Universe at the time of neutrino decoupling.

Shortly after neutrino decoupling, the mean photon temperature became too small to allow the production of $e^- - e^+$ pairs and electrons started to decouple. The energy density of electrons transferred to photons and those photons were reheated by this annihilation process. Therefore, temperature of photons (T_γ) from hereafter became slightly higher than neutrino temperature.

The Universe entered in the *photon epoch* between 10 seconds after the Big Bang where due to lepton epoch, the Universe was dominated by photons and most of the mass-energy density was in the form of neutrinos and relativistic particles. Therefore, the energy of the Universe and majority of its behaviour was dominated by photons due to their interaction with other particles till next 370,000 years.

The *early Universe* is the phase of the evolution of the Universe when various subatomic particles were formed, these particles included almost equal amount of matter and antimatter resulting into quick annihilation leaving a small excess of matter in the Universe. This early period also includes formation of light elements and favours conditions suitable for *Big Bang Nucleosynthesis*. In this phase (roughly about 20 minutes after the Big Bang) the temperature and pressure of the Universe continued to drop making favourable conditions for nuclear fusion to occur. This resulted into formation of nuclei of few lighter elements beyond hydrogen. This phase is responsible for the formation of deuterium, helium-3, helium-4 and small amount of lithium. Until then, the Universe was dominated by relativistic particles such as photons and neutri-

nos. Throughout the early Universe era, the reaction rates of particles in thermal bath Γ were much greater than the Hubble expansion rate H which maintained the local thermal equilibrium (LTE) [5]. In this case, entropy per comoving volume element remained constant.

By 47,000 years after the Big Bang, the Universe due to expansion got sufficiently cold enough to become matter dominated than initial radiation dominated opaque phase. In this phase, the energy density of matter exceeded the energy density of radiation and the vacuum energy density. According to the ΛCDM model, the Universe by this phase was almost 84% dominated by Cold Dark Matter and approximately 15% by ordinary matter. Dark matter is responsible for the structure formation of the observable Universe. Dark matter gathers in huge filaments under gravitational attraction and this results into fast collapse compared with ordinary matter since dark matter collapse is not slowed by radiation pressure. This amplified the inhomogeneities seeded during cosmological inflation and with progressing time, slightly denser regions became more dense and slightly empty regions became more rarefied. There have been many evidences supporting existence of dark matter but the true particle nature of dark matter is still unknown. In early phases, photons and baryons were tightly coupled into a single primordial plasma which was in thermal equilibrium by Thompson scattering. The opposite effect of gravity and radiation pressure produced propagation of acoustic waves. When the Universe became cold and diluted enough, the interaction eased to effectively couple the photons and baryons, and the acoustic waves ceased to propagate. These oscillations, which are known as the Baryonic Acoustic Oscillation (BAO) left the imprints on the distribution of matter with a characteristic scale approximately that of the sound horizon.

And finally at about 370,000 years later, the Universe entered an era of *Recombination* and *photon decoupling*, when the temperature was cold enough for ionized particles to combine forming neutral atoms and these newly formed atoms settled into more stable states releasing photons making the Universe transparent for the first time. Till then, the Universe was opaque as the baryonic matter in the Universe was in form of hot plasma and most of the photons could not travel enough distance due to frequent interactions with ionized particles. These photons were scattered around the space uniformly and can be detected as CMB today. Observations of the temperature anisotropies prove that early Universe was not completely homogeneous, but the inhomogeneities were small enough (at the 10^{-5} level) so that these inhomogeneities can be treated as a linear perturbation around a homogeneous background. The temperature anisotropies seen in the CMB are due to the primordial quantum fluctuations created during the inflationary era at about 10^{-34} seconds. Inflation stretched the microscopic quantum fluctuations in the energy density which can be observed as the cosmic large scale structures. After a density perturbation exit the horizon, it remained frozen with constant amplitude until it reached again the horizon at some later time under the expansion following the standard hot Big Bang model. The fluctuations associated with cosmological structures re-entered the horizon when the Universe was about $100,000$ years old, a shorter time before the photon decoupling.

After CMB decoupling, matter perturbations evolved under gravitational attraction and formed the large scale structure. The matter perturbations on small scales ($\leq$ 10Mpc) have grown non-linearly, while large scale perturbations are still small similar to the CMB anisotropies [4]. Gravity attracts matter to grow in form of galaxies and gradually pulls galaxies together to form galactic clusters and super clusters.

These structures on scale smaller than 100Mpc follow cosmological principle and can be treated linearly, however their actual treatment need cosmological simulations and numerical methods with introducing perturbations in the spacetime metric. From about 9.8 billion years of cosmic time, observations show that the expansion of the Universe has been gradually accelerating. The later stage of the evolution of the Universe include accelerated expansion which is supposed to be due to elusive Dark Energy, also referred to as *Cosmological constant* denoted by Λ. Dark energy is the single largest cosmological component constituting about 68% of the entire mass-energy of the physical Universe. The whole evolution cycle which the Universe underwent to make our life possible can be schematically shown as Fig.2.1:

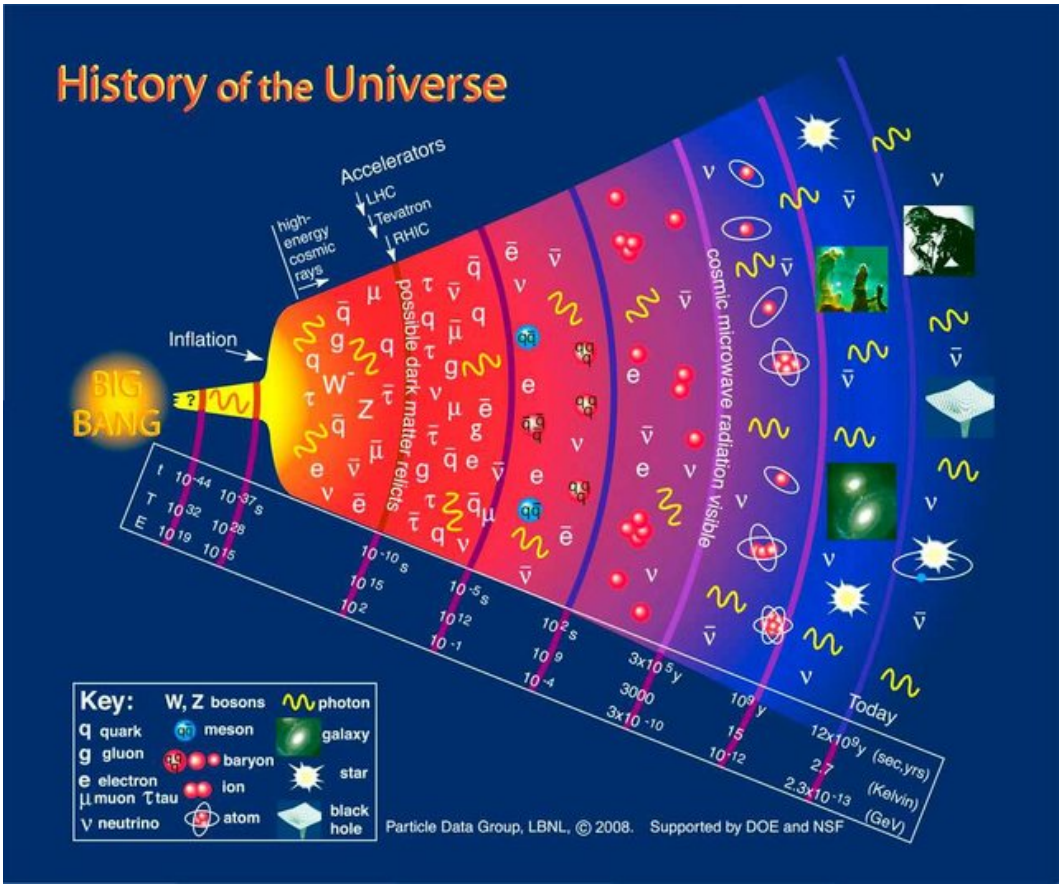

Figure 2.1: Schematic history of the Universe, image reproduced from [25].

2.2 Cosmological inflation

This section is inspired by classic texts by *Weinberg*, *Longair*, *Kolb & Turner*, *Mukhanov*, *Peacock* and *TASI lecture notes 2009* by Baumann. Other references when needed are cited therein.

Cosmological inflation is the paradigm proposed by Alan Guth [26, 22] and Alexei Starobinsky [27] to solve the cosmological conundrums posed by the standard ΛCDM model such as flatness, horizon and the magnetic monopole problem. It is a plausible theory to explain statistical deviations from large scale homogeneity and isotropy. Inflation is assumed to be the early Universe era (also known as the de Sitter phase)

when vacuum energy was the dominant component of energy density of the Universe leading to exponential expansion (energy scale $\simeq 10^{15}$ GeV) of the scale factor which lead to an accelerated expansion of the Universe, or in other words, the Hubble length shrank relative to any fixed scale caught up in the rapid expansion. Simply, inflation can be defined as the early era of exponential acceleration, $\ddot{a} > 0$, which implies that the fluid that drive inflation violates the *strong energy condition* (SEC): $w < -1/3$. If $w \simeq 1$, then the space will expand quasi-exponentially. In exotic theories violation of the null energy condition (NEC)- $w < -1$, is allowed. Here we restrict only the simple inflation model with validity of SEC.

During inflation, the energy density of the Universe remained constant whereas the curvature radius grew exponentially. The main merit of this paradigm is that it provides a natural way to generate the primordial perturbations breaking the perfect homogeneity and isotropy of the Universe to form observable large scale structure [28]. It predicts that primordial scalar perturbations are nearly scale-invariant, Gaussian and adiabatic. In addition to being a promising theory, it also motivates modern cosmologists to find the traces of *Primordial Gravitational Waves (PGWs)* in the CMB, which is a strikingly characteristic feature of this model. There are different models of inflation leading to different predictions for the observable Universe and observations/experimental evidences can strongly discriminate between them. Here, the model we consider is the most simplest one- the Single Field Slow Roll (SFSR) [29] inflationary model, however different models for inflation are discussed in [30].

Inflation can also be defined in terms of evolution of the comoving Hubble radius $(aH)^{-1}$:

$$\frac{d}{dt}(aH)^{-1} = -\frac{\ddot{a}}{\dot{a}^2} < 0 \Rightarrow \rho + 3p < 0 \tag{2.1}$$

i.e. the comoving Hubble radius decreases during inflation making the observable Universe smaller. The condition for accelerated expansion implies:

$$\epsilon \equiv -\frac{\dot{H}}{H^2} = 1 - \frac{\ddot{a}a}{\dot{a}^2} < 1 \tag{2.2}$$

And, the exponential expansion can be achieved by taking the limit,

$$\epsilon \to 0 \Rightarrow H \to const., \quad a(t) \to e^{Ht} \tag{2.3}$$

As we defined Friedmann equation (Eq.(1.45)) in Chapter 1, it shows which kind of perfect fluid would drive the dynamics of the Universe. The cosmological inflation is the accelerated expansion of the Universe, i.e. $\ddot{a} > 0$ and, $p \approx -\rho$, which means that the evolution of the scale factor would be:

$$\boxed{a(t) = a_I e^{H_i(t-t_i)}} \tag{2.4}$$

where subscript i indicates the beginning of the inflationary era and the Hubble parameter is nearly constant in time i.e. $H = H_i \equiv const.$ This period characterized by evolution of the scale factor is known as the *de Sitter phase*. The exact $\epsilon = 0$ case corresponds to have the de Sitter background, which is the vacuum solution of the Einstein equations with a positive cosmological constant. In a de Sitter model, the physical Hubble radius is constant in time while it is the physical length that continues to grow making it possible to cross the Hubble radius at some 'horizon-crossing time'.

The requirement for a sufficiently long inflationary time corresponds to the requirement that all scales relevant for cosmological observations were able to exceed the Hubble radius during inflation. The four widely used equivalent definitions of inflation can be summarized as below:

- *Decreasing comoving horizon*: The shrinking Hubble sphere is defined as mentioned in Eq.(2.1)

$$\boxed{\frac{d}{dt}(aH)^{-1} < 0} \tag{2.5}$$

- *Accelerated expansion*: From Eq.(2.1),

$$\boxed{\frac{d}{dt}(aH)^{-1} = \frac{-\ddot{a}}{(aH)^2}} \tag{2.6}$$

  i.e. a shrinking comoving Hubble radius implies accelerated expansion.

- *Violation of SEC*:
  From Friedmann equation,

$$\boxed{\dot{H} + H^2 = \frac{\ddot{a}}{a} = -\frac{4\pi G}{3}(\rho + 3p)} \tag{2.7}$$

  where for $\ddot{a} > 0$ needs $p > -\frac{1}{3}\rho$, i.e. it needs negative pressure or violation of the *strong energy condition.*

- *Slowly varying H*: From Eq.(2.2), the condition needed is,

$$\boxed{\epsilon = -\frac{\dot{H}}{H^2} < 1} \tag{2.8}$$

2.2.1 Scalar field dynamics

Considering the SFSR inflaton potential $V(\phi)$, dynamics of a minimally gravitationally coupled scalar field ϕ is governed by the action term:

$$S = \int d^4x\sqrt{-g}\Big[\frac{1}{2}R + \frac{1}{2}g^{\mu\nu}\partial_\mu\phi\partial_\nu\phi - V(\phi)\Big] = S_{EH} + S_\phi \tag{2.9}$$

The action in Eq.(2.9) is the sum of the gravitational Einstein-Hilbert action S_{EH} and the action of the scalar field with canonical kinetic term S_ϕ. The potential $V(\phi)$ describes the self-interaction of the scalar field. Dynamics of the inflaton field from the time CMB fluctuations were created (at ϕ_{CMB}) to the end of inflation (at ϕ_{end}) is determined by the shape of the inflationary potential $V(\phi)$ such as *single-field inflation* and *large-field inflation* [31].

Fig.2.2 shows the SFSR inflation scenario:

A minimally coupled scalar field ϕ with potential energy $V(\phi)$ can be further described by following Lagrangian:

$$\mathcal{L} = -\frac{1}{2}\partial^\mu\phi\partial_\mu\phi - V(\phi) \tag{2.10}$$

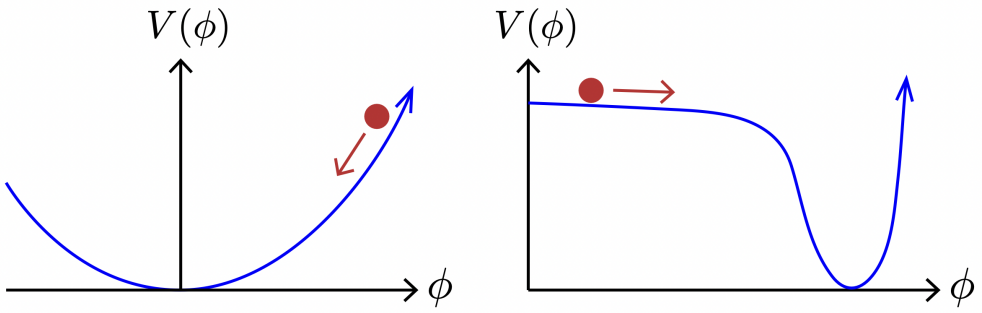

Figure 2.2: According to inflation, the cosmic energy density was dominated by the vacuum energy associated with the displacement of some scalar field ϕ from the minimum of its potential. Figure illustrates the two toy models for the inflaton potential, *left*: a quadratic potential, *right*: a hilltop potential. Image taken from [32].

By varying the action term w.r.t. ϕ, we can obtain the Klein-Gordon equation ($\Box\phi = \partial V/\partial\phi$) describing the equation of motion for the field which with the FLRW becomes,

$$\ddot{\phi} + 3H\dot{\phi} - \frac{1}{a^2}\nabla^2\phi + V'\phi = 0 \tag{2.11}$$

where $V'\phi = dV(\phi)/d\phi$. Also varying action Eq.(2.10) w.r.t the metric tensor, the expression for the stress-energy tensor for the minimally-coupled scalar field becomes:

$$T_{\mu\nu} = -2\frac{\partial\mathcal{L}}{\partial g^{\mu\nu}} + g_{\mu\nu}\mathcal{L} = \partial_\mu\phi\partial_\nu\phi + g_{\mu\nu}\Big[-\frac{1}{2}g^{\alpha\beta}\partial_{\alpha\phi}\partial_{\beta\phi} - V(\phi)\Big] \tag{2.12}$$

$$\rho_\phi = \frac{\dot{\phi}^2}{2} + V(\phi), \quad p_\phi = \frac{\dot{\phi}^2}{2} - V(\phi) \tag{2.13}$$

This gives the equation-of-state of the inflaton:

$$w_\phi \equiv \frac{p_\phi}{\rho_\phi} = \frac{\frac{1}{2}\dot{\phi}^2 - V}{\frac{1}{2}\dot{\phi}^2 + V} \tag{2.14}$$

Eq.(2.13) shows that a scalar field can lead to a negative pressure, $w_\phi < 0$), and accelerated expansion, ($w_\phi < -1/3$), respectively, if its potential energy V dominates over the kinetic energy $\frac{1}{2}\dot{\phi}^2$.

Further, from Friedmann equation we obtain,

$$\rho_\phi + 3p_\phi = 2[\dot{\phi}^2 - V(\phi)] \tag{2.15}$$

So, $V(\phi) > \dot{\phi}^2$ is sufficient condition to obtain accelerated expansion, in particular to obtain a *quasi-de Sitter expansion* we need,

$$\boxed{V(\phi) \gg \dot{\phi}^2} \tag{2.16}$$

Therefore a scalar field with its potential energy dominating its kinetic energy gives rise to an inflationary expansion which can be achieved by introducing a *scalar field* slowly rolling towards minimum of its potential.

Assuming spatially flat Universe, the equations of motion becomes,

$$H^2 = \frac{1}{3M_{Pl}^2}\left[V(\phi) + \frac{1}{2}\dot{\phi}^2\right] \tag{2.17}$$

and,

$$\boxed{\ddot{\phi} + 3H\dot{\phi} = -\frac{dV}{d\phi}} \tag{2.18}$$

This equation is also called the *scalar wave equation* and provided that $\dot{\phi}^2 < V(\phi)$, the condition for inflation is satisfied.

2.3 Slow-roll conditions

The acceleration equation for a Universe dominated by a homogeneous scalar field can be written as [31],

$$\frac{\ddot{a}}{a} = -\frac{1}{6}(\rho_\phi + 3p_\phi) = H^2(1-\epsilon) \tag{2.19}$$

where, the *slow-roll parameter* ϵ is,

$$\epsilon \equiv \frac{3}{2}(w_\phi + 1) = \frac{1}{2}\frac{\dot{\phi}^2}{H^2} \tag{2.20}$$

ϵ can be related with the evolution of the Hubble parameter,

$$\boxed{\epsilon = -\frac{\dot{H}}{H^2} = -\frac{d\ln H}{dN}} \tag{2.21}$$

where, $dN = Hdt$, and the condition for accelerated expansion is $\epsilon < 1$. In the de Sitter limit ($p_\phi \to \rho_\phi$) the slow-roll parameter corresponds to $\epsilon \to 0$. In this case, potential energy dominates over the kinetic energy,

$$\dot{\phi} \ll V(\phi) \tag{2.22}$$

Accelerated expansion will only sustain for a sufficiently long period of time if the second time derivative of ϕ is small enough,

$$|\ddot{\phi}| \ll |3H\dot{\phi}|, |V_{,\phi}| \tag{2.23}$$

which requires the smallness of a second-order slow-roll parameter,

$$\boxed{\eta = -\frac{\ddot{\phi}}{H\dot{\phi}} = \epsilon - \frac{1}{2\epsilon}\frac{d\epsilon}{dN}} \tag{2.24}$$

where, $|\eta| < 1$ is ensuring the fact that the fractional change of ϵ per e-fold is small and the slow-roll conditions can be expressed as conditions on the shape of the inflationary potential:

$$\boxed{\epsilon_V(\phi) \equiv \frac{M_{Pl}^2}{2}\Big(\frac{V'}{V}\Big)} \tag{2.25}$$

and,

$$\boxed{\eta_V(\phi) \equiv M_{Pl}^2\Big(\frac{V''}{V}\Big)} \tag{2.26}$$

where subscripts $'$ and $''$ denote first and second order derivative w.r.t the field ϕ. In the slow-roll region,

$$\epsilon_V, |\eta_V| \ll 1 \tag{2.27}$$

with the background evolution,

$$H^2 \sim \frac{1}{3}V(\phi) \simeq const. \quad \dot{\phi} \simeq -\frac{V'}{3H} \tag{2.28}$$

and the spacetime is approximately de Sitter,

$$a(t) \simeq e^{Ht} \tag{2.29}$$

The parameters ϵ_V and η_V are called the *potential slow roll parameters* to distinguish them from the *Hubble slow roll parameters* ϵ and η. In the slow roll approximation, the Hubble and potential slow-roll parameters are related as follows:

$$\boxed{\epsilon \approx \epsilon_V\,, \quad \eta \approx \eta_V - \epsilon_V} \tag{2.30}$$

Slow-roll inflation occurs only if both slow-roll parameters are small, $\mathcal{O}(10^{-12})$. If these conditions are satisfied, then the background evolution is given by $H^2 \equiv V(\phi)/3M_{Pl}^2$ which is a constant term and $\ddot{\phi} = -\partial_\phi V/3H$.

Inflation ends when the slow-roll conditions are violated (known as the phase of reheating),

$$\epsilon(\phi_{end}) \equiv 1, \quad \epsilon_V(\phi_{end}) \approx 1 \tag{2.31}$$

The number of e-folds before inflation ends is,

$$N(\phi) \equiv \ln\frac{a_{end}}{a} = \int_t^{t_{end}} H dt \approx \int_{\phi_{end}}^{\phi} \frac{V}{V'} d\phi \tag{2.32}$$

Which becomes:

$$N(\phi) = \int_{\phi_{end}}^{\phi} \frac{d\phi}{\sqrt{2\epsilon}} \approx \int_{\phi_{end}}^{\phi} \frac{d\phi}{\sqrt{2\epsilon_V}} \tag{2.33}$$

2.4 Reheating

Since inflation is a decent framework supporting the SMC, it must end allowing transition from radiation dominated to matter dominated era in order to form light elements following particle abundance supported by *primordial nucleosynthesis* and allow the formation of the CMB. As inflation terminates, the inflaton field starts quasi-periodic motion with slowly decreasing amplitude [33].

In the single field slow-roll scenario, when inflaton field starts rolling fast along its potential, it reaches the minimum and then bounces back oscillating around it. This process by which the Universe transits from the end of inflation to the radiation dominated phase is known as *reheating* [34, 35, 36, 37]. At the end of inflation, most of the energy density of the Universe was stored in the scalar fields as accelerated expansion of the Universe dilutes other components. The temperature of the Universe at the time of this process is called the *reheat temperature*. This decay resulted into formation of other ϕ particles or other bosons due to broad parametric resonance [38]. Models proposed to describe reheating include the perturbative decay of inflaton, other models include non-perturbative decay such as parametric resonance decay. If the fluctuations are sufficiently small then inflaton could decay into relativistic particles as soon as the inflaton decay rate Γ becomes comparable to Hubble constant. If the decay is slow, only fermionic decays are available and usually each decay is supposed to thermalize quickly so that their energy distribution can be described by a black-body function with the reheating temperature for a sudden process given by $T_{reh} \equiv \sqrt{M_{Pl}\Gamma}$. After the decay, a mechanism is supposed to take place leading to energy transfer of the decay products into radiation called as *preheating phase* [38].

Fig.2.3 schematically shows inflaton field slowly rolling down towards the true vacuum representing the end of inflation. False vacuum within particle physics language refers to a stage with lower energy. As shown in this figure, the Universe at early times is dominated by potential energy density of a scalar field ϕ where the classical motion of ϕ is shown by red arrows. When ϕ is near region (a), the energy density will remain nearly constant $\rho \equiv \rho_f$ (ρ_f being the energy density of false vacuum) even as the Universe expands. Cosmic expansion acts like a fractional drag, slowing the motion of ϕ, near regions (b) and (d), ϕ behaves like an oscillator/marble entrapped slowly moving towards the side of its potential, rather than like a marble sliding down inside a polished bowl. During this period of "slow roll", the energy density ρ remains nearly constant. Only after ϕ has slid most of the way down its potential, it will begin to oscillate around its minimum. The region (c) shows how inflation ends.

After inflation ends, the scalar field begins to oscillate round the minimum of the potential where the scalar field acts like pressureless matter:

$$\frac{d\bar{\rho}_\phi}{dt} + 3H\bar{\rho}_\phi = 0 \tag{2.34}$$

and due to coupling of inflaton field ϕ to other particles leads to a decay of the inflaton energy:

$$\frac{d\bar{\rho}_\phi}{dt} + (3H + \Gamma_\phi)\bar{\rho}_\phi = 0 \tag{2.35}$$

where, the *coupling parameter* Γ_ϕ depends on complicated and model-dependent [31] physical process. Generally, inflationary energy density is converted into standard

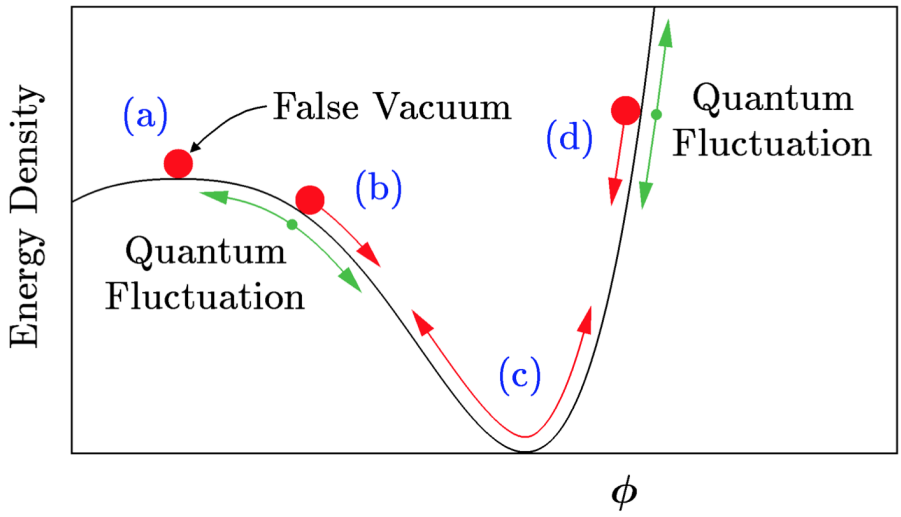

Figure 2.3: slow-roll inflation towards true vacuum, image taken from [39].

model degrees of freedom. The field of reheating too like early Universe is largely unknown.

2.5 Power spectra of cosmological perturbations

The standard model assumes adiabatic, Gaussian perturbations. Adiabaticity indicates the common perturbation for all types of material in the Universe, so that if the spacetime is foliated by the constant-density hypersurfaces, then all fluids and fields are homogeneous on those slices, with perturbations completely described by the variation of the spatial curvature of the slices. Gaussianity means that the initial perturbations obey Gaussian statistics, with amplitudes of waves of different wavenumbers being randomly drawn from a Gaussian distribution of width given by the power spectrum [40]. Since gravitational instability generates non-Gaussianity, Gaussianity refers to a property of initial perturbations before they evolved. And isocurvature perturbations arise due to perturbations of relatively different amount of material while leaving the total density constant.

If the perturbations obey Gaussian statistics, then the dimensionless *power spectrum* denoted by Δ^2 provides a complete description of properties of cosmological perturbations.

2.5.1 Scalar and tensor primordial power spectra

Inflation provides the simplest mechanism to generate the observed perturbations through the amplification of quantum fluctuations which were stretched to astrophysical scales by rapid initial expansion. Density perturbations from scalar field experienced gravitational instability and lead to structure formation, whereas the Primordial Gravitational Waves (PGWs) lead to imprints on the polarization anisotropies of the

CMB.

Using quantities defined in previous section showing statistical prediction for the initial conditions from inflationary paradigm, we can check how these initial conditions affect the shape of the matter power spectrum. The inflation field is a scalar field responsible for accelerated expansion of the Universe. However inflaton is not a homogeneous field but due to quantum non-zero energy, inflaton keeps fluctuating. These fluctuations are also stretched due to expansion of the Universe and once they become larger than the Hubble horizon, the quantum fluctuations are frozen. At the end of inflationary era when inflaton field scatters into particle production (reheating and pre-heating respectively), the primordial particles and the frozen quantum fluctuations of the inflaton field outside the horizon generate primordial fluctuations in the energy density.

Considering again the SFSR model, Fourier transform of the fluctuations in the inflaton field will be,

$$\delta\phi(\mathbf{k},t) = \int d\mathbf{k} e^{i\mathbf{k}x}\delta\phi(\mathbf{x},t) \tag{2.36}$$

The evolution equation for such perturbations become,

$$\delta\ddot{\phi} + 3H\delta\dot{\phi} + \delta\phi\frac{k^2}{a^2H^2} = 0 \tag{2.37}$$

Then we can define the primordial power spectrum as [31]:

$$\langle\phi_{in}(\mathbf{k})\phi_{in}(\mathbf{k}')\rangle = (2\pi)^3\delta(\mathbf{k}+\mathbf{k}')P_\phi(k) \tag{2.38}$$

where $\phi(\mathbf{k})$ is the primordial gravitational potential, angular brackets $\langle ...\rangle$ denote the ensemble average and the primordial power spectrum is defined as:

$$P_\phi(k) = A_s(k_0)\Big(\frac{k}{k_*}\Big)^{n_s-1} \tag{2.39}$$

where, A_s is the amplitude of the primordial spectrum, k_* is the pivot scale and n_s is the spectral index. This gives following relation:

$$\boxed{n_s - 1 = \frac{d\ln P_\phi(k)}{d\ln k}} \tag{2.40}$$

Above Eq.(2.40) defines the scale dependence of the power spectrum or the *scalar spectral index* which is also known as the *tilt*. Inflation predict a nearly scale-invariant power spectrum where the derivative in above equation is zero and $n_s \sim 1$ corresponding to a slowly rolling inflaton field and a slowly varying $H(t)$.

Quantum fluctuations during inflation source not only the primordial power spectrum of scalar perturbations but also the one of tensor perturbations.

Analogous to above discussion, power spectrum for the amplitude h_k of the two states of polarization of primordial gravitational waves is defined as,

$$\langle h_k h_{k'}\rangle = (2\pi)^3\delta(\mathbf{k}+\mathbf{k}')P_h(k) \tag{2.41}$$

$$\Delta_h^2 = \frac{k^3}{2\pi^2}P_h(k) \tag{2.42}$$

The power spectrum of the tensor perturbations can be defined as the sum of the power spectra of two polarization state:

$$\Delta_t^2 \equiv 2\Delta_h^2 = \frac{2}{\pi^2}\frac{H_*^2}{M_{Pl}^2} \tag{2.43}$$

Given that $H^2 \propto V$ during inflation, the GW amplitude can thus be determined by the energy density of the Universe.

The scale-dependence can be defined as,

$$n_t \equiv \frac{d\ln\Delta_t^2}{d\ln k} \tag{2.44}$$

which gives,

$$\Delta_t^2(k_*) = A_t(k_*)\Big(\frac{k}{k_*}\Big)^{n_t(k_*)} \tag{2.45}$$

In terms of $\Delta^2 \equiv k^3P(k)/2\pi$, for scalar and tensor fluctuations it is possible to show that:

$$\Delta_s^2(k) = \frac{1}{8\pi^2}\frac{H^2}{M_{Pl}^2}\frac{1}{\epsilon} \tag{2.46}$$

and,

$$\Delta_t^2(k) \equiv 2\Delta_h^2(k) = \frac{2}{\pi^2}\frac{H^2}{M_{Pl}^2} \tag{2.47}$$

where both quantities are measured at scale $k = aH$ and,

$$\epsilon = -\frac{d\ln H}{dN} \tag{2.48}$$

The *horizon crossing condition* $k = aH$ ($k < aH$ is known as super-horizon whereas $k > aH$ is known as sub-horizon scale) makes Eq.(2.46) and Eq.(2.47) functions of the comoving wavenumber k making the tensor-to-scalar ratio:

$$r \equiv \frac{\Delta_t^2}{\Delta_s^2} = 16\epsilon_* \tag{2.49}$$

Following Eq.(2.42), the scalar and tensor spectra at the horizon crossing can be expressed in terms of $V(\phi)$ and ϵ_V [31]:

$$\Delta_s^2(k) \simeq \frac{1}{24\pi^2}\frac{V}{M_{Pl}^4}\frac{1}{\epsilon_V}, \quad \Delta_t^2(k) \simeq \frac{2}{3\pi^2}\frac{V}{M_{Pl}^4} \tag{2.50}$$

The scalar spectral index is,

$$\boxed{n_s - 1 = 2\eta_V^* - 6\epsilon_V^*} \tag{2.51}$$

the tensor spectral index is,

$$\boxed{n_t = -2\epsilon_V^*} \tag{2.52}$$

And, the tensor-to-scalar ratio becomes,

$$\boxed{r = 16\epsilon_V^*} \tag{2.53}$$

SFSR models satisfy a consistency condition between the tensor-to-scalar ratio and the tensor tilt:

$$\boxed{r = -8n_t} \tag{2.54}$$

In the slow-roll approximation measurements of the scalar and tensor spectra relate directly to the shape of the potential $V(\phi)$ i.e. H is a measure of the scale of the potential, ϵ of V' and η_V of V''. Therefore measurements of amplitude and the scale-dependence of the cosmological perturbations encode information about the potential driving the accelerated expansion. The simplest inflationary models based on one dynamical field predict adiabatic perturbations and a level of non-Gaussianity which is too minute to be detected by any experiment designed so far. Large scale non-Gaussianity can arise if inflation interactions are significant during inflationary phase and it can be significant in models with multiple fields, higher-derivative interactions or non-standard initial states [31].

2.5.2 The matter power spectrum

The distribution of matter in the universe is usually described by the power spectrum, $P_m(k)$, of matter density perturbations, δ_k, defined via:

$$\langle \delta_k \delta_{k'} \rangle = (2\pi)^3 \delta^3(k - k') P_m(k) \tag{2.55}$$

Power spectrum describes the distribution of matter in the Universe and variance in the matter distribution: a larger power spectrum denotes a significant larger amount of overdense and underdense region, whereas the smaller power spectrum denotes smooth distribution of matter. Fig.2.4 shows the matter power spectrum in four different models: the Harrison-Zel'dovich spectrum, CDM, hot dark matter(HDM) with standard model neutrinos and dark matter in form of baryons.

The shape of the matter power spectrum also depends strongly on the properties of matter. If dark matter consisted of baryonic particles, the power spectrum would exhibit oscillations on large scale due to strong baryon-photon coupling prior to recombination as can be seen in figure 2.4 in form of green solid curve. Therefore, the absence of such oscillations in observational data provides further evidence that DM is non-baryonic.

Now, if linear evolution of cosmological perturbations is considered, the shape of the matter power spectrum $P_m(k)$ can be split in three different regions [42]:

The low-k limit: These scales include modes that are today outside the horizon. In Newtonian gauge potential modes and density modes both are constant. Therefore the matter power spectrum is expected to reproduce the scale-dependence of the primordial spectrum:

$$P_m(k) \sim k^{-3}, \quad \text{for} \quad k < aH. \tag{2.56}$$

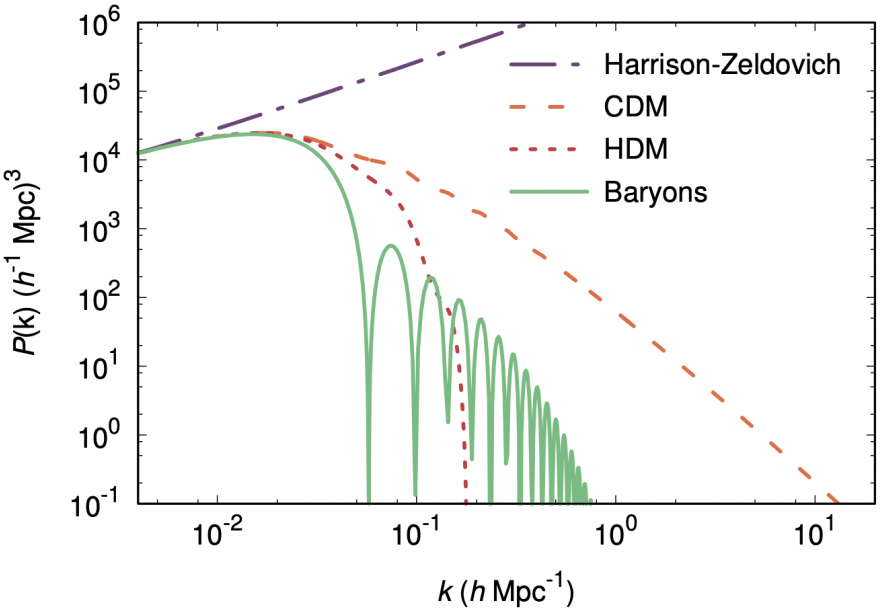

Figure 2.4: The linear matter power spectrum for four different models: the Harrison-Zel'dovich spectrum (purple dashed-dotted), CDM (orange dashed), hot dark matter(HDM) with standard model neutrinos (red dotted) and dark matter in form of baryons (green solid). Image taken from: [41].

Modes entering the horizon in MD era: For the modes entering the horizon in the matter dominated era, the density fluctuation grows as the scale factor. The smaller modes, i.e. the modes that enter the horizon at earlier time are expected to have a larger amplitude. Therefore, the matter power spectrum is expected to grow with k and reach maximum amplitude corresponding to $k = k_{eq}$. The slope of the power spectrum in this range can be computed from the primordial spectrum and the Poisson equation which relates the density and the gravitational potential. The result is,

$$P_m(k) \sim k \quad \text{for} \quad aH < kc < k_{eq} \tag{2.57}$$

Modes entering the horizon in RD era: Such modes have a logarithmic growth after the horizon crossing. Therefore after the matter-radiation equality, the power spectrum is expected to decay as primordial spectrum modulated by a logarithmic factor:

$$P_m(k) \sim k^{-3}[\ln(\text{const}\, k)]^2, \quad \text{for} \quad k > k_{eq} \tag{2.58}$$

It is important to note that a cosmological constant is expected to maintain the shape of the matter power unaltered. However the accelerated expansion is expected to contrast dark matter clustering, this results into slight suppressing of the amplitude of power spectrum.

Fig.**??**, some of which will be discussed in the next chapter.

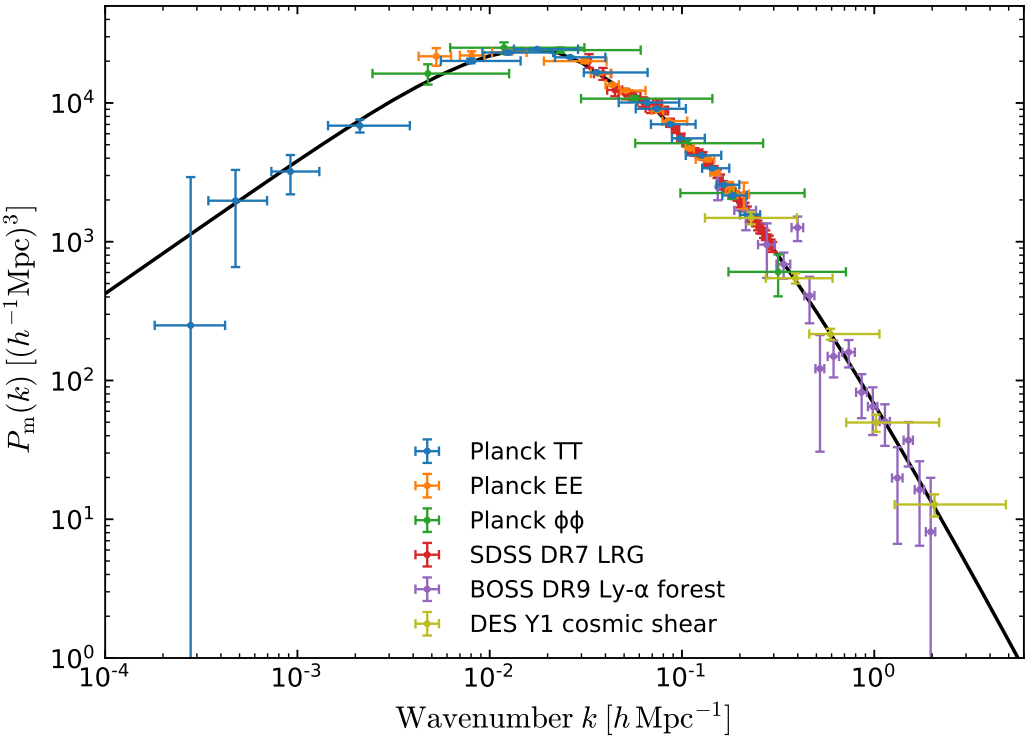

Figure 2.5: From The Planck Collaboration et al., 2020 [43]. The matter power spectrum (at $z = 0$) inferred from different cosmological probes. The solid black line is the ΛCDM prediction that provide a good fit on these scales.

Chapter 3

Cosmological large scale structure

If you look up,
there are no limits.

Japanese proverb

The ΛCDM model is the minimal model having only six cosmological parameters to describe evolution of the Universe. This model is exquisitely able to reproduce all cosmological probes including CMB [44, 2, 45, 46], galaxy clustering [47], cosmological distance measurement from supernovae [48] and the statistics of weak gravitational lensing [49]. In different perspective, the standard model of cosmology is presented in [50]. In this chapter we provide a brief overview of cosmological structure formation and observational constraints on cosmological parameters thanks to ongoing science missions, and motivate the application of the DEMNUni simulations in this project to infer effects of large scale structure on GW propagation.

3.1 Cosmological structures

According to the cosmological principle, the Universe is described on larger scales as a fluid of nearly constant density with homogeneous and isotropic distribution of matter and radiation. Large scale homogeneity and isotropy is valid in two cases: in the early Universe when it was in the form of a primordial plasma and today only if the Universe is observed on very large scales i.e., $r > 100$Mpc which is evident by the CMB isotropy, isotropic X-ray background and number counts of radio sources. However on scales smaller than 100Mpc, the Universe is enormously rich having stars, planets, galaxies, voids, galaxy clusters and superclusters as can be clearly visible from the SDSS map of the Universe as shown in Fig.3.1.

It can be seen that the matter distribution is actually clustered in coherent patterns forming large voids and a network of filamentary structures which merge into large overdense regions. The existence of cosmological structure provides us a key to unlock mystery of the evolution and composition of the Universe. Inflationary epoch as described in Chapter 2 predicts generation of small scale initial irregularities in the initially homogeneous Universe and then due to *gravitational instability*, primeval density perturbations grew into larger inhomogeneities that we can observe today.

Gravitational instability arises due to irregular matter distribution in the Universe

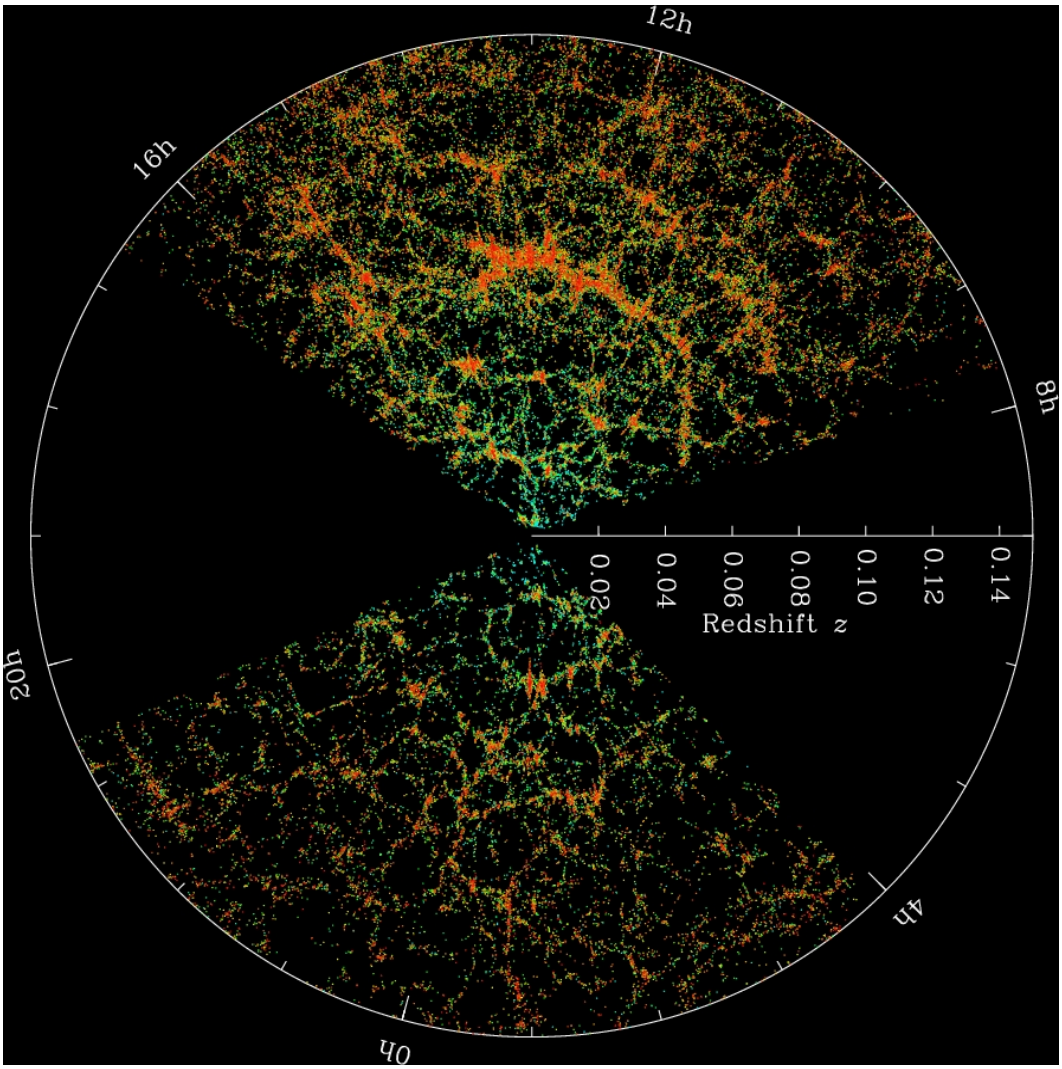

Figure 3.1: The SDSS map of the Universe showing richness of the non-linear structure, shown each dot is a galaxy and the color is the g-r color of that galaxy. Image is taken from: https://www.sdss.org/science/orangepie/.

where overdense regions provide extra gravitational attraction and pull matter towards them making them more overdense. Thus evolving Universe has more pronounced irregularities under the action of gravity. These irregularities can be treated linearly as long as they were small.

The decreasing comoving horizon during inflationary era is the key feature for the generation of cosmological perturbations. Quantum fluctuations are generated on the sub-horizon scales but they exit the horizon when the Hubble radius becomes smaller than their comoving wavelength. This in physical coordinates corresponds to the superluminal expansion stretching perturbations to the acausal distances. Such perturbations become classic superhorizon density perturbations which re-enter the horizon in the subsequent Big Bang evolution and gravitationally combine to form the large scale structure. The primeval density inhomogeneities generated during inflation are hence necessary condition to initiate structure formation which results into predictable temperature fluctuations in the CMB.

Density inhomogeneities are generally indicated in terms of Fourier transformation

[5]:

$$\frac{\delta\rho(\vec{x})}{\bar{\rho}} = (2\pi)^{-3} \int \delta_k \exp(-i\vec{k}\cdot\vec{x}) d^3k \,, \tag{3.1}$$

where ρ is the density field, $\bar{\rho}$ is the mean density of the Universe, $\vec{k}$ is the *comoving wavenumber* associated with a given Fourier mode and δ_k is its amplitude. For a density perturbation of small amplitude $(\delta_\rho/\delta) << 1$, its physical wavenumber and wavelength scales with the scale-factor as $k_{phys} = k/(2a(t)\pi)$ with $\lambda_{phys} = a(t)(2\pi/k)$. Generally the scale factor is normalized to unity at redshift zero, so that $\lambda_{phys} = \lambda$ at $z = 0$. When a perturbation becomes nonlinear, it separates from the background expansion.

The growth of these density inhomogeneities might have begin as soon as the Universe entered into matter-dominated era assuming the Universe was dominated by non-baryonic dark matter, because baryonic inhomogeneities can not grow until after decoupling as baryons are tightly coupled to the photons. The matter contribution at the time of matter-radiation equality ($1 + z_{eq} = 2.4 \times 10^4 \Omega_m h^2$ [6]) takes into account baryons, charged leptons and non-relativistic dark matter component at the time of decoupling, including other non-relativistic species which includes massive neutrinos after their non-relativistic transition. At redshifts higher than z_{eq}, the dynamics of the Universe was dominated by radiation, and as the density of radiation decreases faster than density of matter, the Universe reached *matter-radiation equality* when the energy density of matter and that of radiation became equal. Before this epoch, the radiation density acts as a pressure that prevented the collapse of perturbations in the matter density. The epoch of matter-radiation equality has special importance for the generation of large scale structure and development of CMB anisotropies. After this epoch the Universe started to be matter dominated, allowing for structures to form.

However matter perturbations underwent a complex evolution up until the time they are observed in the present Universe. Approaches needed to explain non-linear growth of such perturbations include higher order perturbation theory, renormalization group mechanisms, analytical models of gravitational collapse, the halo-model or N-body simulations [51]. When the perturbations are small, linear Boltzmann solver codes, such as CAMB or CLASS [52], can be used, but for density perturbations on small scales, non-linear evolution needs a variety of semi-analytical and numerical approaches.

Fluctuations of density ρ around the mean density $\bar{\rho}$ can be parameterized by density contrast by rewriting Eq.(3.1) in a compact form:

$$\delta = \frac{\rho - \bar{\rho}}{\bar{\rho}} \tag{3.2}$$

For non-relativistic perturbations in the MD era on scales smaller than the horizon, Newtonian physics suffices to describe the evolution of the fluctuations [53]. The density contrast of an ideal fluid of zero pressure is related to the gravitational potential via Poisson equation,

$$\nabla^2\Phi = 4\pi G a^2 \bar{\rho}\delta \tag{3.3}$$

The differential equation describing the evolution of δ typically has to be solved numerically, the solution that increases with time is called *growing mode*. The time-dependent function is the linear growth factor D_+ which relates the density contrast

at time a to earlier initial epoch a_i with $\delta(a) \propto D_+(a)\delta(a_i)$. In a matter dominated Einstein-de Sitter Universe D_+ is proportional to the scale factor a. Due to the presence of dark energy, growth of structures is suppressed.

In order to understand structure formation, we need initial data in form of: (1) total amount of non-relativistic matter quantified by Ω_m, (2) the composition of the Universe as quantified by the fraction Ω_i to the critical density, where suffix i stands for different components of the Universe energy budget and, (3) the spectrum and type of primeval density perturbations. Having these initial data, one can use *numerical simulations* to test the observable Universe. On scales $k \leq 0.2hMpc^{-1}$, structure formation can be described by mildly non-linear perturbation theory; on smaller scales, wavenumbers correspond to collapsed objects which are non-linear i.e. $\delta(k) \geq 1$ requiring numerical simulations to follow their evolution. The main goal of cosmological numerical simulations is that they provide robust modelling of LSS, which once compared against present and future observations, can allow to constrain cosmological parameters [54].

3.1.1 Gravitational lensing

When photons travel from their source to the receiver, their propagation paths are affected by the mass distribution of the Universe w.r.t those they would have followed in a perfectly homogeneous Universe. The phenomena of these deflected photons is in many ways similar to the description of propagation of light through any other media, hence this branch is known as *gravitational lensing* or *gravitational optics* [55].

Gravitational lensing is one of the basic predictions of Einstein's theory of general relativity where mass present in the geodesic of photons (or gravitational waves) travelling from a source to an observer experiences bending in proportion to the mass of the lens.

In the whole phenomena of gravitational lensing, there are three key components: the source (which can be a single stellar object or galaxies), lens (this could be cluster of galaxies on large scale or even a black hole) and an observer/detector. Fig.3.2 depicts the scenario of gravitational lensing, by reproducing image taken from ESA[1]:

Gravitational lensing has emerged as one of the most powerful probes to untangle the dark Universe as lensing is sensitive to mass only and independent of the physical state of the source and the lens. Gravitational lensing can provide crucial information on the geometry of the Universe, on the cosmological scenario of formation of its large scale structures as well as on the evolution of its components. The properties and the interpretation of gravitational lensing depend on the projected mass density integrated along the line of sight and on the cosmological angular distances to the observer, the lens and the source. Hence, gravitational lensing can probe the mass of deflectors/lenses regardless their dynamical stage and the nature of the deflecting matter [56].

Massive cosmological structures exert such a powerful gravitational pull that they can wrap the surrounding spacetime and act as a gravitational lens. These gravitational lenses can bend, distort and magnify light behind them. Gravitational lensing of faint background galaxies provide a powerful probe of the mass distribution in and around clusters and of large-scale structure [57].

On the one hand, deep gravitational potential wells including galaxies and galaxy clusters generate *strong lensing* leading to arcs, arclets, and multiple images. In case

[1]https://www.esa.int/esearch?q=microlensing

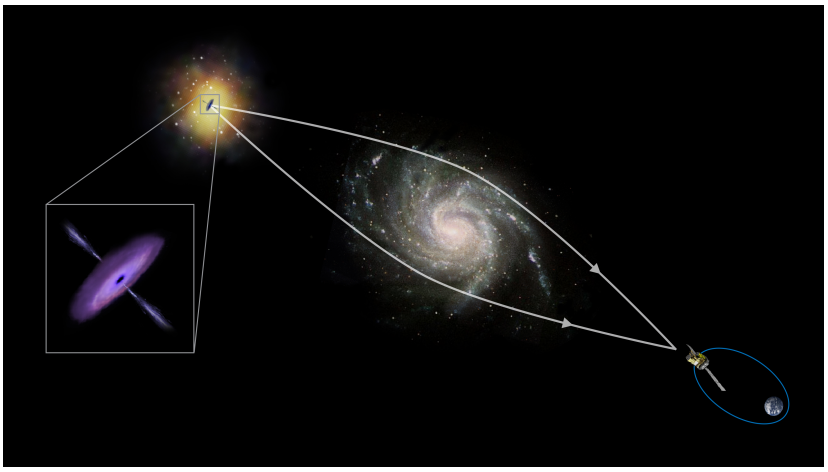

Figure 3.2: Massive objects (stars, clusters of stars or galaxies) present in between the source and the observer which acts as a lensing resulting into bending of light according to their gravity. Due to bending, the image of the lens is distorted either in form of change in their brightness or even in number of images. Image shows the 'magnifying effect' of the stars located in a spiral galaxy to 'zoom in' to another galaxy known as PSK 1830-211. Image shows the vicinity of the supermassive black hole devouring material from its surroundings while firing powerful jets of particles that emit light up to the high energies of gamma particles. Observing these jets with ESA's INTEGRAL and NASA's Fermi and Swift satellites, the astronomers could measure the size of the region around the black hole where they originate. Original image is reproduced from ESA.

of strong fields involved, if the source, massive lens and observer lie in the straight line, the source will appear as a ring behind the massive object, usually known as the *Einstein ring*. The actual image of the first ever lensed image of a quasar which looks like a group of five stars is shown in figure 3.3. The multiple image effect seen in the Hubble picture is produced by gravitational lensing due to gravitational field of a cluster of galaxies which bends and amplifies light of the background quasar. This 'quintuple quasar' is so far the only case in which multiple quasar images are produced by an entire galaxy cluster acting as a lens. The image is taken from HST/NASA[2]:

On the other hand, more moderate perturbations give rise to *weak lensing* which is widely used to measure the matter power spectrum in the selected regions of the sky. In fact, matter distributed inhomogeneously in the Universe on scales larger than galaxy clusters also gravitationally lenses background sources. These distortions in the galaxy shapes by weak gravitational lensing of intervening structures along the line of sight are known as galaxy lensing or cosmic shear. Such images are coherently distorted by the tidal force of matter inhomogeneities along the line of sight. By measuring galaxy shape correlations, properties and evolution of LSS as well as geometry of the Universe can be untangled.

While considering gravitational lensing in a cosmological context, we assume that gravitational lensing inhomogeneities have weak gravitational fields (i.e. their Newtonian potential is small, $\Phi << c^2$) and the sources of gravitational potential are assumed to move slowly with respect to the mean cosmic flow such that their peculiar velocities

[2]https://hubblesite.org

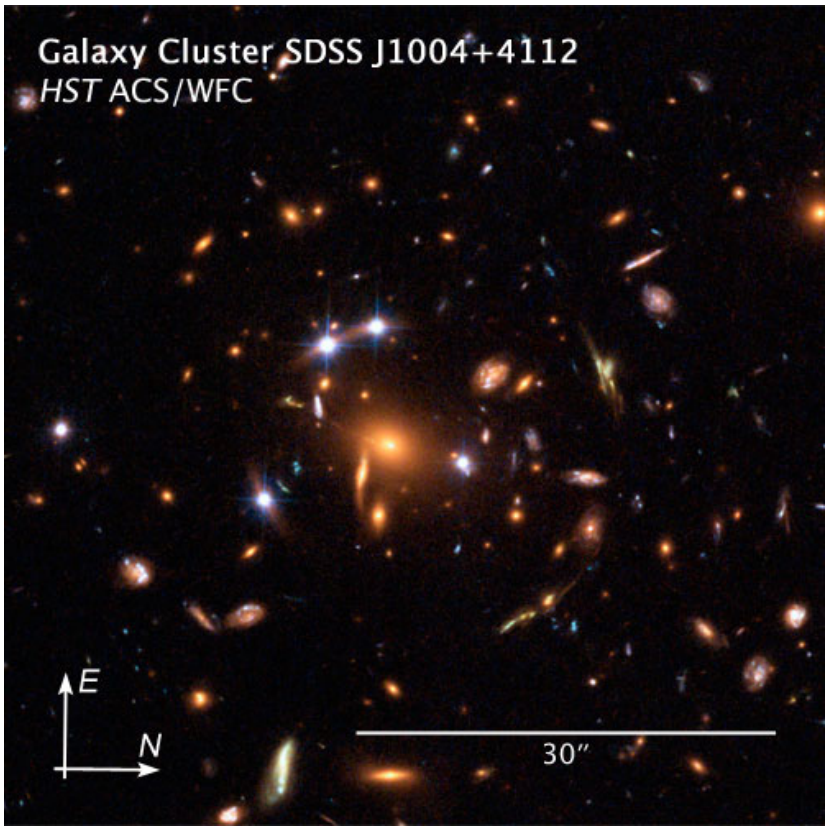

Figure 3.3: The background quasar in the core of the galaxy at a distance of 10 billion light years which can be seen in the image as multiple faint red arcs. The galaxy cluster creating the lens is known as SDSS J1004+4112 and was discovered in the Sloan Digital Sky Survey. This is one of the most distant (7 billion light years away) clusters, and is seen as it appeared when the Universe was about half of its present age. This is a rare event as a supernova exploding is discovered in one of the cluster galaxies. Original image is taken from HST/NASA.

are small compared to the speed of light [58].

Weak gravitational lensing

Weak lensing carries information about the spacetime geometry and LSS of the Universe. In this case, the net effect is statistical because image distortions are very small. Weak lensing can be detected by analysing large number of objects to find distortions only of a few percents. In particular, magnification and distortion effects due to weak lensing can be used to probe the statistical properties of matter distribution between an observer and ensemble of sources. A statistical association of foreground objects with background sources can indicate magnification caused by the foreground objects on the background sources [58]. Since galaxies are intrinsically elliptical and the weak gravitational lensing signal is weak enough, a very large number of galaxies must be used to extract information from weak lensing surveys.

Born approximation: In astrophysical lensing cases, generally the light behaviour is well described by the geometrical optics limit which requires that the wavelength of light is much smaller than its typical travel distance as well as the radius of curvature of the Universe which is approximately H_0^{-1}. In this limit, light can be treated as if it

were a particle excluding wave-like effect and the angular distances. Moreover, the flat sky approximation can be applied when the radial extension of the involved entities is much smaller than their relative distances. As a result source, lens and observer can be thought of lying on the plane. The spatial coordinates can be separated into a radial coordinate along the line of sight and two angular ones (θ, ϕ) lying on a plane perpendicular to it and characterizing the angular displacement from the polar axis. The geometry of this approximation is depicted in figure 3.4: a mass concentration at redshift z_d or angular diameter distance D_d acts as a deflector for the light rays from a source at redshift z_s or angular diameter distance D_s. The angular position of the source is denoted by $\vec{\beta}$ which is seen by the observer at the origin as arriving from an apparent angular position $\vec{\theta}$, i.e. the image is deflected from its real position by an angle $\hat{\alpha}$ which is known as the *deflection angle*.

In the limit of Born approximation, it becomes sufficient to calculate all the relevant integrated quantities, i.e. the lensing potential and its angular gradient, the deflection angle, along the *undeflected* rays. In the absence of other deflectors along the line-of-sight, and if the extent of the deflecting mass along the line-of-sight is very much smaller than D_d and D_{ds} as shown in figure, the actual light rays which are smoothly curved in the neighbourhood of the deflector can be replaced by two straight lines with a kink near the deflector. The deflection angle depends on the mass distribution of the deflector and the impact vector of the light ray.

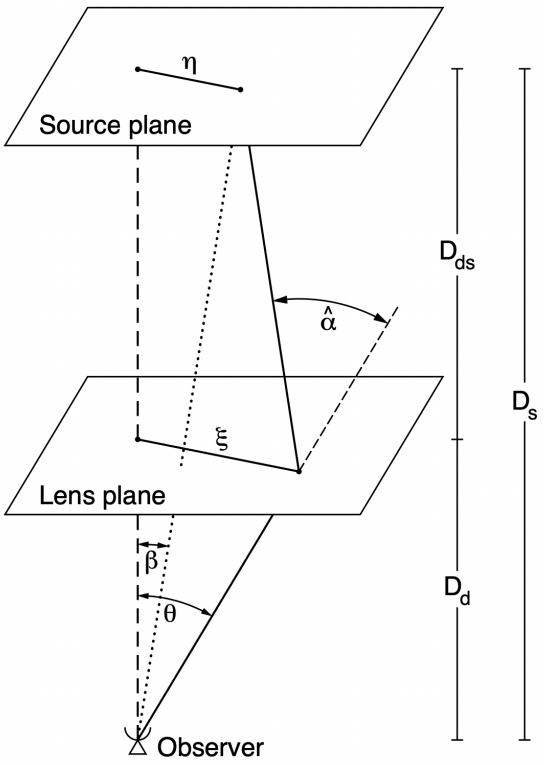

Figure 3.4: A typical gravitational lens system indicating structure of Born approximation. Original image is taken from [58].

The *first Born approximation* exploits the *small-angle scattering limit*, where *the change in the comoving separation of source light-rays due to the deflection caused by lensing from a matter distribution is small compared to the comoving separation of the*

undeflected rays. In this case, the treatment of light deflection can be linear in the metric perturbations. We consider lensing only by density perturbations and deal in the so-called conformal Newtonian gauge. Then, the line element reduces to,

$$ds^2 = a^2(\eta)[-(1+2\phi)d\eta^2 + (1-2\psi)\gamma_{\alpha\beta}dx^\alpha dx^\beta] \tag{3.4}$$

where, the unperturbed spatial metric, $\gamma_{\alpha\beta}$, assuming flat space, is

$$\gamma_{\alpha\beta}dx^\alpha dx^\beta = d\chi^2 + r^2(\chi)(d\theta^2 + sin^2\theta d\phi^2)\,. \tag{3.5}$$

In GR and in the absence of anisotropic stress which is the case of large scale structure, the two potentials ϕ and ψ are equal [51]. If these perturbations vanish, Eq.(3.4) reduces to the FLRW metric. Solution of $r(\chi)$ is defined as,

$$r(\chi) = \begin{cases} k^{-1/2}\sin(\sqrt{k}\chi) & k > 0 \\ \chi & k = 0 \\ (-k)^{-1/2}\sinh[(\sqrt{-k})\chi] & k < 0 \end{cases} \tag{3.6}$$

We can divide the line element by $[-a^2(\eta)(1-2\psi)]$ and use the related conformal metric at first order in the perturbations θ and ψ as we are only calculating path of the null geodesic for lensing,

$$d\hat{s}^2 = (1+4\Phi)d\eta^2 - \gamma_{\alpha\beta}dx^\alpha dx^\beta \tag{3.7}$$

where, $\Phi \equiv (\phi+\psi)/2$ is known as the 'Weyl potential' [59]. In the linear limit, for matter perturbations in the absence of stress perturbations, $\phi = \psi = 0$ holds and therefore Φ is related to the matter-distribution density via the corresponding expression for the Poisson equation. This is also applicable for the weak-field limit on the small scale [60].

To obtain the incident photon trajectories, we should solve the geodesic equation expressed in new conformal metric $\hat{\lambda}$ whose 0-component becomes:

$$\frac{d^2\eta}{d\hat{\lambda}^2} + 2\Big(\frac{d\eta}{d\hat{\lambda}}\Big)^2\frac{d\Phi}{d\eta} + 2\frac{d\eta}{d\hat{\lambda}}\frac{dx^\alpha}{d\hat{\lambda}}\frac{\partial\Phi}{\partial x^\alpha} = 0 \tag{3.8}$$

where, the derivative:

$$\frac{d\Phi}{d\eta} = \partial_\eta\Phi + \frac{dx^\alpha}{d\eta}\partial_\alpha\Phi \tag{3.9}$$

is along the perturbed ray and $\hat{\lambda}$ differs from λ in original reference frame. With Eq.3.8 we could eliminate the affine parameter $\hat{\lambda}$ in favor of η, and obtain the spatial component of the geodesic equation [59],

$$\frac{d^2x^\alpha}{d\eta^2} - 2\frac{dx^\alpha}{d\eta}\Big(\frac{d\Phi}{d\eta} + \frac{dx^\beta}{d\eta}\frac{\partial\Phi}{\partial x^\beta}\Big) + 2\gamma^{\alpha\beta}\frac{\partial\Phi}{\partial x^\beta} + {}^{(3)}\bar{\Gamma}^\alpha_{jk}\frac{dx^\beta}{d\eta}\frac{dx^k}{d\eta} = 0 \tag{3.10}$$

where, $\bar{\Gamma}^\alpha_{jk}$ are the connection coefficients of the unperturbed 3D geometry $\gamma_{\alpha\beta}$ [24].

For convenience, consider an observer located at the origin of the spatial coordinates where we are interested in the rays focusing at $x^\alpha = 0$. For such rays, $d\chi/d\eta = -1 + O(\Phi)$ and $d\theta/d\eta = O(\Phi)$ with an equivalent result for ϕ. Substituting these results in Eq.(3.10) and evaluating the background connection coefficients [59],

$$\frac{d^2\chi}{d\eta^2} + 2\frac{d\Phi}{d\eta} = 0 \tag{3.11}$$

$$\frac{d^2\theta}{d\eta^2} - 2\frac{d\ln r(\chi)}{d\chi}\frac{d\theta}{d\eta} + \frac{2}{r^2(\chi)}\frac{\partial\Phi}{\partial\theta} = 0 \tag{3.12}$$

$$\frac{d^2\phi}{d\eta^2} - 2\frac{d\ln r(\chi)}{d\chi}\frac{d\phi}{d\eta} + \frac{2}{r^2(\chi)}\frac{1}{sin^2\theta}\frac{\partial\Phi}{\partial\phi} = 0 \tag{3.13}$$

determining the perturbed rays up to first order in Φ [59]. Eq.(3.11) has $d\chi/d\eta + 2\Phi$ as a first integral which must be -1 by the null geodesic condition for the perturbed ray. Integrating again we obtain,

$$\chi = \eta_0 - \eta - 2\int_{\eta_0}^{\eta} \Psi d\eta^{'} \tag{3.14}$$

where the integral is along the ray. Since we only consider first order in Ψ, we can evaluate the integral along the unperturbed path $\theta = cont.$, $\phi = const.$ and $\chi = \eta_0 - \eta$. Integrating Eq.(3.14) to a fixed η implies a radial displacement. Alternatively if we integrate Eq.(3.14) to a fixed χ, it implies to a variation in the conformal time at emission. This defines the time delay if the potential is negative on-average along the ray, i.e. it passes mostly through overdense regions.

Eq.(3.12) and Eq.(3.13) can be integrated twice back to a conformal time $\eta_0 - \eta_* = \chi_*$ using the zero order result $\chi = \eta_0 - \eta$, since it only appears in the argument of a function multiplying first order terms. Then, changing the integration order, the integral over $r^{-2}(\eta_0 - \eta^{'})d\eta^{'}$ can be done using the explicit form in Eq.(3.6), which gives [59]:

$$\theta(\eta_0 - \chi_*) = \theta_0 - \int_0^{\chi_*} d\chi \frac{r(\chi_* - \chi)}{r(\chi_*)r(\chi)} 2\frac{\partial}{\partial\theta}\Psi(\chi\hat{\mathbf{n}}; \eta_0 - \chi) \tag{3.15}$$

$$\phi(\eta_0 - \chi_*) = \phi_0 - \int_0^{\chi_*} d\chi \frac{r(\chi_* - \chi)}{r(\chi_*)r(\chi)} \frac{2}{sin^2\theta}\frac{\partial}{\partial\phi}\Psi(\chi\hat{\mathbf{n}}; \eta_0 - \chi) \tag{3.16}$$

where θ_0 and ϕ_0 denote the line of sight $\hat{\mathbf{n}}$ and $\eta_0 - \chi$ is the conformal time at which the photon was at position $\chi\hat{\mathbf{n}}$. This is the first order solution and it can be continued to obtain solutions for the photon trajectories of arbitrary accuracy. From Eq.(3.12), and Eq.(3.13) we obtain the *displacement vector* or the *deflection angle* α on the sphere,

$$\boxed{\alpha(\chi, \hat{\mathbf{n}}) = -2\int_0^{\chi_*} d\chi \frac{r(\chi_* - \chi)}{r(\chi_*)r(\chi)} \nabla_{\hat{\mathbf{n}}}\Phi(\chi\hat{\mathbf{n}}; \eta_0 - \chi)} \tag{3.17}$$

In Eq.(3.15) and Eq.(3.16), the small angular displacements $\theta - \theta_0$ and $\phi - \phi_0$ form the components of the displacement vector α on the sphere. The vector $\hat{\mathbf{n}'}$ is a covariant derivative on the sphere, which can be obtained from $\hat{\mathbf{n}}$ by moving its end on the surface of a unit sphere by a distance $|\nabla_{\hat{\mathbf{n}}}\Psi(\hat{\mathbf{n}})|$ along a geodesic in the direction of $\nabla_{\hat{\mathbf{n}}}\Psi(\hat{\mathbf{n}})$ where, $[1/r(\chi)]\nabla_{\hat{\mathbf{n}}}$ is the 2D transverse derivative w.r.t. the line of sight [59, 61, 62, 63]. Adopting conformal time and comoving coordinates in flat geometry [64], the integral for the projected lensing potential due to scalar perturbations without anisotropic stress would become:

$$\boxed{\Psi(\chi_*, \hat{\mathbf{n}}) \equiv -2 \int_0^{\chi_*} d\chi \frac{r(\chi_* - \chi)}{r(\chi_*) r(\chi)} \Psi(\chi \hat{\mathbf{n}}, \eta_0 - \chi)} \tag{3.18}$$

Which defines the *lensing potential*. where, $r(\chi)$ is the comoving distance, $r(\chi_*) \approx 10^4$Mpc is the comoving distance at the last scattering surface, η_0 is the present conformal time and Φ is the physical peculiar gravitational potential generated by density perturbations [61, 58, 65, 59]. As can be seen in Eq.(3.18), the lensing potential is formally divergent near $r(\chi) = 0$ which affects the lensing potential monopole only. The deflection angle is the derivative of lensing potential on the sphere at $\hat{\mathbf{n}} : \alpha = \nabla_{\hat{n}} \Psi$.

Due to the statistical features of weak lensing, we deal with lensing potential averaged over the source distance distribution $n(\chi)$:

$$\Psi(\hat{\mathbf{n}}) = \int d\chi_* n(\chi_*) \Psi(\chi_*, \hat{\mathbf{n}}) = -2 \int d\chi g(\chi) \Phi(\chi \hat{\mathbf{n}}, \eta_0 - \chi) \tag{3.19}$$

where,

$$g(\chi) \equiv \frac{1}{r(\chi)} \int_\chi^\infty d\chi' n(\chi') \frac{r(\chi' - \chi)}{r(\chi')} \tag{3.20}$$

is a bell shaped function which peaks roughly half of the background source distance and is normalized so that $\int d\chi n(\chi) = 1$ [60, 65, 61].

Galaxy Clustering

In order to understand the structure of the Universe, it is important to analyse the galaxy distribution in a representative large volume of cosmological scales by obtaining sky positions, velocities and distances for a few millions galaxies. The simplest description of galaxy clustering is the two-point correlation function (2PCF) ξ, which measures the excess over random probability of finding two galaxies separated by a given distance r. At small scales, it is found empirical to follow a power law: $\xi = (r/6h^{-1}Mpc)^{-1.8}$ [66]. After Fourier transforming the galaxy correlation function, we can obtain the power spectrum of the galaxy distribution. This power spectrum can be directly compared with theoretical predictions from inflation and CDM models.

More specifically, the galaxy 2PCF measures the excess over random probability that two galaxies at volume elements dV_1 and dV_2 are separated by distance $r \equiv |\mathbf{r}_1 - \mathbf{r}_2|$, i.e.

$$dP_{12} = n^2 \left[1 + \xi(r)\right] dV_1 dV_2 \tag{3.21}$$

where n is the galaxy average number density. If the distribution is random[3] i.e. there is no clustering, then $\xi(r) = 0 \; \forall r$.
Since the probability of having a galaxy in the volume element dV_1 is $n \times dV_1$, the conditional probability that there is a second object at dV_2 given that there is one at dV_1 is:

$$dP(2|1) = n \left[1 + \xi(r)\right] dV_2. \tag{3.22}$$

[3]The statistics of a random catalogue is that of a Poisson distribution.

Hence, if objects are clustered (i.e. $\xi(r) > 0$), then the conditional probability is enhanced, whereas if objects are anticorrelated (i.e. $\xi(r) < 0$) the conditional probability is suppressed over the random case, as expected.

Now if we consider the continuous random density contrast field $\delta(\mathbf{r})$, the 2PCF can be written as the cumulant moment of the field computed at a position $\mathbf{x}$ and another position $\mathbf{x} + \mathbf{r}$:

$$\xi(\mathbf{r}) \equiv \langle \delta(\mathbf{x} + \mathbf{r}) \delta(\mathbf{x}) \rangle_{\mathbf{x}} \tag{3.23}$$

where the ensemble average is done over all $\mathbf{x}$.
Using Eq. (3.2), we can write:

$$\xi(\mathbf{r}) = \frac{\langle \rho(\mathbf{x} + \mathbf{r}) \rho(\mathbf{x}) \rangle_{\mathbf{x}}}{\bar{\rho}^2} - 1 \tag{3.24}$$

Also, we can write an analogous formula to that of Eq. (3.21):

$$\langle \rho(\mathbf{x} + \mathbf{r}) \rho(\mathbf{x}) \rangle_{\mathbf{x}} = \bar{\rho}^2 \big[1 + \xi(\mathbf{r}) \big] \tag{3.25}$$

Fig.3.5 and Fig.3.6 respectively shows the distribution of galaxies in 2dF Galaxy Redshift Survey and a large slice of the Universe from the VIMOS Public Extragalactic redshift Survey [67]:

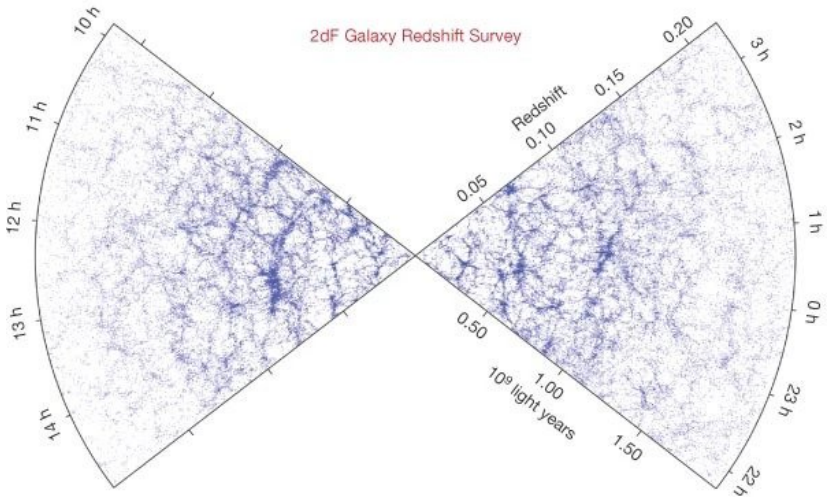

Figure 3.5: The galaxy distribution from the 2dF Galaxy Redshift Survey, the angular extent of the map is given in terms of right ascension (h) with 24h being 360°. Each piece of the map spans about 75° across the sky in a narrow strip of declination. This survey contains approximately 250,000 galaxies selected in the blue light. On large scales, statistical analysis finds good match with ΛCDM model. This image is taken from: [68].

3.2 N-body simulations

A widely used numerical approach to describe the nonlinear evolution of cosmic structures is to implement N-body simulations. At the initial time of the simulation, the particles must reproduce a given initial condition. To do so, the simplest method is to

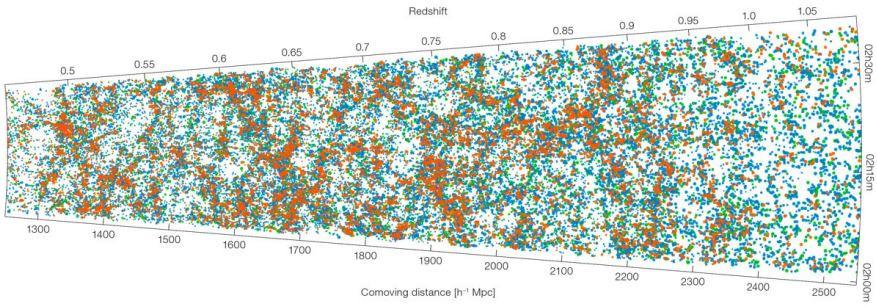

Figure 3.6: The position of some of the galaxies verified by the VIPERS survey: this is one of the two slices produced by the survey which shows where the galaxies lie as we look to ever greater distance in space corresponding to look further back in time. This helps to study evolution of galaxies and of the space in the Universe itself. Image is reproduced from [67].

place these particles on a grid and compute initial displacements such that the resulting distribution has the same power spectrum as the desired one. Such displacements can be computed e.g. by using perturbation theory. Then, the actual simulation can start. It follows the gravitational evolution of this set of particles by computing, at each new time step, the force exerted on each particle and consequently updating its position and velocity.

There exist many methods to compute the force acting on the i-th particle, e.g. the particle-particle method where the force on the particle is computed as the sum of the forces exerted by each of the other particles, computed separately. This is the most precise and accurate method, but it is certainly very expensive from the computational point of view. Other very used approaches are the *Particle-mesh* (PM) method and *Tree* methods for dark matter simulation. In the PM methods, the masses of the particles are projected onto a regular lattice in order to estimate on each point the density field. On the regular grid the Fast Fourier Transform (FFT) algorithm is used to solve the Poisson's equation in efficient way. In the Tree method, for each particle, the force is computed as the sum of the contribution of several hierarchical groups such that only the neighbouring particles are treated individually. The contribution of distant groups of particles are approximated as if all particles in the group were located at their center of mass [42]. Other methods include hybrid approaches and combinations of PM and Tree methods.

If other phenomena such as hydrodynamic interactions are required to be taken into account, then other kinds of laws that govern the behaviour of particles must be implemented. Hydrodynamic simulations are the best choice when one is interested in galaxy formation or baryonic matter flows, but they are very expensive from the computational point of view. However, there are two less expensive ways to simulate the distribution of galaxies, which consist in taking a DM simulation and placing galaxies inside the DM halos or sub-halos following a so-called Halo Occupation Distribution (HOD) model or a so-called Halo Abundance Matching (HAM) technique. These methods are often implemented comparing real data to halo catalogs in N-body simulations and exploiting empirical models.

In fact, the formation and growth of galaxies is connected to the growth of the

halo in which they form. Galaxies form by the cooling and condensation of gas in the centres of the potential wells of extended virialised dark matter haloes. According to modern models of structure formation, a dark matter halo is the basic unit in which the matter collapses. It is a collapsed region that is decoupled from the Hubble expansion. It contains gravitationally bound matter. In numerical simulations it is often defined with mass and radius specified by a given overdensity:

$$M_{vir} = \frac{4\pi}{3} R_{vir}^3 \Delta \rho_m \tag{3.26}$$

The value of Δ corresponds to the overdensity predicted for a virialised region that has undergone spherical collapse and can take different values accordingly to the halo definition. A single dark matter halo may contain multiple virialised clumps of dark matter bound together by gravity, known as subhaloes. They are smaller than the host halo and they orbit within the gravitational potential of the host halo.

In this work we have exploited mock galaxy catalogs obtained via a sub-halo abundance matching (SHAM) modelling that is an empirical method tackling the issues of connecting observed galaxies to simulated dark matter halos and subhalos using a correspondence between a particular property of the galaxies and a property of the halos in which they live.

Figure 3.7 gives an example of dark matter distribution and the corresponding galaxy distribution, obtained with an abundance matching model.

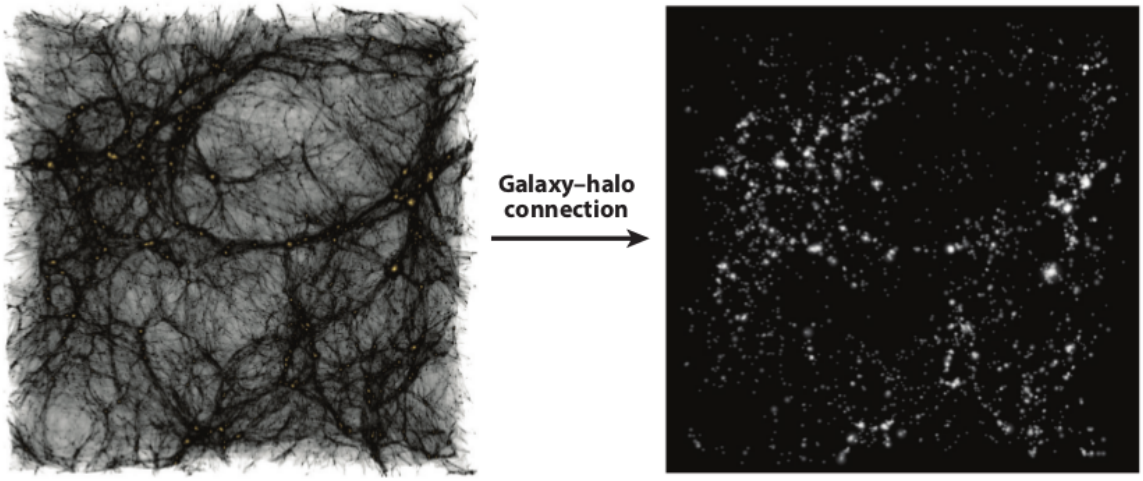

Figure 3.7: Dark matter distribution in a $90 \times 90 \times 30$ Mpc h^{-1} slice of a cosmological simulation (left) compared with the galaxy distribution using an abundance matching model (right) [69].

3.2.1 The DEMNUni simulations

The "Dark Energy and Massive Neutrino Universe"[4] (DEMNUni) project [70] consists of a set of 16 large N-body numerical simulations to study the evolution of large scale structures in the presence of massive neutrinos and dynamical (i.e. time-dependent) dark-energy, parameterised according to Chevallier, Polarski & Linder (CPL).

[4] https://www.researchgate.net/project/DEMN-Universe-DEMNUni

The simulations are characterised by a box side $L = 2$ Gpc/h, a particle number of $N = 2 \times 2048^3$ (the factor of 2 stands for CDM and neutrino particles), and a mass resolution for CDM particles of about $8 \times 10^{10}\ M_\odot$/h. They have been produced via a modified version of the GADGET-3 code which includes massive neutrinos as a particle component and accounts for dark energy models in the background evolution.

Given their large volume and mass resolution, the DEMNUni simulations are used to generate mock data catalogues, and to study different probes including clustering features of LSS [71], cosmic voids [72, 73, 74], and linear point of the correlation function [75], CMB- and weak-lensing [70], and their cross-correlations in the presence of massive neutrinos and dynamical dark energy.

The baseline cosmology is assumed to agree with parameter constraints from Planck 2015 [76], namely a flat ΛCDM model generalised to a $\nu\Lambda CDM$, i.e. a massive neutrino model, by varying only the sum of the neutrino masses over the values $\sum m_\nu = 0, 0.16, 0.32$ eV (and consequently the corresponding values of Ω_ν and Ω_c, while keeping fixed Ω_m and the amplitude of primordial curvature perturbations). In addition, the simulations account for different dark energy equations of state, consisting of four different combinations of the CPL parameters w_0 and w_a in the dark energy EoS:

$$w(a) = w_0 + w_a(1 - a) \tag{3.27}$$

The EoS parameters are set within the Planck-2015 constraints: $w_0 = -0.9, -1.1$ and $w_a = -0.3, 0.3$. Each simulation starts at the initial redshift $z_i = 99$, producing 63 different time outputs down to $z = 0$, which are logarithmically equispaced in the scale factor $a = 1/(1 + z)$. In this work we consider outputs in the range $0 < z < 2$, because this is the redshift range of interest for upcoming galaxy surveys, such as Euclid.

In order to build halo catalogues, each of the 63 particle snapshots has been post-processed with the friends-of-friends (FoF) algorithm [77], setting to 32 the minimum number of particles, thus fixing the halo minimum mass to $M_{\rm FoF} \simeq 2.5 \times 10^{12}\, h^{-1} M_\odot$. Finally, the FoF catalogues have been processed via the SUBFIND algorithm [78] so that the initial FoF parent halos are split into multiple sub-halos, with the result of an increase in the total number of identified objects and of a lower minimum mass limit. Here, a minimum number of 20 particles have been adopted in order to constitute a valid sub-halo. Fig.3.8 shows the effect of massive neutrinos on one of the largest DM halo within the DEMNUni simulations.

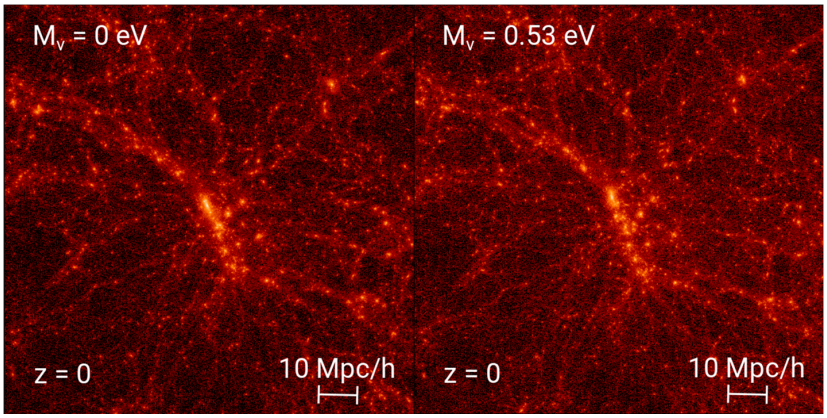

Figure 3.8: Effect of massive neutrinos on one of the largest DM halo within the DEMNUni simulations.

Chapter 4

The Cosmic Microwave Background

To find is the thing.

Pablo Picasso

In this section we would reveal how the uninterrupted travel of photons emitted as the oldest light since decoupling when the Universe was about 380, 000 year old is captured in the form of a first ever snapshot of the Universe.

The surprising discovery of the Cosmic Microwave Background (CMB) by A. Penzias and R. Wilson [79] in 1965, is a uniform black body radiation characterised by a mean temperature $T = 2.725K$ with root mean square variations of only $18\mu K$ after subtraction of the dipole anisotropy from the Doppler shift of the background radiation. Their discovery of isotropic temperature at around $4GHz$ frequency which remains constant regardless seasonal variation was coming from unknown sources with the confirmation of measurement provided by Dicke et al. [80].

CMB is the thermal relic radiation left over from the time of recombination in the ΛCDM model. In the first 3.8×10^5 years after the Big Bang, the Universe was made by a plasma of photons, electrons and baryons. At this stage, photons were constantly scattered by electrons making the Universe optically *opaque*. The primordial plasma was a very hot mixture of photons, free electrons and ionized nuclei which mainly were protons. Due to Compton scattering, photons and electrons were tightly coupled providing very small mean free path for photons. In turn, electrons strongly interacted with protons via Coulomb scattering. Finally, due to formation of neutral hydrogen, electromagnetic reactions kept baryons and photons in thermal equilibrium.

Due to expansion of the Universe, the plasma and the relic radiation filling the spacetime grew cooler to temperature about $0.4eV$ until a point estimated approximately to be at 10^{13} seconds (around 400,000 years) after the Big Bang. This era is known as the recombination epoch when the expansion of the Universe provided temperature to cool enough for photons and electrons to combine and form neutral hydrogen atoms. Before recombination, the baryons and photons were tightly coupled where for the fluid baryons provided the weight and photons provided pressure, and the perturbations oscillated in the potential wells generated by the dark matter perturbations. After decoupling, baryons were free to collapse into these potential wells and the CMB carries a record of these processes at the surface of last scattering. Since these atoms could no longer absorb thermal radiation, the Universe became transparent for the first time when photons travelled freely through the space rather than being con-

stantly scattered by electrons and protons in plasma. This radiation which is coming form about 380000 years after the Big Bang in form of CMB defines the period called *time of last scattering*. In the early Universe, the matter and radiation were in thermal contact because of frequent interactions between photons and electrons. Eventually due to expansion and evolution of the Universe, the density of free electrons became too low to maintain thermal contact which resulted into decoupling of matter and radiation when $\Gamma_\gamma \approx H$ or when the mean free path of the photons became $\lambda_\gamma \approx \Gamma_\gamma^{-1}$ larger than the Hubble distance H^{-1} [5]. By this time, photon-electron scattering was governed by Thompson scattering, which is the low-energy limit of Compton scattering. The interaction rate of the photons is given by,

$$\Gamma_\gamma = n_e \sigma_T \tag{4.1}$$

where, n_e is the *number density of free electrons* and $\sigma_T = 6.65 \times 10^{-25} cm^2$ is the *Thompson cross-section*. The number density of free electrons n_e got reduced by the increasing amount of neutral hydrogen and the Thompson scattering rate Γ_γ dropped. When $\Gamma_\gamma \leq H$, the mean free path of photons became longer than the horizon size and the photons decoupled from matter. This results into CMB formation when the Universe reached a temperature of about $T \simeq 0.26$eV and $z \simeq 1090$.

The cosmological recombination era marks an important phase in the history of the Universe by precisely determining how CMB photons decoupled from baryons around redshift $z \approx 10^3$. If decoupling occurred at redshift of $1+z_{dec} \approx 1100$ then, temperature at decoupling was,

$$T_{dec} = T_0(1 + z_{rec}) = 3030\text{K} = 0.26\text{eV} \tag{4.2}$$

And considering matter domination, the age of the Universe at decoupling was [5],

$$t_{dec} = \frac{2}{3} H_0^{-1} \Omega_0^{-1/2} (1 + z_{dec})^{-3/2} = 5.64 \times 10^{12} (\Omega_0 h^2)^{-1/2} \text{sec} \tag{4.3}$$

When we look at the CMB photons, they are reaching to us from all directions in the sky giving us a snapshot of the spherical surface in the Universe that surrounds us at a distance of $\approx 10^4$Mpc when the Universe was about 300,000 years old.

After the era of decoupling, photons propagate unperturbed to us providing us a snapshot of the Universe at the time of recombination and its polarization and temperature fluctuations carry information about the initial conditions at the end of inflation including imprints of Primordial Gravitational Waves (PGWs) [10, 81, 82, 4]. The presence of such PGW background at the time of recombination give rise to both temperature and polarization anisotropies, the most important signature is a "curl" like or the *"B-mode"* polarization pattern in the CMB polarization. CMB radiation gets linearly polarized via Thompson scattering between photons and electrons at last scattering in presence of a quadrupole anisotropy in the intensity field of photons [83, 84, 85]. In the tight coupling regime between photons and electrons, Thompson scattering isotropizes the radiation field in the rest frame of the electron and erases any incident quadrupole. Therefore in general, polarization angular power spectra have smaller amplitude than temperature power spectrum as only a few percent of CMB photons get polarized. Polarization is thus generated mostly around temperature dissipation scales and close to recombination, in a photon-electron mild-coupling regime. The polarization pattern is obtained by solving the Einstein-Boltzmann equations for the photon distribution

characterized by a generic polarization tensor [86, 32]. The Boltzmann equation for photons encodes all information about correlations about intensity and polarization of the CMB. On the observational side, CMB intensity and polarization are analysed by re-expressing the real space data in a spherical harmonic expansion. The intensity measurements can be expanded in the standard spherical harmonics whereas the polarization data must be expanded in spin weighted spherical harmonics [87].

4.1 CMB temperature anisotropies

The CMB is the direct evidence that the Universe began from a hot Big Bang and the surface of the last scattering was at redshift $z \approx 1100$ and age of $180,000(\omega_0 h^2)^{-1/2} yr$ [5] and is one of the most powerful probes of the early Universe containing imprints of primordial gravitational potential fluctuations [88] which are considered as origins of the large scale structures. The energy density of photons is known to high accuracy which is dominated in the microwave background with blackbody temperature T = 2.728K [89] giving us,

$$\Omega_{\gamma,0} h^2 = 2.48 \times 10^{-5} \tag{4.4}$$

A photon with an energy $K_B T_0$ has a wavelength $\bar{h}c/K_B T_0$. In the early Universe when the scale factor was smaller than its present value, this wavelength could have been correspondingly smaller. Since the energy of a photon is inversely proportional to its wavelength, the photon energy would have been larger than today by a factor of $1/a$. Assuming three massless neutrino spices ($T_\nu \propto 1/a$), the total energy density in relativistic particles would be [10] (subjected to minute changes considering mass of any spice of neutrinos):

$$\Omega_{rad,0} = 4.17 \times 10^{-5} h^2 \tag{4.5}$$

The temperature of CMB is astonishingly uniform- $\delta T/T \leq 10^{-5}$ on angular scales ranging from 10 arc seconds to 180°. The first direct detection of anisotropies in the CMB was made by the *Cosmic Background Explorer (COBE)* satellite. CMB temperature anisotropies are generally defined by a dimensionless quantity,

$$\Theta(\hat{n}) = \frac{T(\hat{n}) - \langle T \rangle}{\langle T \rangle} \tag{4.6}$$

showing deviations form the average temperature $\langle T \rangle$ in a given direction on the sky $\hat{n} = \theta, \phi$. The temperature anisotropies can be further expanded as,

$$\Theta(\hat{n}) = \sum_{l=0}^{\infty} \sum_{m=-l}^{l} a_{lm} Y_{lm}(\hat{n}) \tag{4.7}$$

where,

$$a_{lm} = \int d\Omega Y^*_{lm}(\hat{n}) \Theta(\hat{n}) = \int_{\theta=-\pi}^{\pi} \int_{\phi=0}^{2\pi} d^2\hat{n} \Theta(\hat{n}) Y^*_{lm} \hat{n} \tag{4.8}$$

Here, $l = 0$ and $l = 1$ represents the monopole (average temperature over the whole sky) and dipole term (depends linearly on the velocity of the observer) respectively. $l =$

2 shows the quadrupole and the magnetic quantum numbers satisfying $m = -l, ..., +l$. The multipole moments a_{lm} maybe combined into the rotationally invariant angular power spectrum described further. Generally, in CMB data analysis, dipole term is removed from the sum. The upper bound of the sum is dictated by the resolution of the experiment and the expansion coefficients a_{lm} are called the *multipole* or *harmonic coefficients*.

The COBE maps show structure with characteristic anisotropy of $\delta T/T \cong 6 \times 10^{-6}$ [90]. The largest anisotropy is a fluctuation of about 1/1000 forming a dipole pattern across the sky. The dominant contribution to δT comes from the motion of our solar system with respect to the CMB rest frame which can be seen as a Doppler shift in the CMB temperature. Since this changes with the orbital motion of the Earth around the Sun, the dipole is modulated throughout the year. The induced Doppler effect gives rise to overall dipole anisotropy which is generally subtracted to get primordial anisotropy $\delta T(\hat{n})$ where, $\hat{n}$ indicates the line-of-sight direction in the sky. The resulting CMB temperature map showing fluctuations of the order of $\delta T/T \simeq 10^{-5}$ as shown in Fig. 4.1:

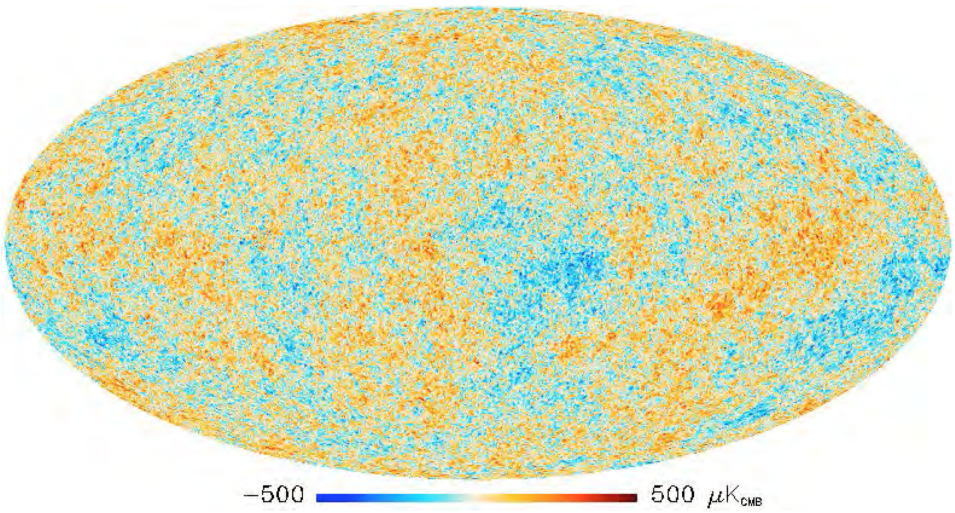

Figure 4.1: CMB intensity map at 5 arcmin resolution based on Planck observations using SMICA component separation algorithm. A small strip of galactic plane was masked and subsequently filled in by a constrained realization with the same statistical properties as the rest of the sky with characteristic spot size about 1°, original plot is taken from [91].

An overdense region at decoupling with gravitational potential $\Phi < 0$ leads to a hot spot in the large-scale CMB map as photons climbing out these potential gain more energy than they had at the bottom of the well due to the accelerated expansion of the Universe. Analogously, cold spots in the CMB sky map are representing locations of underdense regions.

As can be seen in Fig. 4.1, the temperature fluctuations when projected on a 2D spherical sky surface can be expanded in spherical harmonics as,

$$Y_{lm} = \sqrt{\frac{2l+1}{4\pi}\frac{(l-m)!}{(l+m)!}} P_l^m(cos\theta)e^{im\phi} \tag{4.9}$$

where multipole l runs from 0 to ∞, $-l \leq m \leq l$ and P_l^m are the associated Legendre functions. l represents the angular scale on the sky of π/l degrees.

Considering statistical homogeneity and isotropy, and demanding rotation invariance, the power spectrum of the temperature fluctuations C_l^{TT} is given by,

$$\langle a_{lm} a^*_{l'm'} \rangle = C_l^{TT} \delta_{ll'} \delta m m' \tag{4.10}$$

The average is taken over the ensemble of realizations of fluctuations. According to predictions of inflationary models, the fluctuations at early times should be Gaussian which means that the multipole coefficients have Gaussian distributions with zero mean and variance $= C_l^{TT}$.

The CMB power spectrum can be estimated by,

$$C_l^{TT} = \frac{1}{2l+1} \sum_m |a_{lm}|^2 \tag{4.11}$$

The angular power spectrum is an important tool in the statistical analysis of the CMB describing the cosmological information contained in the millions of pixels of a CMB map in terms of a much more compact data representation. The CMB power spectrum is an unbiased estimator, $\langle C_l^{TT} \rangle = C_l^{TT}$, including an error in the estimation of any given C_l^{TT} of $\Delta C_l^{TT}/C_l^{TT} = \sqrt{2/(2l+1)}$. This limit on precision is called the *cosmic variance* which arises as we have only one Universe and one location to make measurements from.

For a Gaussian random process, the angular power spectrum completely characterizes the CMB temperature anisotropies. In a typical cosmological model, the anisotropy power spectrum is usually plotted as the rescaled spectrum $D_l \equiv l(l+1)C_l/2\pi$ so that there is equal power per log interval in l. Figures 4.2 and 4.3 respectively shows the 7 year TT power spectrum from the WMAP and the TT spectra from Planck 2015 data compared with the base ΛCDM fit.

The 2015,2018 Planck data release shows seven observed peaks in the temperature power spectrum, six peaks in the temperature-polarization cross-power spectrum and five peaks in the polarization power spectrum all agreeing the predictions of the ΛCDM model [9] which finds support also from the Wilkinson Microwave Anisotropy Probe (WMAP) temperature and polarization data [94]. The shape of D_l^{TT} for latest 2018 Planck results in Fig.4.3 is very characteristic as the Sachs-Wolfe (SW) effect dominates on large scale (small multipole l), the acoustic oscillations are observed on intermediate scales and the smallest scales are exponentially damped. Since the initial power spectrum is almost scale-invariant, all features in the CMB power spectrum arises form the evolution of cosmic sound waves being captured at the moment of last-scattering, i.e. the observed oscillations are a snapshot of these waves caught at different phases of their evolution. The angular power spectrum features a flat plateau at large angular scales (i.e. small l) followed by a series of oscillatory features at high angular scales with the first and the most prominent being around one degree $l \equiv 200$. These features are known as the acoustic peaks and represent the oscillation of the photon-baryon fluid around the time of decoupling. The positions of the peaks in the CMB spectrum are sensitive to the distance to the last-scattering. In fact, the angular size of the sound horizon at decoupling θ_s is a direct measure of the first peak location at an angular scale of about 1° which is the size of the characteristic spots in the CMB map shown in Fig.4.1. Since ΛCDM takes zero curvature, the peak positions provide a

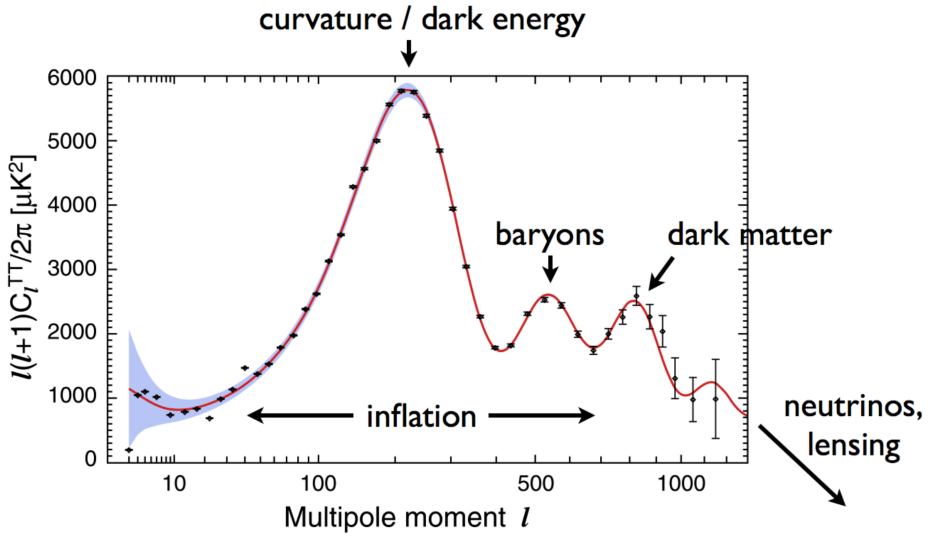

Figure 4.2: The 7 year TT power spectrum $D_l \equiv l(l+1)C_l^{TT}/2\pi$ as a function of multipole l from the WMAP, original plot taken from [92] along with annotations added from [93]. It shows the peak corresponding to cosmological information bought to us. The best fit ΛCDM power spectrum is plotted as a red line and the cosmic variance is indicated by the shaded region.

precise measurement of the expansion history of the Universe, and hence of the Hubble parameter and of matter density. Since the amplitude of cosmic sound waves depends on the time of matter-radiation equality through the radiation driving effect, the height of the peaks relative to the large scale plateau are more sensitive to matter density. This leads to the consequence that the small-scale modes entering the horizon in the RD era are enhanced in comparison to the modes which started evolving latter during matter domination.

The 2018 data release from *Planck* gives the most robust results on the spectrum of CMB temperature anisotropies, with a precision determination of the temperature power spectrum to beyond $l = 2000$. The Atacama Cosmology Telescope (ACT) and South Pole Telescope (SPT) experiments extend these results to the higher angular resolution. The data from these probes provide an accurate measurement of location of set of acoustic peaks, determining the angular diameter distance of the last scattering surface. CMB data gives a precise measurement of the age of the Universe, affirms the need of DM and DE and being consistent with a cosmological constant ($w = -1$), CMB shows no evidence of dynamical dark energy. Planck has also made the first all-sky maps of the *CMB lensing field* which probes the entire matter distribution in the Universe. The CMB photons undergo interactions at the surface of last scattering which are known as the *primary anisotropies* and, on the way reaching the detectors, undergo various processes such as time-varying gravitational potential (the Integrated Sachs-Wolfe/ISW effect), gravitational lensing and scattering from ionized gas at low redshifts, resulting into the so-called *secondary anisotropies*.

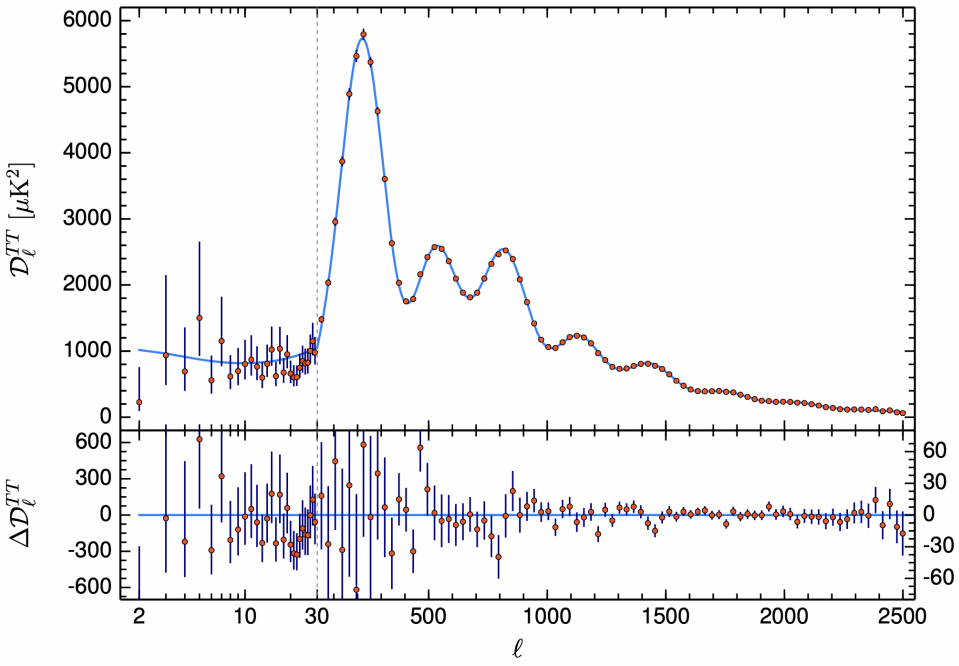

Figure 4.3: Planck 2018 temperature power spectrum $D_l^{TT} \equiv l(l+1)C_l^{TT}/2\pi$ as a function of multipole l, related to the angular scale $\theta \sim \pi/l$ is compared with the base ΛCDM fit with plot taken from [2]. Theoretical spectrum best fit to the Planck TT,TE,EE+lowE+lensing likelihoods plotted in light blue and the lower panel shows the residuals with respect to this model. The error bars show $\pm 1\sigma$ diagonal uncertainties, including cosmic variance approximated as Gaussian.

4.1.1 Physics of CMB anisotropies

CMB temperature fluctuations would help us to understand inflationary predictions about the geometry of the Universe and primordial density fluctuations. CMB polarization can be used to study GWs predicted by inflationary paradigm [81].

The main concern in analysing temperature anisotropies is that on a given angular scale, anisotropy is related to density perturbations on the surface of last scattering of a given wavelength. The multipole moment l receives its dominant contribution from Fourier mode k related by $l = kr$ where r is the comoving distance to the last scattering surface. As shown in Fig.4.3, at large angular scales/ lower multipoles, there is a plateau resulting into a series of bumps and wiggles which damp quasi-exponentially on small angular scales. These regimes are separated by two angular scales: first at about one degree and the second at a few arc minutes.

The large angular scale Sachs-Wolfe plateau ($l < 30$) arises from perturbations with periods of evolution longer than the age of the Universe at last scattering surface, so they have wavelengths lager than horizon of the surface of last scattering. This waves are essentially frozen in their initial configuration and provide us a tool to quest physics that created them. Since CMB γs lose energy climbing potential wells associated with this long wavelength density perturbations, the temperature differences on the sky reflect the gravitational potential differences on the last scattering surface [88, 95]. If the density fluctuations are approximately scale invariant, the plateau in the angular

power spectrum would be flat.

At scales smaller than the horizon at the last scattering surface, the baryon-photon fluctuations that produce anisotropies on sub-degree angular scales ($10 < l < 100$) have sufficient time to undergo oscillations. At maximum compression/rarefaction, the CMB temperature is higher/lower than average. Neutral compression corresponds to velocity maxima of the fluid which lead to a Doppler shifted CMB temperature. But this Doppler effect is sub-dominant as we can only see the line-of-sight component of the velocity and the speed of sound is less than the speed of light. A given multipole l is dominated by the effects of a narrow band of Fourier modes which leads to peaks and valleys observed in the power spectrum. Since the power spectrum is square of amplitude and the troughs correspond to velocity maxima, these peaks show the modes which were maximally under- and over-densed at the last scattering surface.

On scales $l \geq 10$, the finite duration of recombination has an observable effect [96, 97]. During this time, the photons can random walk a distance given by the mean free path which increases during recombination, multiplied with the square root of the number of scattering with electrons. Thus photons can diffuse out of any overdensity on scales smaller than this, which leads to an exponential damping of the spectrum on small scales known as *Silk damping*. Approximating the surface of last scattering as an instantaneous event, the damping is exponential with an e-folding scale given by the geometric mean of the last scattering surface horizon and the photon mean path.

It is important to note that in addition to gravitational potential, photons also interact with other metric perturbations such as vector and tensor metric modes. Tensor perturbations do not alter baryon-photon oscillations but they contribute to the Sachs-Wolfe plateau [88]. These tensor modes distort the distribution of passing photons. While traveling on their way, photons gravitationally interact with matter inhomogeneities. If gravitational potentials are still evolving, additional temperature perturbations are generated by the ISW effect [88]. In this case, a photon falling into gravitational potential gains more energy and if the potential itself evolves while photon's travel, the energy lost climbing back the potential well would be different than the gained one while falling in. This difference in energy leads to net anisotropies. To linear order in perturbations, gravitational potential is constant when matter dominates the energy budget of the Universe and the change in time of the potential is vanishing. If either curvature or a cosmological constant dominates in the later times, this could lead to the so-called late ISW effect.

As mentioned earlier, Rees-Sciama effect is due to non-linear structure formation: once fluctuations leave their linear regime, due to their evolution, gravitational potential vary with time owing to both the growth and the movement of bound haloes which leads to anisotropies through the RS effect. Since the smallest scales are first associated non-linearly, the effect peaks towards small scales and the scale at which fluctuations become non-linear is also imprinted on the CMB. Although this effect is very small and not the dominant source of anisotropies on any scale.

CMB secondary anisotropies

On their journey from last scattering surface to reaching towards us, CMB γs interact with intervening cosmological matter inhomogeneities causing the change in their frequency, energy and geodesic. Such post-decoupling anisotropies are referred to as *secondary anisotropies*. Generally, secondary anisotropies can arise mainly due to: (1)

gravitational effects on photons due to interaction with gravitational potential wells and, (2) scattering between photons and free electrons. The anisotropies due to gravitational interactions include *ISW effect* [88], the *Rees-Sciama effect* (RS) [84] and gravitational lensing of CMB [59]. What we can observe today is the snapshot of the Universe which became neutral at redshift $z \sim 10^3$ after which CMB photons can travel almost freely to us. At epochs $6 \leq z \leq 20$ free electrons due to reionization scatter some of the CMB photons, damping the small scale anisotropies. In addition to this, the CMB quadrupole from the surface of last scattering will scatter from the free electrons giving rise to a polarization signal which can dominate the expected signal from the last scattering surface on large scales. Effect such as SZ, is generated at lower redshift and remains almost unaffected by lensing [98, 82, 99, 100].

These effect produce subdominant secondary anisotropies imprinted on the CMB at late times, which can be measured as a function of redshift by cross-correlating CMB temperature and CMB-lensing maps with galaxy surveys [101].

The late integrated Sachs - Wolfe effect Travelling along the geodesic from the last scattering surface to the observer, CMB γs are red/blue shifted as they cross growing/decaying gravitational potential well. This effect is called the late Integrated Sachs - Wolfe (ISW) effect [88] resulting into one kind of secondary anisotropies. During the matter dominated era, the background expansion and gravitational attraction compensate each other so that the total linear gravitational potential Φ produced by large scale structure distribution in the Universe is constant in time and the ISW effect which depends on $\dot{\Phi}$ vanishes. Whereas during the DE dominated era, the background expansion rate of the Universe increases resulting into the decaying gravitational potential perturbations. In this case, a CMB γ passing through an overdense region gain more energy falling into the potential well w.r.t the energy lost while climbing out of it. Therefore due to non-vanishing $\dot{\Phi}$, overdense regions correspond to hotter spots in the CMB sky-maps and the colder spots correspond to the underdense regions.

The temperature anisotropies created by the total (linear and non-linear) ISW and RS effect in a direction $\hat{\mathbf{n}}$ on the sky can be computed as the integral of the time derivative of the peculiar gravitational potential $\dot{\Phi}$ along the line-of-sight from the last scattering (LS) surface to the present epoch t_0 [88, 70]:

$$\Delta T(\hat{\mathbf{n}}) = \frac{2}{c^2}\bar{T}_0 \int_{t_{LS}}^{t_0} \dot{\Phi}(t, \hat{\mathbf{n}}) dt \tag{4.12}$$

where, t is the cosmic time, t_{LS} is the age of the Universe at the LS surface, $\bar{T}_0 = 2.7$K is the present CMB temperature, and c is the speed of light. Re-writing Eq.(4.12) as the integral over the radial comoving distance r,

$$\Delta T(\hat{\mathbf{n}}) = \frac{2}{c^2}\bar{T}_0 \int_{0}^{r_{LS}} \dot{\Phi}(r\hat{\mathbf{n}}) a dr \tag{4.13}$$

where, r_{LS} is the radial comoving distance to the LS surface, and a is the scale factor of the Universe.

Weak lensing of the CMB In addition to ISW-RS effect, intervening matter inhomogeneities induce *gravitational lensing of CMB*. The net effect of these deviations is reshuffling of power in the modes of the primordial power spectrum of the total

intensity and gradient-like (E-modes) components of the CMB polarization. Lensing results into distortion of the primordial polarization pattern converting E-modes into B-modes [102] and generates a power on the sub-degree scale where primordial signal is expected to be negligible [59].

Measuring these anisotropies is enormously difficult task, but thanks to successful temperature experiments such as the Atacama Cosmology Telescope (ACT)[1], the South Pole Telescope (SPT)[2] and Planck[3] we can now have robust measurements at the arc-minute scale and with polarization experiments such as QUIET[4], BICEP2 and Planck[5] we can obtain low-noise maps of the CMB polarization.

Weak lensing of CMB arises due to the deflection of CMB photons coming from the last scattering surface by potential gradients along our line of sight [103, 104, 105, 106, 107]. The weak lensing affects the CMB temperature power spectrum as well as introduces quantitatively new non-Gaussian and polarization signals [59]. Since lensed CMB signal has the same frequency as the unlensed CMB, it cannot be easily distinguished. For CMB lensing on scales ≥ 1 arcmin, only weak lensing is expected to be important in which case the perturbations of the rays are small. In this case, the integral for the projected CMB lensing potential due to scalar perturbations in the absence of anisotropic stress becomes [70]:

$$\phi(\hat{\mathbf{n}}) \equiv -2 \int_0^{r_{LS}} \frac{r_{LS} - r}{r_{LS} r} \frac{\Phi(r\hat{\mathbf{n}}; c\eta_0 - r)}{c^2} dr \tag{4.14}$$

where, η_0 is the present conformal time, Φ is the physical peculiar gravitational potential generated by density perturbations. The corresponding deflection angle becomes:

$$\alpha(\hat{\mathbf{n}}) \equiv -2 \int_0^{r_{LS}} \frac{r_{LS} - r}{r_{LS} r} \nabla_{\hat{\mathbf{n}}} \frac{\Phi(r\hat{\mathbf{n}}; c\eta_0 - r)}{c^2} dr \tag{4.15}$$

where, $[1/r]\nabla_{\hat{\mathbf{n}}}$ is the 2D transverse derivative w.r.t the line-of-sight pointing in the direction $\hat{\mathbf{n}} \equiv (\nu, \theta)$.

The CMB lensed field can be described as $T_{obs}(\hat{n}) = T_{int}(\hat{n} + \alpha)$ where T_{int} is unlensed temperature field, $\hat{n}$ is the direction and $\vec{d}$ is the deflection field. The deflection field is the measure of the effect of the spacetime between us and the decoupling surface and hence probes different physical processes than done by primary anisotropies [108]. Weak lensing of CMB deflects γs from an original direction $\hat{\mathbf{n}'}$ on the last scattering surface to a direction $\hat{\mathbf{n}}$ on the observed sky. Hence the lensed CMB field is given by, $\tilde{X}\hat{\mathbf{n}} = X\hat{\mathbf{n}'}$ in terms of the unlensed field $X = T, Q, U$ [59]. The vector $\hat{\mathbf{n}'}$ is obtained from $\hat{\mathbf{n}}$ by moving its end on the surface of a unit sphere by a distance $|\nabla_{\hat{\mathbf{n}}}\Psi(\hat{\mathbf{n}})|$ along a geodesic in the direction of $|\nabla_{\hat{\mathbf{n}}}\Psi(\hat{\mathbf{n}})|$ [61, 109, 63] i.e. $(\hat{\mathbf{n}'} = \hat{\mathbf{n}} + \nabla_{\hat{\mathbf{n}}}\Psi(\hat{\mathbf{n}}))$. It is often assumed that $|\nabla_{\hat{\mathbf{n}}}\Psi|$ is constant between $\hat{\mathbf{n}}$ and $\hat{\mathbf{n}'}$ which is consistent with lensing potential in the Born approximation. Since CMB deflections are of the scale of arcminutes making it appropriate to use this approximation.

[1] http://www.physics.princeton.edu/act/
[2] http://pole.uchicago.edu/
[3] http://www.rssd.esa.int/index.php?project=planck
[4] http://quiet.uchicago.edu/
[5] http://www.rssd.esa.int/index.php?project=planck

Due to gravitational lensing of CMB, the relative temperature fluctuation observed in the direction $\hat{\mathbf{n}}$ becomes $\tilde{T}(\hat{\mathbf{n}})$ where unlensed temperature in the deflection direction is given by,

$$\tilde{T}(\hat{\mathbf{n}}) = T(\hat{n}') = T(\hat{n} + \alpha) \tag{4.16}$$

where, α is the deflection angle which at lowest order becomes a pure gradient $\alpha = \nabla\psi$ [59].

Figure 4.4 (image is taken from ESA[6]) shows how CMB photons deflected from the last scattering surface were gravitationally lensed due to large scale structure present in their geodesic which acted as gravitational 'lens'.

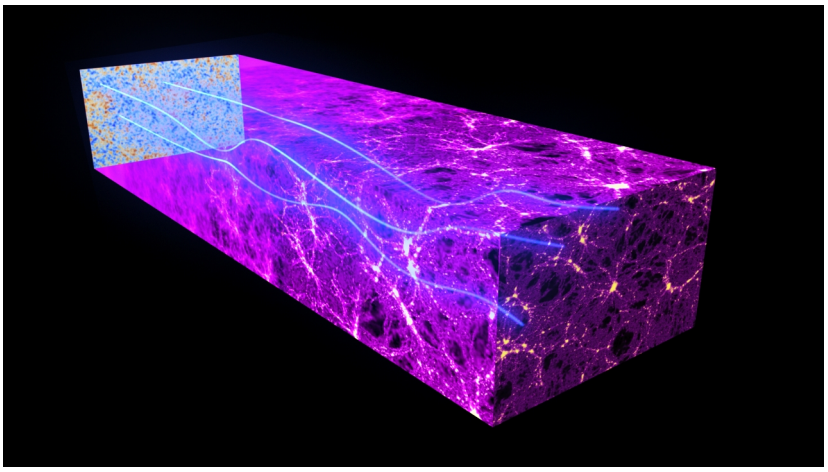

Figure 4.4: The artist's impression shows how photons in the CMB are deflected by the gravitational lensing effect of massive cosmic structure as they travel across the Universe. Gravitational lensing effect creates tiny, additional distortions to mottled pattern of the CMB temperature fluctuations. A small fraction of the CMB is polarized, one such component, the so-called B-modes have been given an additional signature by gravitational lensing. This imprint has been found for the first time by combining data from the ground based South Pole Telescope and ESA's Herschel space observatory. Original image is taken from ESA.

If the gravitational potential Φ is Gaussian, the lensing potential is also Gaussian. However the lensed CMB is non-Gaussian as it is a second order cosmological perturbation effect onto CMB anisotropies, yielding a finite correlation between different scales and hence non-Gaussianity. The lensed CMB is non-Gaussian even if the underlying lenses are following Gaussian distribution. The non-linear evolution of the large scale structure produces a degree of non-Gaussianity in the distribution of lenses which contributes to the non-Gaussian statistics of the lensed CMB on small scales [110].

CMB weak-lensing smoothes out features in the temperature power spectrum where lensing effects become visible at $l \geq 500$ corresponding to an angular scale of $\theta \leq (\pi/500)\text{rad} \simeq 20'$ corresponding to the scale where coherent gravitational light deflection sets in. As shown in figure 4.5, at the high multipole tail of the temperature power spectrum, the lensed power spectrum falls systematically above the unlensed one by power transfer from large to small scales [58, 111, 112, 112, 113, 114, 106, 115]

[6]https://www.esa.int/esearch?q=weak+lensing&start=11

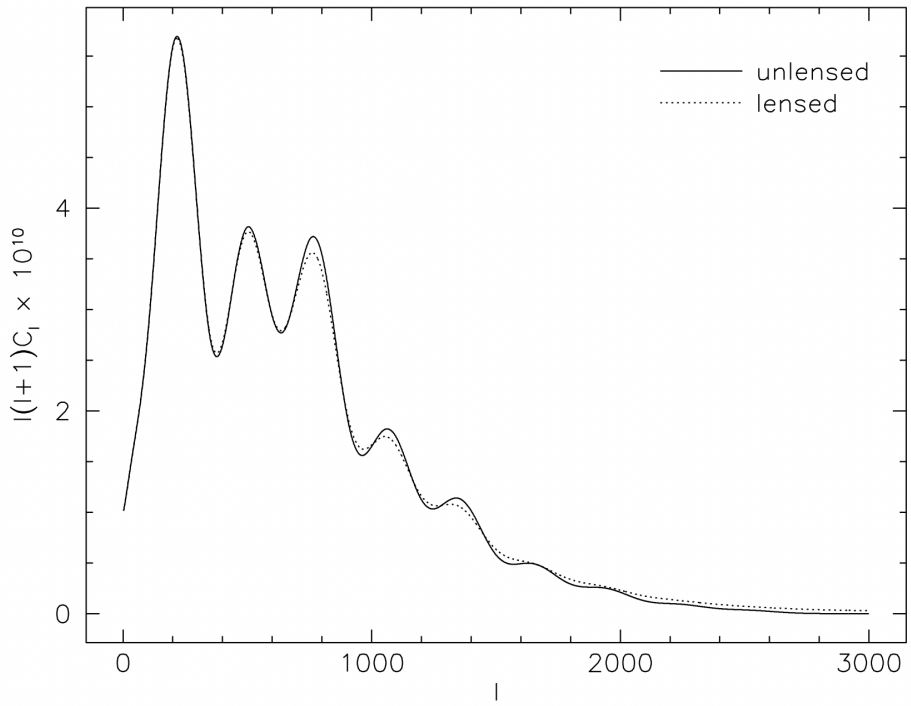

Figure 4.5: The unlensed and lensed CMB power spectra CDM in an Einstein-de Sitter Universe. The CMB power spectrum coefficients $l(l+1)C_l$ are shown as a function of l. The solid line displays the intrinsic power spectrum and the dotted line shows the lensed power spectrum for an Einstein-de Sitter Universe filled with CDM. Lensing smoothes the power spectrum at large l while it has no visible effects on larger scales. The curves are produced by CMBfast code and plot is taken from [58].

4.2 Observational constraints on the cosmological parameters

Thanks to weak lensing of CMB, we can infer cosmological parameters with more precision, e.g. Planck 2018 [45] gives constraints on values of Ω_m, σ_8 and H_0 as shown in Fig.4.6:

In order to describe the global nature of the Universe, our current model of cosmology uses six fundamental parameters known as the *cosmological parameters* which extensively constrains different cosmological models by mentioning geometry/global dynamics (i.e. the expansion rate and curvature) and building blocks of the Universe with their precise proportion. Thanks to the recent advances in precision cosmology, many of the key cosmology parameters can be obtained to one or two significant figure accuracy. Prominent sources of such derivations are the measurements of CMB anisotropies combining information from the temperature and polarisation maps and the lensing reconstruction with the highest precision observations made from the Planck satellite [2]. These parameters allow us to untangle the mystery of the evolution of the Universe, at least back until an epoch when interactions allowed interchanges between different spices, describing global dynamics of the Universe such as its expansion rate and curvature, etc. Since we know neutrinos are not massless, even the smallest mass

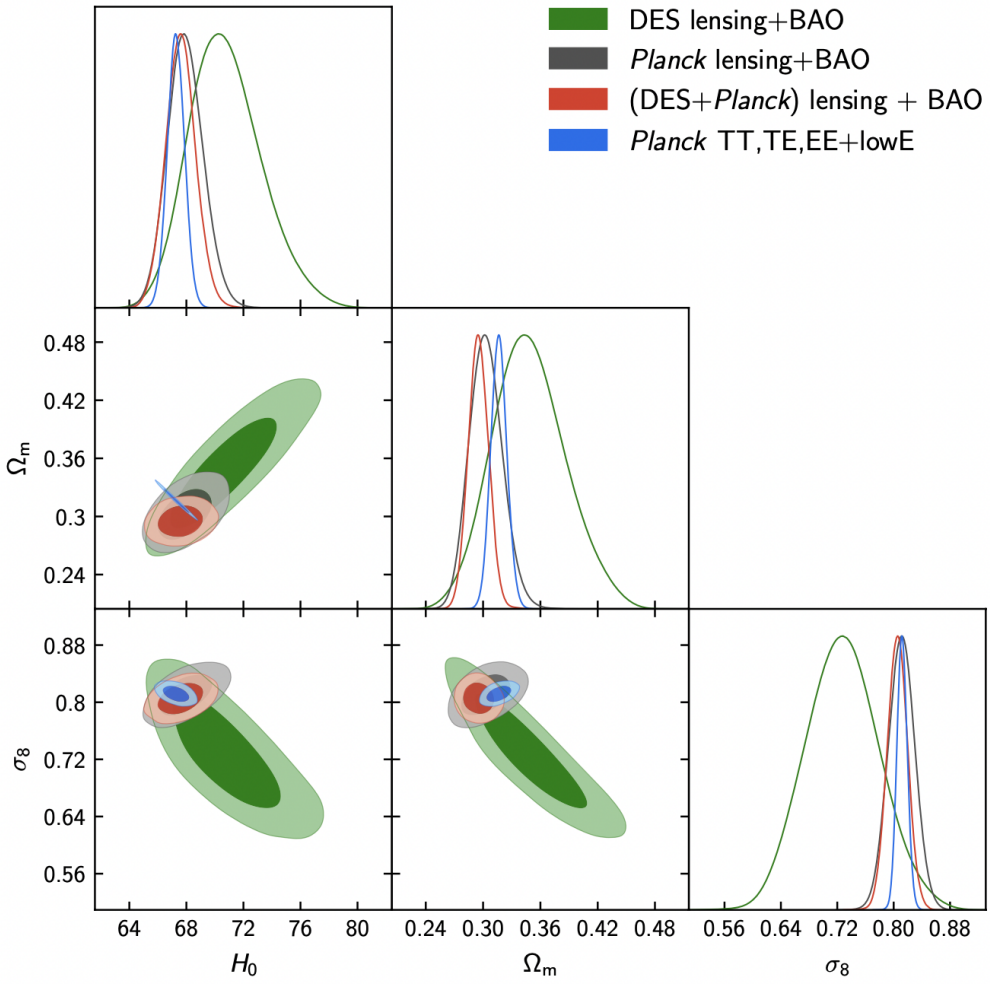

Figure 4.6: ΛCDM model constraints on Ω_m, σ_8 and H_0 from DES galaxy lensing+BAO (green), Planck CMB lensing+BAO (grey) and the joint constraint of DES lensing, CMB lensing and BAO (red). The Planck power spectrum constraints are shown in blue, contours contain 68% and 95% of the probability. Original plot taken from [45].

has a potentially observable effect on the formation of structures as neutrino free-streaming damps the growth of perturbation. Analyses commonly either assume a neutrino mass sum fixed at the lower level, or allow the neutrino mass sum to be a variable parameter. The inclusion of the neutrino mass sum as a free parameter can affect the derived values of other cosmological parameters [40].

The joint constraints with BAO measurements on spatial curvature are consistent with a flat Universe, and combining with Type Ia SNe, the dark energy equation of state parameter is measured to be $w_0 = -1.03 \pm 0.03$ consistent with a cosmological constant. No evidences of deviation from a purely power-law primordial power spectrum, primordial non-Gaussianity- neither isocurvature perturbations nor cosmic defects have been found. Combining with data from BAO, BICEP2 and Keck Array data a limit on tensor-to-scalar ratio is $r_{0.002} < 0.06$. The acoustic oscillations in l seen in the CMB power spectra correspond to a sharply-defined acoustic angular scale on the sky, given by $\theta_* \approx r_*/D_M$ where r_* is the comoving sound horizon at recombination quantifying

the distance the photon-baryon perturbations can influence and D_M is the comoving angular diameter distance that maps r_* into an angle on the sky. The CMB angular acoustic scale measured robustly at 0.03% precision to be $\theta_* = (0°.5965 \pm 0°.0002)$ is one of the most accurately measured parameter in cosmology. The primordial fluctuations are consistent with Gaussian purely adiabatic scalar perturbations characterised by a power spectrum with a spectral index n_s shown in table 4.1 consistent with the predictions of single-field, slow-roll inflation. Figure 4.7 shows the Planck constraints in the $n_s - r$ plane where r is added as a single additional parameter to the base model and plotted at pivot scale 0.002 Mpc^{-1}.

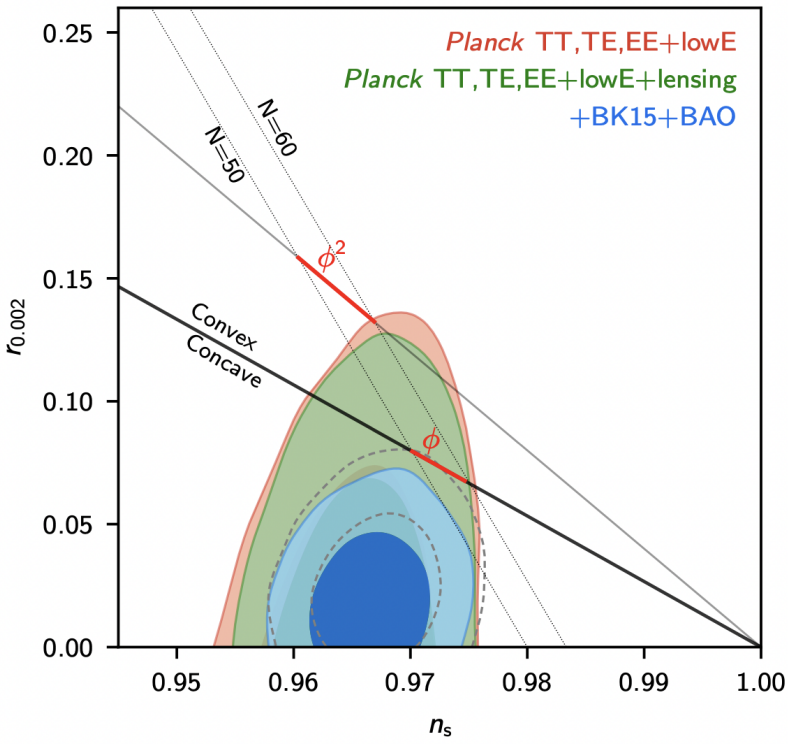

Figure 4.7: Constraints on the tensor-to-scalar ratio $r_{0.002}$ in the ΛCDM model using Planck TT,TE,EE+lowE (red) and Planck TT,TE, EE+lowE+lensing (green) and joint constraints from BAO and BICEP2/Keck (blue) assuming the inflationary consistency relation and negligible running. Dashed grey contours show the level of modelling uncertainty in the polarization results. Dotted lines show the loci of approximately constant e-folding number N assuming simple $V \propto (\phi/m_{Pl})^p$ single field inflation. Solid lines show the $n_s - r$ relation for locally quadratic and linear potentials to first order in slow-roll. Red lines show the approximate allowed range $50 < N < 60$ and black solid line separate the concave and convex potentials. Original plot is taken from [2].

Ω_γ is accurately measured thanks to COBE satellite FIRAS experiment determining $T_{CMB} = 2.7255 \pm 0.0006$K corresponding to $\Omega_\gamma = 2.47 \times 10^{-5} h^{-2}$. This constraints the cosmological parameters varied and leave concordance model defined by six cosmological parameters.

Derived parameters include the age of the Universe, the present horizon distance, the present neutrino background temperature, the epoch of matter-radiation equality, the epochs of recombination and decoupling, the epoch of transition to accelerating

Universe, the baryon-to-photon ratio and the baryon-to-dark matter density ratio. The age of the Universe from CMB data gives $13.797 \pm 0.023 Gyr$ as the position of the first peak is strongly correlated with the age [40].

Finally, we present the cosmological parameters reported from the Planck measurement of seven acoustic peaks in the CMB temperature power spectrum [2] which combines information from the temperature and polarization maps and lensing reconstruction. These results show good consistency with the standard spatially flat ($k = 0$), 6 parameter ΛCDM model having Gaussian, adiabatic and nearly scale-invariant initial perturbations with a power-law spectrum of adiabatic scalar perturbations as framed in simple inflationary models. This is consistent with observations such as WMAP and Planck collaboration et al. [9],[2]. The constraints on the cosmological parameters include the Hubble constant H_0, the physical baryon density ($\omega_b = \Omega_b h^2$) $\Omega_{b,0}$, the dark matter density ($\omega_c = \Omega_c h^2$) $\Omega_{m,0}$, the curvature parameter $\Omega_{k,0}$, the radiation density parameter $\Omega_{r,0}$, fluctuation amplitude at the present day σ_8, scalar spectral index n_s which defines the slope of the primordial scalar power spectrum, the optical depth $\tau = 0.054 \pm 0.007$ defining the scale-independent suppression of power in the CMB anisotropies by free electrons generated during reionization, and the matter fluctuation amplitude A_s. Since the CMB fluctuations are linear up to lensing corrections and the lensing corrections are largely oscillatory, the average observed CMB power spectrum amplitude scales nearly proportionally with the primordial comoving curvature power spectrum amplitude A_s which is defined at the scale $k_0 = 0.05\text{Mpc}^{-1}$. The sub-horizon CMB anisotropies are scattered by free-electrons present after reionization hence, the observed amplitude actually scales with $A_s e^{-2\tau}$ where τ is the reionization optical depth. All these parameters reported by planck 2018 results are as follows:

$$
\begin{gathered}
H_0 = (67.4 \pm 0.5)\text{kms}^{-1}\text{Mpc}^{-1} \\
\Omega_{m,0} = 0.315 \pm 0.007 \\
\Omega_{b,0}h^2 = 0.0224 \pm 0.0001 \\
\Omega_{\Lambda,0} = 0.6889 \pm 0.0056 \\
\Omega_{k,0} = 0.001 \pm 0.002 \\
n_s = 0.965 \pm 0.004 \\
A_s e^{-2\tau} = (1.884 \pm 0.012) \times 10^{-9} \\
\sigma_8 = 0.811 \pm 0.006
\end{gathered}
$$

Table 4.1: Parameters of ΛCDM model that best fits the data from the Planck measurements of the CMB [2].

where, the matter densities can be measured from the CMB spectra using the scale-dependence of the amplitude, since for fixed θ_* a larger matter density reduces the small-scale CMB power. The matter density also affects the amount of lensing in the CMB spectra and the amplitude of the CMB lensing reconstruction spectrum. Fig.4.8 shows the constraints in the $\Omega_m - \sigma_8$ plane from DES lensing compared to the constraints from the CMB power spectra and CMB lensing and Fig.4.9 shows parameter constraints using galaxy auto- and cross-correlations respectively:

If the dark energy is a generic dynamic fluid, its equation of state parameter $w \approx p/\rho$ would be a function of time, where p and ρ are the spatially averaged background dark energy pressure and density. A time varying equation of state is of the form:

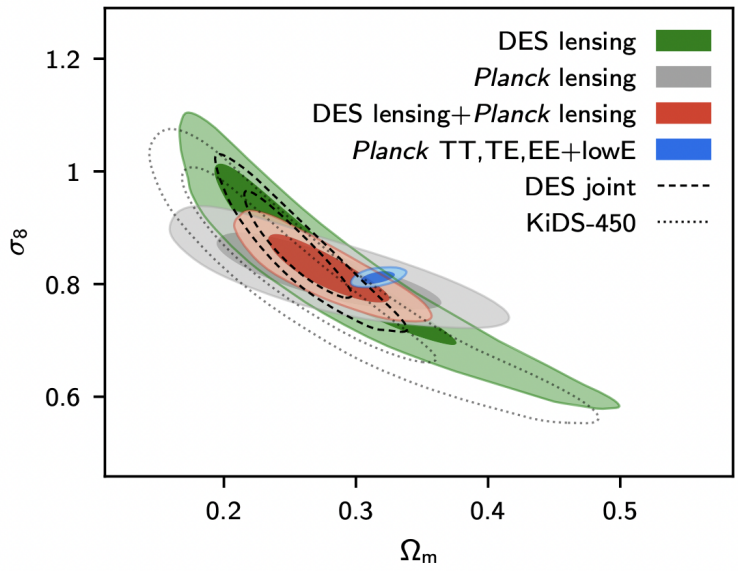

Figure 4.8: Base-ΛCDM model 68% and 95% constraint contours on the matter density parameter Ω_m and the fluctuation amplitude σ_8 from the Dark Energy Survey (DES) lensing, Planck CMB lensing (grey) and the joint lensing constraint (red). The dashed lines show the constraint from the DES cosmic shear plus galaxy clustering joint analysis, the dotted line show the constraint from original KiDS-450 analysis, and the blue filled contour show the independent constraint from Planck CMB power spectra. Original plot is taken from [2].

$$w(a) = w_0 + (1 - a)w_a \tag{4.17}$$

where w_0 and w_a are constants which in ΛCDM framework are $w_0 = -1$ and $w_a = 0$. Marginalized contours of the posterior distribution of w_0 and w_a are shown in figure 4.10. Here CMB lensing has only small effect on the constraints from Planck alone.

The Planck base ΛCDM assumes a normal mass hierarchy with the minimal mass $\sum m_\nu = 0.06$eV allowed by neutrino flavour experiments. In the normal hierarchy, the lowest two mass eigenstates have the smallest mass splitting and can give $\sum m_\nu \geq 0.06$eV whereas in inverted hierarchy, the most massive eigenstates have the smallest mass separation requiring $\sum m_\nu \geq 0.1$eV, hence a constraint $\sum m_\nu < 0.1$eV would be rule out by inverted hierarchy.

These results constrain the extra effective degrees of freedom to be $N_{eff} = 2.99 \pm 0.17$ in agreement with the Standard Model prediction $N_{eff} = 3.046$ and find that the neutrino mass is tightly constrained to $\Sigma m_\nu < 0.12$eV. Increasing the neutrino mass leads to lower values of H_0 and hence aggravates the tension in H_0 with distance-ladder determination of [116] as shown in Fig.4.11 :

Additional dark relativistic degrees of freedom arising due to new light particles in the Standard Model of Particle Physics are usually characterized by N_{eff}. The total relativistic energy density after electron-positron annihilation is given by,

$$\rho_{rad} = N_{eff}\frac{7}{8}\left[\frac{4}{11}\right]^{4/3}\rho_\gamma \tag{4.18}$$

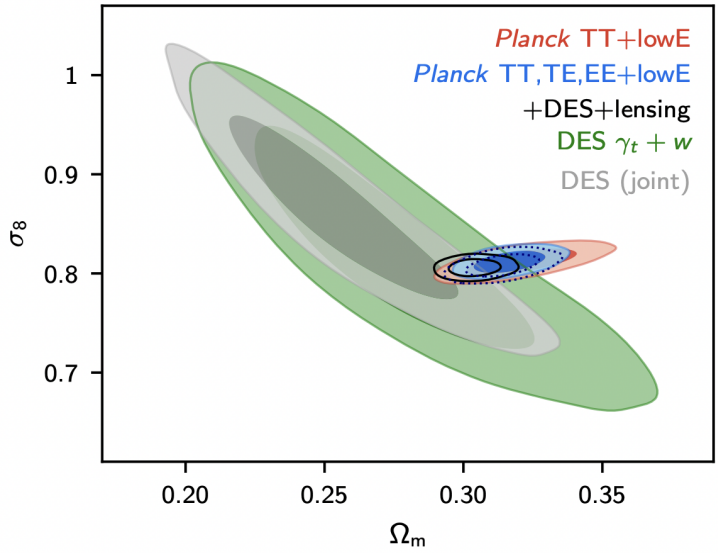

Figure 4.9: Base-ΛCDM model 68% and 95% constraint contours on the matter density parameter Ω_m and the fluctuation amplitude σ_8 from the Dark Energy Survey (DES) using the shear galaxy correlation and the galaxy auto-correlation data (green) and the joint result DES lensing (grey) compared with Planck results showing TT+lowE and TT, TE, EE+lowE+lensing+DES by assuming the difference between the data set is purely statistical. The dotted line shows the Planck TT, TE, EE+lowE result using CamSpec likelihood, contours show 68% and 95% probability. Original plot is taken from [2].

Any additional massless particles produced well after recombination can be treated as additional contribution to N_{eff}. Any species that were initially in thermal equilibrium with the Standard Model particles produce a $\Delta N_{eff} \equiv N_{eff} - 3.046$ which depends only on number of degrees of freedom and decoupling temperature. Using conservation of entropy, fully thermalized relics with degrees of freedom (g) contribute,

$$\Delta N_{eff} = g\left[\frac{43}{4g_s}\right]^{4/3} \times [4/7(\text{boson})\text{or}1/2(\text{fermion})] \tag{4.19}$$

where g_s is the effective degrees of freedom for the entropy of the other thermalized relativistic species that were present when they decouple. Thus varying N_{eff} allows the tension with [116] to be somewhat eased as shown in Fig.4.12.

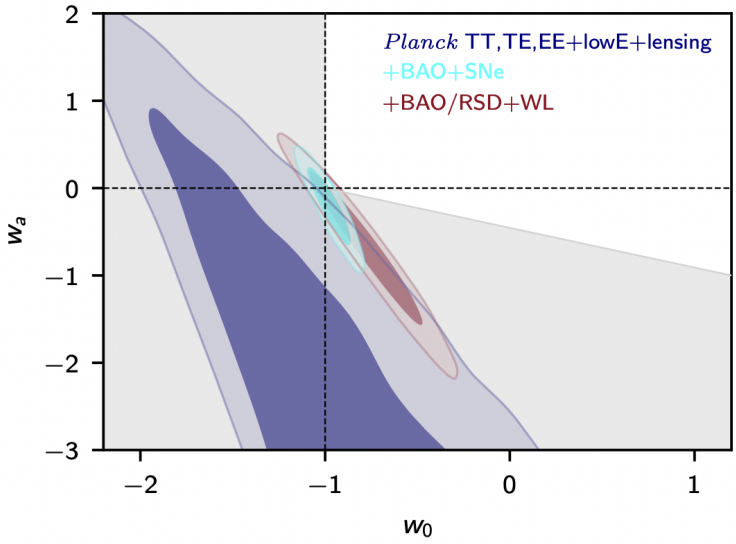

Figure 4.10: Marginalized posterior distribution of the (w_0, w_a) parameters for various data combinations. The tightest constraints come from the combination Planck TT,TE,EE+lowE+lensing+SNe+BAO and are compatible with the ΛCDM. The dashed lines indicate the point corresponding to the ΛCDM model. Original plot is taken from [2].

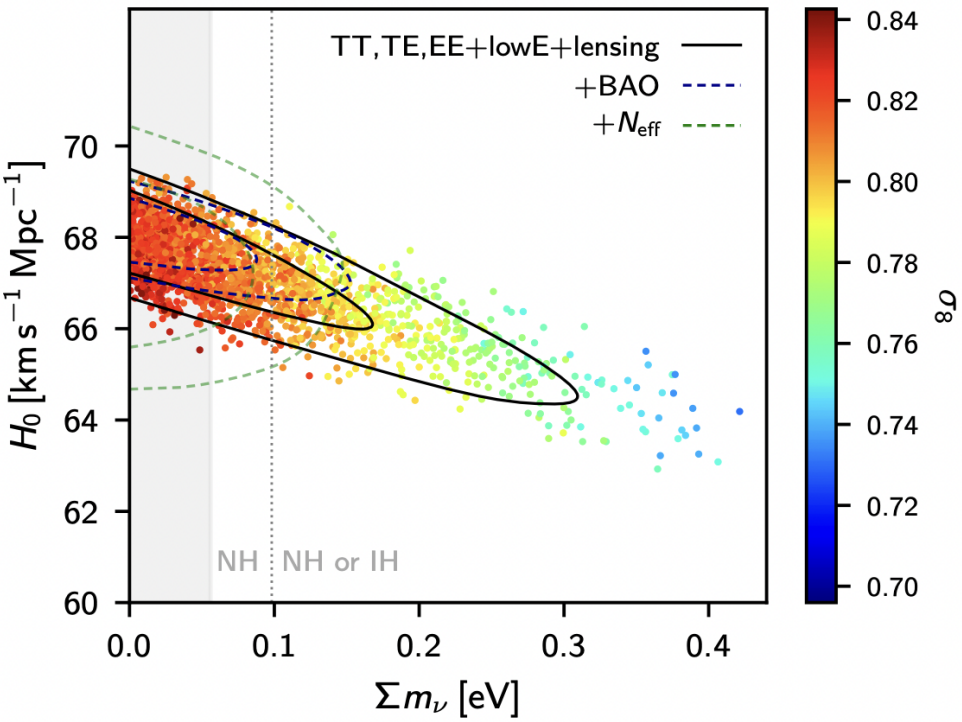

Figure 4.11: Samples from Planck TT,TE,EE+lowE+lensing chains in the $\sum m_\nu - H_0$ plane, colour coded by σ_8. Solid black contours show the constraint from Planck TT,TE,EE+lowE+lensing while dashed blue line shows the joint constraint from Planck TT,TE,EE+lowE+lensing+BAO, and the dashed green line are additionally marginalized over N_{eff}. The grey band on the left shows the region with $\Sigma m_\nu < 0.056$eV ruled out by neutrino oscillation experiments. Region on the left of dotted vertical line indicate a normal hierarchy (NH) while on the right could either be normal or inverted hierarchy (IH). Original plot is taken from [2].

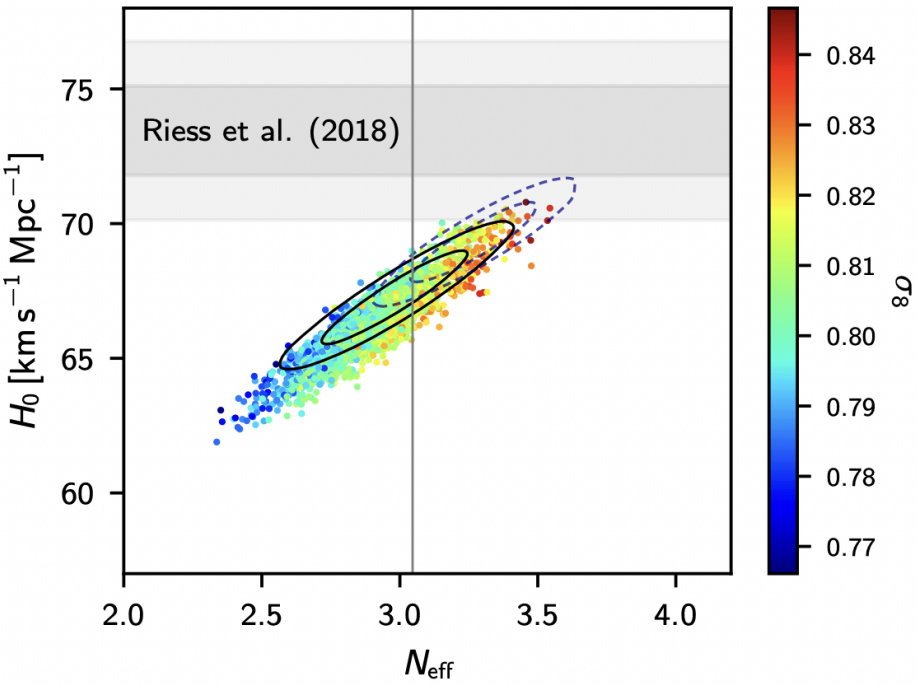

Figure 4.12: Samples from Planck TT,TE,EE, +lowE chains in the $N_{eff} - H_0$ plane, colour-coded by σ_8. The grey bands show the local Hubble parameter measurement $H_0(73.45 \pm 1.66) kms^{-1}Mpc^{-1}$ from [116]. Solid black contours show the constraints from Planck TT,TE,EE+lowE+lensing+BAO, while dashed line include joint constraints. On the left of the solid vertical line shows models with $N_{eff} < 3.046$. Original plot is taken from [2].

Chapter 5

Gravitational Waves

> In all things of nature, there is something of the marvelous.
>
> *Aristotle*

General relativity is based upon the assumption of a dynamical curved spacetime where the presence of mass-energy curves the spacetime locally but its effect can be experienced even by a distant object. However, this effect at larger distance cannot be instantaneous as special relativity imposes causality in form of speed limit c for the propagation of waves. This suggests the possibility of curvature oscillations that travel through space, the natural outcome of General Relativity is hence Gravitational Waves (GWs). GWs are the solution of Einstein's Field Equations propagating at the speed of light in the fabric of the spacetime emitted by accelerated massive objects. GWs are also defined as the tensor fluctuations of the metric tensor and their evolution is regulated by the traceless spatial part of the Einstein field equations. When two massive objects rotate around each other, their orbital distance decreases and their speed increases. This results into the increase of frequency of the rotating system until the moment of their coalescence. What differentiates GWs from electromagnetic radiation is the weak interaction of GWs with matter; hence when detected, provide us the almost unaltered snapshot of the surrounding of extreme masses just before their collision. In this work, we focus on the *geometric optics approximation* where *the propagation of GWs can be treated as that of a massless particles moving on a null geodesic in the spacetime*. It is important to note that in the vicinity of strong field regime, geometric approximation breaks down and we need to consider wave effects of gravitons. However, [117] shows general framework for polarization through diffusion by massive structures applicable to AGWB/CGWB in any frequency band and GW propagation beyond geometric optics limit is shown in [118]. Direct detection of GWs from the LIGO-Virgo interferometers have offered us profound physical understanding of the Universe and also have shed light on the population of compact objects in the Universe and their formation mechanism [119], tests of General Relativity [120, 121] and enabled first measurement of the Hubble constant using GW sources [122].

5.1 Linearized equations in flat spacetime

The line element in arbitrary spacetime can be written as,

$$ds^2 = g_{\mu\nu} dx^\mu dx^\nu \tag{5.1}$$

Here, $g_{\mu\nu}$ is a covariant (0,2) tensor taking dx^μ and dx^ν as input line intervals to maintain the invariant scalar property ds^2. The symmetric metric tensor $g_{\mu\nu}$ can have non-vanishing off-diagonal elements as well as non-unity elements which describe the curvature of spacetime under consideration. In a flat, Minkowski spacetime, the metric can be written as,

$$g_{\mu\nu} = \eta_{\mu\nu} = \begin{bmatrix} -1 & 0 & 0 & 0 \\ 0 & 1 & 0 & 0 \\ 0 & 0 & 1 & 0 \\ 0 & 0 & 0 & 1 \end{bmatrix} \tag{5.2}$$

where, $\eta_{\mu\nu}$ is the *Minkowski metric.*

Linearized gravity is an appropriate approximation to general relativity where the spacetime metric $g_{\mu\nu}$ can be treated as deviating only slightly from the flat metric:

$$g_{\mu\nu} = \eta_{\mu\nu} + h_{\mu\nu}, \quad |h_{\mu\nu}| \ll 1 \tag{5.3}$$

where $h_{\mu\nu}$ is the small metric perturbation in the metric tensor $g_{\mu\nu}$. The condition $|h_{\mu\nu}| \ll 1$ require both- the gravitational field to be weak and constraints the coordinate system to be approximately Cartesian [123]. The metric perturbation $h_{\mu\nu}$ transforms as a tensor under Lorentz transformation but not under general coordinate transformations.

The Gravitation action is given by, $S = S_E + S_M$, where the Einstein action is given by [124, 125],

$$S_E = \frac{c^3}{16\pi G} \int d^4x \sqrt{-g} R \tag{5.4}$$

where, S_M is the matter action, R is the Ricci scalar, $g_{\mu\nu}$ is the 4D metric and $g = \det(g_{\mu\nu})$. In order to generate gravitational waves EFEs must be perturbed, we begin from Einstein's Field Equations assuming units $G = \hbar = c = 1$:

$$R_{\mu\nu} - \frac{1}{2}\mathcal{R} g_{\mu\nu} = 8\pi T_{\mu\nu} \tag{5.5}$$

Eq.(5.5) contains 16 differential equations which upon symmetric nature of $G_{\mu\nu}$ and $T_{\mu\nu}$ reduces to 10 and further reduces to six using Bianchi identity. Here, $R_{\mu\nu}$ is the Ricci Curvature tensor, $\mathcal{R}$ is the Ricci scalar, $g_{\mu\nu}$ is the metric tensor and $T_{\mu\nu}$ is the stress-energy tensor of the mass-energy components of the source. Upon substituting the perturbed metric $g_{\mu\nu}$ from Eq.(5.3) into Einstein's equation Eq.(5.5) the wave equation in vacuum becomes,

$$\Box \bar{h}_{\mu\nu} = 0 \tag{5.6}$$

which using *trace-reversed* perturbations ($\bar{h}_{\mu\nu} = h_{\mu\nu} - 1/2\eta_{\mu\nu}h$, where $h \sim \eta_{\mu\nu}h^{\mu\nu}$ and $\Box = \eta^{\mu\nu}\partial_\mu\partial_\nu$) gives the *linearized Einstein equation*,

$$\boxed{\Box \bar{h}_{\mu\nu} = -16\pi T G_{\mu\nu}} \tag{5.7}$$

This is the wave equation for gravitational wave similar to that for photons in electromagnetism, the solution of Eq.4.7 is given by,

$$\bar{h}_{\mu\nu} = 4 \int \frac{T_{\mu\nu}(t - |\vec{x} - \vec{x'}|, \vec{x'})}{|\vec{x} - \vec{x'}|} dx'^3 \tag{5.8}$$

This solution using TT gauge reduces to,

$$h_{ij}^{TT} = 4 \Big[\int \frac{T_{\mu\nu}(t - |\vec{x} - \vec{x'}|, \vec{x'})}{|\vec{x} - \vec{x'}|} dx'^3 \Big]^{TT} \tag{5.9}$$

i.e. we can calculate the measurable gravitational wave created by a source from the ij components of the stress-energy tensor alone. This solution is used to find the gravitational waveform from a compact binary coalescing system. Whereas, the solution for vacuum case, Eq.(5.6) becomes,

$$\boxed{\bar{h}_{\mu\nu} = \mathcal{R} A_{\mu\nu} e^{ik_\mu x^\mu}} \tag{5.10}$$

Here, each $\mu\nu$ component of this $\bar{h}$ is a sinusoidal wave traveling along the vector k^μ with amplitude $A_{\mu\nu}$.

We can summarize properties of transverse-traceless (TT) gauge as:

$$h_{0\mu}^{TT} = h^{TT} = h_{ij}^{TT,j} = 0 \tag{5.11}$$

This condition gives us two residual degrees of freedom in metric $h_{\mu\nu}$ which are commonly decomposed in two linearly independent polarizations for GWs, known as the + *plus* and the × *cross* polarization modes. Each polarization mode has amplitude h_+ and $h_\times$ respectively. So, GW spacetime perturbations $h_{\mu\nu}$ can be decomposed in plus and cross polarization modes. Fig.5.1 shows the pictorial representation of GWs propagating in the $+z$ direction:

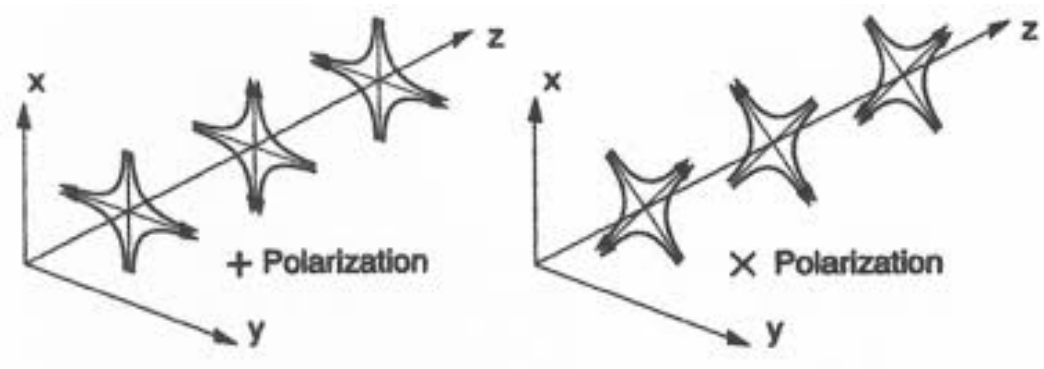

Figure 5.1: Stretching and squeezing of space transverse to the detection of a GW. The wave is travelling in the +z direction and stretching and squeezing occurs in the x and y dimensions, image is taken from [126].

For GWs propagating in the $+z$ direction, a perturbation metric in the TT gauge can be written as,

$$h_{\mu\nu}^{TT} = h_{\mu\nu}^{TT}(t - z) \tag{5.12}$$

is a valid solution for the wave equation $\Box\bar{h}_{\mu\nu} = 0$. The Lorentz gauge condition $(\partial_z)h^{TT}_{\mu\nu} = 0$ implies that $h^{TT}_{z\nu}(t-z)$ is a constant which must be zero since $h^{TT}_{\mu\nu} \to 0$ as the distance of the source of GWs become infinite. Then the only non-zero components of $h^{TT}_{\mu\nu}$ are $h^{TT}_{xx}, h^{TT}_{xy}, h^{TT}_{yz}$ and h^{TT}_{yy}. Following traceless condition and symmetry we obtain,

$$\begin{aligned} h^{TT}_{xx} &= -h^{TT}_{yy} \equiv h_+(t-z), \\ h^{TT}_{xy} &= h^{TT}_{yz} \equiv h_\times(t-z) \end{aligned} \tag{5.13}$$

where, $h_+(t-z)$ and $h_\times(t-z)$ are two independent waveforms which can be represented in TT gauge as:

$$h^{TT}_{\mu\nu} = \begin{bmatrix} 0 & 0 & 0 & 0 \\ 0 & h_+ & h_\times & 0 \\ 0 & h_\times & -h_+ & 0 \\ 0 & 0 & 0 & 0 \end{bmatrix} \tag{5.14}$$

Using Lorentz (Hilbert) gauge $\bar{h}^{\mu\nu}{}_{,\mu} = 0$, Eq.(5.10) gives plane wave solution analogous to the electromagnetic case [123],

$$\bar{h}_{\mu\nu}(\mathbf{x}, t) = Re \int d^3k A_{\mu\nu}(\mathbf{k}) e^{i(\mathbf{k}\cdot\mathbf{x})-\omega t} \tag{5.15}$$

where, $\omega = |\mathbf{k}|$, k is the four-vector satisfying $k^2 = 0$, $A_{\mu\nu}$ is the *constant polarization tensor* depending on wavevector $\mathbf{k}$ but is independent of $\mathbf{x}$ and t. This polarization tensor, under application of Lorentz condition mentioned as below:

$$0 = \partial^\mu \bar{h}_{\mu\nu} = \eta^{\mu\rho}\mathcal{R}][ik_\rho A_{\mu\nu} e^{i(\mathbf{k}\cdot\mathbf{x})}] \tag{5.16}$$

reduces to 4 equations that constraint the tensor $A_{\mu\nu}$ and further reduce the number of its independent components to 6. In linearized theory, using gauge freedom, infinitesimal coordinate changes,

$$x^\mu \Rightarrow \tilde{x}^\mu = x^\mu + \zeta^\mu, |\zeta^\mu| \ll 1 \tag{5.17}$$

If we specialize to global vacuum spacetime where $T_{\mu\nu} = 0$ everywhere and is asymptotically flat, the gauge needed to make metric perturbation purely spatial is,

$$h_{tt} = h_{ti} = 0 \tag{5.18}$$

and traceless,

$$h = h^i_i = 0 \tag{5.19}$$

Then, applying Lorentz gauge condition, the spatial metric perturbation is transverse:

$$\partial_i h_{ij} = 0 \tag{5.20}$$

This is known as *transverse-traceless gauge* or *TT gauge*. The TT gauge leaves only two independent polarizations out of the original ten ensuring that, $\bar{h}_{\mu\nu} = h_{\mu\nu}$

For a plane gravitational wave Eq.(5.12) propagating in the $\hat{z}$ direction ($k^\mu = (\omega, 0, 0, \omega)$), along with the TT gauge and Lorentz gauge condition (Eq.(5.14), Eq.(5.15)), the wave equation would be,

$$h_{ij}^{TT} = \begin{pmatrix} h_+ & h_\times & 0 \\ h_\times & -h_+ & 0 \\ 0 & 0 & 0 \end{pmatrix} cos[\omega(z-t)], \quad h_{\mu 0}^{TT} = 0 \tag{5.21}$$

Here, h_+ and $h_\times$ called the two polarization states of the gravitational waves. These polarization states contain information in form of metric can be written as,

$$\begin{aligned} g = ds^2 = -dt^2 + [1 + h_+ cos\omega(z-t)dx^2 + [1 - h_+ cos\omega(z-t)]dy^2] + \\ dz^2 + 2dxdyh_\times cos\omega(z-t]) \end{aligned} \tag{5.22}$$

Again, considering Eq.(5.10), for each $\mathbf{k}$ the polarization tensor $A_{\mu\nu}(\mathbf{k})$ has two degrees of freedom $(+/\times)$ and is orthogonal to the direction of propagation $\mathbf{n} = \mathbf{k}/k^0$. So by choosing 2 orthonormal vectors $\mathbf{u}, \mathbf{v}$ in this plane, *basis vectors* for these polarization state can be given as,

$$\begin{aligned} e_{ij}^+(\mathbf{n}) &= [\mathbf{u} \otimes \mathbf{u} - \mathbf{v} \otimes \mathbf{v}]_{ij} = u_i u_j - v_i v_j \\ e_{ij}^\times(\mathbf{n}) &= [\mathbf{u} \otimes \mathbf{v} + \mathbf{v} \otimes \mathbf{u}]_{ij} = u_i v_j + v_i u_j \end{aligned} \tag{5.23}$$

which satisfying $e_{ij}^a e^{bij} = 2\delta^{ab}$ gives,

$$A_{ij}(\mathbf{k}) = A_+(\mathbf{k}) e_{ij}^+(\mathbf{n}) + A_\times(\mathbf{k}) e_{ij}^\times(\mathbf{n}) \tag{5.24}$$

where, $A_{+,\times}$ represent the amplitudes of the wave in the plus and cross polarization states respectively.

5.2 Linearized equations in curved spacetime

In the previous section, we derived propagation of gravitational waves in almost ideal flat spacetime scenario which is not the real case as we work on large cosmological scale. On these scales, due to expansion of the Universe and massive objects, the background spacetime metric is curved/perturbed as below:

$$g_{\mu\nu} = g_{\mu\nu}^B + \epsilon h_{\mu\nu} + \epsilon^2 j_{\mu\nu} + \mathcal{O}(\epsilon)^3 \tag{5.25}$$

where, $g_{\mu\nu}^B$ is the dynamical background, $h_{\mu\nu}$ is the first order metric perturbation, $j_{\mu\nu}$ is the second order metric perturbation and ϵ is the smallness parameter. Since while propagating in the curved spacetime, gravitational waves receive contribution from different sources, a frequency/wavelength and the time-scales/length-scales of GWs in the background metric must be distinguished. Therefore, if the background metric has variations on spatial scales L_B or temporal scales f_B, then for a gravitational wave moving on this background may satisfy following conditions for its typical wavelength λ or frequency f:

$$\lambda \ll L_B, \text{and} \quad f \gg f_B \tag{5.26}$$

Since, f_B and L_B are two unrelated scales, in order to discriminate perturbations, one of these conditions should be satisfied. From Eq.(5.25), the Ricci tensor keeping terms up to the second order in perturbation would be,

$$R_{\mu\nu} = R^B_{\mu\nu} + R^{(1)}_{\mu\nu} + R^{(2)}_{\mu\nu} + \mathcal{O}(|h|)^3 \tag{5.27}$$

with,

$$R^B_{\mu\nu} = -\langle R^{(2)}_{\mu\nu}\rangle + 8\pi G\langle T_{\mu\nu} - \frac{1}{2}g_{\mu\nu}T\rangle \tag{5.28}$$

Eq.(5.28) describes the evolution of the background spacetime accounting for energy of matter and energy of gravitational waves contained in the term $\langle R^{(2)}_{\mu\nu}\rangle$ which can be interpreted as energy momentum tensor of GWs.

$$R^{(1)}_{\mu\nu} = -[R^{(2)}_{\mu\nu}]^{high} + 8\pi G[T_{\mu\nu} - \frac{1}{2}g_{\mu\nu}T]^{high} \tag{5.29}$$

where, $[A]^{high} = A - \langle A\rangle$. Eq.(5.29) describes the propagation and generation of GWs in the background. Eq.(5.28) can be rewritten as,

$$R^B_{\mu\nu} - \frac{1}{2}g^B_{\mu\nu}R^B = 8\pi G(\langle T_{\mu\nu}\rangle + t_{\mu\nu}) \tag{5.30}$$

where, the *energy-momentum tensor* of GWs $t_{\mu\nu}$ shows the effect of GWs on the background (assuming $c = 1$):

$$\boxed{t_{\mu\nu} = -\frac{1}{8\pi G}\langle R^{(2)}_{\mu\nu} - \frac{1}{2}g^B_{\mu\nu}R^{(2)}\rangle} \tag{5.31}$$

This quantity depends on perturbation $h_{\mu\nu}$ and not on the matter. As an energy-momentum tensor, $t_{\mu\nu}$ should be conserved and gauge-invariant which can be shown by considering isolated sources and assuming the background spacetime is asymptotically flat. Then in the region far from source (imposing TT and Lorentz gauge conditions) reduces to [125]:

$$\partial^\mu t_{\mu\nu} = 0 \quad \text{and,} \tag{5.32}$$

$$t_{\mu\nu} = \frac{1}{32\pi G}\langle \partial_\mu h^{TT}_{\alpha\beta}\partial_\nu h^{TT}_{\alpha\beta}\rangle \tag{5.33}$$

and in the TT gauge the energy density of GWs given by the 00th component,

$$t_{00} = \frac{1}{16\pi G}\langle \dot{h}^2_+ + \dot{h}^2_\times\rangle \tag{5.34}$$

And, the GW energy flux per unit is given by,

$$\frac{dE}{dtdA} = \frac{1}{16\pi G}\langle \dot{h}^2_+ + \dot{h}^2_\times\rangle \tag{5.35}$$

This expression can be expressed in terms of its Fourier component of the wave to find the spectrum. Integrating Eq.(5.34) over time and using Fourier transformed variable,

$$\frac{dE}{dAdf} = \frac{\pi}{2G} f^2 (|\tilde{h}_+(f)|^2 + |\tilde{h}_\times(f)|^2) \tag{5.36}$$

where $f = \omega/2\pi$ is the wave frequency and $\tilde{h}_{+,\times}$ are the Fourier components of the gravitational waves.

From Eq.(5.29) to first order in metric perturbation and keeping only leading and next-to leading terms in the expansion parameter, the equation governing the *propagation of GWs* is given by,

$$R^{(1)}_{\mu\nu} = 0 \tag{5.37}$$

If we introduce the variable $\bar{h}_{\mu\nu} = h_{\mu\nu} - 1/2 g^B_{\mu\nu} h$ and impose the Lorentz gauge condition in the following form:

$$\bar{\nabla}^\mu \bar{h}_{\mu\nu} = 0 \tag{5.38}$$

where $\bar{\nabla}$ is the covariant derivative w.r.t the background metric then Eq.(5.38) becomes,

$$\bar{\nabla}^\rho \bar{\nabla}_\rho \bar{h}_{\mu\nu} = 0 \tag{5.39}$$

For an astrophysical source, an apparent luminosity of GW radiation $\mathcal{F}$ at distance far away from the source in terms of gravitational wave amplitude is given by [127, 128],

$$\mathcal{F} \sim \frac{|\dot{h}|^2}{16\pi} \tag{5.40}$$

Above relation can be used to make an order-of-magnitude estimate of GW amplitude from knowledge of the rate at which energy is emitted by a source in the form of GWs. If a source at distance r radiates away energy E in time T with frequency f then using $\dot{h} = 2\pi f h$ and $\mathcal{F} \sim E/(4\pi r^2 T)$, the amplitude of GWs is given by [128],

$$h \sim \frac{1}{\pi f r} \sqrt{\frac{E}{T}} \tag{5.41}$$

Having known the time development of the signal, one can filter the detector output through a copy of the expected signal following *matched filtering* method which leads to an enhancement in the SNR roughly by a square root of the number of cycles the signal spends in the detector band. Therefore, we can define an *effective amplitude* of a signal which is a better measurement of its detectability than its raw amplitude:

$$h_{eff} \equiv \sqrt{n} h \tag{5.42}$$

A signal lasting for a time T around a frequency f would produce $n \simeq ft$ cycles which can be used to eliminate T from Eq.(5.42) and get the effective amplitude of the signal in terms of the energy, emitted frequency and the distance to the source:

$$h_{eff} \sim \frac{1}{\pi r} \sqrt{\frac{E}{f}} \tag{5.43}$$

Eq.(5.43) depends only on energy through the total *fluence* or time integrated flux $E/4\pi r^2$ of the wave.

5.2.1 The geometrical optics approximation

The regime where the wavelength of the gravitational waves λ is much smaller than the characteristic length scale of the variation of background L_B characterizing the background curvature ($\lambda \ll L_B$) is known as the *geometric optics limit*. In addition to L_B, the wavelength of the waves is also small compared to the scale of variation of GW amplitude L_a. In this approximation, propagation of GWs can be treated as that of the massless particles on a null geodesic of background spacetime by neglecting other wave-like effects such as diffraction or interference. However, this approximation breaks down in the strong gravity regime such as in the vicinity of compact objects.

In terms of smallness parameter $\epsilon = \lambda/min[L_B, L_a]$, we can expand amplitude of GWs as,

$$h_{\mu\nu}(x) = [A_{\mu\nu}(x) + \epsilon B_{\mu\nu}(x) + \epsilon^2 C_{\mu\nu}(x) + ...]e^{\theta(x)/\epsilon} \tag{5.44}$$

where, $\theta(x)$ is the phase. If we set $\epsilon = 1$ and use it in the Lorentz gauge condition Eq.(5.38) and in the wave equation Eq.(5.39) to the leading order in ϵ, we obtain:

$$e_{\mu\nu}k^{\mu} = 0 \tag{5.45}$$

and

$$k^{\mu}k_{\mu} = 0 \tag{5.46}$$

where following definitions are used: $k_{\mu} \simeq \partial_{\mu}\theta$, $A_{\mu\nu} = ae_{\mu\nu}$ and $e_{\mu\nu}e^{\mu\nu} = 1$. Now taking the covariant derivative of Eq.5.46, we obtain,

$$\begin{aligned} 0 = \nabla_{\rho}k^{\mu}k_{\mu} = 2k^{\mu}\nabla_{\rho}k_{\mu} = \\ 2k^{\mu}\nabla_{\rho}\nabla_{\mu}\theta = 2k^{\mu}\nabla_{\mu}\nabla_{\rho}\theta = 2k^{\mu}\nabla_{\mu}k_{\rho} \end{aligned} \tag{5.47}$$

This means that k_{μ} is parallely transported along itself i.e., the wave propagates on null geodesic of the background spacetime. Using Eq.(5.39) again and keeping terms of next-to-leading order,

$$0 = 2k^{\rho}\nabla_{\rho}A_{\mu\nu} + A_{\mu\nu}\nabla_{\rho}k^{\rho} = 2k^{\rho}e_{\mu\nu}\partial_{\rho}a + 2k^{\rho}a\nabla_{\rho}e_{\mu\nu} + A_{\mu\nu}\nabla_{\rho}k^{\rho} \tag{5.48}$$

which upon contracting with $e_{\mu\nu}$ and using $e_{\mu\nu}\nabla_{\rho}e_{\mu\nu} = 0$ gives,

$$0 = 2k^{\rho}\partial_{\rho}a + a\nabla_{\rho}k^{\rho} \Rightarrow k^{\rho}\partial_{\rho}a = -\frac{1}{2}a\nabla_{\rho}k^{\rho} \tag{5.49}$$

which gives the evolution of the amplitude a. This can be also written as,

$$\nabla_{\rho}(a^2k^{\rho}) = 0 \tag{5.50}$$

which further reduces to,

$$k^{\rho}\nabla_{\rho}e_{\mu\nu} = 0 \tag{5.51}$$

i.e. the polarization tensor is parallely transported along the trajectory of the wave. These equations are analogous to the equations found for propagation of electromagnetic waves in curved background. This means that from the point of view of geometric

optics, gravitons and photons propagate in the same manner while travelling on the null geodesic of the spacetime.

Further in the geometric optic approximation, Issaccson showed that [129, 130] the gauge transformation of the Ricci and Riemann curvature tensor have following properties:

$$\bar{R}^{(1)}_{\mu\nu} - R^{(1)}_{\mu\nu} \simeq \left(\frac{\lambda}{L}\right)^2 \tag{5.52}$$

and,

$$\bar{R}^{(1)}_{\alpha\mu\beta\nu} - R^{(1)}_{\alpha\mu\beta\nu} \simeq \left(\frac{\lambda}{L}\right)^2 \tag{5.53}$$

where, $R^{(1)}_{\mu\nu}$ and $R^{(1)}_{\alpha\mu\beta\nu}$ are the first order Ricci and Riemann tensors and the overbar denotes their values after the gauge transformation. Further, by evaluating the effective stress-energy tensor on a smooth background metric in a Loretnz gauge and performing the average, we obtain the *Isaacson tensor* [131],

$$T^{(GW)}_{\mu\nu} = \frac{1}{32\pi}\langle h_{\mu\nu;\alpha} h^{\mu\nu}_{;\beta}\rangle \tag{5.54}$$

which localizes energy in short-wavelength gravitational waves to regions of the order of a wavelength.

5.3 The quadrupole formula

Electromagnetic radiation and GWs both originate from variation of a charge and a mass respectively and present some similarities e.g. the waveform and the same propagation velocity in General Relativity. However the electromagnetic radiation is associated to a *dipole* or a higher moments such as quadrupole, octapole etc. whereas GWs are generated by a quadrupole or higher moments such as octapole. This makes reasonable to quest why monopoles and dipoles do not contribute GW emission. The quadrupole formula plays the same role in theory of gravity as played in electromagnetism and allows us to estimate the magnitude of the GW strain for a given source.

Here we define the moments of the object generating gravitational waves, assuming no internal motion. The zeroth moment M_0 of the mass distribution which is also known as the *monopole moment* is the mass of the object itself:

$$M_0 = \int \rho d^3x = M \tag{5.55}$$

where ρ is the mass density of the object. The first moment M_1 of the mass distribution which is also known as the *dipole moment* term is given by,

$$M_1 = \int \rho x_i d^3x = ML_i \tag{5.56}$$

where, L_i is the vector having dimension of a length describing the displacement of the center of the mass from the origin. The second moment M_2 or the *quadrupole moment* of the mass distribution is,

$$M_2 = \int \rho x_i x_j d^3x = ML_{ij} \tag{5.57}$$

Here L_{ij} is a tensor with dimension of length squared. It can be shown that M_0 and M_1 cannot generate GWs because as h is proportional to $1/r$ (where r is the distance from the source) and since the coefficients that make the strain dimensionless we can write,

$$h \sim \frac{GM_0}{c^2 r} \tag{5.58}$$

But as the mass-energy conservation principle states that M_0 cannot change in time for an isolated system, Eq.(5.58) cannot be associated with emission of any GW signals. Similarly for the dipole term, to obtain a dimensionless strain we use first time derivative and use c^3 factor,

$$h \sim \frac{G}{c^3 r}\frac{dM_1}{dt} = \frac{GP}{c^3 r} \tag{5.59}$$

where P is the total angular momentum of the source, which again is a conserved quantity and hence in a similar fashion to the monopole term, dipole moment too cannot produce GW signals.

Finally, for the second order term, the *quadrupole moment* would be:

$$M_2 \equiv \int \rho x_i x_j d^3x = ML_{ij} \tag{5.60}$$

where L_{ij} is a tensor with dimension of length squared. The associated strain for quadrupole term in this case becomes,

$$h \sim \frac{G}{c^4 r}\frac{d^2}{dt^2}M_2 \tag{5.61}$$

Here, M_2 is not related to any conservation laws and hence can be associated with emission of GWs. Since gravitational interactions are the weakest of all four fundamental interactions, even extremely large energies radiated from GWs would produce small strain. In Eq.(5.61), in the actual quadrupole formula, the second moment is a traceless tensor,

$$M_2 = I_{ij} - \frac{1}{3}\delta_{ij} I \tag{5.62}$$

where I_{ij} is the tensor of inertia and $I = I_i^i$ is its trace. It can be shown that the correct quadrupole formula is:

$$h_{ij} = \frac{2G}{c^4}\frac{1}{r}\frac{d^2 M_2}{dt^2} \tag{5.63}$$

which differs from Eq.(5.61) by a multiplicative factor of 2. From dimensional analysis we can approximate the second time derivative of M_2 with twice the kinetic energy:

$$h_{ij} = \frac{4G}{c^4}\frac{1}{r}\frac{E_k}{c^2} \tag{5.64}$$

where $\frac{E_k}{c^2}$ has the dimension of a mass. Since GWs emitted so far include astrophysical source, more precisely CBCs, we consider a binary system of masses m_1 and m_2 with their relative position denoted by R and orbital frequency Ω. For the binary system of two masses m_1 and m_2 the total mass becomes $M = m_1 + m_2$ and the reduced mass is given by $\mu = m_1 m_2/M$ along with mass ratio defined as $q = m_1/m_2$. Generally it is assumed that $m_1 \geq m_2$ so that $q \geq 1$. Therefore from Eq.(5.63), a non-zero component of h_{ij} is given by,

$$h = \frac{4\mu\Omega^2 R^2}{r} \tag{5.65}$$

Which upon using Kepler's third law gives,

$$h = \frac{4\mu M^2 \Omega^2}{r} \tag{5.66}$$

Further, the GW strain h at a luminosity distance d_L from a system whose traceless mass quadrupole moment is Q_{ij} is given by,

$$h_{ij} = \frac{2G}{c^4 d_L} \frac{d^2 Q_{ij}}{dt^2} \tag{5.67}$$

and the rate at which the energy is carried away by these GWs is given by the quadrupole formula:

$$\frac{dE_{gw}}{dt} = \frac{c^3}{16\pi G} \int\int |\dot{h}|^2 dS = \frac{1}{5} \frac{G}{c^5} \sum_{i,j=1}^{3} \frac{d^3 Q_{ij}}{dt^3} \frac{d^3 Q_{ij}}{dt^3} \tag{5.68}$$

where the strain amplitude is,

$$\boxed{|\dot{h}|^2 = \sum_{i,j=1}^{3} \frac{dh_{ij}}{dt} \frac{dh_{ij}}{dt}} \tag{5.69}$$

and the integral is over sphere of radius d_L and the quantity over right-hand side must be averaged over one orbit. Eq.(5.68) gives the rate of loss of orbital energy to GWs within the limit that velocity of orbiting objects is less than c and the strain is not too large [123]. Further, to describe GW emission from a binary system, *chirp mass* $\mathcal{M}$ is defined which is related to the component mass by,

$$\mathcal{M} = \frac{(m_1 m_2)^{3/5}}{(m_1 + m_2)^{1/5}} \tag{5.70}$$

Due to energy emitted in the orbital phase, the orbit gets shrunk and this shrinking makes an observed gravitational signal enhanced in terms of its frequency with time. This is called a *chirp*. A chirp (or a sweep) signal is a signal in which the frequency increases (up-chirp) or decreases (down-chirp) with time. The *chirp mass* determines the phase evolution during inspiral of a binary and can be related with frequency and frequency derivative of emitted GWs by [132, 133],

$$\mathcal{M} = \frac{c^3}{G} \Big(\Big(\frac{5}{96} \Big)^3 \pi^{-8} (f_{gw})^{-11} (\dot{f}_{gw})^3 \Big)^{1/5} \tag{5.71}$$

where $\dot{f}_{gw} = df_{gw}/dt$ is the rate-of-change of frequency. Here, quantities involved in addition to the reduced mass and total mass include the *symmetric mass ratio* denoted by $v = \mu/M$. This equation is expected to hold as long as Newtonian approximation is valid. Alternatively, Eq.(5.71) can be integrated to obtain,

$$f_{gw}^{-8/3}(t) = \frac{(8\pi)^{8/3}}{5}\Big(\frac{G\mathcal{M}}{c}\Big)^{5/3}(t_c - t) \tag{5.72}$$

which does not involve $\dot{f}_{gw}$ explicitly and can be used to calculate $\mathcal{M}$ directly from the time periods between zero crossings in the strain data. t_c which is the constant of integration which shows the time of coalescence.

Within geometric optics limit, the phase of the GWs remain unaltered and the primary effect of gravitational wave lensing is evident in the strain of the signal and in the temporal and spatial aspects of the signal [134]. Due to matter perturbations between the source and the observer several observable effects such as (i) time-delay (ii) magnification/demagnification (iii) shift in the sky position and, (iv) formation of multiple lensed images can be seen [135]. For example, magnification leads to change in the amplitude of the GW strain $h_{+,\times}(f_z)$ by the magnification factor μ [136, 137, 138, 125],

$$h_{(+,\times)}f(\hat{n}) = \sqrt{\mu}\sqrt{\frac{5}{96}}\frac{G^{5/6}\mathcal{M}_z^2(f_z\mathcal{M}_z)^{-7/6}}{c^{3/2}\pi^{2/3}d_L}\mathcal{I}_{\pm}(\hat{L}\cdot\hat{n}) \tag{5.73}$$

where, $f_z = f(1+z)$ is the redshifted frequency, d_L is the luminosity distance to the GW source, $\mathcal{I}_{\pm}(\hat{L}\cdot\hat{n})$ captures the projection of the angular momentum $\hat{L}$ on the line-of-sight $\hat{n}$ and, $\mathcal{M}_z$ is the redshifted chirp mass which can be well measured from the phased part of the GWs [137].

Sources and spectrum of GWs Gravitational wave signal can broadly classified as *continuous GWs* and *GW bursts*. These signals can be distinguished from each other based on characteristic evolution time τ and the observation time T. For the continuous GW signals, τ is very long compared to the observational time T, whereas for fast evolving GW bursts, characteristic evolution time τ is much smaller than the observation time T. Sources of GWs can be broadly classified based on their phase and phase coherence into three categories:

- *Bursts sources/ gravitational wave transients*: Short duration sources with modelled (e.g. compact binary coalescence) or unmodelled (e.g. supernovae) phase evolution having evolution time intervals which are comparatively shorter than the observational time (bounded in time). e.g. signals emitted from core collapse of a supernova, ring-down phase of black hole coalescence etc.,

- *Continuous sources*: Long duration sources with phase coherence i.e. bound in frequency (e.g. spinning neutron stars),

- *Periodic sources*: Periodic signals are continuous gravitational signals which are expected to have a duration much greater than the observation time and are emitted at a nearly constant frequency,

- *Stochastic background*: created by superposition of unresolved and independent sources without phase coherence (e.g. coalescing binaries, millisecond pulsars in a galaxy clusters).

In order to make a clear distinction, the waveform signal from an inspiral[1], continuous signal[2] and gravitational wave signal from a burst[3] is shown in Fig.5.2, Fig.5.3 and Fig.5.4 respectively.

Fig.5.5 shows the GW spectrum with different frequencies corresponding to different gravitational wave sources either of astrophysical or cosmological origin along with detection methods. Quantum fluctuations from inflation span over all frequencies.

Similarly, the complete spectrum of gravitational wave astronomy in terms of different ground- and space-based missions targeting different frequency bands to quest cosmological evolutionary phases can be shown below in Fig.5.6.

The era of GW astronomy began by the first indirect detection in 1974 by Hulse and Taylor [139] from binary neutron star system where one of them was a pulsar. First breakthrough came in the year 2015 when LIGO Hanford and Livingston detected the first ever whisper of the cosmic dance by two merging binary black holes with initial masses $36^{+5}_{-4}M_{\odot}$ and $29^{+4}_{-4}M_{\odot}$ respectively located at 410Mpc away, resulting into final black hole with mass $62^{-4}_{+4}M_{\odot}$ and total energy $3.0^{+0.5}_{-0.5}M_{\odot}c^2$ radiated in form of GWs [1]. The schematic of phases before GW signal emission and signal detected in both detectors is shown in below Fig.5.7.

This detection has demonstrated the existence of BHs more massive than the previously observed in X-ray binaries in our galaxy. Based on this detection authors of [141] have proposed framework to calculate mass distribution of merging binary black holes and its evolution with redshift and the implications of this evolution for the stochastic gravitational wave background from mergers and from core collapse events. As a special application to astrophysics, GWs emitted from BNS system can bring us information about the nuclear structure because the tidal deformation effects present in the coalescence of the neutron stars are embedded into the GW waveforms and features present within the waveforms originated from the inspiral of the binary black holes provide us information about the spacetime surrounding such extreme gravity objects.

5.4 Cosmological distance measurement methods

Expansion of the Universe influences distance measurements in cosmology. On cosmic scales, we can not directly measure the proper distance or proper size of astronomical objects but we infer these quantities from measurements of their redshift, luminosity or angular size. In this section we describe methods which are mainly used for cosmological distance measurements and from it we motivate how GWs as standard sirens can be used as a potential probe for cosmological distance measurement.

On cosmological scales, distance measurement can be classified as large scale distance determination, intermediate scale and local scale measurements. For large scale distance measurements, we must use methods based on global properties of galaxies. Some of the methods used for such distance determination include using *Faber-Jackson*

[1]https://www.ligo.org/science/GW-Inspiral.php
[2]https://www.ligo.org/science/GW-Continuous.php
[3]https://www.ligo.org/science/GW-Burst.php

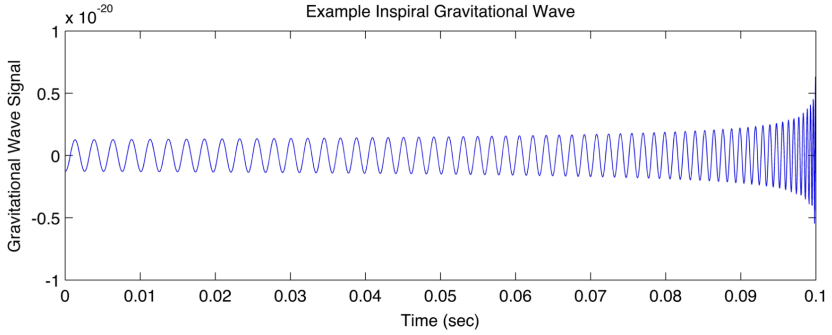

Figure 5.2: Waveform example of GW signal from an inspiralling GW source, image taken from "LIGO Science".

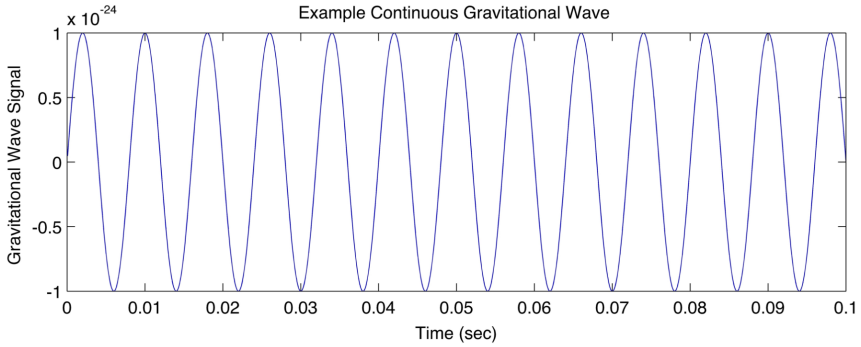

Figure 5.3: Waveform example of GW continuous signal from a rotating neutron star, image taken from "LIGO Science".

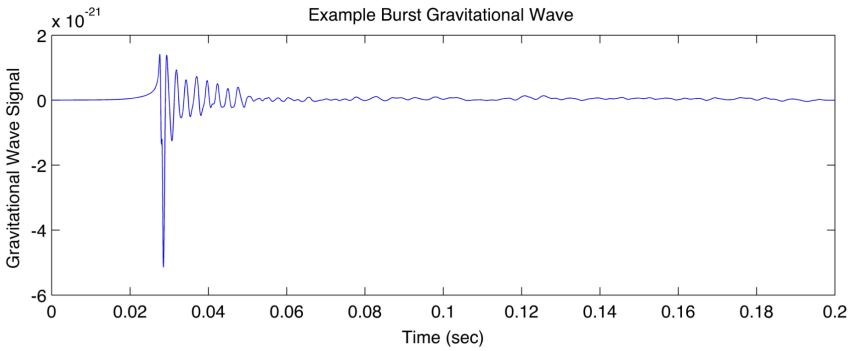

Figure 5.4: Waveform example of GW signal from a burst from a supernova core collapse, image taken from "LIGO Science".

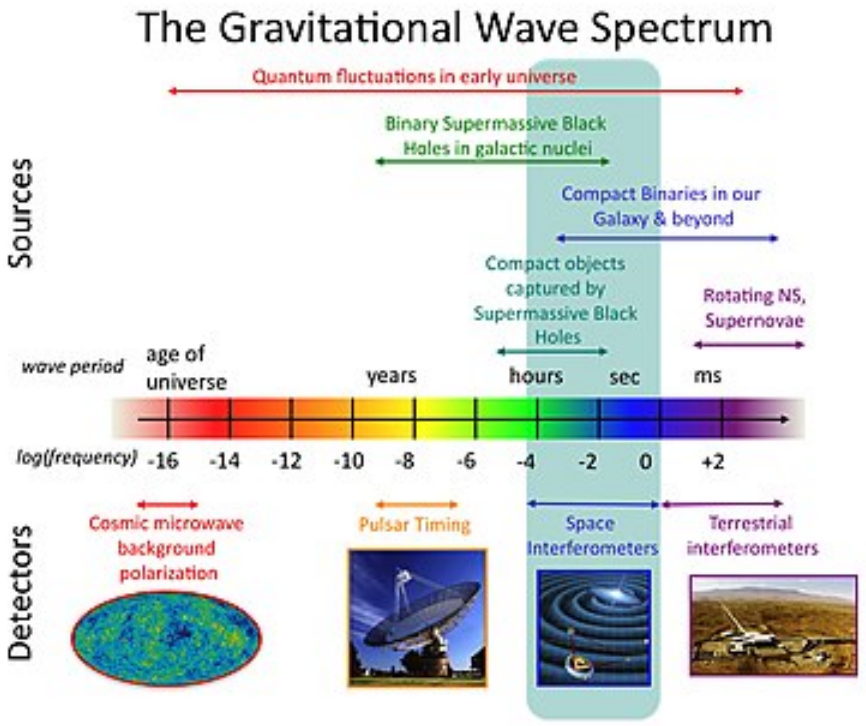

Figure 5.5: Gravitational wave spectrum showing different approaches and instruments targeted to probe different frequency ranges and the sensitivities of several detection methods.

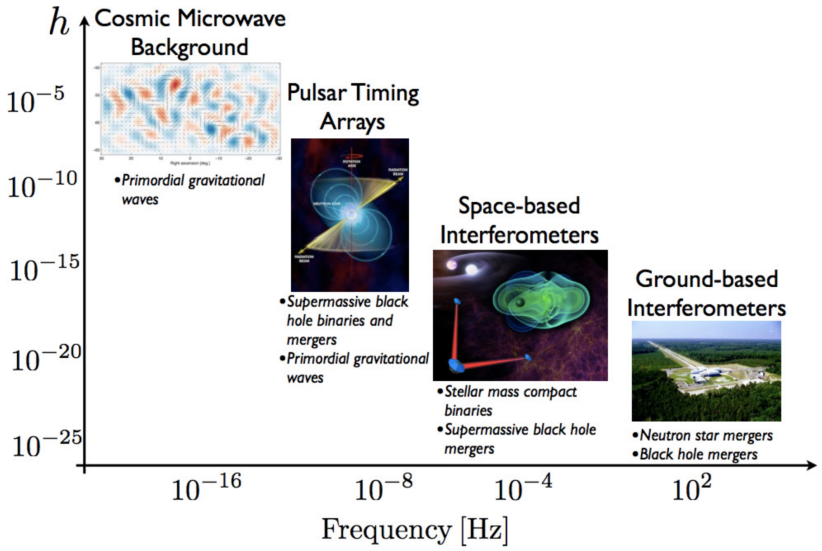

Figure 5.6: Gravitational wave spectrum taken from https://www.skatelescope.org

relation, *Tully-Fisher relation* and galaxy clustering e.g. the Coma-Virgo cluster distance. On intermediate scale, the methods used include surface-brightness fluctuations, planetary nebulae and measurements by the M31-Virgo distance, similarly on local scale, Cepheid variables can be used [6].

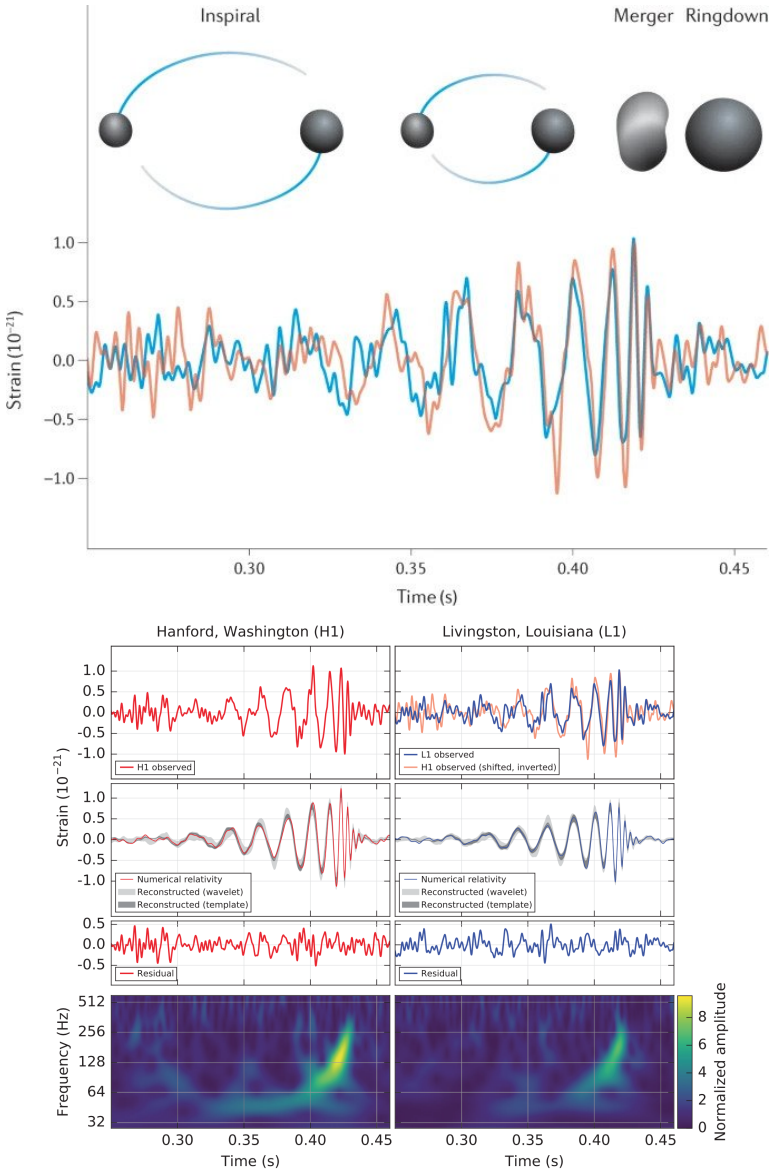

Figure 5.7: *Top*: Detected gravitational wave strain amplitude is shown as a function of time. The waveforms are shifted and inverted to compensate for the slightly different arrival times and different orientations of the different detector sites (red: LIGO Hanford and blue: LIGO Livingston). The upper insert is a simulation of the merger produced using numerical relativity to illustrate the evolution of the BH event horizon as the system coalesces and mergers [140]. *Bottom*: GW150914 observed by the LIGO Hanford, H1 in left column panels and Livingston, L1 in the right panels. Top raw left: H1 strain, top raw right: L1 strain. Second raw shows GW strain projected onto each detector in the $35-350$Hz band. Solid lines show a numerical relativity waveform for a system, third raw shows residuals after subtracting the filter numerical waveform from the filter detector time series. Finally the bottom raw shows the time-frequency representation of the strain data [1].

Considering expansion, distance measurements in the Universe is one of the most challenging task as we have to consider two distances- *comoving distance* which is the distance measured in the comoving reference frames which is independent of scale

factor and the other is the *physical distance* which depends on comoving distances and also on evolution of the scale factor. One important comoving distance is the distance light can travel without any interactions since $t = 0$. Since light can travel a distance $dx = dt/a$ in time dt, the total comoving distance is (in units $c = 1$) given by,

$$\eta = \int_0^t \frac{dt}{a(t)} \tag{5.74}$$

Here, η is called *comovig horizon* or *conformal time* which holds prime importance in cosmology as it is the maximum distance at which information could propagate in time t in a particular comoving reference frame. Regions separated by distances greater than η are causally disconnected.

The corresponding *physical distance* is the distance in direct proportion to the scale factor. It is the farthest distance we can observe today and is known as the *horizon distance*:

$$d_H(t_0) = a(t_0) \int_0^t \frac{dt}{a(t)} \tag{5.75}$$

where $a(t_0) = 1$ and points separated by distances greater than the horizon distance are causally not connected. Using the FLRW metric in polar coordinates in Eq.1.10, the physical distance between two objects at time t can be written as,

$$d_p(t) = a(t) \int_0^r \frac{dr}{\sqrt{1 - kr^2}} \tag{5.76}$$

which for $k = 0$ becomes:

$$d_p(t) = a(t)r \tag{5.77}$$

Therefore due to expansion, the present value of the angular distance of an object is larger than it was in the past. In order to determine H_0, we must determine the distance d_p. The redshift can be used to connect the physical distance d_p with the *luminosity distance* d_L of an object where the luminosity distance can be defined as the distance at which an observer P_0 at $t = t_0$ measures a flux f from a source P emitting a power L:

$$d_L = \left(\frac{L}{4\pi f}\right)^{\frac{1}{2}} \tag{5.78}$$

Unlike the angular diameter distance, the luminosity distance measured is lower than it was in the past. This is due to expansion of the Universe which dilutes the number of photons emitted per unit area. As the magnitude of power L for a given source is generally not known, determination of the luminous distance is difficult. The spherical surface centered at observer P and passing through the source P_0 at a time t_0 has an area $4\pi a_0^2 r^2$. Expansion of the Universe redshifts photons by a factor a_0/a_e, this helps us to derive the relation between the luminous and the physical distance:

$$d_L = \frac{r}{a_e} = (1 + z)d_p \tag{5.79}$$

At higher redshifts Eq.(1.61) is not accurate, however, the distance-to-redshift relation can be used to test the expansion of the Universe using the sample of standard candles.

Standard candles are the astronomical objects emitting electromagnetic radiation with the same intrinsic luminosity L and whose redshift can be measured. Example of standard candles include Type Ia supernovae, which results due to merging of white dwarf with another star in a binary system. [142] and [143] compared measurements of the luminosity distance of about 50 astronomical objects and theoretical expectations for homogeneous and isotropic Universe. This survey inferred that the current Universe is experiencing accelerated expansion. Commonly used standard candles include Cepheid variable starts whose intrinsic brightness is related to the period of variation and type Ia Super Novae (SNIa) which always have the same emission power. Type Ia supernova can be used as a standard candle to measure extragalactic distance indicating how fast the Universe has expanded in past. Since expansion of the Universe is currently ascribed by *Dark Energy* and observations indicate [2] almost spatially flatness of the Universe, the total energy density of the Universe should be $\Omega_t \cong 1$ with measured dark energy density $\Omega_\Lambda \cong 0.690$ and observed matter energy density $\Omega_b \cong 0.0482$ with negligible radiation energy density. This gives $\Omega_{DM} \cong 0.258$ hinting towards existence of non-luminous dark matter.

Measuring *angular diameter distance* d_A is another way of distance measurements. If we consider an object of length l aligned perpendicular to the line of sight with angular size $\delta\theta$, then angular diameter distance becomes,

$$d_A = \frac{l}{\delta\theta} \tag{5.80}$$

The angular diameter distance can be related with the physical distance through:

$$d_A = \frac{d_L}{(1+z)^2} \tag{5.81}$$

$$d_A(z) = \frac{1}{1+z} r_{comov}(z) \tag{5.82}$$

Similar to the luminous distance, angular diameter distance measurement which is used to study separation distance of galaxies is also difficult as determining size l of sources is complicated.

In this section, we tried to mention conventional methods used for distance measurement. However in the era of GW physics, it becomes increasingly important to note that GWs can be used to measure cosmological distances more precisely by using them as standard sirens compared to other probes. Gravitational Wave Standard Sirens are sources of gravitational waves of known loudness: by observing the waveform, the power (rate of energy emission) of the gravitational waves can be computed. Just as with standard candles given the emitted and received amplitudes, the inverse-square law determines the distance to the source. There are some differences with standard candles, e.g. GWs are not emitted isotropically, but measuring the polarisation of the wave provides enough information to determine the angle of emission.

5.5 Standard Siren Cosmology

Gravitational Waves not only offers a way to understand physics of the electromagnetically dark Universe but they also potentially trace the late time geometry of the Universe. Advanced LIGO and Advanced Virgo detectors made the celebrated detection of first standard siren from a BNS system (GW170817) with redshift $z = 0.0008^{+0.002}_{-0.003}$ by identifying the host galaxy NGC4993 with an associated electromagnetic counterpart which was a γ-ray burst GRB 170817A [144, 145] detected by Fermi-GMB about 17.7s after the coalescence [146, 147, 148, 149, 150, 151]. As the orbit of the BNS system shrinks, the gravitational-wave luminosity increases which accelerates the inspiral. This process has long been predicted to produce considerable GW signal observable by ground-based detectors in the final minutes before the star collide [151]. The source was localized within a sky region of $28 deg^2$ and had a luminosity distance of 40^{+8}_{-14}Mpc making it the most precise GW signal detected yet. A time-frequency representation of the data from all three detector around the time of detection is shown in Fig.5.8. The signal is visible clearly in LIGO Hanford and Livingston data but not in the Virgo data due to the lower BNS horizon and the direction of source with respect to the detector's antenna pattern. Here, the maximum distance at which the LIGO-Livingston and LIGO-Hanford detectors could detect a BNS system (SNR=8) is known as the BNS *detector horizon* which were 218 Mpc, 107Mpc and 58Mpc for LIGO-Livingston, Hanford and Virgo respectively [152, 153, 154].

This event- GW170817 is remarkable because for the first time, gravitational and electromagnetic waves from a single source have been detected and also these observations confirm the hypothesis that GW170817 was produced by the merger of two neutron stars in NGC4993 followed by a short GRB and a kilonova/macronova powered by the radioactive decay of r-process nuclei synthesized in the ejecta [145, 144]. The merger rate of BNS estimated from this event suggests that distant, unresolvable binary neutron stars create a significant astrophysical stochastic background where the binary neutron star component will add to the contribution from binary black holes, increasing the amplitude of the total astrophysical background relative to previous expectations [155]. One of the most promising application of the data from this event includes the determination of Hubble constant which is given by $70.0^{+12.0}_{-8.0} kms^{-1}Mpc^{-1}$ [122].

This detection was complemented by the Dark Energy Camera (DECam) discovery [156] and statistical standard siren analysis [157] considering each galaxies in the GW170817 localisation region as a host compared to single EM counterpart. This marks the beginning of an era of Gravitational Wave Standard Siren (GWSS) cosmology because whether considered a *bright standard siren* with an associated EM counterpart or *dark standard siren* following a statistical approach as followed in [158, 157], GWSS method has potential to constraint cosmological parameters, investigate tension in Hubble parameter H_0 and understand nature of DE and gravity from the plethora of possible alternative theories.

GWs for cosmography

As proposed by [159] GWs can determine a system's location on the sky and its distance to the source. A chirping signal from the well-localized inspiraling binaries measures the amplitude and the mass of the object and hence it infers the luminosity distance

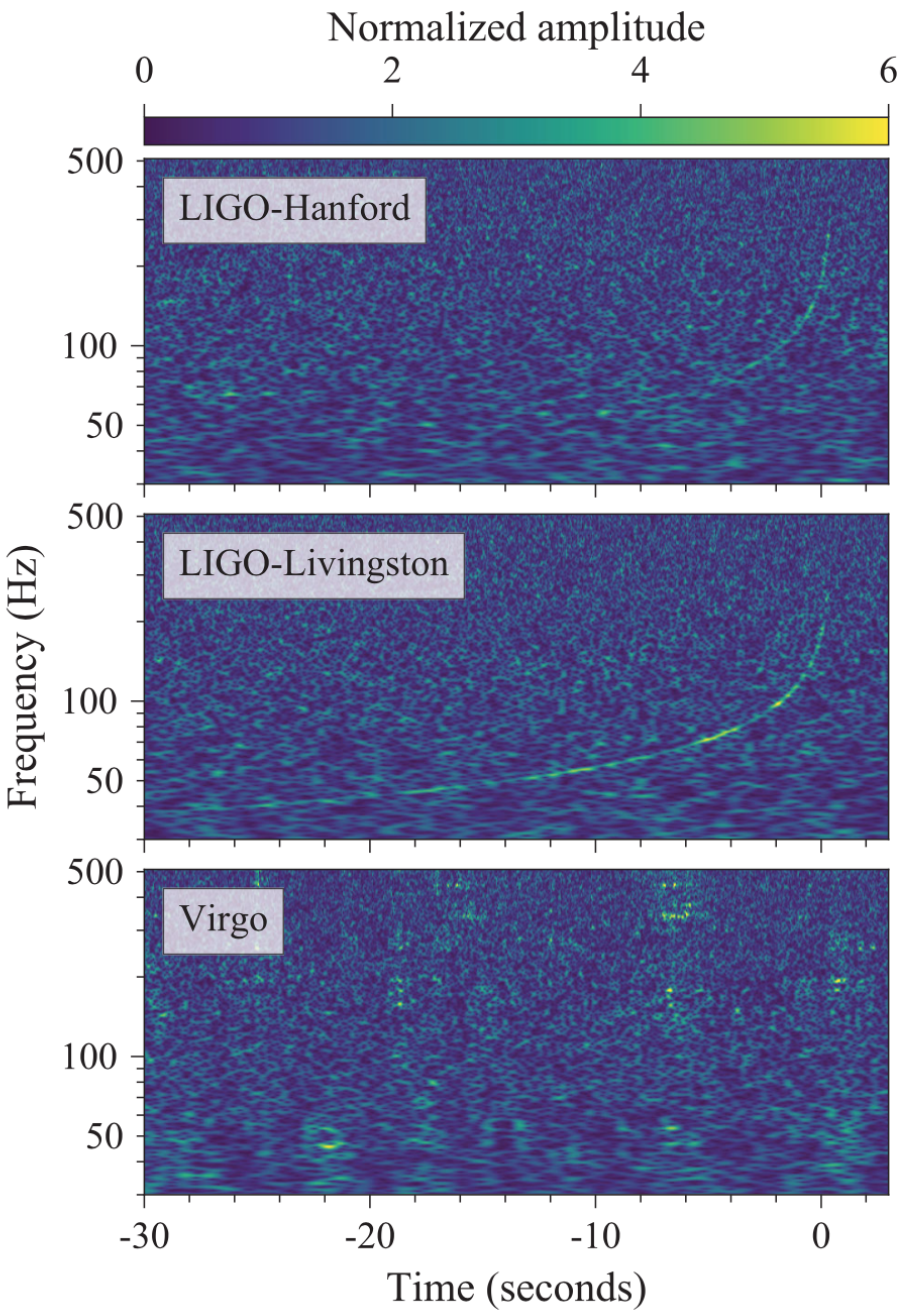

Figure 5.8: Time-frequency representation of GW170817, observed by the LIGO-Hanford (top), LIGO-Livingston (middle) and Virgo (bottom) detectors [151].

d_L and direct measurement of the Hubble constant. If we could measure redshift of the source which can either be obtained directly from counterparts to the GW sources [160], by cross-correlating gravitational wave localization posterior with catalogues of galaxy redshifts [161, 162, 163, 157, 164, 158, 165], using neutron star equation of state [166], or by using the redshifted masses inferred from the GW observations and assumptions about the mass distribution of the sources [167, 168, 169, 170]. Then $d_L - z$ relation provides direct limits on DE because with d_L we can measure the time from emission of GWs and thanks to z we can measure the size of the Universe yielding us a package to solve evolution history of the Universe from single luminosity-distance relation.

As the calibration of GWSS depends only on validity of General Relativity, GWSS becomes a *self-calibrating method*. It is worth to mention that in GR, the GW luminosity distance is equal to EM luminosity distance ($d_L^{gw} = d_L^{em}$) which restricts $d_L - z$ relation assuming validity of GR. Since this is not universal in theories beyond GR, GWSS offers a potential probe to measure cosmological distances [171] and put a stringent bound to check different models of gravity. Additionally modifications in GR leave their imprint on cosmic expansion history and in the evolution of cosmological perturbations. This results into modification in the standard GW luminosity distance which differs from the standard electromagnetic luminosity distance and can be studied with GWSS with the help of upcoming LISA or third generation ground based detectors [172].

5.6 H_0 Discrepancy

Astronomers have long argued for the systematic uncertainties in various methods determining derived values of the Hubble constant over a wide range of $40\text{kms}^{-1}\text{Mpc}^{-1} \leq H_0 \leq 100\text{kms}^{-1}\text{Mpc}^{-1}$. An accurate value of H_0 can provide a powerful constraint on the cosmological model describing evolution of the Universe by providing us a bunch of parameters such as the expansion rate of the Universe at current time defining the observable size of the Universe and its inverse setting the expansion age of the Universe [173]. Observations by two independent supernovae groups- [142] and [143] have found that SNe at higher redshifts are fainter than predicted value for a slow expansion which indicate that the expansion is indeed accelerating [66] as shown in Fig.5.9:

Different projects proposed and methods applied to untangle H_0 discrepancy are discussed in [174, 175, 176, 177, 178]. One of the most reliable results of H_0 came from the *Hubble Space Telescope (HST)* key project[179, 19]: ($H_0 = 72 \pm 8\text{kms}^{-1}\text{Mpc}^{-1}$) which used the period-luminosity relation for Cepheid variable stars, and calibrated a number of secondary distance indicators such as SNe Ia, the Tully-Fisher relation, surface-brightness fluctuation and Type II Supernovae. Further improvements [173] include H_0 determination by sample of SNe$\sim$Ia galaxies [48], a geometric measurement of the distance to the nearby galaxy NGC 4258 [180], geometric parallaxes for a sample of milky way Cepheids [181], *spitzer* mid-infrared measurements of Cepheids in the Milky Way and the Large Magellanic Cloud [182].

Other probes such as the *SH0ES project* found $H_0 = 74.0 \pm 1.4\text{kms}^{-1}\text{Mpc}^{-1}$ [183], the *Carnegie Hubble program* (CHP) [184], the *Carnegie Supernovae project* [185, 186, 187] focusing on Type Ia Super Novae (SNe Ia) and the *Carnegie–Chicago Hubble Programme* (CCHP) obtained $H_0 = 69.8 \pm 0.8(\text{stat.}) \pm 1.7(\text{sys})\text{kms}^{-1}\text{Mpc}^{-1}$ [188, 189, 190] using *Tip of the Red Giant Branch* [190, 191, 192, 193] and from the *H0LiCOW* project $H_0 = 73.3^{+1.7}_{-1.8}\text{kms}^{-1}\text{Mpc}^{-1}$ [194]. The motivation and overview of CCHP has been described in [190] which is designed to provide independent determination of H_0 via measurement of the Tip of the Red Giant Branch (TRGB) in the nearby galaxies. TRGB is the discontinuity in the Red Giant Branch (RGB) luminosity function resulting from low-mass stellar evolution which arises as a rapid onset of He-core burning causing the stars to evolve away from RGB to the lower luminosity Horizontal branch [191]. The current Planck results give $H_0 = (67.4 \pm 0.5)\text{kms}^{-1}\text{Mpc}^{-1}$ [2] which gives rice to degeneracy with other parameters such as Ω_m and the neutrino mass. However using "inverse distance ladder" we obtain $H_0 = (67.8 \pm 1.3)\text{kms}^{-1}\text{Mpc}^{-1}$

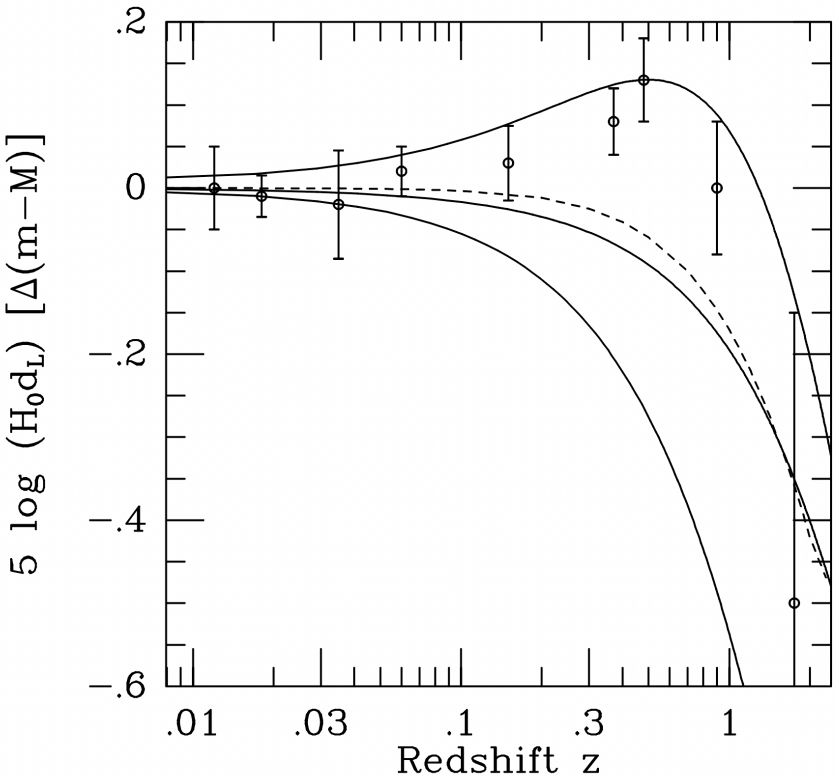

Figure 5.9: Hubble diagram showing high redshift SNe-Ia probing the expansion history revealing that the Universe experiences accelerated expansion
. In this differential Hubble diagram the distance modulus which is 5 times the logarithm of the distance relative to an empty Universe ($\Omega_0 = 0$) is plotted. Measurements from more than 200 type Ia SNe are binned into 9 data points. The solid curve represents three theoretical models: $\Omega_\Lambda = 0.7, \Omega_m = 0.3$, $\Omega_\Lambda = 0, \Omega_m = 0.3$ and $\Omega_\Lambda = 0, \Omega_m = 1$. The broken curve represents a non-accelerating flat Universe, and points above this curve show acceleration of the Universe. Original image is taken from [66].

[195] close to the Planck results which relies on absolute distance measurements from BAO to calibrate intrinsic magnitude of the SNe Ia. It is important to note that the CMB does not measure the Hubble constant independently but through the expansion rate during the time of recombination [196]. This tension between values of H_0 measured from Planck, from DES Y1, via BAO paired with weak lensing and clustering data it is $H_0 = 67.2^{+1.2}_{-1.0}\text{kms}^{-1}\text{Mpc}^{-1}$ [197] and other cosmic distance ladder methods (following Cepheid Leavitt law, it is $H_0 = 73.0 \pm 1.5(\text{stat.}) \pm 2.1(\text{sys.})\text{kms}^{-1}\text{Mpc}^{-1}$ [182] and $H_0 = 74.3 \pm 1.42\text{kms}^{-1}\text{Mpc}^{-1}$ [183]) is currently investigated using different methods. Ongoing studies are addressing the question whether this discrepancy in H_0 measurement from local astrophysics and cosmic scale at about 3-4σ level [189] is due to systematics in or a sign of physics beyond standard model of cosmology or even standard model of particle physics. It is worthy to note that as shown by [198], even in absence of electromagnetic counterpart H_0 can be measured by cross-correlating SNe with redshift surveys such as DESI or Euclid [199]. Figures 5.10 and 5.11 respectively shows H_0 landscape following different methods and the ongoing tension in H_0 as a

function of time and the different methods associated with it respectively:

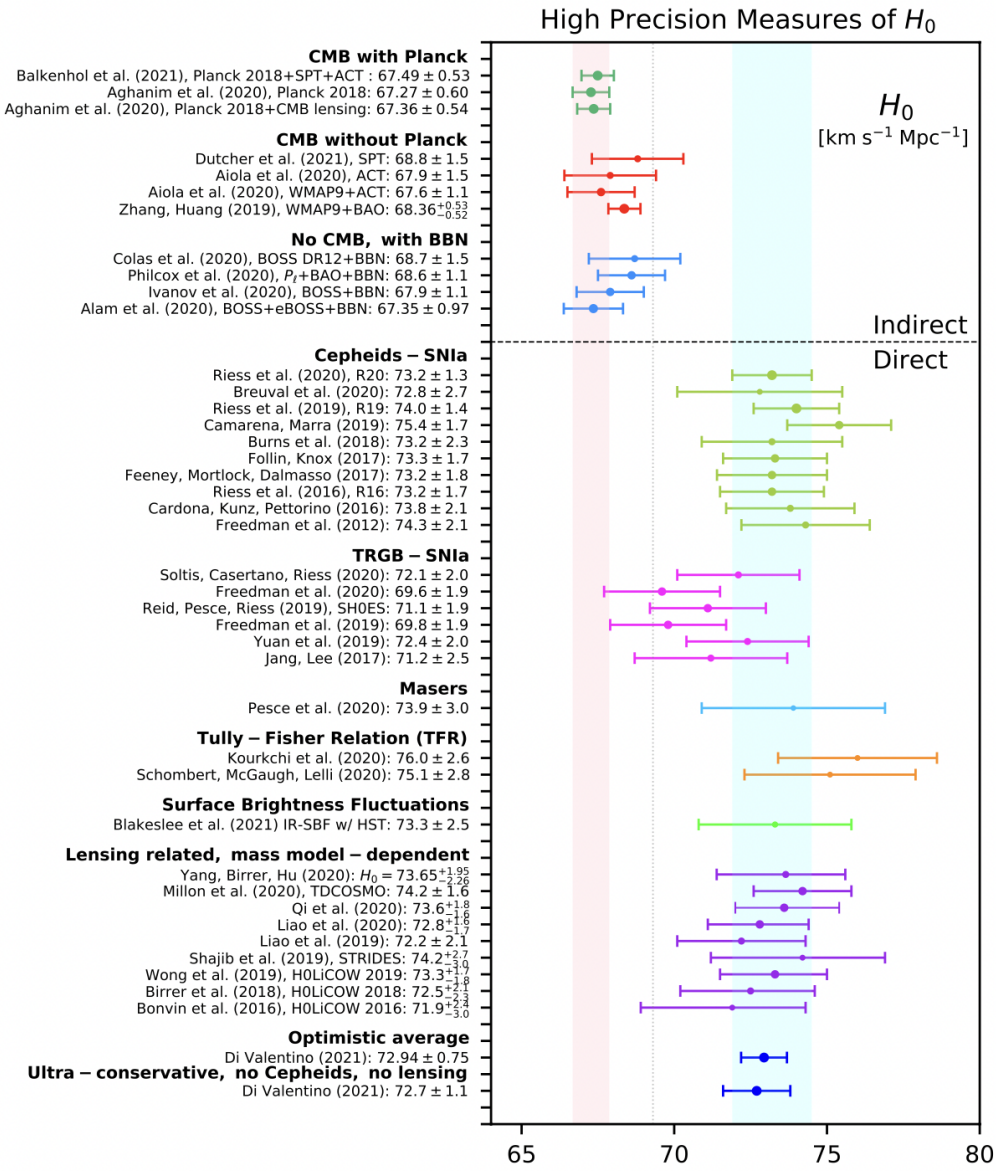

Figure 5.10: 68% CL constraints of the H_0 with error bars less than $3\text{kms}^{-1}\text{Mpc}^{-1}$ for the direct measurements and less than $1.5\text{kms}^{-1}\text{Mpc}^{-1}$ for the indirect estimates. The cyan vertical band corresponds to the latest H_0 measurement from the SH0ES team [200] $H_0 = 73.2 \pm 1.3\text{kms}^{-1}\text{Mpc}^{-1}$ at 68% level. The light pink vertical line band corresponds to the H_0 measurement from Planck 2018 within a ΛCDM scenario. A dotted vertical line for $H_0 = 69.3\text{kms}^{-1}\text{Mpc}^{-1}$ has been added for a quick visualization of the division for the H_0 values obtained from different measurement methods [201].

GWs to ease the Hubble tension

The Hubble constant measured locally and the sound horizon observed from the CMB differ drastically which hints towards a tension needed to untangle expansion history of the Universe. The tension reaches at the level of 3.6σ as a distance ladder measurements

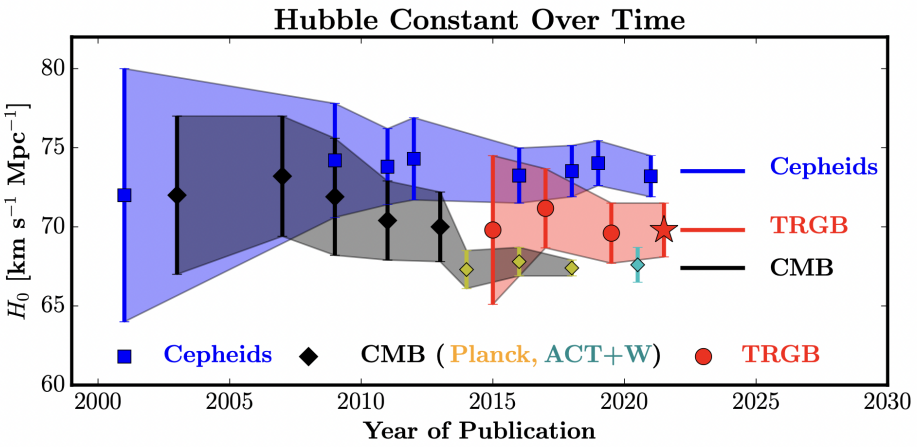

Figure 5.11: Hubble constant values in the past two decades, based on Cepheid variables (blue squares), the TRGB (red filled circles and stars), and estimates based on measurements based on CMB (WMAP:black filled diamonds, Planck:yellow diamonds, ACT+WMAP: cyan diamond) fluctuations. The CMB H_0 value assumes a flat ΛCDM model. The CMB and Cepheid results straddle a range of 67 to 74 kms^{-1}Mpc^{-1}, with the TRGB results falling in the middle and overlapping the CMB results. The tension between the CMB and TRGB results amounts to only 1.3σ. Original image taken from [202].

from Cepheids and Type Ia Supernovae gives a value $H_0 = (73.52 \pm 1.62 kms^{-1}Mpc^{-1})$ [203] which is higher than cosmological model dependent value obtained from CMB which is $H_0 = (67. \pm 0.5 kms^{-1}Mpc^{-1})$ [2]. Current observations of Baryon Acoustic Oscillation (BAO) is in agreement with the Planck results. Combined cosmological probes such as Planck+BAO [2] and CMB+BAO data can constrain the Hubble constant at the level of $1.5 - 2\%$ accuracy [204]. Strong discrepancy in measurement of H_0 on astrophysical and cosmological scale gives a stringent test of the standard cosmological model as extensions in ΛCDM could ease CMB constraint. For example, DE models beyond GR with massive neutrinos ease the tension and a time varying DE equation of state can alleviate the H_0 tension between astrophysical and cosmological probes.

Most current results [200, 201] shows the H_0 discrepancy at the level of $5 - 6\sigma$ level, between the local values of H_0 and those derived from the models of CMB. This claimed tension suggests that the Universe presently is expanding about 8% faster than the predicted assuming ΛCDM model. Below figure 5.12 shows a comparison of several recent determination of H_0 and their published uncertainty [202]:

As can be seen from the figure 5.12, the discrepancy between the early Universe (CMB+BAO) and local Cepheid measurements is apparent, as is the difference between the TRGB and Cepheid local determinations. The CMB, BAO, strong lensing and TRGB yield lower value of H_0 whereas Cepheids yields the highest values.

GWSS can help to explore tension on Hubble parameter H_0 [159, 160, 211, 212, 163, 213, 214, 215, 216]. If the tension is not due to systematic errors in astrophysical and cosmological probes, then it would be a strong hint to explore physics beyond ΛCDM which includes time-dependent dark energy, models beyond general relativity or nonzero curvature of spacetime. Fig.5.13 shows H_0 determination following gravita-

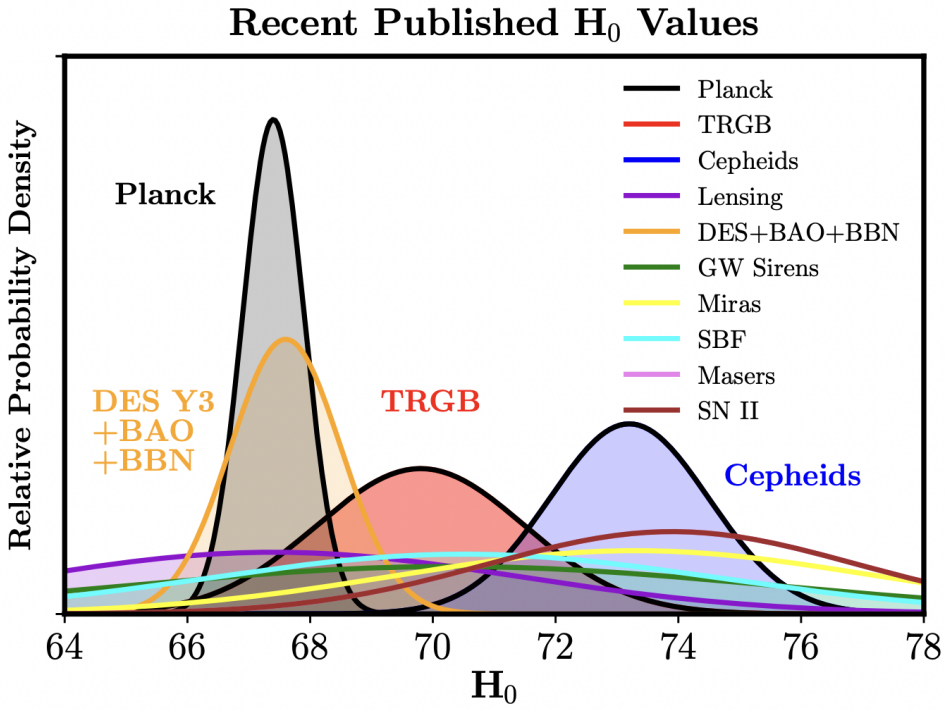

Figure 5.12: The relative probability density functions color-coded as labeled in the legend and include the TRGB, Cepheids (R21), early Universe measurements (CMB Planck 2018 results), the DES Y3+BAO+BBN, GWSS [205], Miras [206], surface brightness fluctuations [207, 208], masers [209] and recent results from strong lensing [210]. The Planck+DES Y3+BAO+BBN, TRGB and Cepheid PDFs are explicitly labelled. This plot is taken from [202].

tional wave standard siren method using electromagnetic counterpart of binary neutron mergers in the galaxy NGC 4993.

After the observational detection of the GWSS from BNS GW170817 [217] and its optical counterpart, it placed an excellent constrain on $H_0 = 70^{+12}_{-8} \mathrm{km} s^{-1} Mpc^{-1}$ whereas from GW190814, following a statistical framework for potential host galaxies, gives $H_0 = 72.0^{+12}_{-8.2} \mathrm{km} s^{-1} Mpc^{-1}$ [218]. To use events without electromagnetic counterparts for cosmological analysis a statistical approach [159] is used. If a complete catalogue of potential host galaxies exist within the event localization region, their redshift distribution can provide the redshift information needed to infer cosmological parameters from the distance-redshift relation. This method is called the *statistical* or *dark standard siren method*. Using Third LIGO-Virgo-KAGRA Gravitational-Wave Transient Catalogue (GWTC-3) the Hubble parameter gets following values: $H_0 = 68^{+12}_{-8} \mathrm{km} s^{-1} Mpc^{-1}$ when combined with the H_0 from GW170817 and its associated electromagnetic counterpart and $H_0 = 68^{+8}_{-6} \mathrm{km} s^{-1} Mpc^{-1}$ following statistical method which is an improvement of 42% with respect to GWTC-1 and 20% with respect to GWTC-2 results. Fig.5.14 and 5.15 respectively show the two different cases:

Additional standard siren measurements from future GW sources are expected to constrain H_0 with high accuracy. Hence in addition to shed light on H_0 tension between low and high-redshift Universe, a precise measurement of the Hubble constant is of prime importance to untangle nature of DE and hence large scale dynamics of the

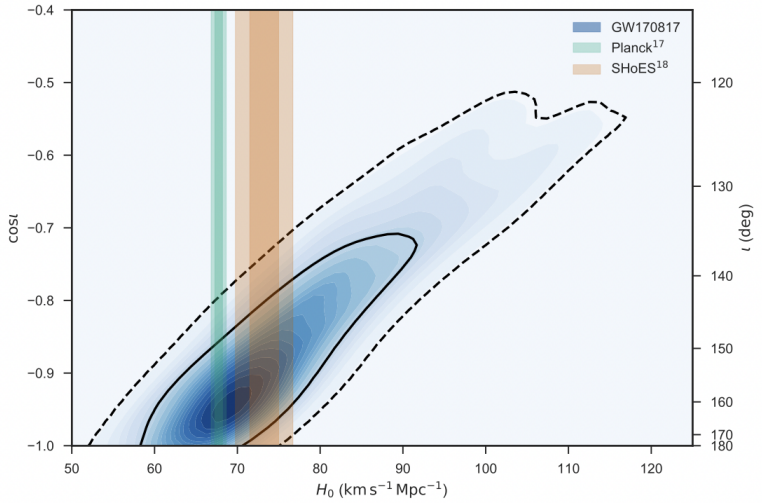

Figure 5.13: H_0 inference and inclination from different measurements. The green and orange band shows the $1-\sigma$ (dark shaded region)and $2-\sigma$ (light shaded region), constraints from CMB and SNe measurements respectively. The blue contours represent the constraints from the GW emission from the BNS merger and its electromagnetic counterpart. The Y axis shows cosine of the inclination angle (angle between the line of sight and the angular momentum of the binary system). Error bars are also displayed from Planck [9] and SH0ES [48].The plot is taken from [122].

Universe.

GWs as probes for Dark Energy and modified gravity

One of the major cosmological conundrums is to understand the nature of Dark Energy which is the omnipresent component within the framework of ΛCDM acting as the driving force for the late time accelerated expansion of the Universe. DE is explained as a cosmic fluid of constant energy density with negative pressure [220]. The existence of late time accelerated expansion of the Universe is confirmed by a series of cosmological observations including SNIa [221, 222], anisotropies in temperature and polarization power spectrum of the CMB [223, 224], Baryon Acoustic Oscillations (BAO) in the Sloan Digital Sky Survey (SDSS) luminous red galaxies [225, 226, 227] and weak lensing [228, 229]. DE is parameterized by its contribution to the total energy density of the Universe and its equation-of-state (EoS) which is a potential probe to check whether DE arises from a time evolving field or is truly a cosmological constant. If the energy density is evolving with time then we enter the realm of dynamical DE sourced by a cosmological scalar field. Due to its extremely low energy density, direct detection of DE is not possible. The two approaches to infer existence of DE is to use luminosity distance-redshift relation and another one is by measuring weak lensing shear power spectrum to infer values for cosmological growth and cosmological distance ratios. *One of the best observational probes of the dark energy is to use standard sirens* because in GWSS method, the estimated value of luminosity distance depends on general relativity whereas considering GW propagation in alternative models of gravity effects GWSS and inference of H_0 would be different than GR due to presence of additional fields. This can significantly affect parameters derived from GW propagation e.g. [230].

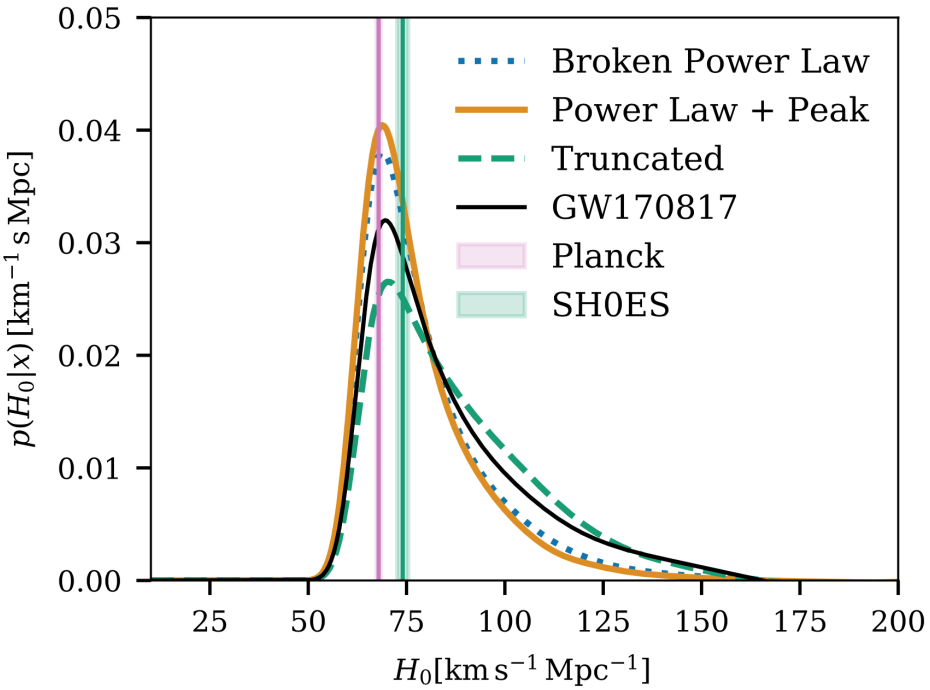

Figure 5.14: Posterior distribution for H_0 obtained by combining the H_0 posteriors from 42 detections and the H_0 posterior inferred from GW170817. The pink and green shaded areas identify the 68% constraints from the CMB anisotropies and in the local Universe from SH0ES respectively. This plot is taken from [219].

GWSS provide a new tool to probe the nature of Dark energy and large scale geometry of the Universe, testing models for gravity and late time acceleration and possibly the discrepancy in the Hubble parameter. *One of the key to test models of gravity is to consider cosmological propagation of GWs which experiences lensing effect due to cosmological matter inhomogeneities. In fact, gravitational lensing modifies GW luminosity distance d_L and hence affects cosmological parameters including H_0.* More generally, cosmological perturbations alter the amplitude of the GW signal producing corrections to the luminosity distance [231] which at the linear level in perturbation theory becomes:

$$\frac{\Delta D_L}{\bar{D}_L} = \Big(1 - \frac{1}{\mathcal{H}\bar{\chi}}\Big)\nu_{||} - \frac{1}{2}\int_0^{\bar{\chi}} d\tilde{\chi}\frac{\bar{\chi}-\tilde{\chi}}{\tilde{\chi}\bar{\chi}}\Delta_\Omega(\Phi+\Psi) + \frac{1}{\mathcal{H}\bar{\chi}}\Phi - \Big(1-\frac{1}{\mathcal{H}\bar{\chi}}\Big) \int_0^{\bar{\chi}} d\tilde{\chi}(\Psi'+\Phi') - (\Phi+\Psi) + \frac{1}{\bar{\chi}}\int_0^{\bar{\chi}} d\tilde{\chi}(\Phi+\Psi) \tag{5.83}$$

where, χ is the comoving distance on real-space from the source to the observer, $\bar{\chi}$ is the comoving distance to the observed redshift in the redshift-GW frame (RGW) and $\tilde{\chi}$ is the comoving distance in the perturbed Poisson gauge with $\Delta_\Omega \equiv \bar{\chi}^2\bar{\nabla}_\perp = \bar{\chi}^2(\bar{\nabla}^2 - \bar{\partial}^2_{||} - 2\bar{\chi}^{-1}\partial_{||}) = (cot\partial_\theta + \partial^2_\theta + \partial_\psi/sin^2\theta)$. In above equation the first r.h.s. term shows the velocity term which is followed by a lensing contribution and final four terms show SW, ISW, volume and Shapiro time delay effects. Although these effects would need very high detection sensitivities to be observer upcoming LISA and ET

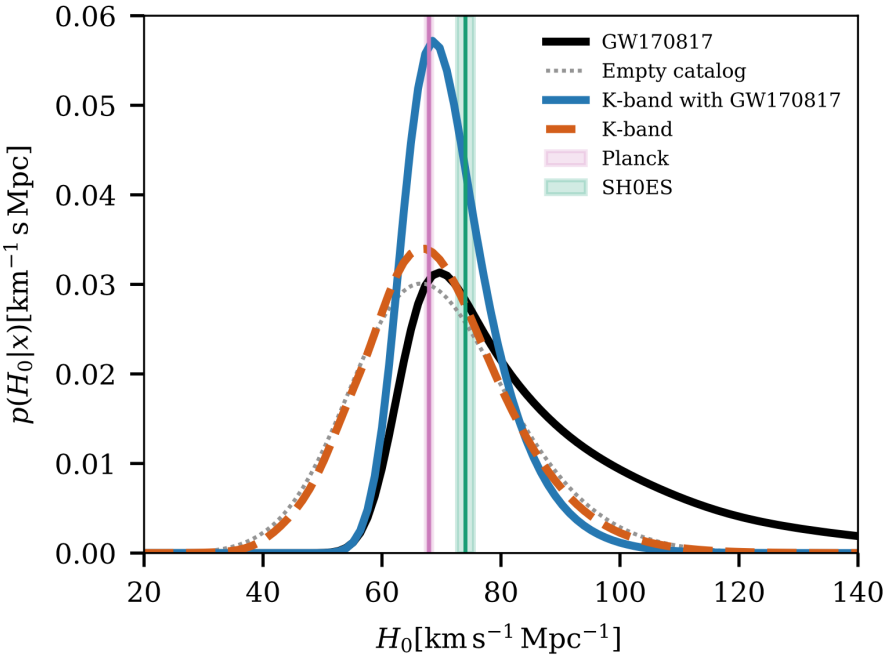

Figure 5.15: Hubble constant posterior for several cases: grey dotted line showing posterior obtained using all dark standard sirens without any galaxy catalogue information and fixing the BBH population model, orange dashed line shows posterior using all dark standard sirens with GLADE+ K-band galaxy catalogue information and fixed population assumptions. Blue solid line shows posterior combining dark standard sirens and GLADE+ K-band catalogue information with GW170817 and its EM counterpart, the pink and green shaded areas identify 68% constraint on H_0 the CMB anisotropies and in the local Universe from SH0ES respectively [219].

space mission would significantly improve constraints on these parameters.

5.7 Primordial GWs

Gravitational waves being weakly interacting and having travelled to use almost being unperturbed by other interactions, it preserves its own relic nature. The CMB is a picture of the Universe at a time about 4×10^5 years after the Big Bang, whereas GWs were produced at the time earlier than 10^{-24} seconds which is the epoch very close to the Big Bang. Such GWs of primordial origin are actually the whispers of the infant Universe emitted due to cosmological interactions such as inflation, cosmic stings and other evolutionary phases of the early Universe. The generation of Stochastic Gravitational Wave Background (SGWB) of *Primordial Gravitational Waves* (PGWs) is a general prediction on any cosmological inflation model [232, 233, 234, 235, 236]. Since PGWs are not expected to be emitted in any non-inflationary model, detecting it would be an undeniable evidence of Inflation. In the standard single-field, slow-roll inflationary scenario, PGWs are characterised by a nearly scale-invariant power spectrum on super horizon scales and the amplitude of the GW signal is usually described by the *tensor-to-scalar ratio* r which is defined as the ratio between the tensor and scalar

power spectrum amplitudes at some pivot scale k_*. Even in the simplest single-field models for inflation, the value of r differs for different models making it crucial to study observational signatures of PGWs in order to probe the valid inflationary framework out of possible plethora of models. Since the energy scale of inflation is directly related to tensor-to-scalar ratio r, detection of PGWs would not only important from the point of view of physics beyond the standard model of particles but would also produce evidence for the quantum gravity phenomena as inflationary tensor fluctuations of the background FLRW metric arise from quantum fluctuations in the gravitational field via a mechanism which is very similar to leading generation of their scalar counterparts. The main observational evidence of inflationary GWB is the "B-mode" i.e. the curl-like pattern in the polarization of the Cosmic Microwave Background (CMB). Here we consider the GWs arising due to first order perturbation on the FLRW background, at this order scalar, vector and tensor modes are independent and evolve governed by uncoupled equations of motion. However this fact does not hold at higher order as at second order suitable combination of scalar modes can give rise to second order vector or tensor perturbations.

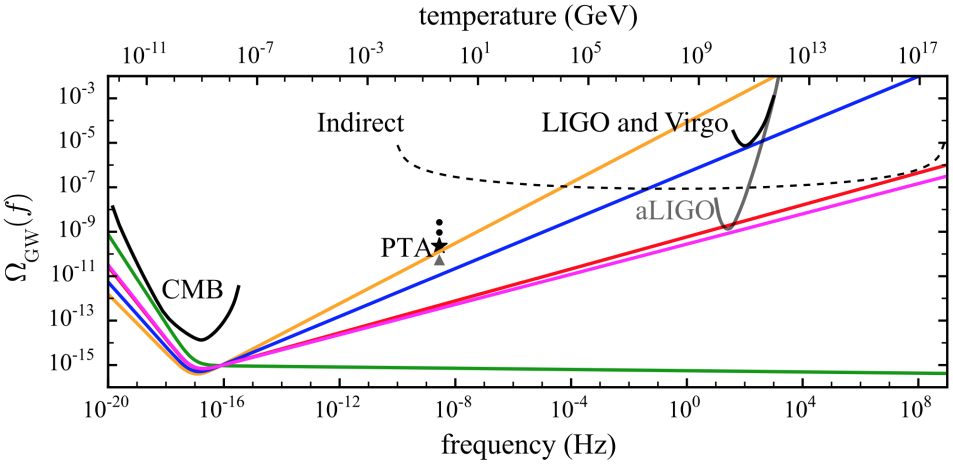

Figure 5.16: Experimental constraints on the energy density $\Omega_{gw}(f)$ of the SGWB emitted from PGW. The black star is the current Parkes Pulsar Timing Array (PPTA) upper limit and all black curves and data points are current 95% confidence upper limits. The grey curve and triangle respectively shows the predicted aLIGO sensitivity and PPTA sensitivity with more than 5 years of data. The indirect GW limits are from CMB temperature and polarization power spectra, lensing, BAOs and BBN. Models predicting a power-law spectrum that intersect with an observational constraint are ruled out at $> 95\%$ confidence. Five predictions for GWB each with $r = 0.11$ and, $n_t = 0.68$ (orange curve), $n_t = 0.54$ (blue curve), $n_t = 0.36$ (red curve), $n_t = 0.34$ (magenta curve) and $n_t = -r/8$ (green curve) corresponding to minimal inflation are shown [237].

5.7.1 GWs from Inflation

The action term for a scalar field minimally coupled to gravity is given by,

$$S = \int d^4x\sqrt{-g}\Big[\frac{1}{2}M_{Pl}^2 R - \frac{1}{2}g^{\mu\nu}\partial_\mu\phi\partial_\nu\phi - V(\phi)\Big] \tag{5.84}$$

where R is the Ricci scalar. Perturbing Eq.(5.84) at first order leads to the *action for tensor perturbations* [238]:

$$S_T^2 = \frac{M_{Pl}^2}{8}\int d^4x a^2(t)\Big[\dot{h}_{ij}\dot{h}_{ij} - \frac{1}{a^2}(\nabla h_{ij})^2\Big] \tag{5.85}$$

where h_{ij} is gauge-invariant object. Varying the action term w.r.t. h_{ij} gives the equation of motion:

$$\nabla^2 h_{ij} - a^2\ddot{h}_{ij} - 3a\dot{a}\dot{h}_{ij} = 0 \tag{5.86}$$

or, varying the action term w.r.t. h_{ij}, we obtain the equation of motion:

$$\boxed{h_{ij}^{''} + 2\mathcal{H}h_{ij}^{'} - \nabla^2 h_{ij} = 0} \tag{5.87}$$

Since h_{ij} is symmetric, traceless and transverse the solution of Eq.(5.86) gives the following form:

$$h_{ij}(\mathbf{x},\tau) = h(\tau)e_{ij}^{(+,\times)}(\mathbf{x}) \tag{5.88}$$

where $e_{ij}^{+,\times}$ is the polarization tensor satisfying the conditions $e_{ij} = e_{ji}, k^i e_{ij} = 0, e_{ii} = 0$ with $+,\times$ the two polarization states [16]. In Fourier space, the polarization tensors e_{ij}^{+} and $e_{ij}^{\times}$ can be expressed by two polarization vectors: $\mathbf{e}_i(\mathbf{k})$ and $\bar{\mathbf{e}}_i(\mathbf{k})$ which are orthogonal to the propagation vector $\mathbf{k}$ [239]:

$$\begin{aligned}\mathbf{e}_{ij}^{+}(\mathbf{k}) &\equiv \frac{1}{\sqrt{2}}[\mathbf{e}_i(k)\mathbf{e}_j(k) - \bar{\mathbf{e}}_i(k)\bar{\mathbf{e}}_j(k)]\\ \mathbf{e}_{ij}^{\times}(\mathbf{k}) &\equiv \frac{1}{\sqrt{2}}[\mathbf{e}_i(k)\bar{\mathbf{e}}_j(k) - \bar{\mathbf{e}}_i(k)\mathbf{e}_j(k)]\end{aligned} \tag{5.89}$$

Eq.(5.88) represents the fact that tensor modes are left with two physical degrees of freedom: starting from six of the symmetric tensor h_{ij}, four constraints are given by the requirement of being traceless and transverse. The most general solution of Eq.(5.87) is:

$$h_{ij}(\mathbf{x},\tau) = \sum_{\lambda=(+,\times)} h^{(\lambda)}(\tau)e_{ij}^{\lambda}(\mathbf{x}) \tag{5.90}$$

To get solution of the equation of motion, it is useful to perform the transformation which gives the shape of $h(\tau)$ from Eq.(5.87):

$$v_{ij} \equiv \frac{aM_{Pl}}{\sqrt{2}}h_{ij} \tag{5.91}$$

In terms of v_{ij}, the solution of Eq.(5.85) becomes:

$$S_T^2 = \frac{M_{Pl}^2}{8}\int d^4x\Big[v_{ij}'v_{ij}' - (\nabla v_{ij})^2 + \frac{a''}{a}v_{ij}v_{ij}\Big] \tag{5.92}$$

which can be interpreted as the action for two scalar fields in Minkowski spacetime with effective mass squared equal to a''/a. Moving to Fourier space,

$$v_{ij}(\mathbf{x},t) = \int \frac{d^3\mathbf{k}}{(2\pi)^3} \sum_{\lambda=(+,\times)} v^{\lambda}_{\mathbf{k}}(t) e^{\lambda}_{ij}(k) e^{i(\mathbf{k}\cdot\mathbf{x})} = \int \frac{d^3\mathbf{k}}{(2\pi)^3} e^{i\mathbf{k}\cdot X} \left[v^{+}_{\mathbf{k}}(\tau) e^{+}_{ij}(\mathbf{k}) + v^{\times}_{\mathbf{k}}(\tau) e^{\times}_{ij}(\mathbf{k}) \right] \tag{5.93}$$

where, $v_{\mathbf{k}}$ is the Fourier transform of the scalar amplitude and from Eq.(5.93), the equation of motion for each mode $v_{\mathbf{k}}$ becomes:

$$\boxed{v^{\lambda\prime\prime}_{\mathbf{k}} + \left(k^2 - \frac{a''}{a}\right) v^{\lambda}_{\mathbf{k}} = 0} \tag{5.94}$$

which is the wave equation in Fourier space. To analyse the solutions of this equation, we consider two cases: (i) when $\frac{a''}{a} \ll k^2$, then by ignoring the second term in the parenthesis, the equation for $v_{\mathbf{k}}$ becomes that of a free harmonic oscillator. So the tensor perturbations h_{ij} oscillate with a damping factor $1/a$ with the solution:

$$v_{\mathbf{k}}(\tau) = A e^{i\mathbf{k}\tau} \tag{5.95}$$

which means that the amplitude of the modes of the original field h_{ij} decrease in time with the inverse of the scale factor due to expansion of the Universe. (ii) Consider the second term being negligible compared to the third term: $k^2 \ll a''/a$, in this case the two possible solutions for Eq.(5.87) are:

$$v_{\mathbf{k}}(\tau) \propto a, \quad \textit{and} \quad v_{\mathbf{k}}(\tau) \propto 1/a^2 \tag{5.96}$$

which respectively corresponds to $h \propto const.$ and decrease in time solution respectively corresponding to a *super-horizon regime*.

Inflation stretches tensor perturbation wavelengths to the super-horizon scales almost freezing their amplitudes. During the subsequent radiation and matter dominated eras, tensor perturbation wavelengths re-enter the horizon sequentially. Since at this time the decaying solution is almost vanishing, it is actually almost scale invariant power spectrum at the time of first horizon crossing which occurred during inflation re-entering the causally connected space. The resulting spectrum has a f^{n_T} dependency where n_T is a tensor spectral index with a small absolute value, of the order of about 10^{-3} [240, 241]. Then, modes inside the horizon stars oscillating with the amplitude damped by a factor $1/a$ which during radiation and matter dominance follows evolution of scale factor as $a \propto \tau$ and $a \propto \tau^2$ respectively. In this case Eq.(5.96) becomes a Bessel equation with the following solutions in terms of h_{ij} modes respectively:

$$h_k(\tau) = h_{k,i} j_0(k,\tau), \quad \textit{and} \quad h_k(\tau) = h_{k,i}\left(\frac{3 j_1((k,\tau))}{k,\tau}\right) \tag{5.97}$$

where $h_{k,i}$ is the amplitude at horizon crossing and j_0 and j_1 are Bessel functions. The dependence of h_{ij} modes on k shows that the tensor perturbations start oscillating with a damping factor greater than for higher frequency waves.

5.7.2 Energy density of GWs

Within weak field limit, GWs can be described as spacetime ripples propagating at the speed of light on a fixed background. The vacuum field equations become $G_{\mu\nu} = 0$ which is equivalent to $R_{\mu\nu} = 0$. Expressing Ricci tensor as a sum of a background term and perturbative terms up to second order:

$$R_{\mu\nu} = \bar{R}_{\mu\nu} + R^1_{\mu\nu}(h) + R^2_{\mu\nu}(h) + \mathcal{O}(h^3) \tag{5.98}$$

where $\bar{R}_{\mu\nu}$ is the background term and the effects of presence of GW on $\bar{R}_{\mu\nu}$ is described by a stress-energy tensor $t_{\mu\nu}$. $R_{\mu\nu} = 0$ can also be represented as a sum of smooth contribution and the one including the fluctuating part. The background term $\bar{R}_{\mu\nu}$ varies only on large scale and hence we are interested in the equation for the smooth contribution. The equation for the smooth part of the vacuum equation reads [16, 125]:

$$\bar{R}_{\mu\nu} + \langle R^2_{\mu\nu} \rangle = 0 \tag{5.99}$$

where, $\langle ... \rangle$ indicates the average over several wavelengths. Similarly the Einstein equations in vacuum becomes:

$$\bar{G}_{\mu\nu} = \bar{R}_{\mu\nu} - \frac{1}{2}\bar{R}\bar{g}_{\mu\nu} = \langle R^2_{\mu\nu} \rangle - \frac{1}{2}\bar{g}_{\mu\nu}\langle R^{(2)} \rangle \tag{5.100}$$

The terms on the RHS shows the effect of GW on the background metric. In terms of the tensor perturbation of the metric this becomes [16]:

$$t_{\mu\nu} = \frac{1}{32\pi G}\langle \partial_\mu h_{ij} \partial_\nu h^{ij} \rangle \tag{5.101}$$

and the energy density on a FLRW background:

$$\boxed{\rho_{gw} = \frac{1}{32\pi G a^2}\langle h'_{ij}(\mathbf{x}, \tau) h'^{ij}(\mathbf{x}, \tau) \rangle} \tag{5.102}$$

5.7.3 GWs production during reheating

The production of gravitational radiation during reheating was proposed by [242]. At the end of inflation, the field which has driven the accelerated expansion starts oscillating around the minimum of its potential. This results into elementary particle production which interacts with each other, eventually leading to a state of thermal equilibrium. In the first stage of the evolution, inflaton field oscillations can be described by perturbation theory, considering the oscillating field as a decaying collection of particles [35, 243]. However if oscillations are large and coherent, they lead to a non-perturbative process. In this case the inflaton energy is moved to a coupled energy sector. This rapid mechanism is called *parametric resonance* [38, 244, 245] in which case perturbative description is not enough. This stage is also known as *preheating* after which phase the produced particles are not in thermal equilibrium. Preheating ends when energy density of the created particles becomes comparable with the energy density of the oscillating field.

When PGWs enter the horizon after the accelerated expansion phase, they start evolving with their amplitude damped by a factor inversely proportional to the scale

factor so that the present GW spectrum reflects the expansion history of the Universe [246]. Detecting PGWs would not only be able to constrain possible models of inflation but it would also untangle early phases including thermal evolution and reheating.

5.7.4 Influence of PGWs on different observables

Inflationary GWs leave undeniable effects on all physical observables along the history of the Universe. We name here a few:

- Influence on CMB: Tensor perturbations present at the time of recombination and at the photon decoupling leads to temperature and polarization anisotropies in the photon distribution [81, 10, 82, 4]. Therefore, CMB features carry information about the GWB filling the space at the time of recombination. As small scale tensor perturbations are damped by the cosmic expansion, GWs contribute to the temperature angular power spectrum only for $l \leq 60$. However temperature anisotropies due to scalar perturbations largely dominate due to GWs. PGWs also alters the time of matter-radiation equality in the CMB power spectra [247, 248]. Also the CMB energy spectrum includes the imprint of possible presence of GWs, more precisely the integrated GW energy density in the frequency range $\simeq 10^{-12} - 10^{-9}$Hz leads to spectral distortions in the CMB energy spectrum [249, 250].

- Influence on LSS: Primordial Gravitational Wave Background (PGWB) modifies the power spectrum of curvature perturbations, leading to a non-vanishing off-diagonal terms in the 2PCF of primordial curvature perturbations. Presence of GWs when matter clusters formed large scale structures lead to a tidal effect due to long wavelength modes. Tensor modes also induce lensing effects which lead to distortions of galaxy shapes with correlation between the ellipticity of galaxies and projection effect [251, 252, 253, 254, 255, 256, 257]. This kind of observations are particularly sensitive to frequencies $\simeq 10^{-9} - 10^{-7}$Hz [258].

- Influence on pulsar signals: GWB affects light propagation, the distortion effect of light emitted from nearby astrophysical object would be small. However ultra-stable millisecond pulsars are characterized by extremely precise signal modulation. If there exist GWB, a non-vanishing and significant correlation between perturbations of pulsar signals is expected. Thanks to pulsar timing array (PTA) system, signals coming from a set of astrophysical objects can be collected and correlated. In such a way, a GWB of frequency $\simeq 10^{-8}$Hz can be captured [258, 259].

GWs and neutrino free-streaming The GW spectral energy density is affected by a damping effect due to the decoupling of particles such as neutrinos and by change in the number of relativistic degrees of freedom [246]. Particle free streaming gives rise to anisotropic stress affecting the GW propagation equation and neutrino free streaming too affect the first and second order of the anisotropic stress tensor. The effect of a first order term is a damping of primordial gravitational wave amplitude, while the second order contribution in addition to providing a damping counterpart acts as a source for second-order GW [260, 261, 262, 246, 263, 264, 265, 266, 267, 268, 269, 270, 239].

Chapter 6

Stochastic Gravitational Wave Background

> The Universe is full of magical things patiently waiting for our wits to grow sharper.
>
> *Eden Phillpotts*

6.1 Introduction

Astrophysical observations infer information about the sources by detection of the radiation they emit- either as a single event or as stochastic background generated by superposition of all signals emitted from resolved and unresolved sources. Examples of the latter include: (i) the Cosmic Microwave Background (CMB) i.e. the electromagnetic radiation emitted at the last scattering surface, (ii) the extragalactic background formed by light emitted by all stellar objects, galaxies and active galactic nuclei, (iii) the relic cosmic neutrino background ($C\nu B$) and, (iv) the omnipresent background of Gravitational Waves (GWs) emitted by sources of astrophysical and cosmological origin. Analysis of such backgrounds provide information on the dynamics of the Universe and on the distribution and evolution of the large scale structure. The CMB detection has shown inhomogeneities in the primordial Universe (primary anisotropies) and in the recent Universe (secondary anisotropies); analogously the detection of the Gravitational Wave Background (GWB) upon obtaining enough detector sensitivity would be a remarkable success to attempt fathoming many mysteries of the primordial and recent Universe which remains vague by means of electromagnetic radiation alone. For instance, GW emission is expected from the very first moments after the Big Bang, detection of such PGWs and their background will provide a unique way to probe early evolutionary phases of the Universe. In addition to such PGWs, an *Astrophysical Gravitational Wave Background (AGWB)* must result from the superposition of all faint and distant sources that have emitted GWs since the beginning of their stellar activity, such objects include Compact Binary Coalescence (CBCs) such as BBH, BNS, BHNS and SNe, Pulsars and burst sources like GRBs. The AGWB, which is the central point of investigation of this thesis, is not only a noise while detecting a single GW event, but

actually is a treasure trove hiding astrophysical aspects (e.g. elucidating star formation history and evolution of astrophysical parameters, mass asymmetry of neutron stars, the equation of state, distribution population etc.) which upon subtracted from the signal could bring us information of cosmological origin too.

Generation of Stochastic Gravitational Wave Background (SGWB) is a fundamental prediction of any inflationary model. This makes it crucial to detect and analyse SGWB in order to verify models for the Early Universe. The detection of SGWB of either cosmological or astrophysical origin would be a treasure trove of many information and also a major scientific goal for the present and upcoming Earth-based and space-based missions. Due to weak coupling of the gravitational interaction, cosmological GWs are expected to decouple from matter in the early Universe much earlier than any other form of radiation, the detection of such a primordial GWB by current ground based detectors [271, 272, 273], proposed space-based detectors [274], or a pulsar timing array [275, 276] would give us the picture of the Universe soon after the Big Bang [277, 234, 278, 279] allowing us to probe physics of the lowest frequency and scale highest energy which would not be achievable by terrestrial experiments [276].

Recent years have witnessed path-breaking series of detection of GWs of astrophysical origin thanks to the Laser Interferometer Gravitational-Wave Observatory (LIGO) and Virgo interferometers. The first reported emission was from a stellar mass Binary Black Hole (BBH) at redshift $z \approx 0.1$ - GW150914 [1] followed by two observations of similar BBH systems GW151226 [280] and GW170104 [281] and from a BNS merger GW170817 [151]. Armed with next generation Earth-based detectors, we will be able to detect GWs signals with very high accuracy in ranges of low frequency and higher redshift Universe. Each of these aforementioned detections are associated with individual loud source coalescence events but there lies a large amount of quite compact binaries which are too far and faint to be detected individually. Signals from these weak, independent and unresolved sources superimpose to create a *Stochastic Gravitational Wave Background* (SGWB) which is hopefully expected to be detected by advanced LIGO/VIRGO after reaching years of design sensitivity and by the forthcoming Laser Interferometer Space Antenna (LISA) and the Einstein Telescope (ET). Different Astrophysical sources include coalescence of compact binaries [282, 283, 284, 285, 286, 287, 288, 289, 290, 291, 292], neutron star formation [293], rotating neutron stars [294, 295, 296, 297, 298, 299, 300], magnetars [301, 302, 303, 304, 305, 306], supernovae [287, 307, 308, 309, 310], first stars [311], white dwarf [312] or depleting boson clouds around black holes [313, 314, 315, 316, 317, 318]. Whereas at much higher redshifts, the cosmological sources of SGWB include GWs from inflationary mechanism [278, 319, 233, 234, 320, 321, 322, 323, 324, 325, 326], first order phase transition [327, 328, 329, 330, 331], strings [332, 333, 334], primordial black hole mergers [335, 336, 337, 338], primordial magnetic turbulence or pre Big Bang scenarios [339, 340, 341] as broadly discussed in [342]. Such astrophysical and cosmological sources create the Astrophysical Gravitational Wave Background (AGWB) and the Cosmological Gravitational Wave Background (CGWB) respectively. The nature of the AGWB differ from the CGWB which is expected to be roughly stationary, unpolarized, statistically Gaussian and isotropic, whereas the AGWB has many inhomogeneous sources leading to anisotropies and hence affects GW propagation which the central point of study of this thesis.

6.2 Characterising the SGWB

In the most broader way, a GW signal detected by the detector can be decomposed into resolved signal and the stochastic signal. The stochastic signal itself can be decomposed into astrophysical and cosmological part which results into seemingly random signal with a waveform as shown below in Fig.6.1:

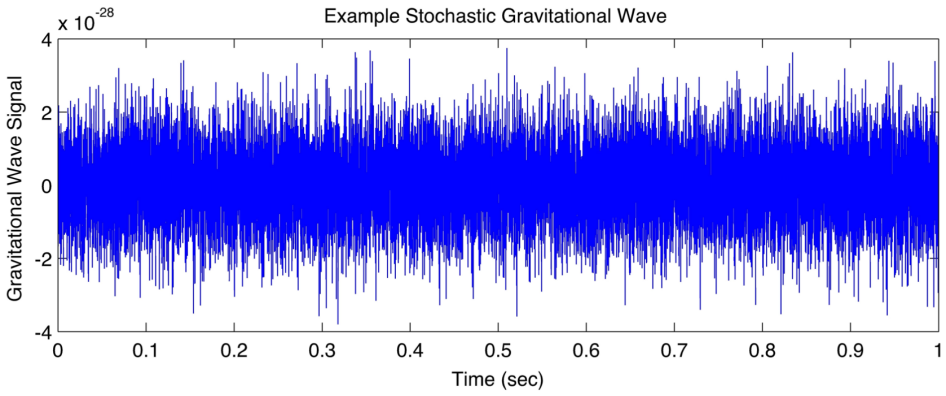

Figure 6.1: An example of waveform of a stochastic gravitational wave signal, image taken from "LIGO Science"- https://www.ligo.org/science/GW-Stochastic.php.

Since GWs decouple much earlier than other radiation, it is expected that cosmological background would carry the earliest information accessible about the infant Universe [240]. Regardless production mechanism of a SGWB, the signal is usually described in terms of the dimensionless quantity known as *gravitational wave spectrum*,

$$\boxed{\Omega_{GW}(f) = \frac{f}{\rho_c}\frac{d\rho_{gw}}{df}} \tag{6.1}$$

where, $d\rho_{gw}$ is the energy density of gravitational radiation contained in the frequency range f to $f + df$ and ρ_c is the critical energy density of the Universe [343]. Eq.(6.1) describes the angular average (i.e. monopole) of the SGWB signal or the so-called *energy density* in GW per logarithmic frequency interval in units of the critical density of the Universe. The total energy density in GWs normalized by critical energy density is,

$$\Omega_{GW} = \int_{f_0}^{f_{max}} d(\ln f)\Omega_{GW}(f) \tag{6.2}$$

where f_{max} is the maximum cut-off frequency. The dimensionless *characteristic strain amplitude* $h_c(f)$ is related to the fractional GW energy density spectrum by,

$$h_c(f) \equiv \sqrt{f\Omega_{GW}(f)} \tag{6.3}$$

The GW characteristic strain is expected to have a power law form,

$$h_c(f) = A_\alpha \Big(\frac{f}{f_{ref}}\Big)^\alpha \tag{6.4}$$

where α denotes the spectral index and f_{ref} is generally set to 1/yr. In terms of Ω_{GW}, this equation becomes:

$$\Omega_{GW}(f) = \Omega_\beta \Big(\frac{f}{f_{ref}}\Big)^\beta \tag{6.5}$$

where,

$$\Omega_\beta = \frac{2\pi^2}{3H_0^2} f_{ref}^2 A_\alpha^2 \tag{6.6}$$

and, $\beta = 2\alpha + 2$.

The *intensity of the stochastic background* can be expressed in terms of the number of gravitons per cell of the phase space n_f with $f = |\mathbf{k}|/(2\pi)$. For an isotropic SGWB,

$$\rho_{GW} = 2 \int \frac{d^3k}{(2\pi)^3} (k n_k) \tag{6.7}$$

thus, the energy density becomes,

$$\Omega_{GW}(f) = \frac{1}{\rho_c} 16\pi^2 n_f f^4 \tag{6.8}$$

where, $n_f = |\beta_f|^2$ is the Bogoliubov coefficient [124]. As a SGWB signal is expected to be much weaker than detector noise and assuming detector noise and the signal both to be Gaussian random variables, it is not feasible to distinguish them with the help of a single detector, hence making cross-correlation of the strain data from a pair or from several pairs of detectors is the optimal method. The sensitivity of cross-correlation analyses among other things depends on the separation between two detectors, the smaller the separation, the better becomes the sensitivity. This makes a co-located pair of detectors more sensitive to GWB than a non-co-located pair [274]. However it is worthy to note that co-located detectors are also expected to suffer from correlated noise signal from instrumental and environmental effects that could contaminate the measurement of the background, hence the methods to identify and mitigate the effects of correlated noise are important to achieve the potential increase in sensitivity of co-located detectors. Here, we briefly mention the simple analysis statistics which includes different quantities involved to distinguish noise and signal in the cross-correlation method.

6.3 Sources of SGWB

Based on different bands in gravitational spectrum, sources of SGWB can be classified as:

- ultra-low frequency with $10^{-18}\text{Hz} \leq f \leq 10^{-13}\text{Hz}$,
- very low frequency with $10^{-9}\text{Hz} \leq f \leq 10^{-7}\text{Hz}$,
- low frequency with $10^{-5}\text{Hz} \leq f \leq 1\text{Hz}$ and,
- high frequency with $1\text{Hz} \leq f \leq 10^{4}\text{Hz}$

In the ultra-low frequency band, gravitational waves generated by inflation are expected to be detected. An order of magnitude for the frequency associated to a GW source of mass M and typical dimension R can be provided by [123],

$$f \sim \frac{1}{2\pi}\sqrt{\frac{GM}{R^3}} \tag{6.9}$$

Here, R could be the characteristic length of the GW emitting body or the distance between the centers of two masses in a binary system. Eq.(6.9) allows us to have a rough estimate of typical source mass in each frequency bands.

Sources of SGWB can be categorized as astrophysical and cosmological [124] based on their progenitors: the astrophysical stochastic background generated by the incoherent superposition of GWs by large population of astrophysical sources that can be resolved individually and the cosmological/primordial stochastic background generated by GW emission in the early evolutionary stages. Supermassive black holes (SMBHs) with masses $\geq 10^6 M_\odot$ reside at the center of every moderate to massive galaxy [344]. Such SMBHs should be powerhouse to produce considerable GWs in frequency band of $\sim 10^{-9} - 10^{-7}$Hz [136, 125]. In addition to the astrophysical sources described above, cataclysmic, transient events such as Gamma-ray bursts (GRBs) are one of the most energetic astrophysical events which are transient flashes of γray radiation. These GRBs are broadly classified as *long* or *short* GRBs based on their duration and spectral hardness. *Long GRBs* have a duration $\sim$ 2s and a softer spectrum with their origin related to rapidly rotating massive stars and the *short GRBs* have a duration of less than $\sim$ 2s and a harder spectrum originated from coalescing BNS or NS-BH systems [150]. In addition to these continuous and transient signals of GWs, *periodic GWs* could be produced by a nearby spinning and slightly non-axisymmetric isolated neutron star in our galaxy [345]. Additionally, pulsars having mass or mass-current asymmetry around its rotation axis are also potential sources emitting GWs. The characteristic difference between AGWB and CGWB is that AGWB will most likely be anisotropic following spatial distribution of sources whereas CGWB like CMB is expected to be predominantly isotropic having relatively monotonic power spectra compared to AGWB with power peaked at particular frequencies [346].

So far, GW signals reported by LIGO-VIRGO are emitted from CBCs, however isolated compact objects may also emit detectable GWs even though being much weaker than CBCs [128]. Such sources for example include highly energised neutron stars and supernovae. Magnetars are highly magnetized isolated neutron stars [347, 348] and give off short bursts of γrays whose origin is yet unknown. The SGWB is expected to be dominated by compact binaries at redshifts inaccessible to direct searches for GW events [349].

On the cosmological side, the CGWB includes GWB by phase transitions in the Early Universe [350, 333] and Primordial GW Background (PGWB) due to inflation [351, 352]. During the epoch of inflation, tensor modes are inflated to super-horizon scales where their comoving amplitude becomes constant. Once they reenter the horizon, during the deceleration phase of the expansion, these modes appear as squeezed GWs. The squeezing results in phase correlations which are possible only in modes that have re-entered the horizon. These phase correlation are a distinguishing feature of a primordial inflationary background, although on observational scales such correlations will be destroyed by sub-horizon metric perturbations. Numerical estimation of SGWB generated by CDM halos during fully non-linear stage of their evolution is

presented by [353]. Such GW signals are expected to be comparable or larger than the signal expected from the early Universe in the inflationary scenario. Astrophysical and cosmological information is contaminated in both- the average (monopole) amplitude Ω_{GW} and anisotropy of any background. The amplitude of the background is an integrated measure of the underlying population which probes very different limits of the distribution than the collection of single, high SNR detections. This information can either be used as an aide to the source separation in conjunction with spectral resolution or as a *tracer of astrophysical or cosmological structure* [354]. In principle, the different backgrounds can be distinguished by their different frequency scalings and statistical properties [355].

In order to perform a detection and characterization of any cosmological backgrounds, the subtraction of galactic extra-galactic foregrounds/backgrounds must be performed with higher accuracy which can be done by cross-correlating data sets in frequency/time domains. For example, while cosmological backgrounds are expected to be stationary, the foregrounds due to unresolved white dwarf binaries in the galaxies is expected to present some yearly modulation which can be used for component separation [356]. Analogously, since the spectral shapes of background arising from different sources are not expected to match, different signals can be disentangled by accurately modelling the different components. In very small frequency range, different signals may appear to degenerate, this degeneracy is broken eventually for sufficiently large intervals. Therefore the ideal configuration maximizes the astrometric resolution in the given frequency range and the angular resolution so that the unresolved signal can also be masked or cross-correlated with other probes efficiently. This can be achieved with *an optimized configuration of detectors whose signal can be cross-correlated over large distances*. An idealized figure-of-merit for the angular resolution can be obtained by integrating the contribution of each frequency to spherical multipoles on the sky. The plan waves at each frequency can be expanded in spherical Bessel functions j_l to obtain an angular response,

$$\mathcal{A}_l = \int_{f_{min}}^{f_{max}} df w(f) j_l\Big(2\pi \frac{fb}{c}\Big) \tag{6.10}$$

where b is the length of the baseline formed by the cross-correlation of detector signals and $w(f)$ is the weighting function determined by the high frequency noise of the detectors. *This figure of merit is idealized and the actual response would be a convolution of full spherical mode expansion with the detector response function and sky modes given a particular phase coverage on the sky* [354]. In Fig.6.2, the normalized response function for four different configurations: single LISA, 2 LISA-type detectors with 0.7AU separation, 2 decihertz detectors with 0.7AU separation and 2 decihertz detectors with 2AU separation are shown. The dominant contribution to the angular resolution is given by the longest cross-correlation baseline length. For a single LISA this is the same order of magnitude as the individual arm lengths. However, having two LISA-type detectors increases the angular resolution. The optical configuration consists of two detectors separated by a distance of the order of an AU with sensitivity peaking in the decihertz range, which would have an angular resolution for stochastic backgrounds around a degree. This resolution would greatly facilitate the separation of galactic and extra-galactic stochastic signals and can search for statistical and cosmological effects by cross-correlating with different large scale structure [357, 358, 359, 360].

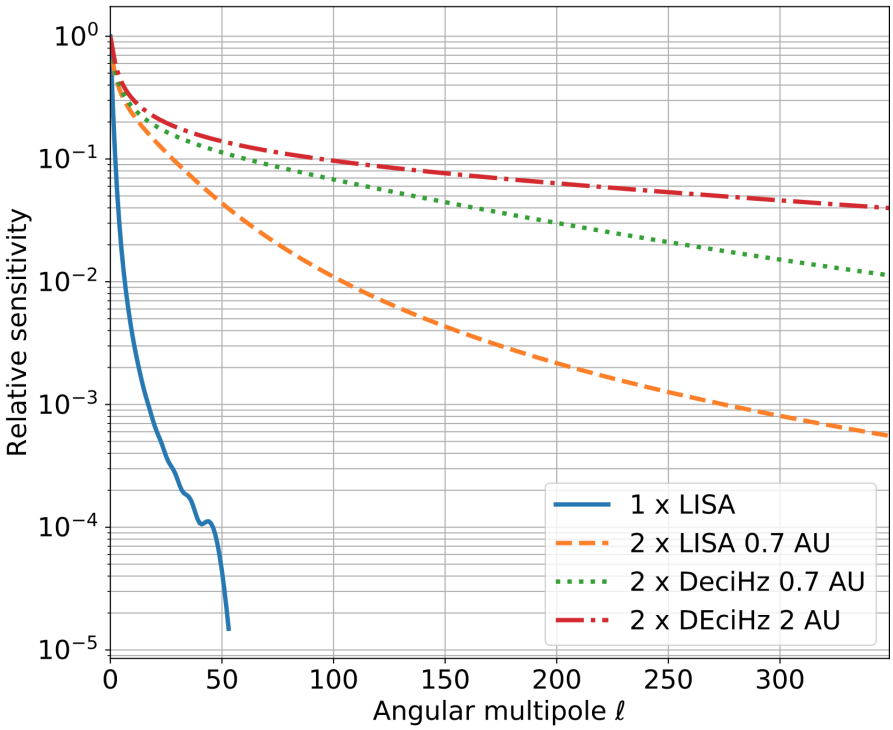

Figure 6.2: Idealised angular resolution for different detector configurations: LISA, 2 LISA-type detectors with 0.7AU separation, 2 decihertz detectors with 0.7AU separation and 2 decihertz detectors with 2AU separation [354].

A GW telescope with a ∼AU effective baseline is the optimal instrument for resolving the angular features of the stochastic background [354].

6.3.1 Astrophysical SGWB

The Astrophysical Stochastic Gravitational Wave Background (AGWB) is generated by superposition/overlapping of astrophysical sources discussed in section 5.2. The concept of overlapping sources can be defined in terms of *duty cycle* DC. For a given astrophysical source, the DC measures the average fraction of the observation period T for which the signal from the given type of source is expected to be present. For a given source, DC=1 implies that a continuous signal emanating from one source is present over the whole measurement period. While a value DC=0.5 implies that the signal is on average present only about 50% of the time. The duty cycle is defined as:

$$DC = \frac{1}{T}\int_0^{z_c} (1+z)\tau R(z) dz \tag{6.11}$$

where, $R(z)$ is the event rate observed in the Earth reference frame as a function of redshift. The integration limit z_c corresponds to the epoch when the events of the given type first started, and the characteristic evolution time τ is the time dilated to $(1+z)\tau$ thanks to expansion of the Universe. Using the definition above, the astrophysical signal recorded by the detector itself can be decomposed further into a contribution from continuous and transient source. For the source emitting continuous

signal, a duty cycle is much greater than 1 ($DC >> 1$) and for the transient signals, a duty cycle is lower than 1 ($DC < 1$). The contribution from a transient signal can be decomposed into a *shot* transient signal when the DC is much lower than 1 ($DC << 1$) and a *popcorn* transient signal when the DC is close to 1, i.e. $DC \sim 1$. Fig.6.3 shows stochastic shot and popcorn signal:

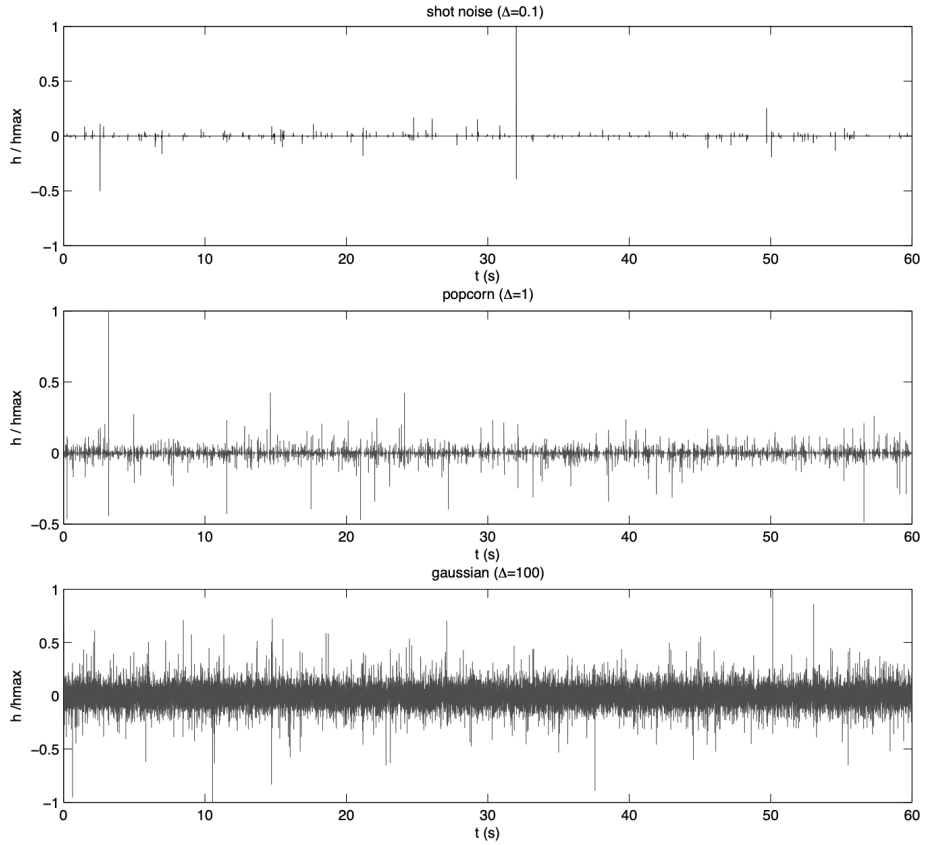

Figure 6.3: Time series representation corresponding to shot noise, popcorn and Gaussian regimes [355].

AGWB would likely be the loudest stochastic background in the observing band of LIGO and Virgo from 10 Hz up to 1000 Hz. Such sources include BBH, BNS, supernovae and rapidly rotating NS and magnetars which due to non-axisymmetric spinning motions release a considerable amount of GWs [361]. GWs would be emitted if neutron stars are not perfectly spherical- asymmetric distortion which might have been resulted due to toroidal magnetic fields within the neutron star [362]. Another source of GW emission from NS would be the presence of a slight mountain on the surface of the neutron star. This effect could happen due to cracking of the crusts through the thermal effects [361]. With such asymmetries of defects, gravitational waves would be emitted at twice the rotation frequency of the neutron star.

6.3.2 Cosmic strings as GW source

In the earliest phases, the Universe may have undergone various symmetry breaking phases due to phase transitions. This may occur at the quantum choromodynam-

ics (QCD) scale (150 Mev) and electroweak scale (100 Gev) or even around grand unification scale [240]. The standard model predicts a smooth transition but its supersymmetric extensions predict a transition from a metastable phase (*false vacuum*) to the state of broken symmetry (*true vacuum*). This transition may have generated a considerable amount of GWs when bubbles of the new phase are nucleated, grow and collide at a very high velocities as they were in abundance. In addition to such GWs emitted due to phase transitions, *strings* are one of the potent sources of generation of gravitational waves in the primordial Universe.

Cosmic strings are topological defects which can be formed in the GUT scale phase transition in the early Universe [363], more precisely, when a $U(1)$ symmetry is broken [364] in multiple casually disconnected regions of spacetime, topological one-dimensional defects are expected to be produced [365]. They were first introduced by Kibble [363]. It is generally assumed that when strings collide, they intercommute by exchanging partners and reconnecting after collision. As a results, closed loops are formed when string self-intersects or two curved strings collide. Loops smaller than the horizon decouple from cosmological evolution and oscillate under their own tension resulting into production of GWs. These oscillating strings have mainly two features-*cusps*- the points where the strings move at the speed of light [366] and *kinks* - discontinuities in the tangent vectors due to intersection of strings. All loops will contain kinks either due to intercommutaion or due to remnant of past intersections. Such cusps and kinks generate GW bursts [333, 367]. As a consequence of such bursts, the GW background emitted by string network is highly non-Gaussian. Other than these subhorizon cosmic strings (so-called "loops"), super-horizon strings (the so-called "infinite strings") emit GWs due to string intercommutations [368]. The dominant contribution is generally produced by superposition of radiation from many subhorizon loops along each line of sight. Their cosmological effects include lensing of distant galaxies [369, 370, 371], producing high energy cosmic rays [372], anisotropies in the CMB [373, 374] and production of GWs [375, 376]. Cosmic strings can give rise to powerful bursts of GWs produced by cusps offering a promising observational signature. These cosmic strings can also produce little (a few percent of the overall) contribution to the observed CMB anisotropies [377, 378, 379].

Cosmic strings are characterized by a single dimensional scale- the *mass per unit length* which is denoted by μ. The string length is defined as the energy of the loop divided by μ. After formation, the network of strings quickly evolves towards an attractor solution called the *scaling regime* where the energy density in long strings/infinite strings remains a constant fraction of the total background energy density [380]. This is achieved by intercommutations and self-interactions of the strings leading to the production of small loops which then decay by emitting gravitational radiation. Cosmic strings are stable against all types of decay except GW emission and hence prove an excellent laboratory to quest for physics beyond standard model for particle physics and the early Universe. Observational constraints on cosmic string models are generally given as bounds on the string tension G_μ where G is the Newton's constant and μ denotes the mass per unit length. The main mechanism for a network of Nambu-Goto (NG) cosmic strings to lose energy is through the production of loops and the subsequent emission of GWs. A promising way to detect cosmic strings and superstrings is searching for GW emission from loops [381, 382, 383] where cosmic strings are produced in string theory motivated cosmological models and grow to cosmic scales [384, 385, 386, 364]. Since cosmic strings are one of the most promising ways to probe

physics beyond the standard model of particles, looking for the background generated by cosmic strings is one of the prime goals of Laser Interferometer Space Antenna (LISA) and other experiments. When two string segments meet, they intercommute or exchange segments with a probability p. The strings oscillates, radiates gravitationally and decays. cosmic strings can form cusps, points along the string with large Lorentz boosts which produces powerful bursts of GWs [333]. The GW emission by cusps depends on the loop size written as a fraction of the horizon at the time of formation $l = \alpha t$ where t is the cosmic time. Two main parameters- ϵ (describing the typical size of the closed loop produced in the string network) and G_μ determine the lowest frequency at a given redshift at which the string loop can emit GWs and hence determine the shape and amplitude of the GW spectrum.

In addition to cosmic strings, *super strings* may have been produced in string theory inspired by inflationary scenarios [387, 388] in M-theory models. The main features which differentiate super strings from cosmic strings are: (i) super strings can reconnect when they meet with probabilities p that can be less than one and, (2)more than one kind of string can be formed [241] (e.g. superstrings can form Y-junctions where 3 different strings meet).

Till now no evidence of GW emission from cosmic string is found but thanks to LIGO-Virgo [381], Advanced LIGO [389] and aLIGO-Virgo [390] data searches, a successful upper limits on the string tension G_μ could be placed. The ability of the LISA to detect a stochastic gravitational wave background produced by cosmic strings and the string tension G_μ in the presence of instrument noise, an astrophysical background from CBCs and the galactic foregrounds from white dwarf binaries has been investigated recently [391]. Considering the astrophysical background and a galactic foreground, a cosmic string tension in the $G_\mu \approx 10^{-16}$ to $G_\mu \approx 10^{-15}$ range or bigger could be measured by LISA with the galactic foreground affecting this limit more than the astrophysical background. A cosmic string stochastic GWB search by LISA in the presence of detector noise is presented by [392]. The ability to conduct parameter estimation and resolve the value of cosmic string tension begin at around $G_\mu \approx 10^{-16}$ [391]. Considering different cosmic string models for the loop distribution [393, 394, 395, 396], the LISA will be able to probe cosmic strings with tension $G_\mu \geq \mathcal{O}(10^{-17})$ assuming: (i) the string dynamics are accurately described by the NG action, (ii) colliding strings always intercommute and, (iii) the average loop size at the formation is $\alpha \approx 1$ which is improving by about ~ 10 orders of magnitude relative to CMB constraints which are ~ 6 orders of magnitude from current Pulsar Timing Arrays (PTA) constraints and potentially ~ 3 orders of magnitude w.r.t expected constraints from next generation PTA observatories. Advanced LIGO and Advance Virgo form the data of three observing runs (O3) have put constrains for one loop cosmic string distribution model allowing $G_\mu \leq 4 \times 10^{-15}$ [390]. The bounds on G_μ from different probes include: $G_\mu \leq 10^{-11}$ from PTA [397, 398], $G_\mu \leq 2 \times 10^{-14}$ from LIGO/Virgo based on the string network model [399, 389].

As shown in Fig.6.4, the galactic foreground is the most important for limiting the cosmic string measurement as it is dominant at low frequencies.

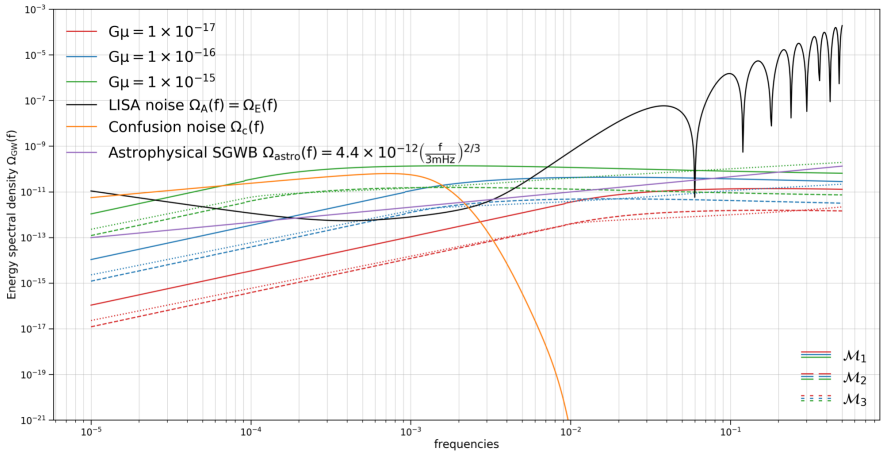

Figure 6.4: Dimensionless GW energy densities $\Omega_{GW,G_\mu(f)}$ for cosmic string models $\mathcal{M}_i$ with $i = 1, 2, 3, 9$ [392] with LISA noise [400], a galactic confusion noise [401] and an astrophysical compact binary background [402]. This figure shows the cosmic string GWB energy density for three string models and for string tension values around the value of LISA detectability [403]. Plot taken from [391].

6.4 SGWB Anisotropies

In this section, we present the formalism developed by authors [404, 358, 403] for anisotropies in the energy density of AGWB. A line of sight approach is followed by [357] assuming that the future detectors will have sensitivity to determine the energy flux in the GWB as a function of direction in the sky and, a unified approach for anisotropies in the AGWB is presented in [405]. A derivation of the angular power spectrum of cosmological anisotropies using a Boltzmann approach has been obtained in [406, 407, 357] including a derivation for angular power spectrum and effects of different stellar models on angular power spectrum are considered by [408, 360, 405]. Additionally, projection effects on the observed angular spectrum which include Kaiser, Doppler and gravitational potential effects have been discussed in [409]. These projection effects are the most important on the largest scales and contribute to up to tens of percent of the angular power spectrum amplitude with the Kaiser term being the largest at all scales. We describe here important quantities and the relations for describing anisotropies in the AGWB based on what in the next section we motivation our work.

Unresolved GW sources of astrophysical and cosmological origin are the progenitors of SGWB. Different backgrounds contribute at different frequencies making it statistically possible to distinguish them [355]. Theoretically, the energy density of GWs have been modelled and parametrized assuming that our Universe and the distribution of sources are homogeneous and isotropic [355, 410]. However by considering distribution of astrophysical sources in cosmic structures, this approximation needs to be relaxed. Therefore the flux of energy from all astrophysical sources is not constant across the sky and has the directional dependence [358]. In order to compute and analyse observed anisotropies in the energy density of SWGB, presence of inhomogeneities in the matter distribution along the line-of-sight and large scale geometry of the Universe must be considered. Anisotropies in the SGWB have two main contributions: one directly re-

lated to the production mechanism of each particular GW source and another belongs to large scale perturbation effect which is common to all the GW sources. Authors of [358] have followed a coarse-graining approach for three different scales: from *local astrophysical* to *galactic scale* and finally have considered the *cosmological scale*. These three different scales are represented in figure 6.5:

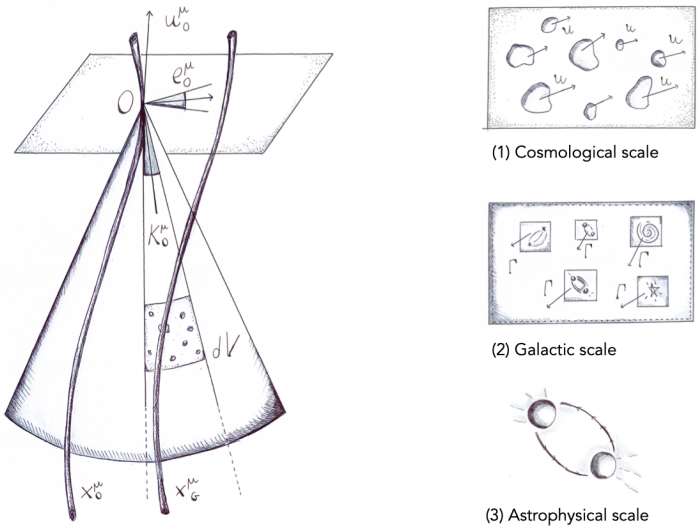

Figure 6.5: Schematic representation for deriving analytic expression of the angular power spectrum from [358]. Figure on left shows space-time representation where the observer detects a signal in the direction e_0^μ with a solid angle $d^2\Omega_0$ around this direction. The physical volume dV is 3-dimensional volume element, defined as the intersection of a 4-dimensional volume element with the observer past lightcone. Figure on right shown three scale: cosmological, galactic and astrophysical.

The first and the largest scale is the *cosmological scale* of the observer for whom galaxies behave as point like GW sources. The total flux of energy density received on this scale is the sum of individual energy densities received from each galaxies in the solid angle under consideration. The flux from a given galaxy is related to the galaxy effective luminosity. The *galaxy effective luminosity* is defined in the galaxy rest frame which takes into account contribution from various sources inside the galaxies. This defines the *galactic scale*. Each of these sources have the peculiar velocity with respect to galaxy rest frame which includes extra dispersion in the signal. The luminosity of an astrophysical source in the galaxy rest frame can be expressed in terms of local quantities characterizing the source in the rest frame defining the *local astrophysical scale*. In this way, the final parameterization for the observed GW flux inherits two main contributions:

- *cosmological origin* related to the specific cosmology i.e. the geometry of the Universe, distribution of large scale structure of the Universe and,
- The *local physics* encoding information on the specific processes of GW emission depending on intrinsic properties of GW sources inside a galaxy.

Therefore, anisotropies of the AGWB encode information about:

1. The different mechanisms for GW production,
2. The astrophysical distribution of GW sources in galaxies,
3. Galaxy formation and distribution of the large scale structure of the Universe and,
4. the space-time geometry along the line-of-sight.

Similar to Eq.6.1, dimensionless density parameter which characterizes the spectrum of the AGWB following conventions by [358] is given by,

$$\Omega_{GW}(\nu_O) \equiv \frac{\nu_O}{\rho_c}\frac{d\rho_{GW}(\nu_O)}{d\nu_O} \tag{6.12}$$

where, $\rho_c \approx 3H_0^2/(8\pi G)$ is the critical density, ν_0 is the frequency measured by the observer and ρ_{GW} is the AGWB energy density [125]. The *spectrum* $d\rho_{GW}/d\nu_0$ is related to the direction dependent spectrum by,

$$\frac{d\rho_{GW}(\nu_O)}{d\nu_O} = \int \frac{d^3\rho_{GW}(\nu_O, e_O)}{d\nu_O d^2\Omega_0} d^2\Omega_O \tag{6.13}$$

As mentioned above, to provide general parameterization of the GW flux from unresolved astrophysical sources, we need to consider following scales:

1. *Cosmological scale*: The observer measures a GW flux in a direction e_0 and solid angle Ω_0, assuming galaxies as point sources emitting GWs comoving with the cosmic flow.
2. *Galactic scale*: On this scale, each galaxy is described by a set of parameters (e.g. mass, mean metallicity etc.). Each galaxy is associated an effective luminosity encoding the global effects of all the GW sources contained in it having a velocity Γ in the galaxy rest frame. Therefore to get the effective luminosity of each type of astrophysical sources, the luminosities of all such single sources need to be summed up averaging over their velocity distribution function in the galaxy rest frame.
3. *Astrophysical scale*: This defines the local scale of single GW sources, for any such source, the astrophysical process of GW production along with its energy spectrum and function of local parameters can be studied characterizing the source.

On cosmological scale, each galaxy is defined by its *effective luminosity* depending on its parameter θ_G (describing its mass M_G, metallicity Z_G, etc.) and it needs to be expressed in terms of the properties of the sources contained in the galaxy. For a galaxy observed at redshift z_G in direction e_0, the total flux of energy received by an observer O in this direction is related to the absolute effective luminosity of the galaxy by following relation,

$$\Phi(z_G, e_O, \theta_G) \equiv \frac{L_G(\theta_G)}{4\pi D_L^2(z_G, e_O)} \tag{6.14}$$

where $D_L(z_G, e_O)$ is the luminosity distance of the galaxy and L_G is the effective luminosity of the galaxy which is the sum of contribution of all GW sources lying within. It depends on the mass of the galaxy as well astrophysical parameters including star formation rates, the stellar evolution and the formation of binary systems (BBHs or BNS). The angular diameter distance is defined as,

$$D_A^2 \equiv \frac{A_G}{\Omega_O} \tag{6.15}$$

where, A_G is the physical area of the galaxy and $\Omega_0 \ll 1$ is its apparent angular size. Luminosity and angular diameter distances are related by,

$$D_L = (1 + z_G)^2 D_A \tag{6.16}$$

The effective frequency spectrum of GW of the galaxy is $\mathcal{L}_G(\nu_G, \theta_G)$ normalized in such a way that,

$$\int_0^\infty \mathcal{L}_G(\nu_G, \theta_G) d\nu_G = L_G(\theta_G) \tag{6.17}$$

which using *effective frequency of the galaxy* of following form,

$$\nu_G = (1 + z_G)\nu_O \tag{6.18}$$

becomes,

$$L_G(\theta_G) = (1 + z_G) \int \mathcal{L}_G[\nu_0(1 + z_G), \theta_G] d\nu_O \tag{6.19}$$

where, z_G is the redshift of the galaxy. We can then define the flux measured by the observer in the frequency range $(\nu_0, \nu_0 + d\nu_0)$ using Eq.(6.14), it follows that,

$$\Phi(z_G, e_O, \nu_O, \theta_G) d\nu_O \equiv \frac{(1 + z_G)}{4\pi D_L^2(z_G, e_O)} \mathcal{L}_G(\nu_G, \theta_G) d\nu_O \tag{6.20}$$

This quantity is called the *specific flux* of GW radiation and defines the expression of the flux of energy received by the observer O in the direction e_O, per unit of observed frequency in terms of quantities defined on galactic and astrophysical scales. The total effective luminosity per unit of effective frequency can be decomposed as a sum of contribution from inspiralling binaries, mergers and SNe.

$$\mathcal{L}_G \equiv \mathcal{L}_G^I + \mathcal{L}_G^M + \mathcal{L}_G^{SN} \tag{6.21}$$

The total intensity of GW observed in direction e_0 can be obtained by summing up the contributions from all the galaxies along the line-of-sight. The contribution between λ and $\lambda + d\lambda$ where λ is the affine parameter, the number of galaxies in the physical 3-volume element becomes:

$$d^3V \sim \sqrt{-g} \epsilon_{\mu\nu\alpha\beta} u^\mu dx^\nu dx^\alpha dx^\beta \tag{6.22}$$

In order to obtain contribution between λ and $\lambda + d\lambda$, the number of galaxies in volume d^3V should be multiplied by the specific flux received form a single galaxy with parameters θ_G and further integrating over a range of values θ_G:

$$\frac{d^3\rho_{GW}}{d\nu_O d^2\Omega_O}(\nu_O, e_O) = \int d\lambda \int d\theta_G \Phi[x^\mu(\lambda), \nu_0, \theta_G] \frac{d^3\mathcal{N}_G}{d\lambda d^2\Omega_O}[x^\mu(\lambda), \theta_G] \tag{6.23}$$

where $\Phi[x^\mu(\lambda), \nu_0, \theta_G]$ is the specific flux received at frequency ν_0 in direction e_0 from a galaxy located at $x^\mu(\lambda)$ defined in Eq.(6.20) and the direction dependent spectrum on the left hand side is related to the GW energy density in Eq.(6.13). $d^3\mathcal{N}_G(x^\mu(\lambda), \theta_G)$ represents the number of galaxies with parameters θ_G contained in the physical volume d^3V defined in Eq.(6.13) seen by the observer O under the solid angle $d^2\Omega_0$. Let $n_G[x^\mu(\lambda), \theta_G]$ be the physical density of galaxies with parameters θ_G,

$$d^3\mathcal{N}_G(x^\mu(\lambda), \theta_G) \equiv n_G[x^\mu(\lambda), \theta_G] d^3V[x^\mu(\lambda)] \tag{6.24}$$

which using Eq.(6.22) becomes,

$$d^3V[x^\mu(\lambda)] = d^2\Omega_O D_A^2(\lambda) \sqrt{p_\mu(\lambda) p^\mu(\lambda)} d\lambda \tag{6.25}$$

where,

$$p^\mu \equiv (g^{\mu\nu} + u^\mu u^\nu) k_\nu = -E e^\mu \tag{6.26}$$

with e^μ is spatial unit vector, u^μ is the four velocity, k^μ is the wave 4-vector and $E = 2\pi\nu \equiv -u_\mu k^\mu$ is the cyclic frequency of the GW signal in the observer's rest frame. Now, the specific flux becomes,

$$\frac{d^3\rho_{GW}}{d\nu_O d^2\Omega_O}(\nu_O, e_O) = \frac{1}{4\pi} \int d\lambda \int d\theta_G \frac{\sqrt{p_\mu(\lambda) p^\mu(\lambda)}}{[1 + z_G(\lambda)]^3} n_G[x^\mu(\lambda), \theta_G] \mathcal{L}_G(\nu_G, \theta_G) \tag{6.27}$$

where the reciprocity relation Eq.(6.16) is used. Eq.(6.27) is the *general expression for the anisotropies in AGWB*. More general unified view on AGWB anisotropies is presented in [411].

While considering cosmological framework, perturbations in in the FLRW metric Newtonian gauge becomes,

$$ds^2 = a^2[-(1 + 2\psi)d\eta^2 + (1 - 2\phi)\delta_{ij} dx^i dx^j] \tag{6.28}$$

where the metric of constant time hypersurfaces is in terms of the comoving radial distance χ,

$$\delta_{ij} dx^i dx^j = d\chi^2 + \chi^2(d\theta^2 + sin^2\theta d\phi^2) \tag{6.29}$$

The two Bardeen potentials are,

$$\psi = \Psi + \Pi, \phi = \Psi - \Pi \tag{6.30}$$

Since all galaxies are assumed comoving with the cosmic flow, to first order in perturbations, four velocity of the cosmic fluid becomes,

$$u^\mu \equiv \frac{1}{a}(1 - \psi, v^i) \equiv \bar{u}^\mu + \delta u^\mu \tag{6.31}$$

where v^i is the peculiar velocity field. Considering equality of Bardeen's potentials, $\psi = \phi = \Phi$ and $\Pi = 0$. Eq.(6.27) reduces to,

$$\frac{d^3\rho_{GW}}{d\nu_O d^2\Omega_O}(\nu_O) = \frac{1}{4\pi H_0}\int d\bar{z}\frac{1}{E(\bar{z})}\frac{1}{(1+\bar{z})^4}\int d\theta_G \bar{n}_G(\bar{z},\theta_G)\mathcal{L}_G(\nu_G,\theta_G) \tag{6.32}$$

where $\bar{n}_G(\bar{z},\theta_G)$ is the background density of galaxies and in FLRW Universe $D_L(\bar{z}) = (1+\bar{z})\chi(\bar{z})$ and $E(\bar{z} \equiv H(\bar{z})/H_0)$.

Next, to consider effect of scalar perturbation in the metric Eq.(6.27), the final expression for GW energy density in terms of conformal time becomes,

$$\begin{aligned}\frac{d^3\rho_{GW}}{d\nu_O d^2\Omega_O}(\nu_O,\mathbf{e}) = \frac{1}{4\pi}\int d\eta a^4\int d\theta_G\bar{n}_G\mathcal{L}_G(\nu_G,\theta_G)\times \\ \Big[1 + b\delta_{CDM} + 4\Psi + 4\Pi - 3\Psi_O - 3\Pi_O - 2\mathbf{e}\cdot\nabla v + 3\mathbf{e}\cdot\nabla\nu_O - 6\int_{\eta_O}^{\eta} d\eta'\dot{\Psi}\Big]\end{aligned} \tag{6.33}$$

where b is bias depending on coordinate time, δ_{CDM} denotes the CDM density contrast and $\nu = \nabla\nu$ as only contribution from scalar perturbations is taken into account. The integration runs along the unperturbed geodesic parameterized as, $\mathbf{x} = \mathbf{x}_O + \mathbf{e}(\eta_O - \eta)$.

Eq.(6.33) can be split into a homogeneous and isotropic background contribution and a first order contribution as,

$$\frac{d^3\rho_{GW}}{d\nu_O d^2\Omega_O}(\eta_O,\mathbf{x}_O,\mathbf{e},\nu_O) = \frac{d^3\bar{\rho}_{GW}}{d\nu_O d^2\Omega_O}(\eta_O,\nu_O) + \varepsilon(\eta_O,\mathbf{x}_O,\mathbf{e},\nu_O) \tag{6.34}$$

Eq.(6.34) is the expression for *AGWB anisotropies specialized to a FLRW Universe with scalar perturbations* and, the perturbation $\varepsilon(\eta_O,\mathbf{x}_O,\mathbf{e},\nu_O)$ is given by,

$$\begin{aligned}\varepsilon(\eta_O,\mathbf{x}_O,\mathbf{e},\nu_O) = \frac{1}{4\pi}\int d\eta a^4\int d\theta_G\bar{n}_G\mathcal{L}_G(\nu_G,\theta_G)\times \\ \Big[1 + b\delta_{CDM} + 4\Pi + 4\Psi - 2\mathbf{e}\cdot\nabla v - 6\int_{\eta_O}^{\eta'} d\eta'\dot{\Psi} + \frac{1}{\mathcal{L}_G}\frac{\partial\mathcal{L}_G}{\partial\nu_G}|_{\bar{\nu}_G} \\ \frac{\nu_O}{a}\Big[e\cdot\nabla v - \Psi - \Pi + 2\int_{\eta_O}^{\eta} d\eta'\dot{\Psi}\Big]\Big]\end{aligned} \tag{6.35}$$

This expresses the emissivity in terms of the astrophysical details of galaxies and hence has frequency dependence. It is worthy to note that the cosmological part in Eq.(6.35) which is a *stochastic variable* has structure very much similar to the Sachs-Wolfe formula for CMB temperature anisotropies. Eq.(6.35) can be compared to Eq.(9) of [357] where the first two terms and the last two terms in the brackets are the Integrated Sachs-Wolfe (ISW) and Sachs-Wolfe (SW) effects respectively [88, 84, 412]:

$$S(k,\eta) = \dot{\Phi} - \dot{\Psi} + \dot{\sigma}(\hat{p}^i\nu_i + \Pi - \Psi) \tag{6.36}$$

The remaining terms in Eq.(6.36) are a Doppler contribution due to the peculiar velocity of an emitter and an intrinsic contribution due to the inhomogeneous distribution of emitters. The emissivity rate $\dot{\sigma}$ defines an emission depth in an analogy to the optical depth parameter τ for the CMB γs.

Eq.(6.34) and Eq.(6.35) can distinguish two different type of contributors: (1) a contribution from local physics proportional to the galaxy effective luminosity $\mathcal{L}_G$ and, (2) a cosmological contribution depending on metric perturbations, matter density contrast and velocities. In the cosmological part, contribution proportional to the CDM overdensity coming from the perturbative expansion of the galaxy density n_G in the covariant expression- (6.27), a *Doppler* contribution due to the peculiar motions of galaxies with respect to the observer rest frame, local contributions and the contribution along the line-of-sight. Authors of [358] expect the local contribution proportional to the CDM overdensity to be the dominant term along with the Doppler one. Here CMB and AGWB are both treated along the line-of-sight approach in the eikonal limit, however for the electromagnetic case, photons are travelling from constant time hypersurface at $z \approx 1100$ while for AGWB, the GW sources have a non trivial redshift distribution. Hence, from a theoretical point of view, like any background of radiation, AGWB is fully characterized in terms of the Stokes parameters, intensity and polarization as a function of direction of frequency [117, 413].

6.4.1 Angular power spectrum of AGWB anisotropies

The final result of the energy density of the AGWB (Eq.(6.27)) has an astrophysical and a cosmological dependence through the galaxy distribution and cosmological gravitational potential and velocity field distributions since they enter in the Geodesic and Sachs equation. Broadly, the anisotropies in the AGWB have the following dependence:

- The underlying cosmological model which in this case is FLRW Universe,
- the large scale structure or galaxy clustering and its effect on GW propagation which is described using linear perturbation and including non-linearity in the matter evolution,
- the local astrophysics on sub-galactic scales given by the astrophysical modeling of the time-dependent GW luminosity $\mathcal{L}_G$ of a given galaxy as a function of halo mass M_G and GW frequency at emission ν_G.

These cosmological variables are correlated on cosmological scales and induces an angular correlation of the AGWB energy density (characterized by its angular power spectrum) and other cosmological probes such as *lensing* and *galaxy counts*. The reason why the GW signal of the AGWB is not correlated but the energy density does correlate is discussed in [404]. Analogous to the CMB intensity which is proportional to the square of the field and characterized by a non-vanishing two point correlation function (2PCF), the energy density of AGWB does correlate too.

Similar to Eq.(6.27), the *observed* energy density of the AGWB along direction $\mathbf{e}_O$ within the solid angle $d^2\Omega_O$ can be written as [404],

$$\frac{d^3\rho_{GW}}{d\nu_O d^2\mathbf{e}}(t_O, \mathbf{x}_O, \mathbf{e}_O) = \frac{c^2}{4\pi}\int d\lambda \int d\theta_G \frac{\sqrt{p_\mu(\lambda)p^\mu(\lambda)}}{[1+z_G(\lambda)]^3} n_G[x^\mu(\lambda), \theta_G] 4\pi (D_L^{prox})^2 \nu_G^2 \sum_A \mathcal{P}_A^G(x^\mu(\lambda), \theta_G; \nu_G) \tag{6.37}$$

where,

$$D_L^{prox} \equiv \sqrt{\frac{A_G}{\Omega_G}} \tag{6.38}$$

with $A_G \equiv A(\lambda_G)$ and Ω_G are the physical size of the source and solid angle subtending the surface of the beam at observer position seen from the source respectively. D_L^{prox} corresponds to the limit of $D_L = (1+z_G)\sqrt{A_O/\Omega_G}$ for $z_G \to 0$ i.e. to the luminosity distance measured by an observer in the vicinity of the source. z_G is the galaxy redshift related by,

$$1 + z_G \equiv \frac{\nu_g}{\nu_O} = \frac{u_G^\mu k_\mu(\lambda)_G}{u_O^\mu k_\mu(\lambda)_O} \tag{6.39}$$

And, $\mathcal{P}_A^G(x^\mu(\lambda), \theta_G; \nu_G)$ shows all incoherent signals from individual events inside a galaxy. The galaxy luminosity (per unit emitted frequency) is related to the emitted strain by,

$$\mathcal{L}_G = 4\pi (D_L^{prox})^2 \nu_G^2 \sum_A \mathcal{P}_A^G(x^\mu(\lambda), \theta_G; \nu_G) \tag{6.40}$$

where, $\nu_G^2 \sum_A \mathcal{P}_A^G$ is the energy flux per units of emitted frequency close to the source and it contains the *incoherent superposition of the energy fluxes of the various sources inside the galaxy considered*. The energy density expressed in Eq.(6.37) is a stochastic quantity depending on galaxy density, redshift and spatial displacement which are stochastic quantities. Therefore, it can be characterized by 2PCF between two directions $\mathbf{e}_1$ and $\mathbf{e}_2$ introduced as:

$$C(\mathbf{e}_1 \cdot \mathbf{e}_2) = \left\langle \frac{d^2\rho_{GW}}{d^2\mathbf{e}_1}(\mathbf{e}_1) \frac{d^2\rho_{GW}}{d^2\mathbf{e}_2}(\mathbf{e}_2) \right\rangle \tag{6.41}$$

Whereas considering cosmological structure present along the line-of-sight the stochastic variable Eq.(6.35) $\varepsilon(\eta_O, \mathbf{x}_O, \mathbf{e}, \nu_O)$ depends on the observer's position and direction of observation. The cosmological variables are correlated stochastic variables whose spectra are related to a scenario of structure formation [414]. ε can be characterized by angular correlation function:

$$C(\theta) \equiv \langle \varepsilon(\eta_O, \mathbf{x}_O, \nu_O, \mathbf{e}_1) \varepsilon(\eta_O, \mathbf{x}_O, \nu_O, \mathbf{e}_2) \rangle \tag{6.42}$$

Due to statistical isotropy, $e_1 \cdot e_2 \equiv cos\theta$. This correlation function can be expanded in Legendre polynomials,

$$C(\theta) \equiv \sum_l \frac{2l+1}{2\pi} C_l P_l(\mathbf{e}_1 \cdot \mathbf{e}_2) \tag{6.43}$$

where multipole l corresponds to the typical scale π/θ and C_l is the estimate of variance of the GW energy density fluctuations on that scale. To get this expression, ε is decomposed in spherical harmonics as,

$$\varepsilon(\eta_O, \mathbf{x}_O, \nu_O, \mathbf{e}) = \sum_{lm} a_{lm}(\eta_O, \mathbf{x}_O, \nu_O) Y_{lm}(e) \tag{6.44}$$

where the coefficients are,

$$a_{lm}(\eta_O, \mathbf{x}_O, \nu_O) \equiv \int d^2e\varepsilon(\eta_O, \mathbf{x}_O, \nu_O, \mathbf{e})Y^*_{lm}(e) \tag{6.45}$$

And using properties of Legendre's polynomials,

$$(2l+1)C_l \equiv \sum_m \langle a_{lm}a^*_{lm}\rangle \tag{6.46}$$

where the brackets denote an ensemble average over the stochastic variables. When expanding ε in Fourier modes we get,

$$\varepsilon(\eta_O, \mathbf{x}_O, \nu_O, \mathbf{e}) = \int \frac{d^3\mathbf{k}}{(2\pi)^3}\hat{\varepsilon}_k(\eta_O, \nu_O, e) \tag{6.47}$$

and the angular power spectrum becomes,

$$C_l(\nu_O) = \frac{2}{\pi}\int dk k^2 |\varepsilon_l(k, \nu_O)|^2 \tag{6.48}$$

which is similar to the CMB temperature and polarization angular power spectrum. This equation expresses the *angular power spectrum of AGWB energy density* which is correlated with lensing and galaxy number counts respectively [358]. Since the angular power spectrum of the AGWB energy density has frequency dependence, the cosmological and astrophysical effects could depend on the frequency band chosen making it possible to distinguish different astrophysical processes. From Eq.(6.48), the variance for each frequency band is defined as,

$$\sigma^2_{GW}(\nu_O) \equiv \langle \delta\rho_{GW}(\nu_O, \mathbf{e}_2)\delta\rho_{GW}(\nu_O, \mathbf{e}_2)\rangle \tag{6.49}$$

and using Eq.(6.43),

$$\sigma^2_{GW}(\nu_O) \equiv \sum_l \frac{2l+1}{2\pi}C_l(\nu_O) \tag{6.50}$$

This correlation function is non vanishing due to the non vanishing corrector of the cosmological variables of the cosmological quantities when specialized to a perturbed FLRW metric. The anisotropies in AGWB are characterized in terms of energy density of the background and its 2PCF while the total amplitude of GW signal received from different directions is uncorrelated. [415] showed how different GW sources are characterized by different angular spectra. The astrophysical dependence of the angular power spectrum on the detail of the underlying astrophysical model has been studied in [403, 408, 360, 405, 416, 417, 418, 419]. The relative important of cosmological and astrophysical effects depend on the frequency band chosen, hence offering the possibility to distinguish different astrophysical processes. The shape and amplitude of angular power spectrum of AGWB depend on both- the astrophysical properties on galactic scale and on cosmological properties. [359] showed that the angular power spectrum behaves as $C_l \propto 1/l$ on large scales. Expressions for the projection effects on observed AGWB angular power spectrum is shown in [409] and the angular power spectrum in the presence of shot noise and the size of shot noise effects for realistic models of the AGWB in the LIGO/Virgo band have been discussed by [416]. Such shot noise dominates over the true astrophysical power spectrum which upon long observing times and removal of foreground sources can provide *true power spectrum*. Method for

estimating true power spectrum based on statistical independence of different shot noise realisations at different times is given in [417]. How shot noise power affects the GW intensity distribution on the sky can be visualized from Fig.6.6:

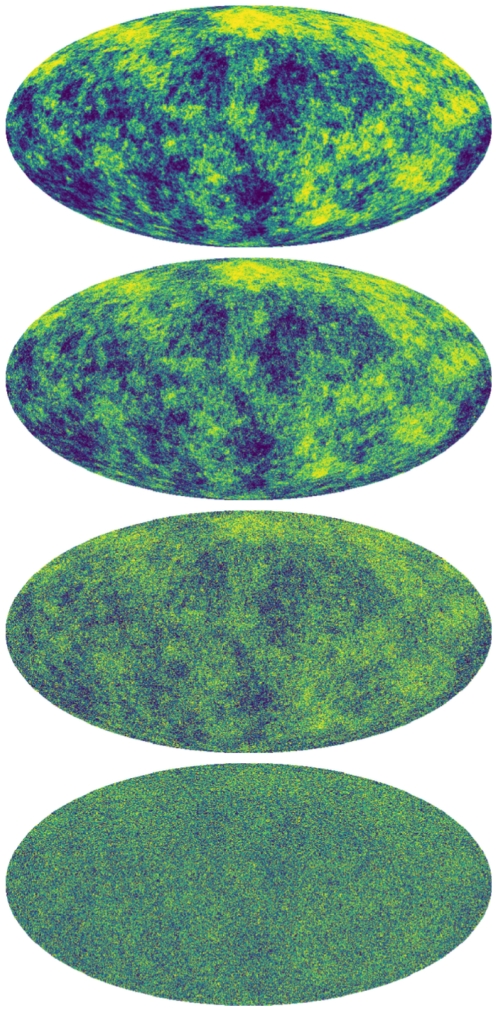

Figure 6.6: A toy-model depiction of shot noise showing HEALPix map [420] with scale invariant angular power spectra $l(l+1)C_l = \text{const.}$ plus varying degrees of shot noise power. From top to bottom, the shot noise power is: $\mathcal{W} = 0$, $\mathcal{W} = 10^{-5}\bar{\Omega}^2$,$\mathcal{W} = 10^{-4}\bar{\Omega}^2$ and $\mathcal{W} = 10^{-3}\bar{\Omega}^2$. They represent different observations of the AGWB, with different observation time intervals leading to different levels of shot noise power. All four maps have the same underlying LSS realisation but the increased level of shot noise leads to much stronger anisotropies on small scales, making it difficult to distinguish the relatively subtle large scale features, plot is taken from [417].

6.5 SGWB as a probe of astrophysics and cosmology

The AGWB which may seem as a nuisance foreground is actually hiding many astrophysical and cosmological information underneath. The anisotropies in the GWB will

contain information about the mechanism that generated the GWs [421, 422, 423, 424, 425, 426, 427] and about the nature of spacetime along the line of propagation of the waves [357, 406, 428, 429].

Anisotropies in the SGWB can be generated by spatially extended sources such as a population of neutron stars in the galactic plane or nearby galaxy [430, 431], due to cosmological perturbation from intervening LSS [432, 433, 434, 404, 358, 357] or due to cosmic strings [403].

On the one hand, the isotropic part of AGWB (i.e. the monopole component) at different frequencies have been investigated for many years and recently a strong evidence of a stochastic process modelled as a power-law has been claimed to have been detected in the 12.5 year Pulsar timing data set collected by the North American Nanohertz Observatory for Gravitational Waves (NANOGrav) [435]. On the other hand, inhomogeneous spatial distribution of GW sources such as magnetars [302], rotating neutron stars [294], galactic and extragalactic compact binaries [436, 437, 285], or the inspiral and collisions of supermassive black holes associated with distant galaxy mergers [438] lead to an AGWB characterized by preferred directions and hence anisotropies in the energy density similar to the measured temperature anisotropies in the CMB. For SGWB, several components contribute at different frequencies and with different statistical properties [355, 285]. The main contribution to such anisotropies in the AGWB is from CBCs following the local distribution of matter. Here, we have accepted the general formalism for the computation of energy density and anisotropies in the SGWB of either cosmological or astrophysical origin as developed in [403]. Theoretical and numerical computation in AGWB anisotropies in intensity and polarisation, together with associated angular power spectra are promising bridge to solve many puzzles of astrophysics and cosmology as the AGWB inherit anisotropies due to various astrophysical and cosmological process. For example, [403] showed that the angular power spectrum of anisotropies is relatively insensitive to the choice of model for the string network but is very sensitive to the string tension G_μ. Hence it becomes interesting to analyse anisotropies in AGWB as upon proper analysis, it can offer to put limits on models for the early Universe.

The energy density of AGWB relies on astrophysical, galactic and cosmological scales [358], hence the observed GW flux per units of solid angle depends on the effective luminosity from all galaxies in the solid angle considered [404]. The final result for the energy density of the background has an astrophysical and cosmological dependence through the galaxy distribution, gravitational potential and velocity field distribution. This makes possible to correlate cosmological probes with AGWB.

We accept the general formalism developed for energy density of the SGWB applicable to AGWB and CGWB including full description of its anisotropies from [403]. Considering only linear order perturbations, the energy density of GWs with observed frequency ν_o arriving from a solid angle σ_o centered on the direction $\mathbf{e}_{\hat{O}}$ is given by,

$$\frac{d^3\rho_{GW}}{d\nu_o d^2\sigma_o}(\nu_o, \hat{\mathbf{e}}_o) = \frac{1}{4\pi}\int_0^{\eta} d\eta a^4 \int d\zeta \bar{n}\mathcal{L}_s\Big[1+\delta_n - 3(\Psi_o+\Pi_o) + 4(\Psi+\Pi) + \hat{\mathbf{e}}_0\cdot(3\nu_0 - 2\mathbf{v}) + 6\int_\eta^{\eta_o} d\eta' \frac{\partial\Psi}{\partial\eta'}\Big] \tag{6.51}$$

Again, subscripts "o" and "s" shows quantities evaluated at the observer and GW source respectively. η is the integral along the line of sight and $\mathbf{x}(\eta, \hat{\mathbf{e}}_o) = \mathbf{x}_o + (\eta_o - \eta)\hat{\mathbf{e}}_o$.

Here, $\nu(\eta, \hat{\mathbf{e}}_o)$ stands for the peculiar 3-velocity of the cosmic fluid, $\mathcal{L}_s(\nu_s, \zeta)$ is the gravitational luminosity at emitted frequency ν_s of a source with parameters ζ with the emitted frequency given in terms of observed frequency ν_o by,

$$\nu_s = \frac{\nu_o}{a}\Big[1 + \Psi_o + \Pi_o - \Psi - \Pi + \hat{\mathbf{e}}_o \cdot (\mathbf{v} - \mathbf{v}_o) - 2\int_\eta^{\eta_0} d\eta' \frac{\partial \Psi}{\partial \eta'}\Big] \tag{6.52}$$

$n(\eta, \hat{\mathbf{e}}_o, \zeta)$ is defined as the source number density per physical volume. The number density inhomogeneities are expressed in terms of the density contrast:

$$\delta_n(\eta, \hat{\mathbf{e}}_o, \zeta) \equiv \frac{n - \bar{n}}{\bar{n}} \tag{6.53}$$

Changing from linear to logarithmic frequency and normalizing with respect to the critical density, we get the *density parameter*:

$$\Omega_{GW}(\nu_o, \hat{\mathbf{e}}_o) \equiv \frac{1}{\rho_c}\frac{d^3\rho_{GW}}{d(\ln \nu_o)d^2\sigma_o} = \frac{8\pi G\nu_o}{3H_o^2}\frac{d^3\rho_{GW}}{d\nu_o d^2\sigma_o} \tag{6.54}$$

Using the density parameter, the dimensionless quantity expressing intensity of stochastic background in the context of a FLRW Universe with scalar perturbations becomes,

$$\begin{aligned}\Omega_{GW}(\nu_o, \hat{\mathbf{e}}_o) = \frac{2G\nu_o}{3H_o^2}\int_0^{\eta_o} d\eta a^4 \int d\zeta \bar{n}\mathcal{L}_s\Big[1 + \delta_n - 3(\Psi_o + \Pi_o) + 4(\Psi + \Pi) + \\ \hat{\mathbf{e}}_o \cdot (3\mathbf{v}_o - 2\mathbf{v}) + 6\int_\eta^{\eta_o} d\eta' \frac{\partial \Psi}{\partial \eta'}\Big]\end{aligned} \tag{6.55}$$

Which can be decomposed in terms of isotropic monopole term $\bar{\Omega}_{GW}(\nu_o)$ and GW energy density contrast $\delta_{GW}(\nu_o, \hat{\mathbf{e}}_o)$:

$$\Omega_{GW} \equiv \bar{\Omega}_{GW}(1 + \delta_{GW}) \tag{6.56}$$

Here, $\bar{\Omega}_{GW}$ corresponds to the average GW flux at frequency ν_o per unit solid angle, so that the total flux at this frequency is $4\pi\bar{\Omega}_{GW}$. Also, the gravitational luminosity $\mathcal{L}_s$ of any astrophysical or cosmological source emitting GWs can be decomposed as,

$$\mathcal{L}_s(\nu_s, \zeta) = \frac{dE_s}{d\nu_s}R(\zeta) \tag{6.57}$$

where, $E_s(\zeta)$ is the total energy lost from the source due to each signal and $R(\zeta)$ is the rate at which the signals are emitted. Here, E_s is computed as a function of the GW strain $h_{\mu\nu}$ by integrating the solid angle $d^2\sigma_s$ over a spherical surface of radius r_s centered on the source where r_s is large enough to use linearized general relativity on a Minkowski background but is small enough to neglect cosmological effects. Defining the total strain magnitude by,

$$\tilde{h} \equiv \sqrt{\frac{|\tilde{h_+}|^2 + |\tilde{h_\times}|^2}{2}} \tag{6.58}$$

Rewriting E_s in terms of $\tilde{h}$ and using Eq.(6.57), *the luminosity spectrum of a single source* is given by,

$$\mathcal{L}_s(\nu_s,\zeta) = \frac{\pi\nu_s^2 R(\zeta)}{2G}\int_{s^2} d^2\sigma_s r_s^2 \tilde{h}^2 \tag{6.59}$$

Using Eq.(6.55) and Eq.(6.59), the density parameter to linear order is given by,

$$\Omega_{GW}(\nu_o,\hat{\mathbf{e}}_o) = \frac{\pi\nu_o^3}{3H_o^2}\int_0^{\eta_o} d\eta a^2 \int d\zeta \bar{n} R\Big[1+\delta_n - \Psi_o - \Pi_o + 2(\Psi+\Pi) + \hat{\mathbf{e}}_0\cdot\mathbf{v}_o + 2\int_\eta^{\eta_o} d\eta' \frac{\partial\Psi}{\partial\eta'}\Big] \times \int_{s^2} d^2\sigma_s r_s^2\tilde{h}^2 \tag{6.60}$$

In order to characterize the anisotropies, setting $\Pi = \Psi = 0$ everywhere and $\nu = 0$ everywhere expect the observer, we get

$$\Omega_{GW}(\nu_o,\hat{\mathbf{e}}_o) = \frac{\pi\nu_o^3}{3H_o^2}\int_0^{\eta_*} d\eta a^2 \int d\zeta \bar{n} R \times (1+\delta_n + \hat{\mathbf{e}}_o\cdot\mathbf{v}_o)\int_{s^2} d^2\sigma_s r_s^2\tilde{h}^2 \tag{6.61}$$

where η_* is the large distance $\eta > \eta_*$ and the emitted frequency is given by,

$$\nu_s = \frac{\nu_o}{a}(1-\hat{\mathbf{e}}_o\cdot\nu_o)) \tag{6.62}$$

We now consider the anisotropic model for AGWB including CBCs [432] as they are expected to be major contributors in the LIGO-Virgo frequency band. Considering a Friedmann-Lemaître-Robertson-Walker model in the absence of any cosmological perturbations, and keeping only the anisotropies due to source density contrast and the dipole induced by the peculiar motion of the observer, the density parameter in Eq.(6.61) becomes,

$$\Omega_{gw}(\nu_o,\hat{e}_o) = \frac{\pi}{3}(t_H\nu_0)^3\int_0^\infty dz\frac{1+z}{E(z)} + \int d\zeta\bar{n}R(1+\delta_n+\hat{\mathbf{e}}_o\cdot\mathbf{v}_o)\int_{s^2} d^2\sigma_s r_s^2\tilde{h}^2 \tag{6.63}$$

where, $t_H \equiv 1/H_0$ is the Hubble time, z is the redshift, ζ represents a set of source parameters, $\bar{n}$ is the homogeneous source number density per comoving unit volume, R is the rate of gravitational wave bursts per source, $\delta_n \equiv (n-\bar{n})/\bar{n}$ is the source number overdensity, $\hat{\mathbf{e}}_o$ is the observation direction, $\mathbf{v_o}$ is the observer's peculiar velocity, $\tilde{h}$ is the GW strain spectrum of a bursts, and the final integral is over a sphere centred on the source.

The angular power spectrum associated to Eq.(6.63) is [432]:

$$\begin{aligned} C_{gw}(\theta_o,\nu_o) = \frac{\pi^2(t_H\nu_o)^6}{9\bar{\Omega}_{gw}^2}\int_0^{z_{max}} dz\frac{1+z}{E(z)}\int_0^{z_{max}} dz'\frac{1+z'}{E(z')} \\ \Big(\Sigma_i\int d\zeta_g\bar{n}(z,\zeta_g)\int d\zeta_b R_i(z,\zeta_g,\zeta_b)\mathcal{S}_i(\nu_s,\zeta_b)\Big) \\ \times\Big(\Sigma_j\int d\zeta_g^{'}\bar{n}(z',\zeta_g')\int d\zeta_b' R_j(z',\zeta_g',\zeta_b')\mathcal{S}_j(\nu_s',\zeta_b')\Big) \\ \Big\langle\delta_n(z,\hat{\mathbf{e}_o},\zeta_g)\delta_n(z',\hat{\mathbf{e}'}_o,\zeta_g')\Big\rangle \end{aligned} \tag{6.64}$$

where, subscripts "b" and "g" denotes binary parameters ζ_b and galaxy parameters ζ_g respectively and the galaxy-galaxy 2PCF is: $\zeta_{gg} \equiv < \delta_n \delta_n >$. In [432] the anisotropies in the SGWB induced by the large scale distribution of astrophysical sources is also performed using mock galaxy catalogues. In such catalogues, the growth of dark matter structure is first simulated and the history of hierarchical mass assembly is then recorded by means of merger trees of haloes and subhaloes within snapshots stored at different time steps. To simulate the visible galaxies without using hydrodynamical simulations, a semianalytical model aiming to reproduce the observed properties of these galaxies at different redshifts can be used.

This was done by using a mock light cone catalogue [439] constructed by applying the "L-galaxies" model [440] to the Millennium simulation [441, 442]. The comoving box of size $500\mathrm{h}^{-1}\mathrm{Mpc}$ on a side of the Millennium simulation exhibits finite volume effects for example, erasing the two-point angular correlation signal at scales larger than a tenth of the simulation box size. The all-sky light cone catalogue [439, 440] containing $5,715,694$ galaxies were used, all limited at apparent AB magnitude of 18 in the r filter from SDSS. It has been built using a random tiling technique applied to 64 postprocessed snapshots saved during the Millennium simulation run with a time step of about 100Myr. Authors queried the data base and retrieved for each galaxy its sky location, metallicity, cosmological redshift and peculiar velocity. In order to calculate the delayed star formation rate of each galaxy on the light cone, Millennium simulations were used to access information about its star formation rate (SFR) at earlier snapshots. This included a total of $973,224,532$ redshift and SFR measurements from the progenitor galaxies. While analysing the mock catalogue, the cosmological parameters used in the Millennium simulation are: $H_0 = 73\mathrm{km}s^{-1}\mathrm{Mpc}^{-1}, \Omega_m = 0.25, \Omega_\lambda = 0.75$.

In this work, GW propagation is assumed to follow the *eikonal approximation* or the so-called *geometrical optics approximation* where the wavelength of GW is smaller than the cosmic scales as explained in Section 5.2.1.

Major contribution to the anisotropies in the AGWB come from the inhomogeneous distribution of GW sources that follow the local distribution of matter i.e. due to galaxy distribution. In this work we define such anisotropies arising at the source distribution level as **primary AGWB anisotropies** in full analogy with the CMB primary temperature anisotropies generated at the last scattering surface [88, 443, 444, 445, 404].

However, still in analogy with the CMB, SGWB while propagating across large scale structures, undergo weak lensing and ISW/Rees-Sciama effects. In this work we define the resulting fluctuations in the energy density of AGWB due to interaction with cosmological structures as **secondary AGWB anisotropies**.

The computation of AGWB intensity anisotropies relies on the following:

1. The local astrophysics on the sub-galactic scales which is given by astrophysical modelling of time dependent GW luminosity as a function of source mass and emitted GW frequency,

2. The underlying background cosmological model which in our case is the standard FLRW model,

3. The source overdensity and velocity distribution with respect to the cosmological background and,

4. The LSS perturbation to the standard FLRW background affecting the GW propagation

In this thesis we have focused on studying primary and secondary anisotropies in the AGWB generated by quantities 3 and 4, assuming 1 as input from previous work in the literature, i.e. the angular power spectrum in Eq.(6.64) associated to the AGWB produced by BBH, BNS and BHNS [432]. The propagation of intensity anisotropies in the AGWB are treated analogously to the CMB photons because we work in the geometrical optics approximation. The two effects- ISW (first order perturbation effect) and weak lensing (beyond first order perturbation level) produces different kinds of anisotropies in the AGWB, which can bring us crucial information about the intervening LSS and cosmological background, as GWs travel from the source to the observer.

6.6 Detection of anisotropies in SGWB

The possibility of measuring and mapping the GWB is described in [446, 447, 448, 346, 449, 413]. Discussion of different methods used by LIGO and LISA to reconstruct an angular resolved map of the sky are presented in [450]. A similar discussion about PTA is presented in [451, 452, 453]. Searches for anisotropies in SGWB using data from the first three observing runs of the aLIGO and AdV found no evidence for GW signals [454, 455]. Different models of cosmology could be distinguish, in principle by characteristic features in the angular distribution [357, 416, 408, 417, 409, 358, 404, 359, 360, 411, 456, 423]. The anisotropies of the SGWB are a unique observable that contains both astrophysical and cosmological information. Astrophysical sources that contribute to the SGWB in the millihertz-decihertz frequency range reside in galaxies and therefore it is expected that the intensity of the background will depend on sky direction analogously to the cosmic infrared background [444]. As shown in [360, 405], both the amplitude and the shape of astrophysical component of stochastic background anisotropies depend on the formation and evolution processes of binary compact objects. One of the limiting factors in observing anisotropies in the SGWB in the $10-100$Hz frequency range accessible to the ground-based detectors is the time-like shot noise which arises because of the signals from merging binary compact objects have a very short duration with respect to the integration time and almost no time overlap in case of BBHs. As a result, shot noise is expected to dominate the signal for any realistic time of integration [416, 360, 417]. However in the decihertz frequency range the astrophysical background can be considered stationary, since each individual signal duration is longer than the time of observation. The ground based interferometers such as LIGO, aLIGO, Virgo, PTA and NANOGrav do not directly measure the AGWB energy density but they observe the quantities related to the strain.

The nearby Universe is expected to create anisotropic SGWB, for example, clusters of galaxies appear as point sources to a network of ground based laser interferometers. [431] showed that the flux of SGWB created by the millisecond pulsars in the Virgo cluster produces a significantly stronger signal than the nearly isotropic background of unresolved sources of the same kind. Such a highly localised source, like the Virgo cluster can be resolved from the isotropic background with very high significance using the directed search algorithms. For backgrounds dominated by nearby sources up to

redshift ~ 3, the directed search for a localised source can have signal to noise ratio more than that for the all sky integrated isotropic search. The directed search is highly sensitive to the anisotropies of a background which is useful to make a sky map of the background [431].

The gravitational wave background is expected to have isolated bright sources superimposed on a diffuse gravitational wave background with two components: a confusion limited background from unresolved astrophysical sources and, a cosmological component formed during the birth of the Universe. A map of the GWB can be made by sweeping GW detectors across the sky. The detector output is a complicated convolution of the sky luminosity distribution, the detector response function and the scan pattern. The general de-convolution problem and the utility of LIGO and LISA to detect anisotropies in the GWB is described in [447]. In the low frequency limit (which correspond to wavelengths large compared to the effective size of the detector), a gravitational wave detector's antenna pattern has only monopole, quadrupole and setxupole components. GW detectors get their directional information from the amplitude and frequency modulation that occur as the antenna pattern is swept across the sky. The frequency modulation is due to the Doppler shift caused by the relative motion of the source and the detector. For example, orbital motion around the Sun creates a periodic frequency shift with amplitude $\delta f/f \sim 10^{-4} \sin\theta$ where θ is the co-latitude in ecliptic coordinates. The amplitude modulation occurs as the antenna lobes are swept across the sky. For the LIGO detectors, this occurs with a fundamental period of one sidereal day whereas for the LISA detector, the fundamental period is one sidereal year. Since the noise in each detector is uncorrelated while the signal is correlated, the SNR improves as the square root of the observation time. This type of correlation has to be done over a finite frequency interval Δf that is large compared to the Doppler modulation δf so the frequency modulation is washed out. Therefore maps of the GWB are made using amplitude modulation alone [447]. How anisotropies in the SGWB will modulate the output from the cross-correlated LIGO detectors is presented in [446]. The impact of astrophysical sources on AGWB in the LIGO/Virgo and LISA band has been investigated by [408] and [405] with contrast conclusions: [408] found that the AGWB monopole (isotropic $\bar{\Omega}_{GW}$) is sensitive to the nature of BBH population with only few percent modification in the anisotropic C_l part, whereas [405, 360] showed that the monopole and anisotropies of the AGWB (amplitude and shape of the angular power spectrum) are complementary and very sensitive to some astrophysical parameters such as the distribution of initial semi-major axis of the binaries, the BH formation scenario and the metallicity of the progenitor stars. AGWB anisotropies in the mHz band show strong dependencies on the modeling of galactic and sub-galactic physics as shown by [405].

6.7 Cross-correlation of AGWB with different cosmological probes

Using a first order perturbation approach, authors of [285] have provided a prediction of the angular power spectrum of the AGWB and its correlation with other cosmological probes such as galaxy number counts and convergence from SKA [457] and Euclid [458]. Any observable on the sphere $\delta\Omega_{GW}(\mathbf{e}, \nu_O)$ can be decomposed in

spherical harmonics, and due to statistical isotropy, its angular correlation function $\langle \delta\Omega_{GW}(\mathbf{e}_1, \nu_O)\delta\Omega_{GW}(\mathbf{e}_2, \nu_O\rangle)$ can be further decomposed in Legendre polynomials to define the angular power spectrum $C_l(\nu_O)$ as [359],

$$C_l(\nu_o) = \frac{2}{\pi}\int dk k^2 |\delta\Omega_l(k, \nu_o)|^2 \tag{6.65}$$

where, the term $\delta\Omega_l(k, \nu_o)$ is given by,

$$\delta\Omega_l(k, \nu_O) = \frac{\nu_O}{4\pi\rho_c}\int_{\eta_*}^{\eta_O} d\eta \mathcal{A}(\eta, \nu_O)\Big[\Big(4\phi_k(\eta) + b\delta_m, k(\eta) + (b-1)3\mathcal{H}\frac{\nu_k(\eta)}{k}\Big) j_l(k\Delta\eta) - 2k\nu(k)\eta j_{lk}^{'}\Delta\eta\Big] + \frac{\nu_O}{4\pi\rho_c}\int_{\eta_*}^{\eta_o} d\eta\mathcal{B}(\eta, \nu_O)[-\Phi_k(\eta)j_l(k\Delta\eta) + k\nu(k)j_l^{'}(k\Delta\eta)] + \frac{\nu_O}{4\pi\rho_c}\int_{\eta_*}^{\eta_O} d\eta[6\mathcal{A}(\eta, \nu_O) - 2\mathcal{B}(\eta, \nu_O)] \int_{\eta}^{\eta_0} d\eta^{\prime}\Phi_k^{'}(\bar{\eta})j_l(k\Delta\bar{\eta}) \tag{6.66}$$

This expression involves following three types of quantities:

- background quantities such as conformal Hubble parameter $\mathcal{H}$ and the look-back time $\Delta\eta = \eta_O - \eta$,
- the cosmological perturbation due to gravitational potential $\Psi(k) \simeq \Pi(k)$ that we introduce as *secondary anisotropy*,
- the velocity field ν_k/Doppler like terms introduced as *primary anisotropy*,
- the source overdensity connected to the galaxy overdensity (*primary anisotropy*) $\delta_g = b\delta_m$ where b is the galaxy bias and,
- the term in the last integral which shows the ISW effect and we consider as a *secondary anisotropy*

The angular power spectrum for different frequencies is shown in the Fig.6.7.

The j_l are Bessel functions and $\mathcal{A}$ and $\mathcal{B}$ are related to the luminosity function per unit of emitted frequency by $\nu_G \equiv (1+z)\nu_O$,

$$\mathcal{A}(\eta, \nu_O) \equiv a^4\bar{n}_G(\eta)\int d\theta_G \mathcal{L}_G(\eta, \nu_G, \theta_G) \tag{6.67}$$

$$\mathcal{B}(\eta, \nu_O) \equiv a^3\nu_O\bar{n}_G(\eta)\int d\theta_G \frac{\partial\mathcal{L}_G}{\partial\nu_G}(\eta, \nu_G, \theta_G) \tag{6.68}$$

Since Eq.(6.66) depends on cosmological perturbations, it correlates with cosmological probes such as galaxy number counts and cosmic convergence map as shown in Fig. 6.8, where, the cross-correlation power spectrum is,

$$B_l^X(\nu_O) \equiv \frac{2}{\pi}\int dk k^2 \frac{4\pi}{\bar{\Omega}_{GW}(\nu_o)}\delta\Omega_l^*(k, \nu_O)X_l(k) \tag{6.69}$$

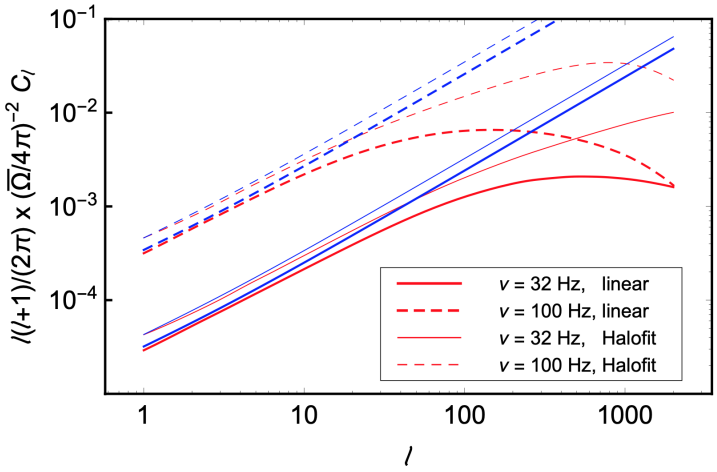

Figure 6.7: Angular power spectrum of AGWB density fluctuation normalized to the monopole for linear and non-linear Halofit [459] spectra of density fluctuations. The straight lines are associated with large scale approximation [359].

Fig. 6.7 provides the general shape of the power spectrum of $\delta\Omega_{GW}$ using analytical method. These spectra depend on cosmology through the transfer functions and the initial power spectrum, and on astrophysics through the merger history of galaxies, the star formation rate, Salpter Initial Mass Function, the stellar evolution that determine the mass distribution of BH and NS.

In Chapter8 we present the cross-correlation of AGWB intensity with CMB convergence, weak lensing maps, galaxy distribution and the CMB ISW/Rees-Sciama effect from the DEMNUni simulations.

Probing the Primordial Universe with GW cross-correlation GWs which are expected to be generated in the primordial Universe due to first order phase transition are targeted to be detected by LISA [460] and when combined with ET, LIGO or BBO these detectors would allow wide possibilities to understand physics of the early Universe and different SGWBs associated with primordial phases of the Universe, e.g. [461] show that the signal coming from phase transitions taking place at $T \approx 1 - 100$ TeV could entirely screen the relic gravitational wave signal expected from standard inflationary models. Various models proposed to study SGWB include sources such as BBH, BNS and BH-NS [462, 463], stellar core collapse [292], primordial black hole mergers [464], ring down of black holes [465], cosmic strings [466], super strings [467], pre-Big Bang models [468] including mapping GW sky with LISA [469] with map making method developed in [448].

The binary coalescence GW background will be a foreground for the third-generation detectors masking the GW background due to early-Universe sources. Accessing the cosmological GWB with third generation detectors will therefore require identification and subtraction of all inspiral signals from all binaries in the relevant frequency band. *Distinguishing AGWB from the CGWB is crucial to get information about SGWB of primordial origin.*

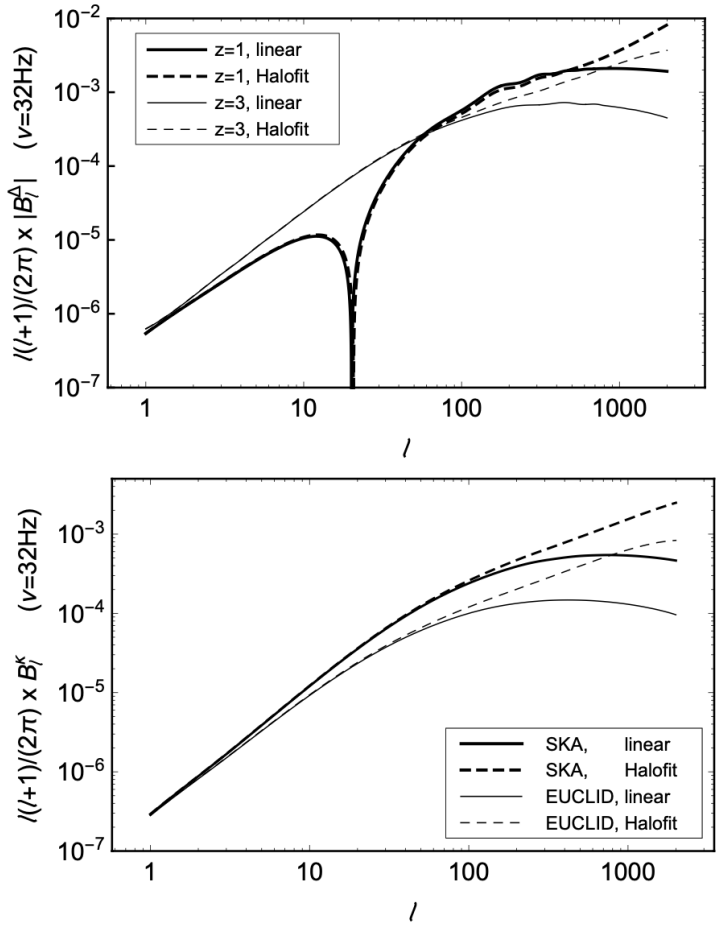

Figure 6.8: Top: cross-correlating angular power spectrum of AGWB with galaxy number count and Bottom: cross-correlating angular power spectrum of AGWB with convergence using the SKA and Euclid redshift distortions [359].

Chapter 7

Gravitational Wave detectors

> All knowledge comes from the stars (the Universal mind). Men do not invent or create ideas; the ideas exist and men are able to grasp them.
>
> *Paracelsus*

Gravitational wave detectors can generally be divided into two types: *beam detectors* and *resonant mass detectors*. In beam detectors, GWs interact with the beam of electromagnetic radiation which is monitored to register the passage of the incoming wave. In case of resonant mass detectors, the incoming GW signal transfers the energy to a massive body from which resultant oscillations are observed. The era of GW astronomy began with the path-breaking first direct detection of GWs from BBH merger GW150914 [217] which has been detected with the Laser Interferometer Gravitational Wave Observatory (LIGO) at the Hanford WA and Livingston LA observatories. The black holes were each of approximately $35M_{\odot}$ orbiting around each other as close as $\sim$ 350km apart and subsequently merged to form a black hole [470]. In the first observing run, advanced LIGO [471] identified two BBH coalescence signals with high statistical significance: GW150914 [217] and GW151226 [280] as well as a less significant candidate LVT151012 [472, 473]. These network of terrestrial GW detectors is sensitive to GWs from the inspiral, merger and ringdown of CBCs. At present, with the Advanced LIGO (aLIGO) [471], Advanced Virgo (AdV) [474] and KAGRA [475, 476, 477] which are the km-scale GW observatories, we can detect GWs within frequencies of $\sim 20 - 2000$Hz.

Till now, LIGO has completed six *Science runs*, the first five of these runs were known as *initial LIGO*. In LIGO's fifth science run (S5) (November 2005-September 2007), the LIGO detectors reached their design sensitivity as they were sensitive to GWs with strain amplitudes of $\sim 10^{-21}$ in the frequency band $400 - 7000$Hz [271]. S6 which is known as *enhanced LIGO* lasted from July 2009 to October 2010. Virgo too has three observing runs, Virgo's first science run (VSR1) overlapped with S5 lasting from May 2007 until October 2007 [478]. Virgo's second and third scientific runs (VSR2 and VSR3) ran from July 2009 to January 2010 and from August 2011 to October 2011 respectively. During these runs, the Virgo detector operated with improved sensitivity over VSR1. O1 began on 18 September 2015 and ended on January

12, 2016 [479], O2 (aLIGO joined by AdV) began on 30 November 2016 and ended on 25 August 2017 and the third observing run O3 combined by aLIGO, AdV and KAGRA collaborations started on April 1, 2019 and was expected to end on April 30, 2020 with a commissioning break from October 1, 2019 to November 1, 2019. In 2011, the LIGO lab and the IndIGO[1] consortium in India proposed installing one of the aLIGO Hanford detectors in India. With operation anticipated in 2025, this detector will be configured including updates identical to the other LIGO detectors. Third-generation future observatories include the Einstein Telescope (ET) [480], the Cosmic Explorer (CE) [481] and the Laser Interferometer Space Antenna (LISA)[2]. Such future planned GW missions are referred to as third generation detectors. In addition to these operational runs which record total number of detection of GW signals emitted by CBC events to 90 in Gravitational-wave Transient Catalogue-GWTC3 [482], the anticipated runs are [479]:

- O3: $2019-2020$ with the aLIGO detectors operating at design sensitivity of $110-130$Mpc and AdV at 50Mpc with KAGRA in the range of $8-25$Mpc,

- O4: late 2021/February 2022 to late 2022/early2023 which would include cluster of aLIGO at $160-190$Mpc, AdV+ at $90-120$Mpc and KAGRA at $25-130$Mpc. The rate of confident GW detections is expected o increase for O4 by factor of 4 and it could be as high as one detection per day [479],

- O5: late 2024/early 2025- 2026 which will begin with a four-detector network incorporating the A+ upgrade for the aLIGO instruments, AdV+Phase2 upgrade for Virgo. The target range for aLIGO is 330Mpc and for AdV is $150-260$Mpc with KAGRA operating at or above its O4 sensitivity of 130Mpc,

- 2025+: Thanks to additional aLIGO interferometer in India, we will be able to have a cluster of five GW observatories with three aLIGO detectors working at design sensitivity of 330Mpc, AdV at $150-260$Mpc and KAGRA at $130+$ Mpc.

The timeline of how future belongs to GW and is summarized in figure 7.1:

The three-detectors network of aLIGO and AdV [483] has demonstrated the ability to localize signals to sky areas of a few tens of square degrees which will be improved upon addition of KAGRA [484] which is the underground observatory in Japan using cryogenic mirrors and LIGO-India network. LIGO India is expected to play a crucial role in locating and deciphering GW sources [485]. This will make detection of BBH a routine and a hundred detection of BBH will allow us to probe the major formation channel and, distinguish between isolated binaries and systems formed in clusters with a BNS detection rate from few per year to a few per month [479]. Hence by mid 2020, there will be five highly sensitive observatories operating as a coherent network [486] which allows for improved parameter estimation and sky localization [479]. On the other hand, co-located and co-aligned detectors respond to GWs from all directions and all frequency below a few kHz.

[1] www.gw-indigo.org

[2] www.lisamission.org

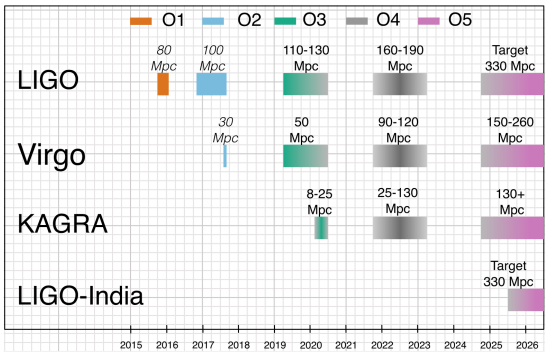

Figure 7.1: Future planned sensitivity evolution and observing runs of aLIGO, AdV and KAGRA detectors where the colored bars show the observing runs, with achieved sensitivities in O1, O2 and O3. The uncertainty in the start or finish date is represented by shading [479].

7.0.1 Interaction of GWs with detectors

To understand interaction of GWs with detectors, general principle is that of interferometry. A gravitational wave interferometer detects a minute signal with the help of Michelson interferometer shown in the Fig.7.2:

As shown in bottom subfigure of Fig.7.2, a cavity is formed by placing a semi-transparent mirror in the near-end of each arm (which is referred to as the input test masses-ITMX and ITMY) to distinguish them from the end test masses (ETMX and ETMY). By keeping the length of these arms close to the resonance of the light, the light bounces around 200 times more [487] before exiting the arms. For the Fabry-Parot cavity to work properly, the interferometer arms on resonance are needed to be 'locked'. This is done by a feedback loop involving a series of servos. By monitoring motions of the mirrors through the output port, servos are actuated in order to keep the mirrors in lock.

The beams then recombine at the beamsplitter, where interferometer patterns can be observed by a photodetector on the output arm. When the arm lengths are exactly fixed, the light destructively interferes causing dark fringes or no detection. Whereas when a GW passes, one or both of the cavities will undergo a length change resulting into a slight detuning of the beams relative to each other. Then the resulting interference pattern can be used to infer the properties of the observed GW signal. The change in length due to passage of GW signal gives us a quantity called the *gravitational wave strain* h,

$$h \equiv \frac{\Delta L}{2L} \tag{7.1}$$

Since GWs are extremely weak, a binary system comprised of two objects with masses $\simeq M_{\odot}$ at a distance of $\simeq$ 10Mpc from Earth will produce a strain of $h \simeq 10^{-21}$ [489]. The strain induced in the intereferometer from any arbitrarily oriented system can be related as [487]:

$$h(t) = F_{+}H_{+}(t) + F_{\times}H_{\times}(t) \tag{7.2}$$

where,

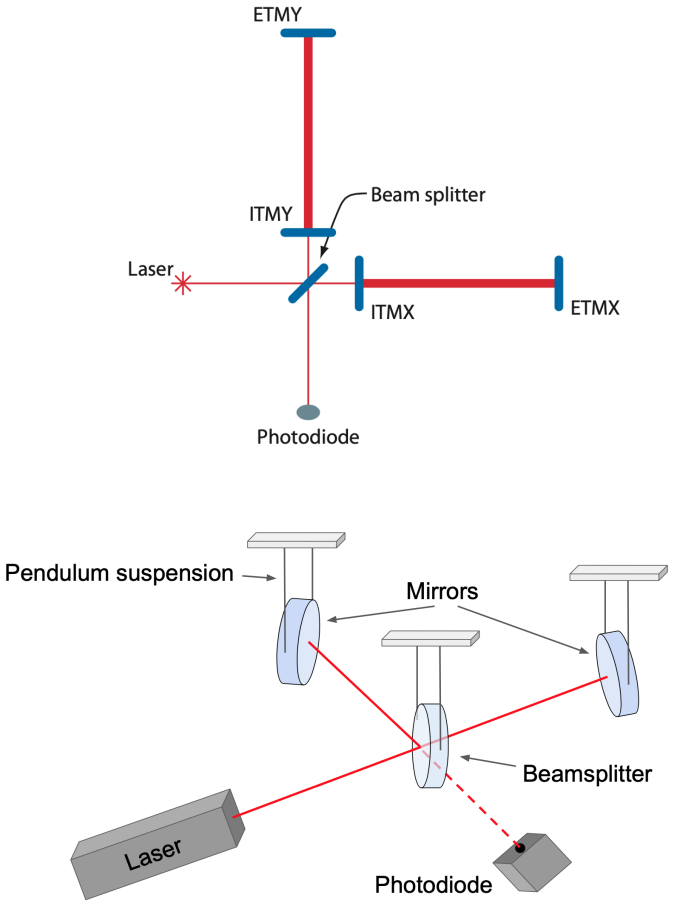

Figure 7.2: *Top*: A schematic of an interferometer with a Fabry-Perot cavity originally published in [487]. *Bottom*: Michelson Gravitational wave interferometer set-up used in LIGO and aLIGO from [488]. In this instrument, a laser beam gets split into two orthogonal arms. With the use of partially reflecting mirrors, a Fabry-Perot cavity shown in bottom is formed, allowing the light to be recycled in each arm to effectively increase the path length travelled.

$$\begin{aligned} F_+ &= -\frac{1}{2}(1+cos^2\theta)cos2\phi cos2\psi - cos\theta sin2\phi sin2\psi, \\ F_\times &= \frac{1}{2}(1+cos^2\theta)cos2\phi sin2\psi - cos\theta sin2\phi cos2\psi \end{aligned} \tag{7.3}$$

Here, angles θ,ϕ and ψ are the Euler angles that relate the frame of the binary to the frame of the detector.

GW interferometers can be characterized by their distribution of power over different frequencies known as the *power spectral density* or referred to as the *detector sensitivity* which is denoted by $S_n(f)$ with dimensions of $\text{Hz}^{-1/2}$.

7.1 Ground based detectors

Here, we present the current and upcoming ground based detectors and their ability to detect particular frequency range of the GW spectrum.

7.1.1 Laser Interferometer Gravitational-wave Observatory

The US based laser interferometer GW detectors are composed of two perpendicular km-scale arm cavities with two-test mass mirrors hung by wires at the end of each cavity. The tiny displacement of mirrors (ΔL) due to a tidal deformation induced by passing GWs are monitored with very high accuracy by measuring the relative optical phase between the light paths in each interferometer arm. The mirrors are actually pendulums with higher quality factor Q and lower resonant frequency $\Omega(\sim 1\text{Hz})$ with a specified typical reference GW frequency (100Hz). Since GWs act as tidal forces, an advantage of interferometers as detectors is that the gravitational wave induced phase shift of the light can be made larger by making the arm-length larger. A detector with arm-length $l = 4km$ responds to a GW with an amplitude of 10^{-21} with

$$\delta l_{GW} \sim \frac{1}{2} hl \sim 2 \times 10^{-18} m \tag{7.4}$$

where δl_{GW} is the change in the length of one arm. If orientation of interferometer is optimum, then the other arm will change by the same amount in the opposite direction so that the interferometer fringe will shift by twice this length [131].

Direct detection of GWs is based on interferometry, first Earth-based interferometers- LIGO and Virgo are following two dual-recycled Fabry-Perot Michelson interferometer structure [471, 490]. A laser interferometer is typically a pair of L-shaped arms where a laser beam is split at the intersection of two arms in order to measure the length of these arms. Half of the laser light is transmitted into one arm whereas the second half is reflected in the second arm. Mirrors are suspended as pendulas at the end of each arm and near the beam splitter. In order to increase the arm-length artificially, one can bounce the light back and forth in these arms to increase the interaction time with gravitational waves. With sufficiently large mirrors, a *Herriott delay line* [491] can be constructed with hundreds of bounces [492]. It was subsequently proposed by [493] to use Fabry-Perot optical resonators in place of the delay lines. Such interferometers measure the phase difference caused by passage of incoming GWs which stretch one arm as they compress the other one.

The goal of LIGO- *Laser Interferometer Gravitational Wave Observatory* [271, 494] is to detect and study GWs emitted by sources of astrophysical sources which include BNS, BBH, BH-NS systems, a stellar core collapse triggering type II supernovae, rapidly rotating, non-axisymmetric NS system and possibly stochastic GW background. The two co-located LIGO detectors are located at the same sight in Hanford, WA, one with 4km arms which are referred to as H1 and H2 respectively and another LIGO interferometer of 4km arm length in Livingston, LA, referred to as L1. Each site hosts each 4-km long interferometer (At Hanford there is a cluster of 4 km and a 2 km detectors in the same vacuum system and at the Livingston there is a single 4 km detector oriented to be as nearly parallel as possible to the Hanford detector.) inside a vacuum envelope with a primary interferometer optics suspended by a cascade, quadrupole suspension system in order to isolate them from external disturbances. The two detectors

are placed so that their antenna patterns overlap as much as possible and yet they are far enough apart that there will be a measurable time-delay in most coincident bursts of gravitational radiation which would give some directional information. The interferometer is illuminated by $1064-$ nm wavelength Nd:YAG laser, stabilized in amplitude, frequency and beam geometry [495, 496]. The interferometer mirrors act as test masses, and *the passage of GWs induce a differential arm-length change which is proportional to the GW strain amplitude* [345]. The GW signal is extracted at the output port using a homodyne readout [497]. These two detectors have wide physical separation, $\sim$ 3000km [498] eliminating the coupling of environmental and local instrumental noise between the two detectors. While physically-separated detectors have the advantage of reduced correlated noise, they have the disadvantage of reduced sensitivity to a SGWB because physically separated detectors respond at different times to GWs from different directions and with differing response amplitudes which depends on the relative orientation and (mis)alignment of the detectors [274, 499, 500, 501]. LIGO data is publicly distributed via the Gravitational-Wave Open Science Center (GWOSC) [502]. It is worth to mention that LIGO's high sensitivity to BBHs with component masses $40 \leq m_1 \leq 100 M_\odot$ represents $\geq 90\%$ of the total sensitive volume, however absence of BHs in the mass range $50 \leq M \leq 135 M_\odot$ is one of the intriguing puzzles in GW astrophysics [503].

If we again consider the example of GW signal propagating in the $+z$ direction and choosing the Cartesian coordinates so that the interferometer's two arms lie along the x and y axis having the beam splitter at the origin, the non-zero components of the perturbation metric would be:

$$\begin{aligned} h_{xx}^{TT} &= -h_{yy}^{TT} \equiv h_+, \\ h_{xy}^{TT} &= -h_{yz}^{TT} \equiv h_\times \end{aligned} \tag{7.5}$$

And, the distance (L) between the mirror at the end of each arm and the beam splitter varies with time according to:

$$\begin{aligned} \frac{\delta L_x}{L} &= +\frac{1}{2} h_+ \\ \frac{\delta L_y}{L} &= -\frac{1}{2} h_+ \end{aligned} \tag{7.6}$$

Eq.(7.6) shows the precise change in the distance measurement by interferometers. The gravitational wave sequentially squeezes one arm while the other one is stretched. δL_x and δL_y are the variations of each arms respectively and in fact the change measured by laser interferometers is actually the change in phase of the photons travelling along the arms. Change in phase of laser photon is related to change in arm length by:

$$\delta\phi = \frac{4\pi \delta L_i}{\lambda} \tag{7.7}$$

where, $i = x, y$ and λ is the photon wavelength.

7.1.2 Advanced LIGO (aLIGO)

In spite of their early success, fundamental limitations at low frequency of the sensitivity of the second generation detectors exists because of the presence of thermal noise of the

Figure 7.3: *Top*: LIGO Livingston site from https://www.ligo.caltech.edu., *bottom*: LIGO Hanford site from https://www.ligo.caltech.edu.

suspension last stage and of the test mass, as well as the seismic noise and the related gravity gradient noise or the so-called *Newtonian noise*. This Newtonian noise cannot be mitigated by adding additional layers of seismic isolation as it is originated due to actual gravitational attraction between the test masses and the density perturbations around the detector. The Advanced LIGO gravitational wave detectors are the second generation detectors which are designed and built for the two LIGO observatories out of which one is located in Hanford site, Washington and another is in Livingston Parish, Louisiana. These two instruments are specialized version of Michelson interferometer and are both identical in design having 4km arm length. The initial LIGO detectors which were constructed in the late 1990s, operated in design sensitivity in a continuous data taking mode from November 2005 to September 2007 [504]. The LIGO Livingston and Hanford sites are shown in Fig.7.3.

Similar to initial LIGO, Fabry-Perot cavities are used in the arms to increase the interaction time with incoming GW and to increase the effective laser power, power recycling method is used. Signal recycling has been added in the aLIGO in order to improve the frequency response. In the most sensitive frequency region around 100Hz, the design strain sensitivity is a factor of 10 better than initial LIGO and

the instrument root-mean-square (rms) strain noise reached an unprecedented level of 2×10^{-22} in this frequency band. aLIGO is designed to provide a factor of 10 increase in strain sensitivity over a broad frequency band and to extend to low end of the band to 10Hz (from 40Hz) [471]. *As the probed volume of the Universe scales as the cube of the strain sensitivity, this represent an enormous increase (of order* $10\times$*)* in the number of potential astrophysical sources detectable by these instruments. This offers a possibility that at design sensitivity, aLIGO is likely to detect dozens of CBC sources per year [505].

Each observatory hosts one aLIGO interferometer with 4km arms with a third instrument for a new location in India, the so-called IndIGo project [479, 506]. The optical configuration of the aLIGO detectors is shown in upper sub-figure of Fig.7.4. As shown in the figure, the instrument is basically a Michelson interferometer with Fabry-Perot resonant cavity in each arm to build up the phase shift produced by an arm-length change. Power Recycling Mirror (PRM) forms a resonant cavity between the laser source and Michelson construction is made to increase the effective laser power. With aLIGO, signal recycling is added to the interferometer [507]. The Signal Recycling Mirror (SRM) at the anti-symmetric output of the Michelson is used to effectively lower the arm cavity fitness for GW signals and thereby maintain a broad detector frequency response. Fig.7.4 shows the simplified layout of aLIGO for O3:

At the input part, there is a pre-stabilized laser light at 1064nm with the phase modulating electro-optic modulator with three radio frequencies used for length and angular control. Fabry-Perot cavities increase the light interaction time with GWs, and these arm cavities are formed from Input Test Masses (ITMs) and End Test Masses (ETMs). The signal recycling cavity formed with signal recycling mirror and the ITMs broadens the detector bandwidth [510, 471].

7.1.3 Virgo

The Virgo interferometer is a French-Italian detector with 3km arms is located at the Cascina near Pisa, Italy [511]. In most respects Virgo is similar to LIGO with a major difference that Virgo implements a very sophisticated seismic isolation system and control of vibrational noise, promising extremely good low frequency sensitivity. Its goal is to observe at the lowest possible frequencies from the ground, at least partly to be able to examine as many pulsars and neutron stars as possible. The aerial view of the Virgo site is shown in Fig.7.5.

Thanks to aLIGO-AdV, not only physics of gravitational waves can be studied but also the cluster of detectors have enabled novel tests of general relativity including direct study of polarization of GWs [512, 513] in addition to being an excellent laboratory for SGWB tests. In the next days, with the cluster of aLIGO-AdV detectors, galactic and extragalactic continuous GWs from neutron stars [514, 515, 516, 517, 518, 519, 520, 521, 522, 523, 524] and boson clouds around spinning black holes are expected to be detected [455]. Other anticipated events including supernovae [525], cosmic strings [390], previously unidentified source [526, 527] or SGWB [528, 454] is expected to be detected [128].

The advanced versions of LIGO and Virgo are designed to operate in the frequency range $\approx 10 - 10^3$Hz whereas space-based detectors will cover the range between $10^{-4} - 10^{-1}$Hz which are expected to be able to measure gravitational wave strains less than $h \simeq 10^{-21}$. At the lower frequency level, the Pulsar Timing Arrays will detect

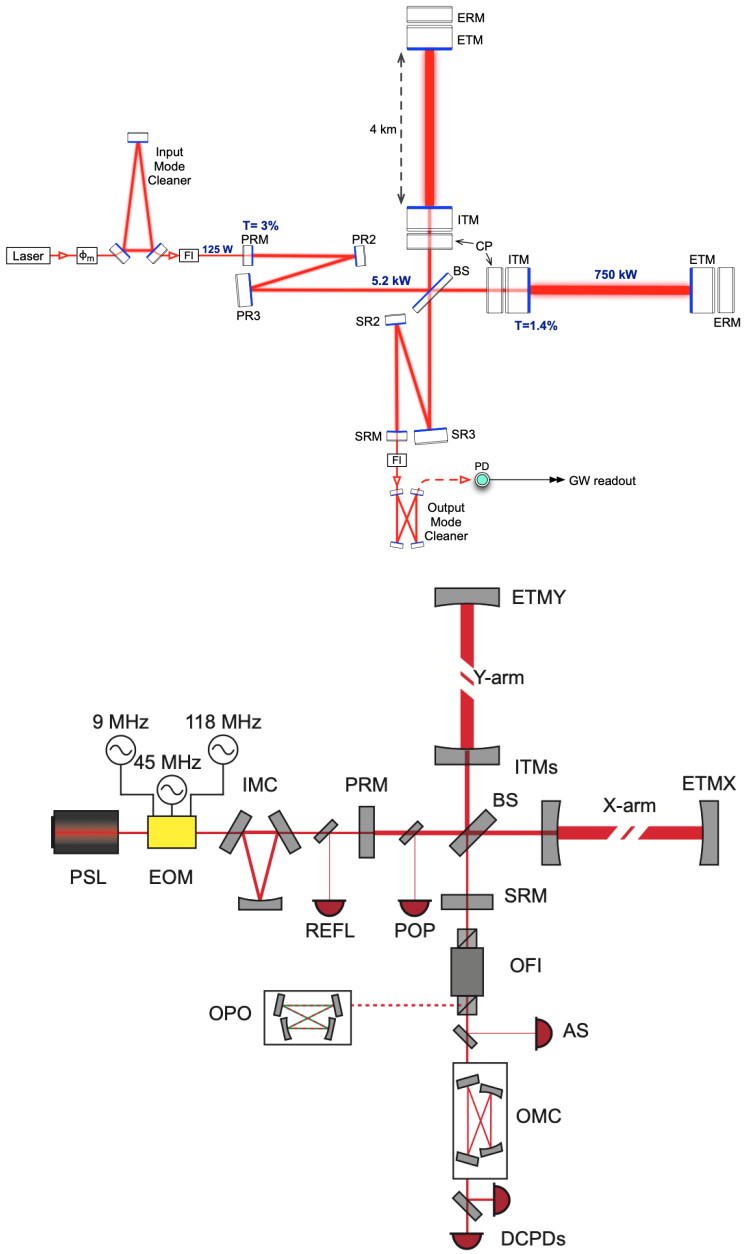

Figure 7.4: *Top*: Advanced LIGO optical configuration from [471]. The mirrors at the input and end of both arms (labelled respectively ETM and ITM) are suspended form quadrupole-stage pendulums in addition to active seismic isolation systems [508]. *bottom*: O3 configuration of aLIGO from [509].

GWs in the range around 10^{-8}Hz. Measurement of CMB polarization will also help us to probe gravitational events at about 10^{-16}Hz. In addition to these experiments, GEO600 with 600m arms which is located near Hannover, Germany [529, 530, 531] is a intereferometer constructed by German-English collaboration. GEO600 with 600m is a leading-edge-technology detector where high performance suspensions and optical tricks like recycling has been applied. Despite its shorter arms, GEO600 with 600m achieves sensitivity comparable to the multi-kilometer instruments using advanced interferometer techniques. Other such mission includes *TAMA* 300 which is a three hun-

Figure 7.5: Aerial view of the Virgo site from https://www.ligo.caltech.edu.

dred meter interferometer operating near Tokyo [532, 533] operates with cryogenically cooled mirrors.

7.1.4 Einstein Telescope

The Einstein Telescope (ET) is an upcoming underground telescope aimed to test Einstein's theory of General Relativity in strong gravity regime. In order to minimize seismic noise and improving the sensitivity at few hertz range, the detector will be placed in the underground region with a depth of $100-200$m. Also cryogenic technology in order to prevent thermal noise will be partially implemented in order to cool down the mirrors to directly reduce thermal vibration of the test masses. The design of ET consists of three detectors arranged in a triangular pattern having each side of triangle 10 km long and composed by two arms of different detectors. The ET similar to the Cosmic Explorer which we discuss below will also consist of three nested detectors, each composed of two interferometers with arms 10 km long. One interferometer will detect low frequency GW signals (2-40 Hz), while the other one will detect the high frequency components. The configuration is designed to allow the observatory to evolve accommodating successive upgrades until reaching a sensitivity expected 100 times more than current instruments.

Each individual detector will comprise two independent interferometers: one working at the low frequency range: $1.5 - 30$Hz and the other at high frequencies 30Hz $- 10$kHz. The one dedicated to the high frequency GWs will operate at room temperature and the interferometer laser will be emitted at a power about 3MW. For the low frequency detector, a cryogenic technology will be used in order to operate at the temperature of 10K and to use a laser power of 18kW. Bottom sub-figure of Fig.7.6 shows the target sensitivity curves of ET compared with those of advanced Virgo:

Deci-Hertz Interferometer Gravitational Wave Observatory The Deci-Hertz Interferometer Gravitational Wave Observatory (DECIGO) is a Japanese space-based

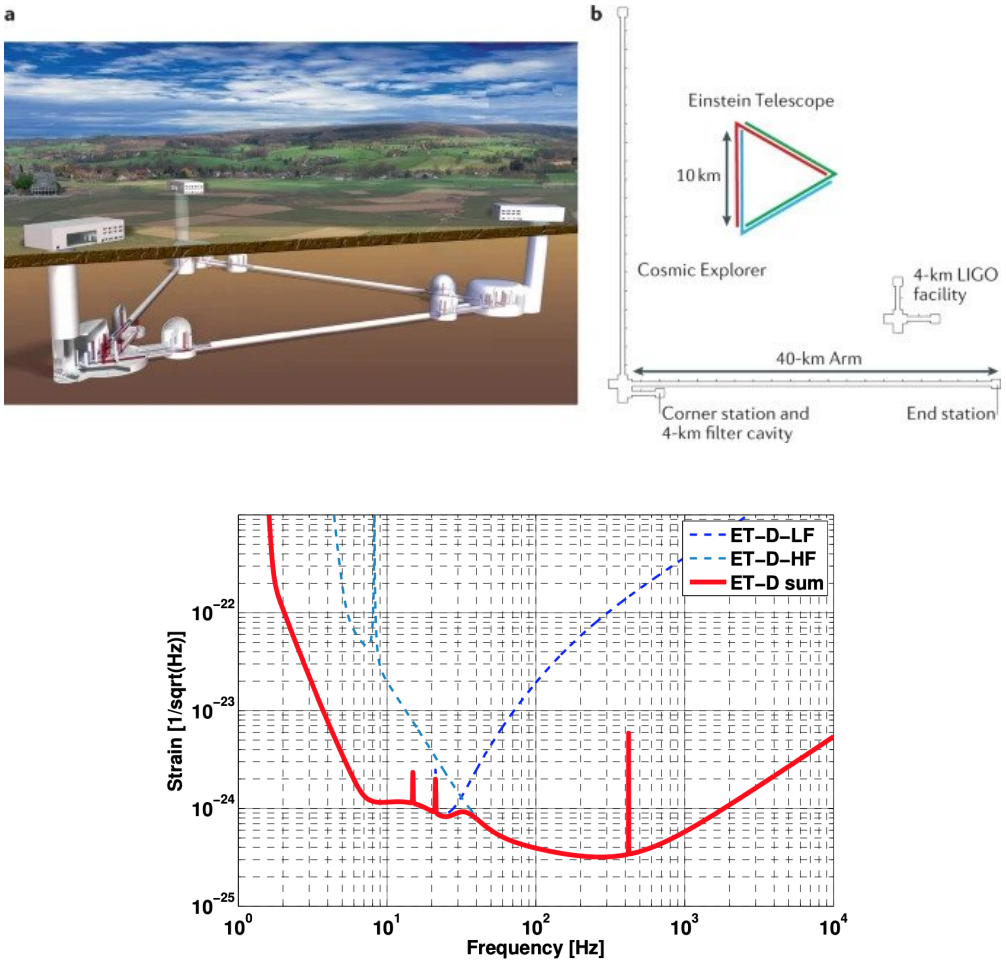

Figure 7.6: *Top*: ET configuration, *bottom*: The separate contributions from the LF (lower frequency) and HF (Higher frequency) instruments to the sensitivity of ET, original plot taken from [534].

observatory in a triangular constellation of satellites orbiting around the Sun. It is a detector with two 10^4km triangular interferometers forming a star-like shape, along with two additional triangular interferometers on independent orbits for improved sky localization, resulting into a total 8 independent interferometers. The interferometry will be sensitive in the band between 0.1Hz and 10Hz with separation about 1000km [535].

7.1.5 Cosmic Explorer

Cosmic Explorer (CE) is a ground based next-generation detector designed with the "L" configuration similar to LISA and Virgo Collaboration (LVC) but with 40km long arms to improve measurement sensitivity significantly [536]. This concept maximizes the scientific output as the 40 km detector can be optimized for deep broadband sensitivity, while the 20 km detector is capable of tuning its sensitivity to the physics of neutron stars after they have merged. These arm-lengths are enclosed in ultra-high vacuum tubes with cryogenic technology to allow up to an order-of-magnitude improvement to aLIGO's design sensitivity O5. This cryogenically cooled vacuum tubes will enable to

perform CE's sensitivity below 10 HZ. With ten times the sensitivity of aLIGO, CE will push the reach of GW astronomy towards the edge of the observable Universe $z \sim 100$ [537]. CE will map the population of compact objects across time, detect mergers of first black holes that contributed to seeding the Universe's structure, and reveal the processes that create black holes and neutron stars along with finite-temperature region of the quantum chromodynamics phase space. Three fundamental science themes CE will address are as follows:

- black holes and neutron stars throughout the cosmic time,
- dynamics of dense matter,
- extreme gravity and fundamental physics.

The optical layout of the CE configuration is shown in Fig.7.7:

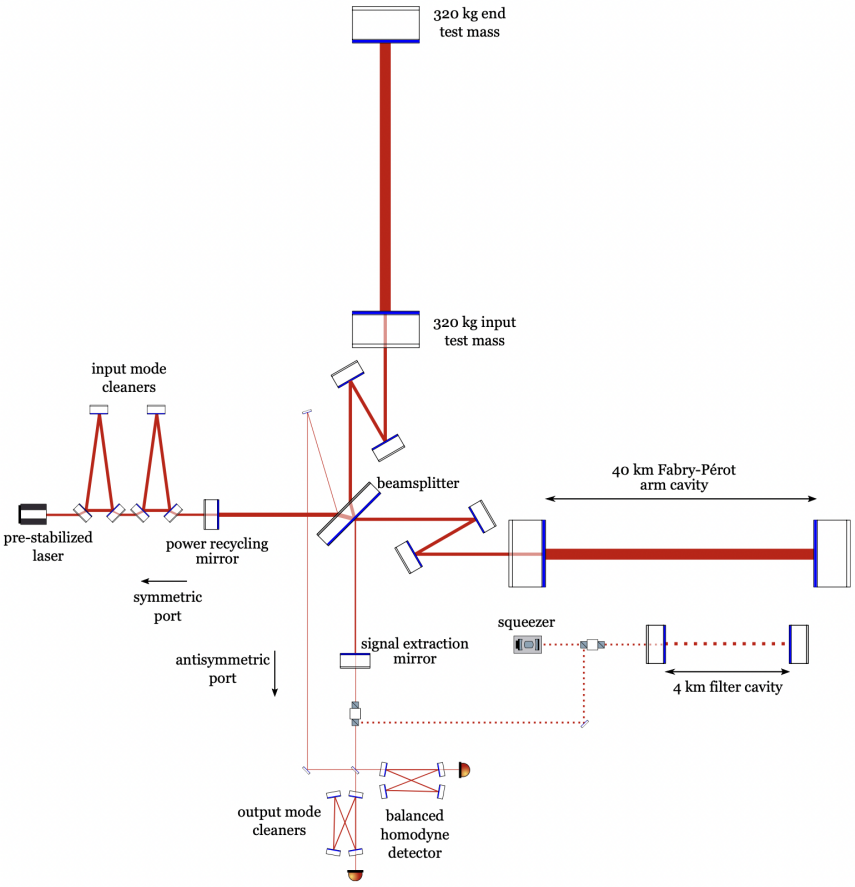

Figure 7.7: Optical layout of the Cosmic Explorer detector concept, original image taken from [537].

CE interferometry All direct detection of gravitational waves till date have been made with laser interferometers using Michelson interferometers enhanced with optical cavities in the so-called "dual-recycled Fabry-Perot Michelson" (*DRFPMI*) configuration. The longer arm-length will increase the amplitude of the observed signal with

effectively no increase in the noise. The DRFPMI is shown in top subfigure of Fig.7.7 is the improved version of the Michelson interferometer. In this configuration, the input test masses are added to each arm to make Febry Perot cavities which increases the power stored in the arms and decreases the quantum shot noise. Also, a *power recycling mirror* is added to the symmetric port which further increases the power stored in the interferometer and provides positive filtering of laser noise. Finally, a *single extraction mirror* is added to the antisymmetric port which forms a *single extraction cavity*. The bandwidth of the interferometer can be tuned to enhance the sensitivity relevant for a particular science case by simply changing the reflectivity of the mirror. This entire structure of input and end test masses from two arm cavities together with the beam splitter, power recycling mirror and signal extraction mirror comprise the core of the DRFPMI. CE will use large 320kg test masses made into highly reflective mirrors through the use of thin-film coatings consisting of alternative layers of high and low refractive index materials. The more massive test masses serve to reduce quantum radiation pressure noise.

The light carrying the GW signal is spatially filtered and read out from the antisymmetric port by a balanced homodyne detector comprised of two photodiodes and output mode cleaners. A high power laser is injected into the symmetric port of the interferometer after passing through two input mode cleaners which assist in producing a frequency and intensity stabilized beam with a spatially clean mode. The squeezer generates squeezed vacuum states which are reflected off of a filter cavity and injected into the antisymmetric port to provide broadband quantum noise reduction. The beamsplitter is shown with the high reflective surface facing the antisymmetric port rather than the laser, unlike current detectors to minimize loss in the signal extraction cavity. The CE sensitivity curves showing the lead in the sensitivities of current and upcoming detecting missions are shown in Fig.7.8:

7.2 Space based detectors

In this section, we describe how GWs can enter the territory of the unknown and bring us the information about the early cosmos by shifting the detection missions to the space. By such missions, thanks to negligible seismic noises and nose reduction methods, we can expect to hear the cosmic sounds from the very far objects.

7.2.1 Laser Interferometer Space Antenna

Laser Interferometer Space Antenna (LISA) has been proposed as a joint NASA-ESA project which is now a project lead by ESA with the support of NASA. LISA is expected to detect GW induced strains in space by measuring changes of the separation between fiducial masses in three spacecraft triangle separated by about 5 million kilometers. As a first step, LISA Pathfinder was launched in December 2015 to test in the flight the concept of low-frequency gravitational wave detection. It put two test masses in a near perfect gravitational free-fall, controlled and measured their motion with unprecedented accuracy. For this, it used inertial sensors, a laser metrology system, a drag-free control system and an ultra-precise micro-propulation system [241]. The result of the experiment was the finding that the test masses in the spacecraft are falling freely through space under the influence of gravity alone and remained unperturbed

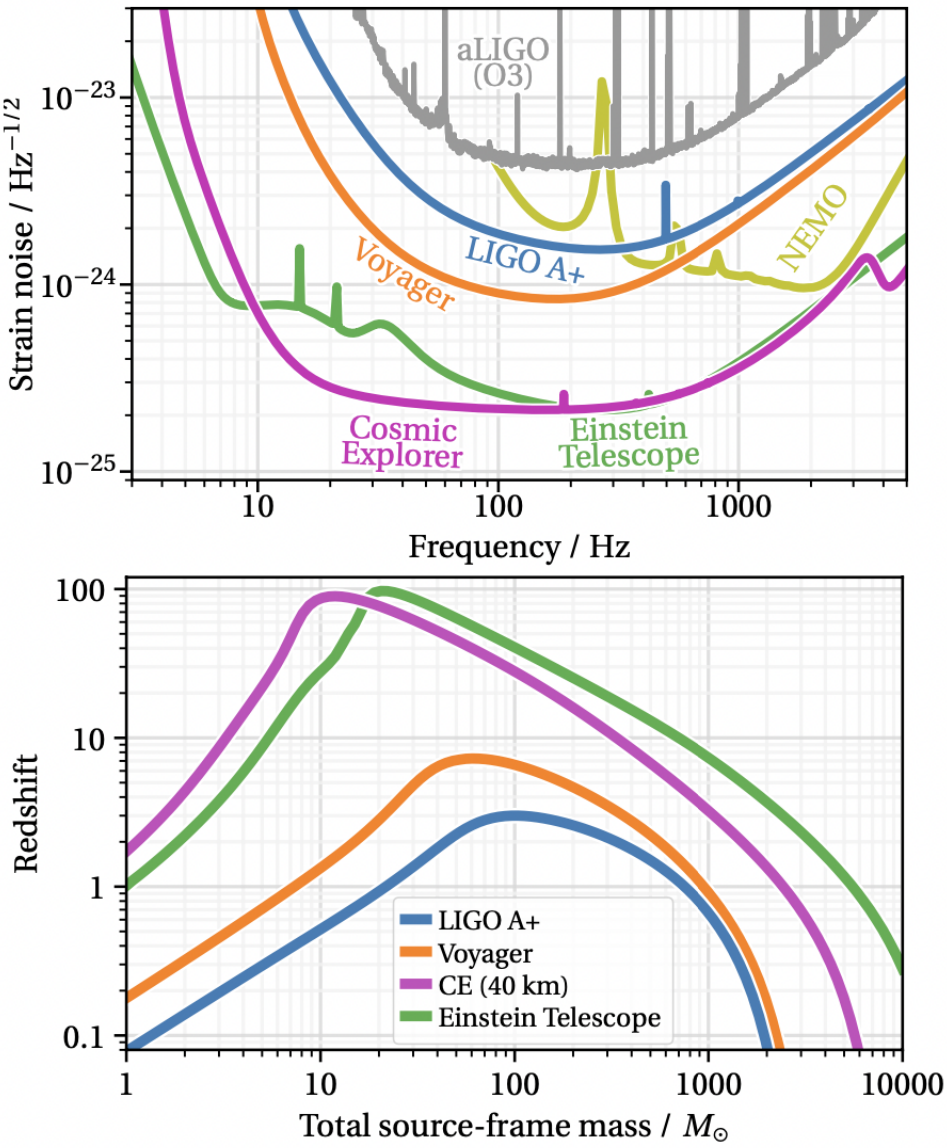

Figure 7.8: *Top:* Amplitude spectral densities of detector noise for CE, the current (O3) and upgraded (A+) for aLIGO, LIGO, NEMO and the three paired detectors of triangular Einstein telescope. At each frequency the noise is referred to the strain produced by a source with optimal orientation and polarization. *Bottom*: maximum redshift (vertical axis) at which an equal mass binary with with an SNR of 8 is shown. Different curves represent different detectors. For BNS, CE will probe $z > 1$ where most of the mergers are expected to happen. For BBHs, it will able to explore redshifts of 10 and above, where mergers of black holes are formed either by the first stellar population in the Universe or by early quantum fluctuation/ primordial black holes might be found. These two images show the leap in the sensitivity between the 2G and 3G detectors with image taken from [537].

by other external forces to a precision substantially better than the required one.

LISA is the first space mission to probe the lowest frequency regime of the Universe which would shed light on the formation of first seed black holes, explore redshifts $z \sim 20$ prior to the epoch of cosmic reionization and also examine systems of Super

Massive Black Holes (SMBHs) with mass $\approx 10^8 M_\odot$. LISA which is expected to be launched in 2034 would be the first mission to study the entire Universe with GWs and would be all-sky monitor providing closet ever view of the TeV scale Universe. The LISA mission will scan the entire sky as it follows behind the Earth in its orbit, obtaining both polarisations of the GWs simultaneously, and will measure the source parameters with astrophysically relevant sensitivity in a band from below 10^{-4}Hz to above 10^{-1}Hz. At about $\approx$ mHz approximately 10^{-20} strain resolution can be achieved. The observatory consists of three arms ($L \simeq 5 \times 10^6$km) [123] with six active laser links between three identical spacecrafts in a triangular formation separated by 2.5 million km. The system of three arms and three identical spacecrafts in a triangular formation in a heliocentric orbit would trail the Earth by 20° and the Sun with 60° inclination w.r.t. the plane of inclination. These three arms can be combined in different ways to form two independent interferometers. During the mission, the configuration of the spacecraft rotates in its plane and the plane rotates as well, leading to sweeping the sky by LISA's antenna pattern. Continuously operating laser hetrodyne interferometers measure with pm/$\sqrt{Hz}$ sensitivity in both directions along each arm, using well-stabilized lasers at 1064nm delivering 2W of power to the optical system. The Interferometry Measurement System is using optical benches in each spacecraft. They will be constructed form ultra-low expansion glass-ceramic to minimize optical path length changes due to temperature fluctuations. 30 cm telescopes transmit and receive the laser light to and fro from the other spacecraft. Three independent inteferometric combinations of the light travel time between the test masses are possible which allows the data processing on the ground the synthesis of two virtual Michelson interferometers plus a third null-system which is known as the "Sagnac configuration". The two independent Michelson interferometers allow simultaneous measurement of the two possible polarisations of GWs and the Sagnac combination can be used to characterise the instrumental noise background. A mission lifetime for LISA is expected to be 4 years extendable to 10 years. The proposed orbit for LISA is an Earth-trailing heliocentric orbit between 50 and 65 million km from Earth [538]. In order to guarantee that the intereformetry is not disturbed by external forces such as fluctuations in solar radiation pressure, the mirror that is the reference point for the interferometry is on a free mass inside the spacecraft. The spacecraft acts as an active shield, sensing the position of the free mass, firing the jets to counteract external forces on itself and ensure that it does not disturb the free mass. This aspect is known as the *drag-free control* [131]. The entire orbital configuration of LISA is shown in top and the expected sensitivity and some potential signals for LISA mission are shown in the bottom of the Fig.7.9 and the expected GW spectral energy density for different values of tensor spectral index corresponding to the consistency relation $r = -8n_T$ is presented in below part of Fig.7.10 respectively:

LISA being the first promising space mission would probe the expansion of the Universe using GW sirens at high redshifts and a broken power-law stochastic background from early Universe. LISA would be the mission to probe low frequency GWs $\approx$ 0.3mHz to about 0.1Hz which will allow us to investigate the history of the Universe when it was less than 200 million years old, test gravity in the dynamical sector and in the strong field regime. The LISA mission will be able to simultaneously observe a GWB produced by the superposition of large number of independent sources of astrophysical or cosmological origin [540], in the LISA frequency band $[10^{-5}, 1]$Hz different independent sources can be distinguished including the galactic foreground from Dou-

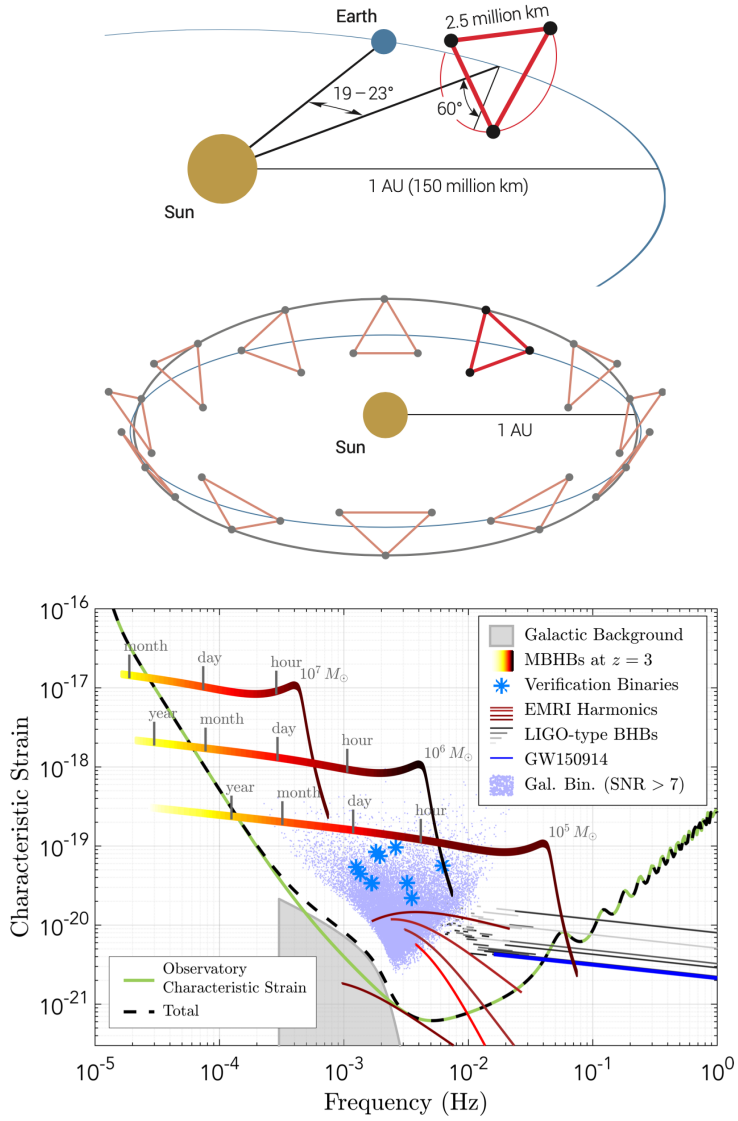

Figure 7.9: *Top*: Depiction of the LISA orbit from [538], *bottom*: Examples of GW sources in the frequency range of LISA compared with its sensitivity for a 3 arm configuration. The data plotted are in terms of dimensionless characteristic strain amplitude [538].

ble White Dwarf binaries in our galaxy [541] observed as a modulated waveform [542] and the astrophysical background produced by BBH and BNS systems which can be predicted from the LIGO/Virgo detections. LISA will be able to detect known binary star systems in the Galaxy and binary coalescence of SMBHs everywhere in the Universe. Also LIGO/Virgo and LISA are able to place model-independent constraints on the stochastic signal from exotic compact objects such as GW emission from compact, horizonless spinning BHs or the black hole mimickers [543]. The ability of LISA to measure the GWB created by cosmic strings has been analysed in [544]. LISA will be able to probe cosmic strings with tension $G_\mu \geq \mathcal{O}10^{-17}$, improving by about 6 orders of magnitude current Pulsar Timing Array (PTA) constraints and about 3 orders of magnitude with respect to expected constraints from next generation PTA observato-

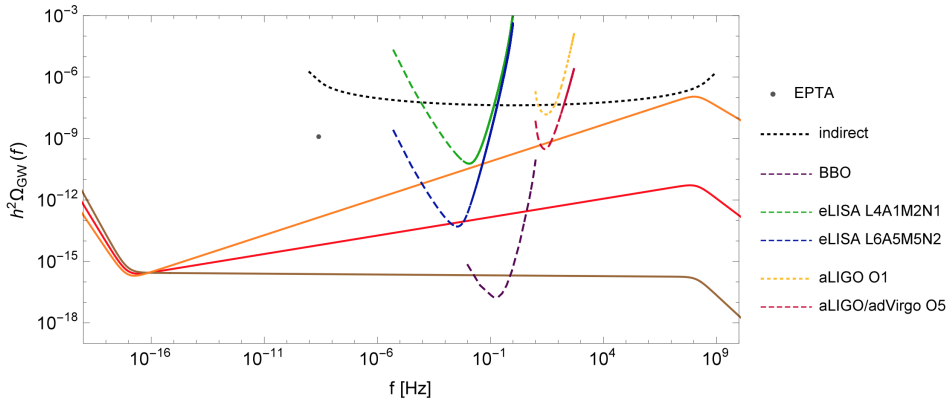

Figure 7.10: GW spectral energy density for different values of n_T are shown with solid lines: $n_T = -r/8$ (brown), $n_T = 0.18$ (red) and $n_T = 0.36$ (orange). The r value is fixed at $r_{0.05} = 0.07$ which is also assumed $T_R = 10^{16}$GeV. Short dashed lines are current bounds related to: aLIGO data corresponding to O1: 2015-16 (yellow), combined analysis of Planck data, BAO and BBN measurements providing integral bound of $\approx \Omega_{GW} < 3.8 \times 10^{-6}$ (black), gray dots corresponding to the bound provided by EPTA (assuming $n_t = 0$). Long dashed lines showing expected power law integrated sensitivity curves for the following missions: BBO (violate), eLISA mission L6A5M5N2 (blue), eLISA mission L4A2M2N1 (green) and aLIGO-AdV O5: 2020-22 (magenta) [239]. The eLISA configuration is described in [539].

ries. The sensitivity of LISA to detect anisotropies of SGWB is investigated in [415]. Also LISA, in addition to advance ground based detectors can probe non-Gaussian and polarized cosmological background as analysed in [406].

In addition to LISA, in 2013 the European Space Agency has approved a GW observatory in space as the L3 mission of its "Cosmic Vision Program" scheduled for lunch around 2030-2034 for which the *evolved LISA* ("e-LISA")- space-based interferometer is the main candidate which is designed to probe the mHz region [545]. eLISA low frequency noise level has been recently tested by the LISA pathfinder mission [3] and according to the first result [546], the expected noise is about one hundred times better than the original requirement of the instrument. The capability of eLISA in probing the acceleration of the Universe and forecast of capability to constraint models of early and interacting dark energy has been developed using GWSS in [547] and [548] respectively. The sources expected to be probes by LISA are as follows [123]:

- Galactic compact objects (BNS, BBHs) in the Milky way would be numerous such that their signal can be interpreted as background noise by LISA, other objects such as supermassive black holes at about $z \simeq 15$ can be detected few times per year,
- Periodic emitters (in the high frequency band) such as isolated neutron stars,
- Coalescing binaries containing black holes formed following the merger of galaxies or pregalactic structures hosting black holes at their cores. Depending on the

[3] https://sci.esa.int/web/lisa-pathfinder

mass of the binaries, the waves from these coalescence could detect fairly large redshifts ($z \sim 5 - 10$) possibly probing an early epoch of cosmological structure formation [343].

- Very low frequency region $10^{-9} \leq f \leq 10^{-7}$Hz, and
- Ultra low frequency $10^{-18} \leq f \leq 10^{-13}$Hz belonging to very early (inflationary) phase of the Universe.

7.2.2 Big Bang Observer

The *Big Bang Observer* (BBO) is a space-based interferometer developed by ESA aimed to detect GWs of cosmological origin. BBO will consist of three different constellations of satellites, two of them composed of three spacecrafts in triangular configuration and the third one with six spacecrafts in a hexagram configuration. The design of BBO is similar to LISA but with twice as many proof masses separated by a shorter distance ($\simeq 100$) times shorter, forming a "Star of David" design. The expected sensitivity of BBO lies in $\simeq 0.1 - 1$Hz frequency range. The sensitivity will improve from LISA with laser power of 300MW for each laser. The distance between the spacecrafts in BBO would be 50000km. Fig.7.11 shows the basic structure of the mission:

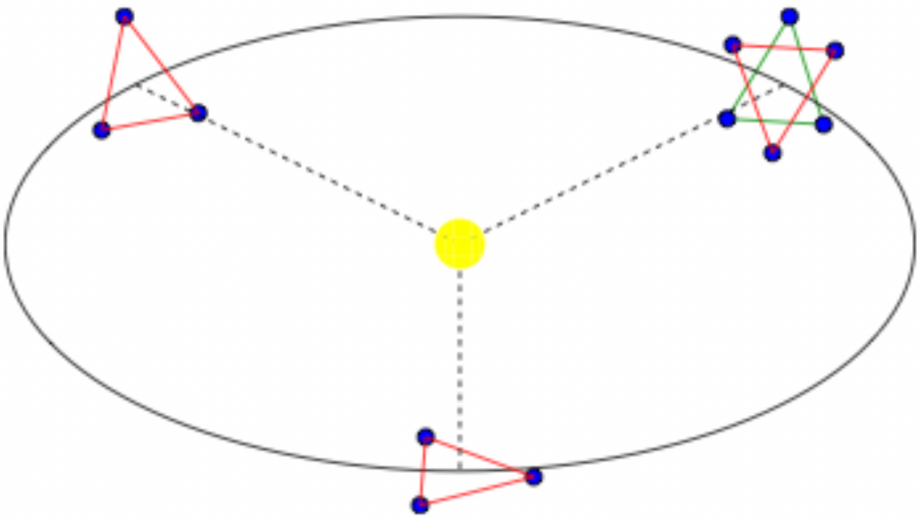

Figure 7.11: Proposed design for the BBO from [549].

Since we are entering the realm of observational GW astronomy thanks to LIGO [471], Virgo [474], KARGA [550] and global observatory network [479], number of detection of GW signal in the range $10 - 1000$Hz has increased [551]. Simultaneously, GW searches in the nHz band with PTAs [552, 553, 554, 555] are expected to make their detections in the coming few years. By the mid 2030s, these experiments are expected to be strengthen by third generation interferometers such as ET [480] and LISA [538] which will shed light on mHz frequency band. [556] have shown that third generation ground based GW detectors such as Einstein Telescope and Cosmic Explorer will have sensitivities sufficient enough to directly observe almost every coalescing BBH

event in the Universe by subtracting confusion background potentially at the level of $\Omega_{GW} \simeq 10^{-13}$ after five years of observation and also opening possibility to detect PGWB. The problem of successfully subtracting confusion noise/binary foreground has been discussed in [557, 558] in the context of Big Bang Observer. The strain sensitivity for different detectors is shown as below in Fig.7.12:

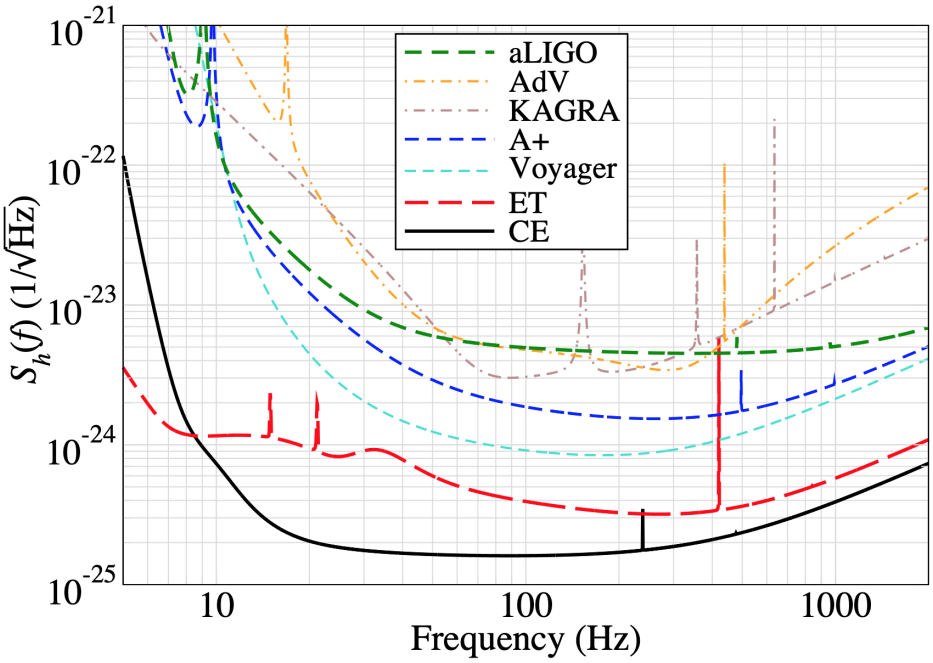

Figure 7.12: Designed power spectral density of second generation detectors: aLIGO, AdV, KAGRA and proposed sensitivity of third generation detectors ET and CE along with expected intermediate sensitivities such as Advanced LIGO Plus ($A+$) and Voyager [556].

As shown in Fig.7.12, we can investigate the evolution of number of detections as the detector sensitivity increases from second to third generations and the number of detections in the network increases from three to five: two advanced version of the LIGO detectors were joined by Virgo and KAGRA. In summary, the observational landscape is intriguing and covers large band of frequencies: at extremely low frequencies $\sim 10^{-16}$Hz bounds mainly come from the analysis of CMB B-modes while at low frequencies at the order $\sim 10^{-10} - 10^{-6}$Hz there lies Pulsar Timing Arrays (PTA) such as the radio telescope Parks Pulsar Timing Array[4] (PPTA), the Large European Array for Pulsar Timing [5] (LEPTA) and the upcoming International Pulsar Timing Array [6] (IPTA). At the frequency range $\sim 10^{6} - 10^{0}$Hz detection depends on space-based detectors such as Laser Interferometer Space Antenna [7] (LISA) and the evolved Laser Interferometer Space Antenna [8] and finally at high frequencies ($10 - 10^{5}$Hz) we

[4]http://www.atnf.csiro.au/research/pulsar/ppta/
[5]http://www.leap.eu.org
[6]http://www.ipta4gw.org
[7]https://www.lisamission.org
[8]https://www.elisascience.org

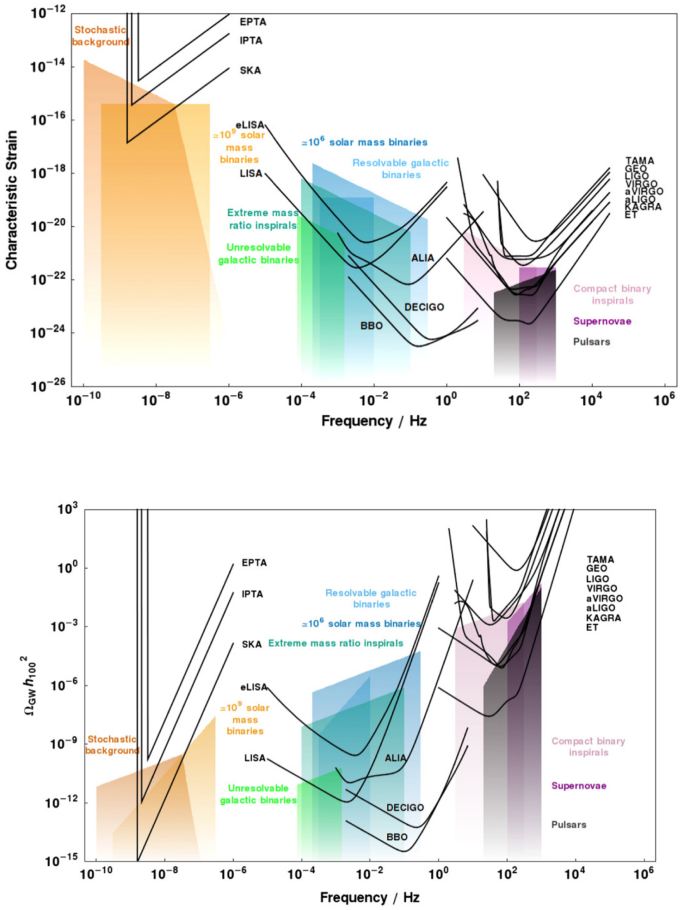

Figure 7.13: *Top*: Characteristic strain against frequency for a variety of detectors and sources [258], *Bottom*: Dimensionless energy density in GWs against frequency for a variety of detectors and sources [258].

have LIGO and its advanced version aLIGO, Virgo [9], the Einstein Telescope [10] and Cosmic Explorer [481]. Thanks to the higher sensitivity, SGWB generated by inflationary and post-inflation related mechanism can be probed by LIGO/Virgo, LISA or ET [240, 239, 559, 342]. In the absence of direct detection of SWGB of either astrophysical or cosmological origin, the upper bounds placed on GW energy density Ω_{GW} from different cosmological probes include: $\Omega_{GW}(f = 25\text{Hz}) < 4.8 \times 10^{-8}$ from LIGO/Virgo, $\Omega_{GW}(10^{-10} < f < 10^{-6}\text{Hz}) < 1.3 \times 10^{-9}$ from PTA [560], also in case of anisotropic upper bound $\Omega_{GW}(f = 25\text{Hz}) < 6 \times 10^{-8}$ from LIGO/Virgo O1+O2 and $\Omega_{GW}(f = 1\text{yr}^{-1}) < 3.4 \times 10^{-10}$ [409]. Plots 7.13 respectively shows different detectors and sources showing characteristic strain and dimensionless energy density in GWs against frequency.

It is important to note that there exist a well-known gap roughly at $10^{-7} - 10^{-4}$Hz frequency in the GW landscape between the sensitivity band of PTA and upcoming space missions such as LISA. This μHz gap can be filled by using "astronomical scale detectors" which is quite futuristic proposal however, [561] proposed searching for the deviations in the orbits of binary systems caused by their resonant interactions with

[9] https://www.ego-gw.it/public/about/whatIs.aspx
[10] http://www.et-gw.eu

GWs. This work shows that Lunar Laser Ranging (LLR) and timing of binary pulsars can place stringent new bounds in the μHz band, while Satellite Laser Ranging (SLR) can be used to explore the LISA band even before LISA flies. Fig.7.14 shows the power-law integrated (PI) sensitivity curves along side the sensitivity curves of various other current and future GW experiments. For each of the binary resonance probes two sensitivity curves: one reflecting data available in 2021 and another one which should be available in 2038 by which time LISA is expected to have completed its nominal 4-year mission. In the late 2030s, in addition to LISA, highly sensitive SGWB searches by the ET, the Square Kilometer Array (SKA) [562] and some km-scale versions of the atom interferometers like AION [563] or MAGIS [564] which occupy the frequency band between LISA and ground based interferometers are expected to join the searches.

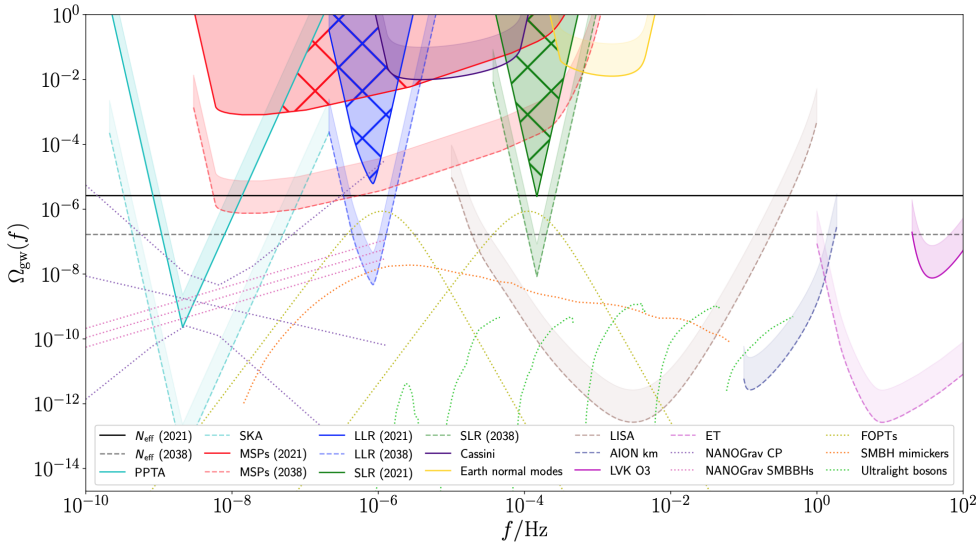

Figure 7.14: SGWB sensitivity curves of current and upcoming GW experiments, solid curves indicate results from LIGO/Virgo/KAGRA (LVK) collaboration, gravimeter monitoring of the Earth's normal modes, Doppler tracking of the Cassini spacecraft, pulsar timing by the Parkes PTA, indirect constraints from N_{eff}, and expected present day sensitivities of binary resonance searches with binary millisecond Pulsars (MSP), LLR and SLR. The shaded region shows the numerical results and the dashed curves indicate binary resonance forecast sensitivities for 2038 along with expected bounds from LISA, ET, SKA, AION and improved N_{eff} constraints. The purple curves indicate the possible signal identified by NANOGrav, the yellow curve shows two First Order Phase Transition (FOPT) spectra, the orange curve shows the predicted spectrum from a population of horizonless Super Massive Black Holes (SMBH) mimickers, and the pale green curve show the predicted spectra for ultralight bosonic condensates around SMBHs [561].

7.3 Pulsar Timing Array

An array of millisecond pulsars distributed across the sky can be used to span the region of ultra-low (nanoHertz) [565] range of frequency spectrum (the domain of SGWB and

GWB by SMBBHs) by searching a correlated signal of arrival time from Pulsars arising from the influence of gravitational waves at the Earth. Third generation ground-based laser interferometers such as ET and CE would be more sensitive in the frequency range $\simeq 1 - 10^4$Hz. However, to observer compact object systems in their earlier phases alongside other low frequency ($[10^{-5}, 1]$Hz) sources such as Extreme Mass Ratio Inspiral (EMRIs) and merging SMBBHs, we need space-based detectors that bypass problems due to seismic noise of the Earth. The Pulsar Timing Array is such a potent methodology which in synergies with other space-based mission such as LISA can help to uncover the sources lying so far and hence can help us to hear the whispers of the very infant Universe. Pulsar Timing Arrays (PTAs) use sets of extremely well-timed pulsars as a Galaxy scale detector [566] with arms extending between Earth and each pulsar in the array.

Neutron stars (NSs) are the collapsed cores of massive stars that have undergone a supernova explosion after the end of nuclear burning and are supported by neutron degeneracy pressure to prevent further collapse [567, 568, 569]. Since NSs are more compact than their progenitor stars, they tend to exhibit very short rotational periods and extremely strong magnetic fields. The magnetic axis is generally not aligned with the spin axis, so the resultant magnetic dipole radiation in the atmosphere of the NS is swept around in space. Depending on the orientation of the beam and its width, Earth may covered by the radiation beam once per rotation which causes the NS to be detected as a source of pulsed radiation or the "pulsar". Below Fig.7.15[11] represents the PTA centering the Earth:

Figure 7.15: Illustrative representation of the Earth embedded in space-time which is deformed by the GWB and its effects on the radio signals coming from observed pulsars.

A pulsar is a highly magnetized, rapidly rotating neutron star that emits beamed radio and high energy X-ray or γ-ray radiation. A pulse of radiation is seen each time the beam crosses the line of sight of an observer which gives rise to a *pulse profile* which

[11] http://nanograv.org/press/2021/01/11/12-Year-GW-Background.html

encodes the information about the structure of the magnetosphere and the emission process [570]. This pulse profile and the rotation of the pulsar itself are observed to be very stable over long timescales. These two factors allow to be used as precision astronomical clocks.

Pulsars typically have periods $P \simeq 10$ms but due to loss of rotational energy, they quickly spin down to $P \simeq 0.1 - 1$s. Radio emission will continue for $\simeq 10 - 100$Myr after which a pulsar will become a quiet neutron star. However, if the pulsar exists in a binary system, it may become a *Millisecond Pulsar* (MSP), where mass and angular momentum are accreted from a companion star, spinning the pulsar back up to periods $P < 10$ms while simultaneously decreasing magnetic field to $B \simeq 10^8 - 10^9$G. Due to their lower magnetic fields, MSPs spin down much slower than non-recycled pulsars, having lifetime greater than 10 billion years [570].

The extremely precise rotational stability of MSPs makes them suitable for measuring minute deviations in the expected *Time of Arrival* (ToA) which is accomplished through phase coherent *pulsar timing* accounting for every rotation of the pulsar over time spans much greater than the star's rotational period. The pulsar ToA are not directly measured but inferred by the observed pulse profile which shows how the pulsar luminosity changes with the pulsar phases [571]. It is important to note that single pulses are too weak to detect independently and it also includes large variability between each observed pulse profile. By subtracting the observed pulsar arrival times with the expected arrival time which are known as *timing residuals*, pulsars can provide information about the the effect of passage of GWs. A common procedure used to increase the SNR [572] and to improve detection stability is to produce the integrated pulse profile taking the average of a series of pulses. This reduces the uncorrelated Gaussian noise, giving more clean and stable pulse profile. Then the corresponding ToA is obtained by cross-correlating it with high signal-to-noise template which typically is the sum of pulse profiles over many epochs [573]. The effect of GWs on pulsar timing was first described by [574] and recently by [575]. A GW passing over the Earth-pulsar system will introduce a time variable redshift into the pulsed signal [566]:

$$z(t, \hat{\Omega}) \equiv (\mathbf{v}(t, \hat{\Omega}) - \mathbf{v}_0)/\mathbf{v}_0 \tag{7.8}$$

where Ω is the direction of propagation of GW, $\mathbf{v}_0$ is the reference frequency and $\mathbf{v}(t, \hat{\Omega})$ is the observed pulse frequency which is defined by the geometry of the system and the GW properties such as polarization and amplitude. The integral of these redshifts quantifies the impact on the timing residuals:

$$r(t) = \int_0^t z(t', \hat{\Omega}) dt' \tag{7.9}$$

To characterize the SGWB statistically, ensemble average of its components i.e. random variable is considered, and assuming that the SGWB is isotropic and the combination of GWB do not have any polarization components, the solution of cross-correlation of timing residuals is solely a function of pulsar angular separation. Plotting this function over angular separation gives the Hellings and Downs curve [576] as shown in Fig.7.16:

Sources of PTA Continuous gravitational wave emitted by a single supermassive binary black holes (SMBBHs) will lead to sinusoidal deviation in timing residuals, while

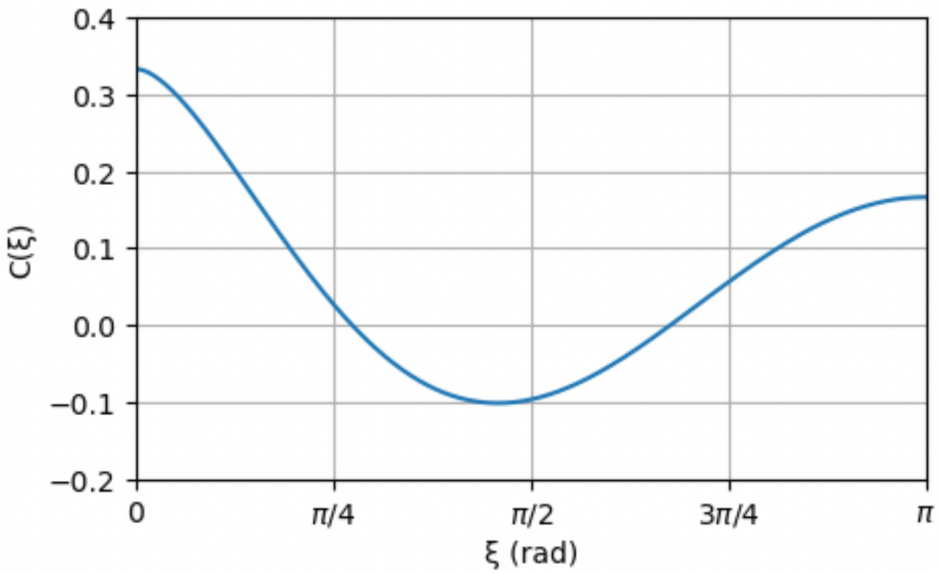

Figure 7.16: The Hellings and Downs function ($C(\zeta)$) plotted as a function of the angular separation (ζ) between the MSPs, expressed in radians. The function $C(\zeta)$ indicates the cross correlation between the monitored MSPs expected in the case of the GWB. Image taken from [571].

the superposition of all GW emitting SMBBHs in the Universe will have a stochastic signature. More precisely contributors to the GWB spanned by PTAs are as follows:

- *Continuous waves*: GWs expected from SMBBHs that are close enough to the Earth [577, 578, 579, 580],
- *GW bursts*: single GW emission events such as encounter between SMBHs and cosmic strings [333] could result into a single burst of GWs which might be detectable provided that the burst lasts sufficiently long for it to affect multiple subsequent pulsar observations and is sufficiently bright to stand out of noise,
- *Bursts with memory* (BWMs): bursts that are too faint to detect individually could still be detected as a memory event where the permanent deformation of the space-time metric [581] leaves a lasting impact on the pulse frequency causing the impact on the timing to accumulate over time.
- Early Universe sources such as cosmic strings [582, 467, 397], GWB due to phase transition [583, 584], QCD matter confinement, inflation [585, 237], dark matter and primordial black holes [586], SGWB due to other models, e.g. quantum mechanical generation of cosmological perturbations [233] etc.
- Astrophysical sources [580] and,
- Physics beyond the standard model of particle physics [587].

The Pulsar Timing Array consortium is known as the *International Pulsar Timing Array* (IPTA) [555] with the goal of facilitating GW science through data and code sharing. The North American Nanoherts Observatory for Gravitational Waves

(NANOGrav) [259, 553, 588], the European Pulsar Timing Array (EPTA) [589, 590] and the Parkes Pulsar Timing Array (PPTA) [591, 591] are the major dedicated missions for the PTAs falling under IPTA. The 12.5 year PTA data set collected by the NANOGrav (NG12) finds strong evidence of a stochastic process modelled as a power-law [592, 593] in the timing behaviours of all pulsars in data set. The resultant power spectrum estimates for a spatially uncorrelated common-spectrum process is shown in Fig.7.17:

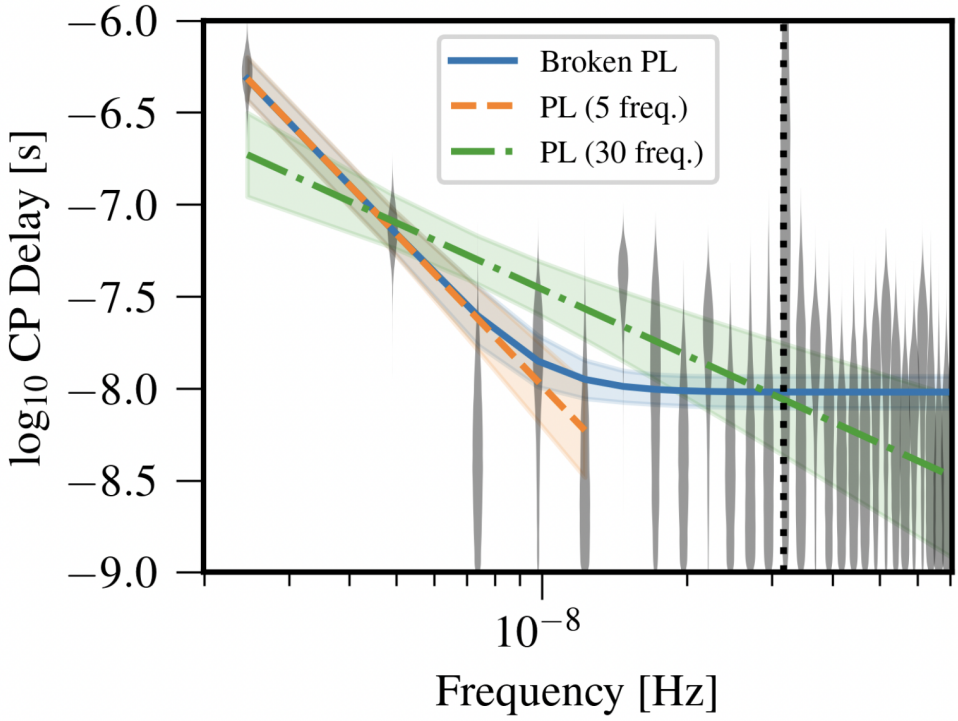

Figure 7.17: Power spectrum estimates for NG12 data set. Posterior for a common spectrum process in NG12 with four models: free-spectrum (grey violin plots), broken power law (solid blue lines and contours), 5-frequency power law (dashed orange lines and contours) and, 30-frequency power law (dot-dashed green lines and contours). Image taken from [592].

Chapter 8

Mock maps of primary and lens-induced AGWB anisotropies from the DEMNUni simulations

> The secret of getting ahead is getting started.
>
> *Mark Twain*

In this chapter, we present the methodology implemented to create from Nbody simulations mock of maps of primary and secondary (lens-induced) anisotropies in the AGWB energy density from Nbody simulations. We show, for the first time in the literature, simulated nonlinear cross-correlation signals between the AGWB density and maps of galaxy distribution, cosmic shear, CMB convergence and ISW/RS effects. To this goal we exploit mock data from the DEMNUni simulations in the ΛCDM model. In a forthcoming work we will also consider the impact of massive neutrinos and dark energy, and introduce the effect of the time derivative of gravitational potentials as a secondary anisotropy of the AGWB energy density from the same set of simulations.

8.1 Cross-correlating *primary* AGWB anisotropies with cosmological probes

The cross-correlations between the SGWB, more precisely between the AGWB and traditional cosmological probes such as CMB, weak lensing and galaxy distributions represent completely new signals that can be exploited at cosmological and astrophysical levels. The information extracted in the upcoming years via future GW observatories from such cross-correlations would be as crucial as those from the cross-correlation between CMB and LSS in past decades. Since the population of gravitational wave sources is a biased tracer of the underlying dark matter distribution, the AGWB cross-correlations with CMB and LSS will provide a new handle on cosmology and structure formation. Such new signals will not only help to put constraints on astrophysical models but also, from the cosmological side, on neutrino masses, modified gravity and dark-energy models, affecting both the AGWB and CMB/LSS probes.

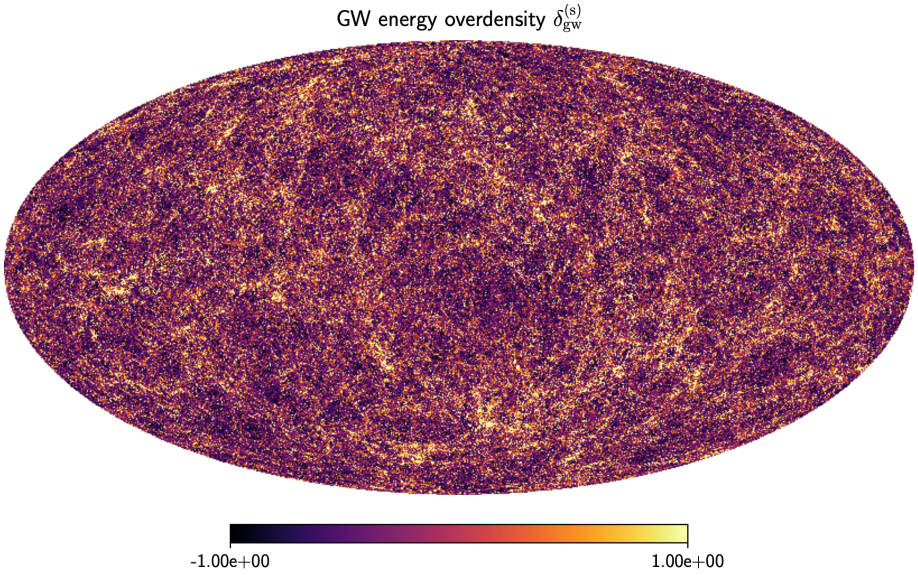

Figure 8.1: Map of the GW overdensity δ^s_{GW} showing distribution of GW sources constructed from Millennium all-sky mock lightcone catalogue ($z$max = 0.78) [439, 440, 441, 442] generated with the HEALPIX $N_{SIDE} = 256$ corresponding to an angular resolution of 13.7 arcminutes and an average of 7.3 galaxies per pixel from [432].

8.2 AGWB synthetic map realisation

As we described in Chapter 6, to construct our mock AGWB overdensity maps we use analytical input C_ls from Eq.(6.64) [432] which include contributions from BNS, BBH and BHNS mergers (and correctly for the aim of this work does not account for any effect from LSS on GW propagation):

$$\begin{aligned} C_{gw}(\theta_o,\nu_o) = \frac{\pi^2(t_H\nu_o)^6}{9\bar{\Omega}^2_{gw}} \int_0^{z_{max}} dz \frac{1+z}{E(z)} \int_0^{z_{max}} dz' \frac{1+z'}{E(z')} \\ \left(\Sigma_i \int d\zeta_g \bar{n}(z,\zeta_g) \int d\zeta_b R_i(z,\zeta_g,\zeta_b)\mathcal{S}_i(\nu_s,\zeta_b)\right) \\ \times \left(\Sigma_j \int d\zeta_g^{'} \bar{n}(z',\zeta_g') \int d\zeta_b' R_j(z',\zeta_g',\zeta_b')\mathcal{S}_j(\nu_s',\zeta_b')\right) \\ \left\langle \delta_n(z,\hat{\mathbf{e}}_o,\zeta_g)\delta_n(z',\hat{\mathbf{e}'}_o,\zeta_g')\right\rangle . \end{aligned} \tag{8.1}$$

After subtracting the dipole contribution from the observer peculiar velocity, the C_ls in Eq.(8.1) correspond to the angular power spectrum of what we call the *primary* anisotropies, δ^s_{GW}, in the total AGWB energy density distribution shown below:

$$\Omega_{gw}(\nu_0,\hat{e}_0) = \frac{\pi}{3}(t_H\nu_0)^3 \int_0^{\infty} dz \frac{1+z}{E(z)} + \int d\zeta \bar{n} R(1+\delta_n + \hat{\mathbf{e}}_0 \cdot \mathbf{v}_0) \int_{s^2} d^2\sigma_s r_s^2 \tilde{h}^2 \tag{8.2}$$

Fig.8.1 shows, after monopole and dipole subtraction, the HEALPix map of the AGWB overdensity distribution, δ^s_{GW}, obtained from the Millennium all-sky mock

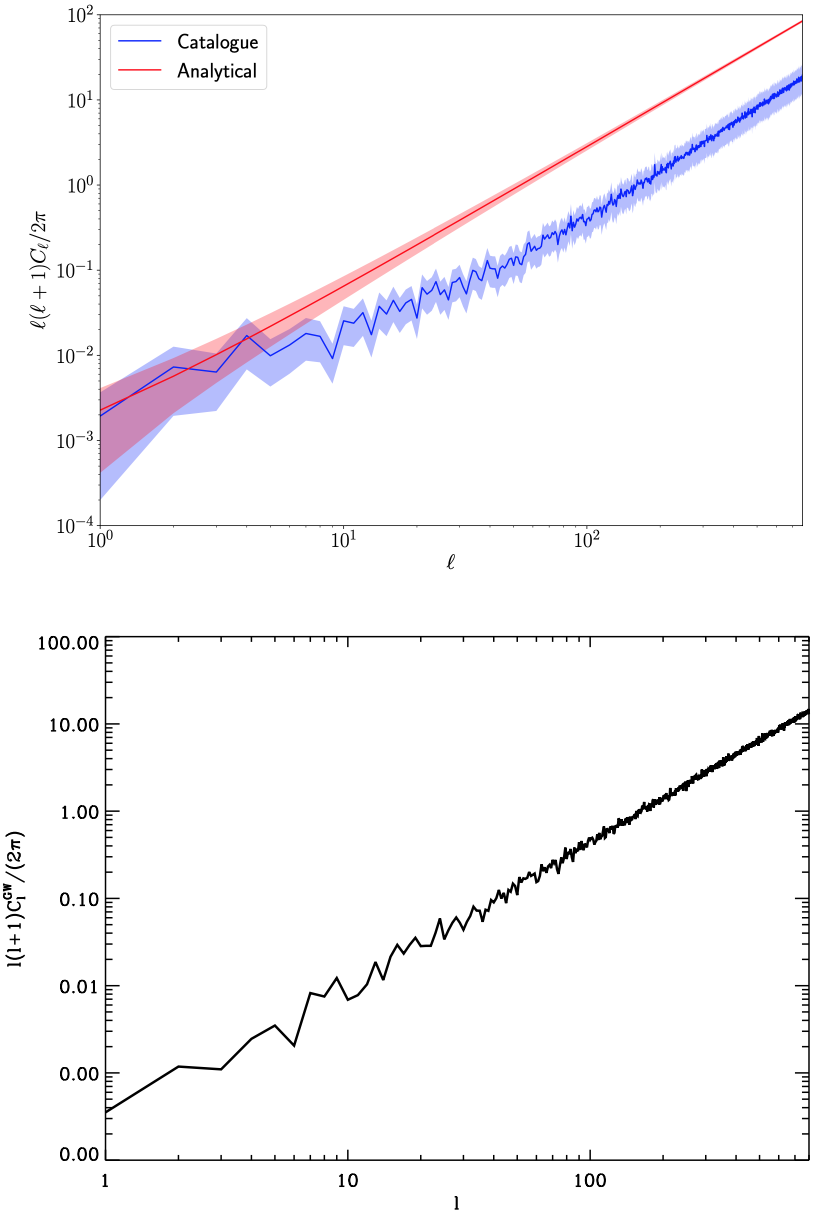

Figure 8.2: *Top*: Angular power spectra showing approximate contribution to the anisotropic variance of δ^s_{GW} as a function of $\ln l$, normalised to the monopole $\bar{\Omega_{gw}} = 5.4 \times 10^{-11}$ at $\nu_o = 100Hz$. The red curve shows the analytic prediction from [432], while the blue curve shows the spectrum computed from the HEALPix map shown in Fig. 8.1. Both curves include error regions from cosmic variance, while the blue curve includes Poisson errors associated with the finite number of galaxies per pixel in the HEALPix map [432]. *Bottom*: Angular power spectrum C_l, associated to the δ^s_{GW} map obtained after summation of δ^s_{GW} partial-maps produced, at the same redshift bins of the Millennium lightcone up to $z = 0.78$, as synthetic all-sky Gaussian realisations of the C_l in Eq.(8.1).

lightcone catalogue ($z_{\max} = 0.78$). The corresponding angular power spectrum is shown in blue in the top panel of Fig.8.2.

Moreover, in the bottom panel of Fig.8.2 we show the total angular power spectrum,

C_l, associated to the δ^s_{GW} map obtained after summation of δ^s_{GW} partial-maps produced (at the same redshift bins of the Millennium lightcone up to $z = 0.78$) as synthetic all-sky Gaussian realisations of the analytical partial-C_l computed in each redshift bin. Such Gaussian maps have been obtained by means of the `synfast` routine of the HEALPix package. We use this routine to create HEALPix maps computed as realisations of random Gaussian fields on a sphere characterised by the input theoretical angular power spectra C_l in Eq. (8.1). The total operation count scales as $\mathcal{O}(N_{\rm pix}^{3/2})$ with a prefactor dependent on the limiting spherical harmonics order $l_{\rm max}$ of the actual problem. For such realisations we have chosen $l_{\rm max} = 1000$ and $N_{\rm side} = 2048$, therefore the map resolution is ~ 1.72 arcmin with $N_{\rm pix} = 50331648$ pixel in total.

As can be observed, on scales $l > 10$ the blue and black curves look very similar, meaning that the analytical approximation in Eq. (8.1) is quite accurate. On scales $l < 10$ finite volume effects and box replication from the Millennium simulation start to dominate producing artificial excess of power.

In order to produce synthetic δ^s_{GW} maps that correctly cross-correlate with the galaxy catalogues from the DEMNuni simulations, we have followed an approach similar to the one used to reproduce the black curve in Fig.8.2, but, this time, not creating via `synfast` Gaussian realisations, rather *constrained realisations* of the δ^s_{GW} partial-maps by using the partial-C_l computed in each redshift bin *together with* the phases extracted from the DEMNUni galaxy partial-maps (which are described in the following Section). In order to extract the phases of the galaxy partial-maps we have used the HEALPix routine `anafast`. This routine performs harmonic analysis of the HEALPix maps up to a user specified maximum spherical harmonic order $\ell_{\rm max}$. The integrals are computed on the whole sphere, unless the user chooses a provided option to excise from the input maps a simple, constant latitude, symmetric cut, and/or apply an arbitrary cut read from an external file. Scalar, or scalar and tensor, spherical harmonic coefficients are evaluated from the maps. The total operation count scales as $\mathcal{O}(N_{\rm pix}^{1/2}\ell^2_{\rm max})$. `Anafast` reads one or two files containing the maps and produces a file containing the their auto- or cross- angular power spectrum C_ℓ. The $a_{\ell m}$ coefficients computed during the execution also can be written to a one or two files if requested. `Anafast` executes an approximate, discrete point-set quadrature on a sphere sampled at the HEALPix pixel centers. Spherical harmonic transforms are computed using recurrence relations for Legendre polynomials on co-latitude, θ, and Fast Fourier Transforms on longitude, ϕ. By mean of `anafast` we have extracted the a_{lm} of the partial-maps, and we have divided such a_{lm} by the square root of the galaxy angular power spectra extracted from the galaxy partial-maps again via `anafast`, divided by 2. Considering a Cholesky decomposition, this amounts to use a correlation coefficient $r = 1$ in order to generate the a_{lm} of the constrained realisations. This approach works properly since in Eq.(8.1) what really matters is the autocorrelation function of the galaxies hosting the GW sources. The distribution of such galaxies, or better its phases in the spherical harmonic domain, can be different from the galaxy distribution in the DEMNUni catalogues only at very small angular separations where nonlinear non-Gaussianity and scale-dependent bias effects become important. However, given the limited angular resolution ($l < 200$) of forthcoming GW interferometers, we are not interested in simulating such small scales and the corresponding very nonlinear effects. Therefore we can assume that, on such large scales, galaxies are linear tracers of the dark matter field with the same phases. Then, the unique difference, with respect to the galaxy distribution in the DEMNUni simulations, is given by the amplitude of the host galaxy

correlation function, i.e. their bias with respect to dark matter. By normalising the a_{lm} of the DEMNUni galaxy partial-maps by their amplitude, we get rid of such a difference, and we account for the correct bias of the host galaxies by inputting in `synfast` the C_l of the δ^s_{GW} partial-maps. Moreover, using the DEMNUni simulations has an important advantage, since their comoving box spans a volume 64 times larger than the Millennium one, and therefore can mimic the AGWB anisotropies on much larger scales than the latter.

Therefore, using the procedure of constrained realisations as explained above, we have produced integrated δ^s_{GW} total-maps from $z = 0$ up to $z = 2$ (i.e. the redshift range covered by the DEMNUni galaxy lightcone), for the AGWB generated by GW sources in the same redshift range and that can be correctly cross-correlated with other observables obtained from the DEMNUni simulations.

8.3 Cross-correlation of AGWB intensity maps with the DEMNUni galaxy distribution

Having implemented the procedure above, we are now able to cross-correlate the synthetic AGWB intensity map with the galaxy distribution in the DEMNUni lightcone. As mentioned in Chapter 3, these galaxy catalogues have been obtained via a SHAM technique applied to the DEMNUni subhalo catalogues (Carella et al. in prep). Then, for each redshift bin, we have created projected all-sky maps of galaxy catalogues. To this aim we have exploited a similar technique developed in [110]. In particular, in order to produce mock maps covering the past lightcone over the full sky, comoving galaxy snapshots have been staked up to $z = 2$ around the observer located at $z = 0$. This implies that the simulation volume needs to be repeated about 2.7 times along both the positive and negative directions of the three principle Cartesian axes x, y, z with the origin at the observer. However the spacing of the time outputs of the DEMNUni suit is such that it corresponds to an average (comoving) distance of $140h^{-1}Mpc$ on the past lightcone. This time resolution has been fully exploited using 30 outputs of the simulation along each integration path. In practice this means that the data corresponding to a particular output time is utilised in a spherical shell of thickness $140h^{-1}Mpc$ around the observer. Due to the finite size of the simulation box, it needs to be repeated. Therefore, a scheme to avoid the repetitions of the same structures along the line of sight is required. In the past, constructed simulated lightcones for small patches of the sky were obtained by simply randomizing each of the repeated boxed along the past lightcone by applying independent random translations and reflections [594]. However, it has been shown that this procedure produces artefacts like ripples in the simulated deflection-angle field as the gravitational field would become discontinuous at box boundaries leading to jumps in the deflection angle. Therefore the volume is divided out to $z = 2$ into spherical shells each of thickness $2000h^{-1}Mpc$ with the innermost shell being a sphere of comoving radius $1000h^{-2}Mpc$ centered at the observer. All the simulation boxes falling into the same shell are made to undergo the same, coherent randomization process i.e. they are all translated and rotated with the same random vectors generating a homogeneous coordinate transformation throughout the shell. Fig.8.3 shows the schematic of this staking process. For simplicity, the diagram does not illustrate the additional shell structure stemming from the different output

times of the simulation. The staking procedure eliminates any preferred direction in the simulated all-sky maps.

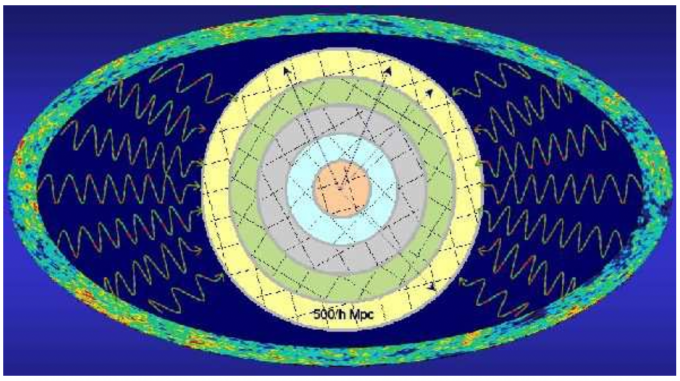

Figure 8.3: Method of staking and randomization process implemented in map-making procedure. The passage of CMB photons through the dark matter distribution of the Universe is followed by staking gravitational potential boxed of the Millennium simulation in this image. The same method is implemented in this study using the DEMNUni simulation comoving boxes. In the image, the thickness of 2Gpc/h are filled with periodic replicas of the box. All the boxes denoted by squares that fall into the same shell are randomized with the same coordinate transformation including rotation and translation which differs from shell to shell. This image is taken from [110].

Both the AGWB and galaxy maps are characterised by $N_{side} = 2048$ corresponding to a pixel angular resolution of $\sim 1.72'$. In Fig.8.4 we show the cross-correlation signal computed by cross-correlating, via the HEALPix routine, ANAFAST, the AGWB synthetic map (normalised to the monopole at $v_o = 100$ Hz) with the simulated galaxy maps. As can be observed, we find a similar trend to that of Ref. [359] which uses linear perturbation theory up to $z = 3$ (corrected via Halofit only with regard to the matter power spectrum), as shown in the top panel of Fig.6.8. However, the sign inversion at $z < 1$ visible in Fig.6.8 is actually not expected, especially at large scales as $l \sim 20$ (i.e. angular separation of about ~ 9 deg), even after accounting for secondary anisotropies, e.g. velocity contributions and/or time varying gravitational potential effects on the GW propagation. The reason why this is not expected is that, since the dominant contribution to such cross-correlation signals comes from the GW source distribution which follows the galaxy distribution, and since on such large scales the cross correlation between the galaxy density and velocity is expected to be linear and sub-dominant, no kind of anti-correlation between the AGWB and galaxy distributions is expected, especially for the linear calculations (as the one presented in Fig.6.8).

8.4 Cross-correlation of AGWB intensity with the DEMNUni weak-lensing maps

In the upper panel of Fig.8.5 we show the cross-correlation between the AGWB and cosmic shear maps. Again, we find a similar trend to the curves obtained analytically by Ref.[359] in the lower panel of Fig.6.8. The approximate difference by a factor of 50

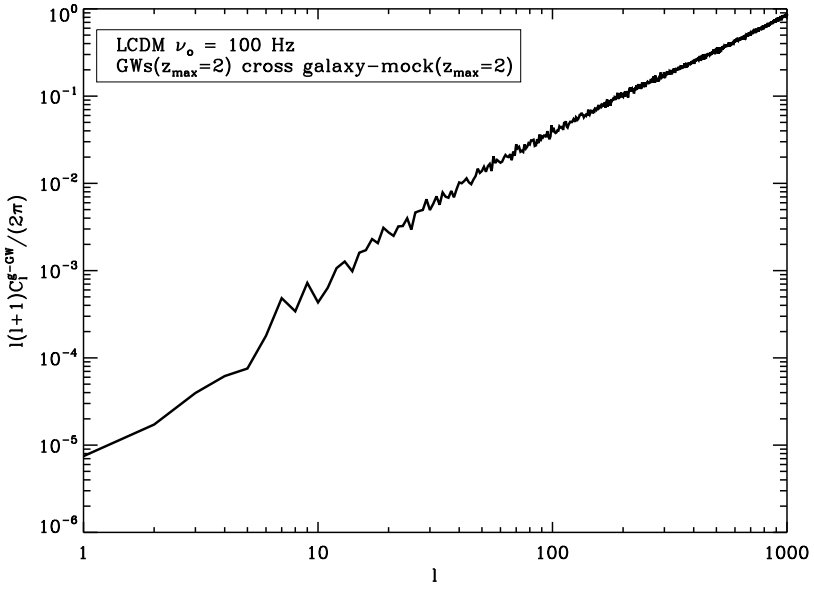

Figure 8.4: Cross-correlation of the AGWB energy density with the galaxy distribution from the DEMNUni simulation in the neutrino massless ΛCDM scenario.

could be due to the different frequency at which the monopole is computed and with respect the signal is normalised to. In fact, Ref.[359] considers a monopole at $v_o = 32$ Hz which is about an order of magnitude larger than the monopole at $v_o = 100$ Hz used here. Other differences may be due to the nonlinearities correctly accounted for via ray-tracing across the DEMNUni simulations. Worth of notice is that in the case of the cross-correlation between the AGWB and the cosmic shear maps Ref.[359] does not find any sign inversion. Since weak-lensing (WL) and galaxy-counts are positively correlated (especially at very large scales), one would expect a sign inversion also in the AGWB-WL cross-correlation, if this were really present in the AGWB-galaxy cross-correlation. The fact that this does not happen for the former suggests that also for the latter the sign inversion should not be present, confirming our results. In the lower panel of Fig.8.5 we show the cross-correlation between the AGWB and CMB-lensing convergence maps, extracted again from the DEMNUni simulations. In this case the trend of the signal is, as expected, very similar to the upper panel, just a bit larger due to the different weight functions involved.

8.5 Cross-correlation of AGWB intensity with the DEMNUni CMB ISW/RS maps

Finally, in Fig.8.6 we show the cross-correlation between AGWB primary anisotropies and maps of the excess of temperature anisotropies present in the observed CMB and due to the late Integrated Sachs-Wolfe effect and its nonlinear counterpart, the Rees-Sciama effect. The ISW-RS maps have been obtained thanks to photon ray-tracing across the DEMNUni time-derivatives of gravitational potential grids [70], which allow to capture nonlinear effects that otherwise are very difficult to be accurately predicted via analytical calculations. In this case, at nonlinear scales ($l \sim 600$), we do observe,

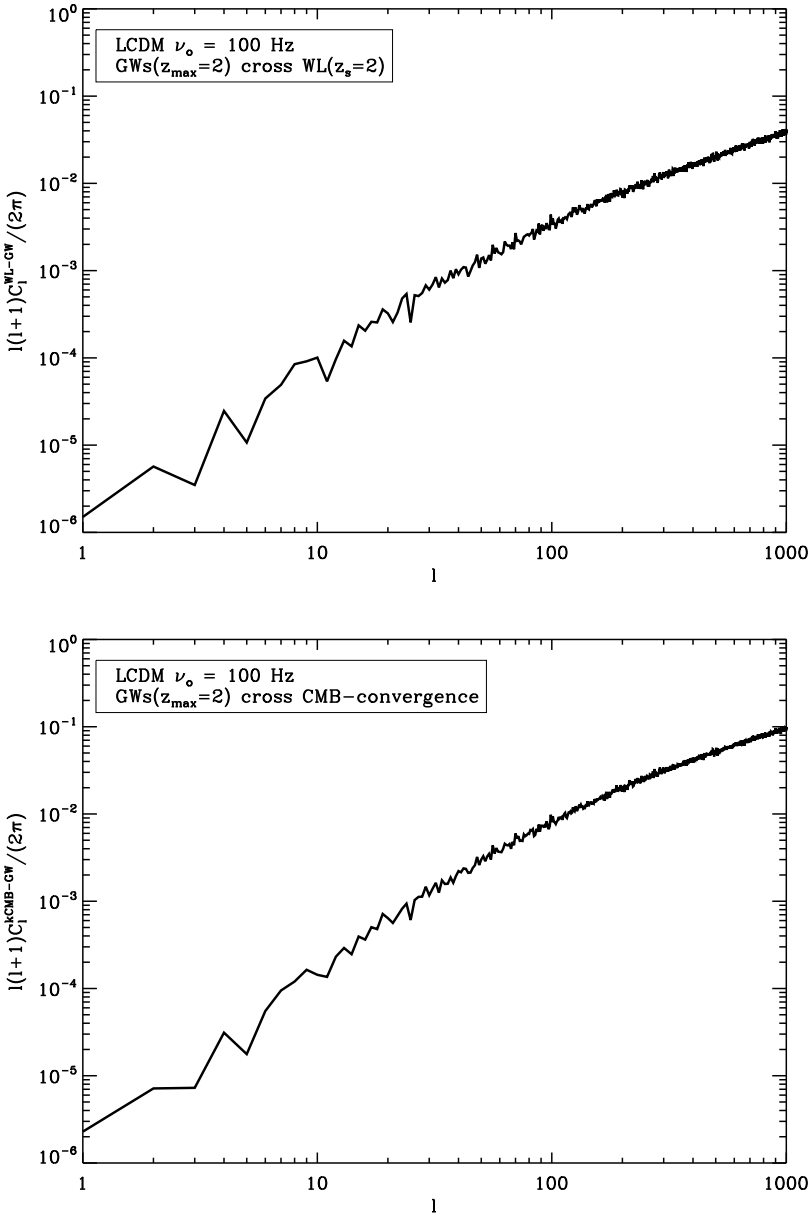

Figure 8.5: *Top*: Cross-correlation of the AGWB energy density with the cosmic shear maps for sources placed at $z_s = 2$, obtained via ray-tracing across the dark matter distribution of the DEMNUni simulation in the neutrino massless ΛCDM scenario. *Bottom*: Same as the upper panel but using a CMB convergence map [70].

as expected, a sign inversion in the cross-correlation signal between AGWB and CMB. This is due to the fact that, while on large cosmological scales (i.e. in the linear regime) the gravitational potential decays owing to the accelerated expansion of the Universe due to dark energy, on small scales (i.e. the nonlinear regime) it grows because of nonlinear structure formation, and therefore is present even in the absence of DE. Consequently, the time derivative of the gravitational potential associated to the ISW-RS effect is negative in the linear regime and positive in the nonlinear one, producing the typical anticorrelation with dark matter tracers as also the GW sources are.

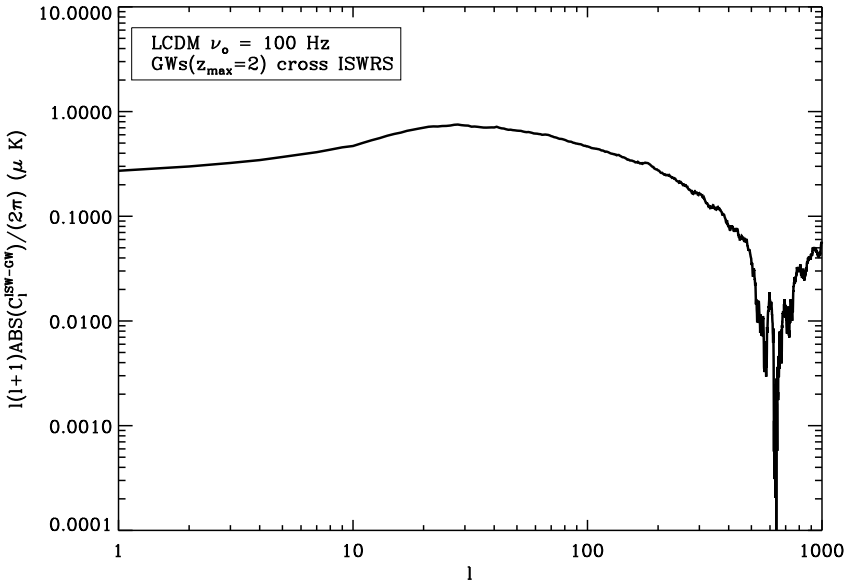

Figure 8.6: Cross-correlation of the AGWB energy density with the ISW/Rees-Sciama maps [70], obtained via ray-tracing across the dark matter distribution of the DEMNUni simulation in the neutrino massless ΛCDM scenario.

8.6 *Secondary* anisotropies in AGWB: weak lensing of the AGWB

In the framework of GR, GWs and photons propagate along the geodesic defined by the FLRW metric. But when the path of the photons/GWs get distorted by underlying large scale structure along the line of sight, the metric gets perturbed [595]:

$$ds^2 = (1-2\Phi)dt^2 - a^2(t)(1-2\Psi)(dx^2+dy^2+dz^2) \tag{8.3}$$

where $a(t)$ is the scale factor, Φ and Ψ denote the scalar perturbations due to the matter distribution of the Universe.

The presence of cosmological perturbations Φ and Ψ can lead to the gravitational Sachs-Wolfe (SW) and Integrated Sachs-Wolfe (ISW) effects in the GW propagation (effect that are already present in the linear perturbation regime) and, even more important, to gravitational lensing which is a nonlinear effect in photon/GW propagation. Fig.8.7 gives a sketch of how trajectories of GWs and photons get affected by weak lensing due to intervening matter distribution.

Gravitational lensing can affect the amplitude and polarization of the SGWB in a similar way as CMB photons, if we consider the GW frequency much larger than the frequency associated to the LSS evolution. In fact, in this case, gravitons behave like photons in their propagation from the source to the observer, wave effects can be neglected, and the limit of geometrical optics is allowed. Modelling unperturbed SGWB and comparing with future high angular resolution observations in GW total intensity and polarization will provide the possibility to extract information about the underlying dark matter large scale distribution.

In this section we focus on the weak lensing of the AGWB intensity in the geo-

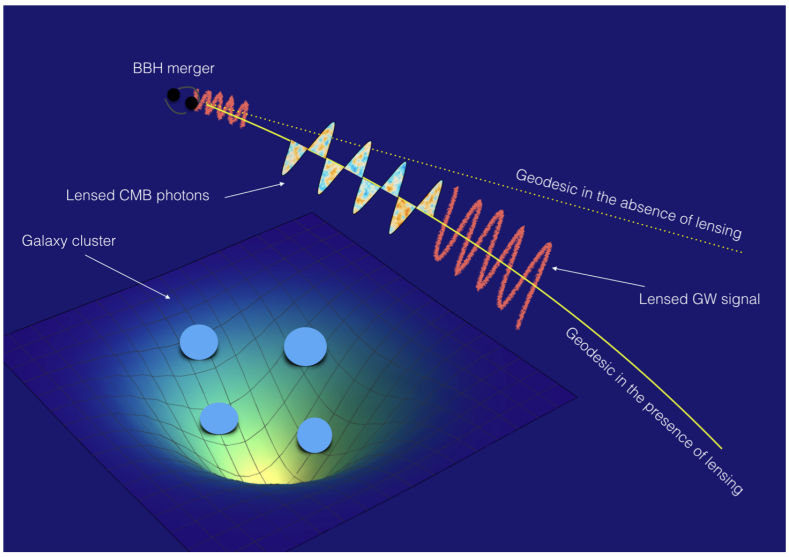

Figure 8.7: Figure shows how CMB photon and gravitational wave follow the same geodesic in geometric optics limit and hence gravitational lensing of AGWB in this limit can be treated in analogous manner to CMB lensing. This schematic diagram also depicts the physical mechanism behind the correlation between the lensed CMB photons and lensed GWs from astrophysical sources [595].

metrical optics limit, produce full-sky maps via ray-tracing across the DEMNUni dark matter distribution, and show how LSS causing AGWB lensing, gets imprinted onto these maps.

8.6.1 AGWB map making procedure

To build AGWB lensed maps, we follow the map making method implemented in [110] for simulated CMB maps via ray-tracing across the DEMNUni dark matter distribution. It is important to note that the lensed AGWB is non-Gaussian, even when we assume that GW sources and gravitational lenses posses a Gaussian distribution. This assumption is true at the linear level, but gets broken in the nonlinear regime. In fact, the nonlinear evolution of the large scale structure is also responsible to produce a degree of non-Gaussianity in the distribution of gravitational lenses leading to an excess of non-Gaussian statistics of the lensed AGWB on smaller scales with respect to the linear case. This non-Gaussian contribution can be computed only using large N-body cosmological simulations which could effectively describe the non-linear evolution of lenses on large scales.

As for CMB photons, we assume the Born approximation and first produce full-sky HEALPix maps of the lensing potential acting as a lens on the AGWB gravitons. Then, we input in the LensPix code[1] the a_{lm} of the DEMNUni lensing potential map, and the AGWB angular power spectrum computed via Eq.(8.1) in small redshift bins centered at different source redshifts. In this case, our aim is to isolate the impact of lensing from intervening LSS along the AGWB propagation. Therefore, we assume that the initial source distribution is Gaussian at the source redshift, as would be for

[1]https://cosmologist.info/lenspix/

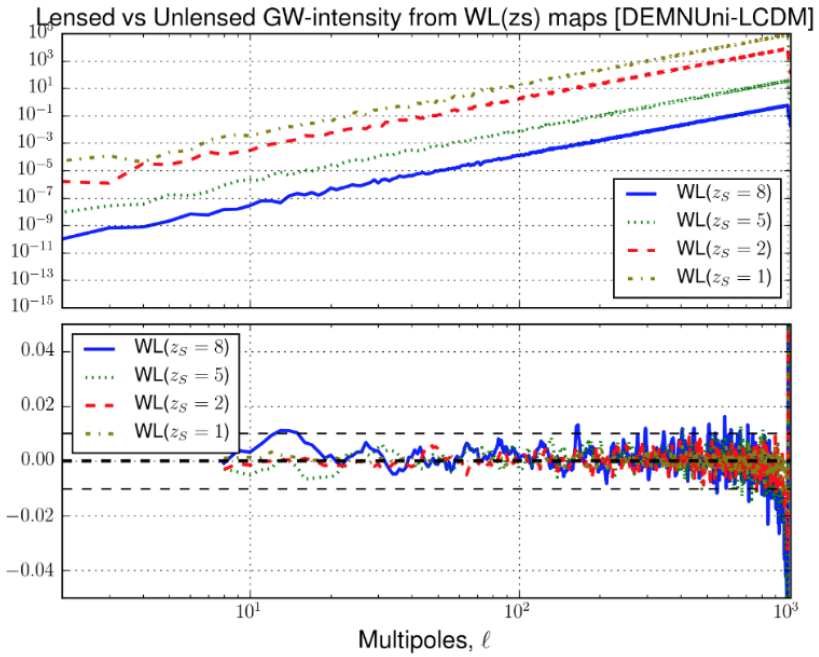

Figure 8.8: *Top*: Lensed C_l of AGWB with sources all placed at redshifts $z = 1, 2, 5, 8$, respectively. *Bottom*: Lensed-to-unlensed AGWB C_l ratios.

the primary CMB. In a future work, we will include also the non-Gaussian statistics of the GW sources distribution by inputting in LensPix directly the a_{lm} partial-maps produced in § 8.2, add the (tiny) secondary ISWRS anisotropies already available from the DEMNUni data, lens each map along the line-of-sight, and finally sum up these maps to obtain the full weak-lensed and ISWRS-ed AGWB maps generated by the GW sources in the DEMNUni simulations.

8.7 Results

In Fig.8.9, we show the simulated maps of the deflection-angle modulus, and the difference maps between the lensed and unlensded AGWB, with all the GW sources placed at redshifts $z = 1, 2, 5, 8$, respectively. As can be observed, the difference maps allow highlighting the dark matter distribution imprinted into the lensed AGWB.

Even if not directly observable, the AGWB difference maps can help to visually understand how large scale correlations are imprinted on the AGWB due to the large scale modes of the LSS intervening along their propagation from the sources to the observer.

However, because of the power law trend of the AGWB spectrum, shown in Fig.8.1 and Fig.8.8, the effect of lensing on the AGWB C_l is very different from the CMB case, and practically negligible. In fact, while the CMB angular power spectrum is characterised by acoustic oscillations which are damped and smeared by weak-lensing, the AGWB spectrum is mostly featureless and therefore lensing, which physically distorts and magnifies the anisotropy patches, can not have the same effect for AGWB as for CMB. This is quantitatively in the lensed-to-unlensed C_l ratios shown in the lower plot of Fig.8.8, where the percent difference is smaller than 1%.

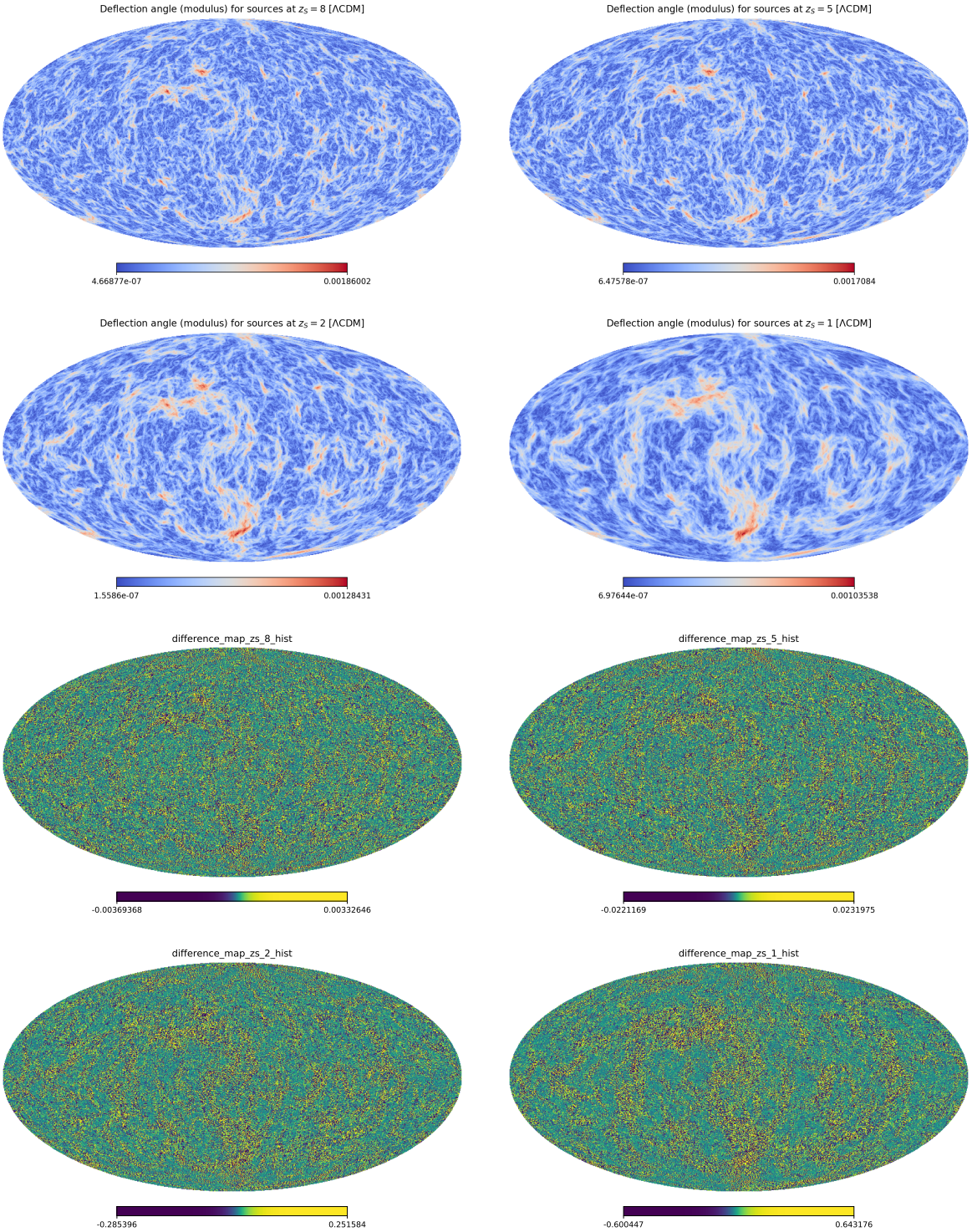

Figure 8.9: *Top*: The simulated all-sky map of the deflection angle modulus (in radians) computed via the map making procedure using the DEMNUni simulation suite. *Bottom*: Difference AGWB maps (lensed-unlensed) showing distribution of gravitational lenses.

Conclusions

> The first gulp from the glass of natural sciences will turn you into atheist, but at the bottom of the glass, God is waiting for you.
>
> *Werner Heisenberg*

In this work we have simulated, for the first time via N-body simulations, the cross-correlation of the AGWB *primary* anisotropies (due to GW source distributions) with other LSS probes such as cosmic shear, SHAM galaxy distribution, and ISWRS CMB maps. To this aim we have exploited the large dataset available as post-processing of the DEMUNni simulations, and made use of constrained realisations via the Cholesky decomposition with correlation coefficient $r = 1$, i.e. we have assumed that GW sources and SHAM galaxies, tracing both the DM distribution of the DEMNUni simulations, are perfectly correlated. For our scopes, the latter is a well motivated assumption since differences due to very nonlinear evolution and baryonic physics would have an impact at smaller angular separations which will not be probed by future GW interferometers as ET and LISA ($l < 200$).

Except for one case, we recover signals similar in trend and amplitude to the one computed via analytical approaches in the linear regime. On the contrary, the AGWB-ISWRS cross-correlation shows a sign inversion at about $l = 600$ which is typical of nonlinear effects and has been shown for the first time in this work, as no analytical estimations are available yet.

Moreover, again for the first time, we have produced AGWB-lensed maps, in the geometrical optics limit, implementing techniques similar to the one used for CMB-lensing. Also this assumption is well motivated since, except for primordial SGWB produced by one-field inflationary mechanisms, the typical frequency characterising AGWBs is much larger than the frequency associated to the evolution of LSS. In the lensed-to-unlensed AGWB difference maps we are able to visualise the tiny perturbation imprinted by the effective deflection angle generated by LSS. However, the resulting AGWB-lensed angular power spectrum results to be negligibly affected by weak-lensing, being the input C_l basically a power law.

We have obtained these results in the context of a LCDM scenario. In a future work we will also consider other cosmologies of the DEMNUni simulations, as dynamical dark energy and massive neutrinos. Moreover, we will produce full ISWRS+lensed AGWB constrained maps, accounting therefore for the primary anisotropies sourced by the GW source distributions and both the *secondary* anisotropies due to lensing and ISWRS from intervening LSS in the graviton propagation. Also in this case we will consider

the different cosmologies implemented in the DEMNUni simulations.

Finally, it is worth mentioning that the data produced in this work will be very useful for the construction of mock extremely realistic AGWB maps that could be exploited for the implementation of the data analysis pipelines from forthcoming gravitational wave observatories.

The woods are lovely, dark and deep,
But I have promises to keep,
And miles to go before I sleep,
And miles to go before I sleep.

Robert Frost

Bibliography

[1] Abbott et al., *Observation of Gravitational Waves from a Binary Black Hole Merger*, Phys. Rev. Lett. **116** (2016) 061102 [1602.03837].

[2] Aghanim N. et al., *Planck 2018 results. VI. Cosmological parameters*, A&A **641** (2020) A6 [1807.06209].

[3] A. Einstein, *Kosmologische Betrachtungen zur allgemeinen Relativitätstheorie*, *Sitzungsberichte der Königlich Preußischen Akademie der Wissenschaften (Berlin* (1917) 142.

[4] S. Dodelson, *Modern cosmology*. 2003.

[5] E. W. Kolb and M. S. Turner, *The early universe*, vol. 69. 1990.

[6] J. A. Peacock, *Cosmological Physics*. 1999.

[7] C. Marinoni, J. Bel and A. Buzzi, *The scale of cosmic isotropy*, J. Cosmology Astropart. Phys. **2012** (2012) 036 [1205.3309].

[8] Planck Collaboration, *Planck 2013 results. XVI. Cosmological parameters*, A&A **571** (2014) A16 [1303.5076].

[9] Ade P. A. R. et al., *Planck 2015 results. XIII. Cosmological parameters*, A&A **594** (2016) A13 [1502.01589].

[10] A. R. Liddle and D. H. Lyth, *Cosmological Inflation and Large-Scale Structure*. 2000.

[11] P. Ntelis, *Probing Cosmology with the homogeneity scale of the Universe through large scale structure surveys.*, theses, Astroparticule and Cosmology Group, Physics Department, Paris Diderot University, Sept., 2017.

[12] A. Terrana, *Modified gravity and cosmology on the largest scales*. Ph. D, 2017.

[13] M. K. Grindstad, *Massive neutrinos and cosmology*. Masteroppgave, University of Oslo, 2010.

[14] R. A. Hlozek, *Probing the early universe and dark energy with multi-epoch cosmological data*, Ph.D. thesis, 2012.

[15] S. Gariazzo, *New Developments in Cosmology*, *arXiv e-prints* (2016) arXiv:1603.09102 [1603.09102].

[16] C. W. Misner, K. S. Thorne and J. A. Wheeler, *Gravitation*. 1973.

[17] J. Lesgourgues, G. Mangano, G. Miele and S. Pastor, *Neutrino Cosmology*. 2013.

[18] E. Hubble, *A Relation between Distance and Radial Velocity among Extra-Galactic Nebulae*, *Proceedings of the National Academy of Science* **15** (1929) 168.

[19] Freedman et al., *Final Results from the Hubble Space Telescope Key Project to Measure the Hubble Constant*, ApJ **553** (2001) 47 [astro-ph/0012376].

[20] A. Liddle, *An Introduction to Modern Cosmology, Second Edition*. 2003.

[21] P. J. E. Peebles, *Principles of Physical Cosmology*. 1993.

[22] A. H. Guth, *Inflationary universe: A possible solution to the horizon and flatness problems*, *Phys. Rev. D* **23** (1981) 347.

[23] F. Hoyle, *The Big Bang in Astronomy*, *New Scientist* **92** (1981) 521.

[24] H. Kodama and M. Sasaki, *Cosmological Perturbation Theory*, *Progress of Theoretical Physics Supplement* **78** (1984) 1.

[25] A. Ferrantelli, *Gravitino phenomenology and cosmological implications of supergravity*, *arXiv e-prints* (2010) arXiv:1002.2835 [1002.2835].

[26] A. H. Guth, *Inflationary universe: A possible solution to the horizon and flatness problems*, Phys. Rev. D **23** (1981) 347.

[27] A. A. Starobinskii, *Spectrum of relict gravitational radiation and the early state of the universe*, *ZhETF Pisma Redaktsiiu* **30** (1979) 719.

[28] N. Bartolo, E. Komatsu, S. Matarrese and A. Riotto, *Non-Gaussianity from inflation: theory and observations*, Phys. Rep. **402** (2004) 103 [astro-ph/0406398].

[29] A. R. Liddle, P. Parsons and J. D. Barrow, *Formalizing the slow-roll approximation in inflation*, Phys. Rev. D **50** (1994) 7222 [astro-ph/9408015].

[30] D. H. D. H. Lyth and A. A. Riotto, *Particle physics models of inflation and the cosmological density perturbation*, Phys. Rep. **314** (1999) 1 [hep-ph/9807278].

[31] D. Baumann, *TASI Lectures on Inflation*, *arXiv e-prints* (2009) arXiv:0907.5424 [0907.5424].

[32] M. Kamionkowski and E. D. Kovetz, *The Quest for B Modes from Inflationary Gravitational Waves*, ARA&A **54** (2016) 227 [1510.06042].

[33] Y. Shtanov, J. Traschen and R. Brandenberger, *Universe reheating after inflation*, Phys. Rev. D **51** (1995) 5438 [hep-ph/9407247].

[34] A. Linde, *A new inflationary universe scenario: A possible solution of the horizon, flatness, homogeneity, isotropy and primordial monopole problems*, *Physics Letters B* **108** (1982) 389.

[35] A. Albrecht, P. J. Steinhardt, M. S. Turner and F. Wilczek, *Reheating an inflationary universe*, *Phys. Rev. Lett.* **48** (1982) 1437.

[36] L. F. Abbott, E. Farhi and M. B. Wise, *Particle production in the new inflationary cosmology*, *Physics Letters B* **117** (1982) 29.

[37] A. Linde, *Scalar field fluctuations in the expanding universe and the new inflationary universe scenario*, *Physics Letters B* **116** (1982) 335.

[38] L. Kofman, A. Linde and A. A. Starobinsky, *Reheating after inflation*, Phys. Rev. Lett. **73** (1994) 3195 [hep-th/9405187].

[39] A. H. Guth and D. I. Kaiser, *Inflationary Cosmology: Exploring the Universe from the Smallest to the Largest Scales*, *Science* **307** (2005) 884 [astro-ph/0502328].

[40] O. Lahav and A. R. Liddle, *The Cosmological Parameters (2019)*, *arXiv e-prints* (2019) arXiv:1912.03687 [1912.03687].

[41] R. Wilkinson, *Deciphering dark matter with cosmological observations*, Ph.D. thesis, Durham University, United Kingdom, Jan., 2016.

[42] F. Lepori, *Relativistic Cosmology from the linear to the non-linear regime*, Ph.D. thesis, SISSA, Trieste, 9, 2018.

[43] Planck Collaboration, Aghanim, N., Akrami, Y. and Ashdown, M. et al., *Planck 2018 results - vi. cosmological parameters*, *A&A* **641** (2020) A6.

[44] Planck Collaboration, *Planck 2018 results. I. Overview and the cosmological legacy of Planck*, A&A **641** (2020) A1 [1807.06205].

[45] Aghanim N. et al., *Planck 2018 results. VIII. Gravitational lensing*, A&A **641** (2020) A8 [1807.06210].

[46] Akrami Y. et al., *Planck 2018 results. X. Constraints on inflation*, A&A **641** (2020) A10 [1807.06211].

[47] A. G. Sánchez, F. Montesano, E. A. Kazin, E. Aubourg, F. Beutler, J. Brinkmann et al., *The clustering of galaxies in the SDSS-III Baryon Oscillation Spectroscopic Survey: cosmological implications of the full shape of the clustering wedges in the data release 10 and 11 galaxy samples*, MNRAS **440** (2014) 2692 [1312.4854].

[48] A. G. Riess, L. M. Macri, S. L. Hoffmann, D. Scolnic, S. Casertano, A. V. Filippenko et al., *A 2.4% Determination of the Local Value of the Hubble Constant*, ApJ **826** (2016) 56 [1604.01424].

[49] C. Heymans, E. Grocutt, A. Heavens, M. Kilbinger, T. D. Kitching, F. Simpson et al., *CFHTLenS tomographic weak lensing cosmological parameter constraints: Mitigating the impact of intrinsic galaxy alignments*, MNRAS **432** (2013) 2433 [1303.1808].

[50] E. V. Linder, *What is the Standard Cosmological Model?*, *arXiv e-prints* (2021) arXiv:2105.02903 [2105.02903].

[51] M. Kilbinger, *Cosmology with cosmic shear observations: a review*, *Reports on Progress in Physics* **78** (2015) 086901 [1411.0115].

[52] A. Lewis, A. Challinor and A. Lasenby, *Efficient Computation of Cosmic Microwave Background Anisotropies in Closed Friedmann-Robertson-Walker Models*, ApJ **538** (2000) 473 [astro-ph/9911177].

[53] P. J. E. Peebles, *The large-scale structure of the universe*. 1980.

[54] *Dark Matter and Dark Energy: A Challenge for Modern Cosmology*, vol. 370 of *Astrophysics and Space Science Library*, Jan., 2011. 10.1007/978-90-481-8685-3.

[55] T. Treu, P. J. Marshall and D. Clowe, *Resource Letter GL-1: Gravitational Lensing*, *American Journal of Physics* **80** (2012) 753 [1206.0791].

[56] Y. Mellier, *Probing the Universe with Weak Lensing*, ARA&A **37** (1999) 127 [astro-ph/9812172].

[57] N. Kaiser, *Small-angle anisotropy of the microwave background radiation in the adiabatic theory*, MNRAS **202** (1983) 1169.

[58] M. Bartelmann and P. Schneider, *Weak gravitational lensing*, Phys. Rep. **340** (2001) 291 [astro-ph/9912508].

[59] A. Lewis and A. Challinor, *Weak gravitational lensing of the CMB*, Phys. Rep. **429** (2006) 1 [astro-ph/0601594].

[60] N. Kaiser, *Weak Lensing and Cosmology*, ApJ **498** (1998) 26 [astro-ph/9610120].

[61] W. Hu, *Weak lensing of the CMB: A harmonic approach*, Phys. Rev. D **62** (2000) 043007 [astro-ph/0001303].

[62] A. Challinor and G. Chon, *Geometry of weak lensing of CMB polarization*, Phys. Rev. D **66** (2002) 127301 [astro-ph/0301064].

[63] A. Lewis, *Lensed CMB simulation and parameter estimation*, Phys. Rev. D **71** (2005) 083008 [astro-ph/0502469].

[64] C.-P. Ma and E. Bertschinger, *Cosmological Perturbation Theory in the Synchronous vs. Conformal Newtonian Gauge*, *arXiv e-prints* (1994) astro [astro-ph/9401007].

[65] A. Refregier, *Weak Gravitational Lensing by Large-Scale Structure*, ARA&A **41** (2003) 645 [astro-ph/0307212].

[66] W. L. Freedman and M. S. Turner, *Colloquium: Measuring and understanding the universe*, *Reviews of Modern Physics* **75** (2003) 1433 [astro-ph/0308418].

[67] L. Guzzo, M. Scodeggio, B. Garilli, B. R. Granett, A. Fritz, U. Abbas et al., *The VIMOS Public Extragalactic Redshift Survey (VIPERS). An unprecedented view of galaxies and large-scale structure at 0.5 ¡ z ¡ 1.2*, A&A **566** (2014) A108 [1303.2623].

[68] P. Coles, *The state of the Universe*, Nature **433** (2005) 248.

[69] R. H. Wechsler and J. L. Tinker, *The Connection Between Galaxies and Their Dark Matter Halos*, ARA&A **56** (2018) 435 [1804.03097].

[70] C. Carbone, M. Petkova and K. Dolag, *DEMNUni: ISW, Rees-Sciama, and weak-lensing in the presence of massive neutrinos*, J. Cosmology Astropart. Phys. **2016** (2016) 034 [1605.02024].

[71] E. Castorina, C. Carbone, J. Bel, E. Sefusatti and K. Dolag, *DEMNUni: the clustering of large-scale structures in the presence of massive neutrinos*, J. Cosmology Astropart. Phys. **2015** (2015) 043 [1505.07148].

[72] C. D. Kreisch, A. Pisani, C. Carbone, J. Liu, A. J. Hawken, E. Massara et al., *Massive neutrinos leave fingerprints on cosmic voids*, MNRAS **488** (2019) 4413 [1808.07464].

[73] N. Schuster, N. Hamaus, A. Pisani, C. Carbone, C. D. Kreisch, G. Pollina et al., *The bias of cosmic voids in the presence of massive neutrinos*, J. Cosmology Astropart. Phys. **2019** (2019) 055 [1905.00436].

[74] G. Verza, A. Pisani, C. Carbone, N. Hamaus and L. Guzzo, *The void size function in dynamical dark energy cosmologies*, J. Cosmology Astropart. Phys. **2019** (2019) 040 [1906.00409].

[75] G. Parimbelli, S. Anselmi, M. Viel, C. Carbone, F. Villaescusa-Navarro, P. S. Corasaniti et al., *The effects of massive neutrinos on the linear point of the correlation function*, J. Cosmology Astropart. Phys. **2021** (2021) 009 [2007.10345].

[76] Planck Collaboration, P. A. R. Ade, N. Aghanim, M. Arnaud, M. Ashdown, J. Aumont et al., *Planck 2015 results. XIII. Cosmological parameters*, A&A **594** (2016) A13 [1502.01589].

[77] V. Springel, N. Yoshida and S. D. M. White, *GADGET: a code for collisionless and gasdynamical cosmological simulations*, New A **6** (2001) 79 [astro-ph/0003162].

[78] K. Dolag, S. Borgani, G. Murante and V. Springel, *Substructures in hydrodynamical cluster simulations*, MNRAS **399** (2009) 497 [0808.3401].

[79] A. A. Penzias and R. W. Wilson, *A Measurement of Excess Antenna Temperature at 4080 Mc/s.*, ApJ **142** (1965) 419.

[80] R. H. Dicke, P. J. E. Peebles, P. G. Roll and D. T. Wilkinson, *Cosmic Black-Body Radiation.*, ApJ **142** (1965) 414.

[81] M. Kamionkowski and A. Kosowsky, *The Cosmic Microwave Background and Particle Physics*, *Annual Review of Nuclear and Particle Science* **49** (1999) 77 [astro-ph/9904108].

[82] W. Hu and S. Dodelson, *Cosmic Microwave Background Anisotropies*, ARA&A **40** (2002) 171 [astro-ph/0110414].

[83] W. Hu and M. White, *A CMB polarization primer*, New A **2** (1997) 323 [astro-ph/9706147].

[84] M. J. Rees and D. W. Sciama, *Large-scale Density Inhomogeneities in the Universe*, Nature **217** (1968) 511.

[85] A. Kosowsky, *Cosmic microwave background polarization.*, *Annals of Physics* **246** (1996) 49 [astro-ph/9501045].

[86] P. Cabella and M. Kamionkowski, *Theory of Cosmic Microwave Background Polarization*, *arXiv e-prints* (2004) astro [astro-ph/0403392].

[87] M. Kamionkowski, A. Kosowsky and A. Stebbins, *Statistics of cosmic microwave background polarization*, *Phys. Rev. D* **55** (1997) 7368.

[88] R. K. Sachs and A. M. Wolfe, *Perturbations of a Cosmological Model and Angular Variations of the Microwave Background*, ApJ **147** (1967) 73.

[89] D. J. Fixsen, *The Temperature of the Cosmic Microwave Background*, ApJ **707** (2009) 916 [0911.1955].

[90] G. F. Smoot, *COBE observations and results*, in *3K cosmology* (L. Maiani, F. Melchiorri and N. Vittorio, eds.), vol. 476 of *American Institute of Physics Conference Series*, pp. 1–10, May, 1999, astro-ph/9902027, DOI.

[91] Adam R. et al., *Planck 2015 results. I. Overview of products and scientific results*, A&A **594** (2016) A1 [1502.01582].

[92] Larson D. et al., *Seven-year Wilkinson Microwave Anisotropy Probe (WMAP) Observations: Power Spectra and WMAP-derived Parameters*, ApJS **192** (2011) 16 [1001.4635].

[93] S. M. Feeney, *Novel algorithms for early-universe cosmology*, Ph.D. thesis, UCL, United Kingdom, Jan., 2012.

[94] D. N. Spergel, R. Bean, O. Doré, M. R. Nolta, C. L. Bennett, J. Dunkley et al., *Three-Year Wilkinson Microwave Anisotropy Probe (WMAP) Observations: Implications for Cosmology*, ApJS **170** (2007) 377 [astro-ph/0603449].

[95] J. A. Peacock and D. Nicholson, *The large-scale clustering of radio galaxies.*, MNRAS **253** (1991) 307.

[96] J. Silk, *Cosmic Black-Body Radiation and Galaxy Formation*, ApJ **151** (1968) 459.

[97] G. Efstathiou and J. R. Bond, *Microwave anisotropy constraints on isocurvature baryon models*, MNRAS **227** (1987) 33P.

[98] R. A. Sunyaev and Y. B. Zeldovich, *The Observations of Relic Radiation as a Test of the Nature of X-Ray Radiation from the Clusters of Galaxies*, *Comments on Astrophysics and Space Physics* **4** (1972) 173.

[99] X.-P. Wu, *Weak lensing of the Sunyaev-Zel'dovich sky*, MNRAS **349** (2004) 816 [astro-ph/0312469].

[100] A. Cooray, D. Baumann and K. Sigurdson, *Statistical imprints of SZ effects in the cosmic microwave background*, in *Background Microwave Radiation and Intracluster Cosmology* (F. Melchiorri and Y. Rephaeli, eds.), p. 309, Jan., 2005, astro-ph/0410006.

[101] Amendola L et al., *Cosmology and fundamental physics with the Euclid satellite*, *Living Reviews in Relativity* **21** (2018) 2 [1606.00180].

[102] M. Zaldarriaga and U. Seljak, *Gravitational lensing effect on cosmic microwave background polarization*, Phys. Rev. D **58** (1998) 023003 [astro-ph/9803150].

[103] A. Blanchard and J. Schneider, *Gravitational lensing effect on the fluctuations of the cosmic background radiation*, A&A **184** (1987) 1.

[104] S. Cole and G. Efstathiou, *Gravitational lensing of fluctuations in the microwave background radiation*, MNRAS **239** (1989) 195.

[105] E. V. Linder, *Analysis of gravitationally lensed microwave background anisotropies*, MNRAS **243** (1990) 353.

[106] U. Seljak, *Gravitational Lensing Effect on Cosmic Microwave Background Anisotropies: A Power Spectrum Approach*, ApJ **463** (1996) 1 [astro-ph/9505109].

[107] R. B. Metcalf and J. Silk, *Gravitational Magnification of the Cosmic Microwave Background*, ApJ **489** (1997) 1 [astro-ph/9708059].

[108] Aguirre J. et al., *Observing the Evolution of the Universe*, *arXiv e-prints* (2009) arXiv:0903.0902 [0903.0902].

[109] A. Challinor and G. Chon, *Geometry of weak lensing of cmb polarization*, *Phys. Rev. D* **66** (2002) 127301.

[110] C. Carbone, V. Springel, C. Baccigalupi, M. Bartelmann and S. Matarrese, *Full-sky maps for gravitational lensing of the cosmic microwave background*, MNRAS **388** (2008) 1618 [0711.2655].

[111] A. Babul and M. H. Lee, *Gravitational lensing by smooth inhomogeneities in the universe*, MNRAS **250** (1991) 407.

[112] E. V. Linder, *The linearly perturbed sky*, MNRAS **243** (1990) 362.

[113] L. Cayon, E. Martinez-Gonzalez and J. L. Sanz, *Gravitational Lensing and the Cosmic Microwave Background*, ApJ **403** (1993) 471.

[114] L. Cayon, E. Martinez-Gonzalez and J. L. Sanz, *Does a Cosmological Constant Increase the Effect of Gravitational Lensing on the Cosmic Microwave Background?*, ApJ **413** (1993) 10.

[115] R. B. Metcalf and J. Silk, *On Breaking Cosmic Degeneracy*, ApJ **492** (1998) L1 [astro-ph/9710364].

[116] A. G. Riess, S. Casertano, W. Yuan, L. Macri, J. Anderson, J. W. MacKenty et al., *New Parallaxes of Galactic Cepheids from Spatially Scanning the Hubble Space Telescope: Implications for the Hubble Constant*, ApJ **855** (2018) 136 [1801.01120].

[117] G. Cusin, R. Durrer and P. G. Ferreira, *Polarization of a stochastic gravitational wave background through diffusion by massive structures*, Phys. Rev. D **99** (2019) 023534 [1807.10620].

[118] G. Cusin and M. Lagos, *Gravitational wave propagation beyond geometric optics*, Phys. Rev. D **101** (2020) 044041 [1910.13326].

[119] Abbott et al., *Binary Black Hole Population Properties Inferred from the First and Second Observing Runs of Advanced LIGO and Advanced Virgo*, ApJ **882** (2019) L24 [1811.12940].

[120] Abbott et al., *Tests of General Relativity with GW170817*, Phys. Rev. Lett. **123** (2019) 011102 [1811.00364].

[121] Abbott et al., *Tests of general relativity with the binary black hole signals from the LIGO-Virgo catalog GWTC-1*, Phys. Rev. D **100** (2019) 104036 [1903.04467].

[122] Abbott et al., *A gravitational-wave standard siren measurement of the Hubble constant*, Nature **551** (2017) 85 [1710.05835].

[123] É. É. Flanagan and S. A. Hughes, *The basics of gravitational wave theory*, *New Journal of Physics* **7** (2005) 204 [gr-qc/0501041].

[124] A. Buonanno, *Gravitational waves*, *arXiv e-prints* (2007) arXiv:0709.4682 [0709.4682].

[125] M. Maggiore, *Gravitational Waves. Vol. 1: Theory and Experiments*, Oxford Master Series in Physics. Oxford University Press, 2007.

[126] F. J. Raab and D. Reitze, *The first direct detection of gravitational waves opens a vast new frontier in astronomy*, *Current Science* **113** (2017) 657.

[127] B. Schutz, *A First Course in General Relativity*. 2009.

[128] B. S. Sathyaprakash and B. F. Schutz, *Physics, Astrophysics and Cosmology with Gravitational Waves*, *Living Reviews in Relativity* **12** (2009) 2 [0903.0338].

[129] R. A. Isaacson, *Gravitational radiation in the limit of high frequency. i. the linear approximation and geometrical optics*, *Phys. Rev.* **166** (1968) 1263.

[130] R. A. Isaacson, *Gravitational radiation in the limit of high frequency. ii. nonlinear terms and the effective stress tensor*, *Phys. Rev.* **166** (1968) 1272.

[131] B. F. Schutz and F. Ricci, *Gravitational Waves, Sources, and Detectors*, *arXiv e-prints* (2010) arXiv:1005.4735 [1005.4735].

[132] P. C. Peters, *Gravitational radiation and the motion of two point masses*, *Phys. Rev.* **136** (1964) B1224.

[133] L. Blanchet, T. Damour, B. R. Iyer, C. M. Will and A. G. Wiseman, *Gravitational-Radiation Damping of Compact Binary Systems to Second Post-Newtonian Order*, Phys. Rev. Lett. **74** (1995) 3515 [gr-qc/9501027].

[134] M. Oguri, *Strong gravitational lensing of explosive transients*, *Reports on Progress in Physics* **82** (2019) 126901 [1907.06830].

[135] S. Mukherjee, T. Broadhurst, J. M. Diego, J. Silk and G. F. Smoot, *Inferring the lensing rate of LIGO-Virgo sources from the stochastic gravitational wave background*, MNRAS **501** (2021) 2451 [2006.03064].

[136] S. W. Hawking and W. Israel, *Three Hundred Years of Gravitation*. 1989.

[137] C. Cutler and É. E. Flanagan, *Gravitational waves from merging compact binaries: How accurately can one extract the binary's parameters from the inspiral waveform\?*, Phys. Rev. D **49** (1994) 2658 [gr-qc/9402014].

[138] E. Poisson and C. M. Will, *Gravitational waves from inspiraling compact binaries: Parameter estimation using second-post-Newtonian waveforms*, Phys. Rev. D **52** (1995) 848 [gr-qc/9502040].

[139] R. A. Hulse and J. H. Taylor, *A High-Sensitivity Pulsar Survey*, ApJ **191** (1974) L59.

[140] M. Bailes, B. K. Berger, P. R. Brady, M. Branchesi, K. Danzmann, M. Evans et al., *Gravitational-wave physics and astronomy in the 2020s and 2030s*, *Nature Reviews Physics* **3** (2021) 344.

[141] I. Dvorkin, E. Vangioni, J. Silk, J.-P. Uzan and K. A. Olive, *Metallicity-constrained merger rates of binary black holes and the stochastic gravitational wave background*, MNRAS **461** (2016) 3877 [1604.04288].

[142] S. Perlmutter, G. Aldering, M. della Valle, S. Deustua, R. S. Ellis, S. Fabbro et al., *Discovery of a supernova explosion at half the age of the Universe*, Nature **391** (1998) 51 [astro-ph/9712212].

[143] A. G. Riess, A. V. Filippenko, P. Challis, A. Clocchiatti, A. Diercks, P. M. Garnavich et al., *Observational Evidence from Supernovae for an Accelerating Universe and a Cosmological Constant*, AJ **116** (1998) 1009 [astro-ph/9805201].

[144] Abbott et al., *Gravitational Waves and Gamma-Rays from a Binary Neutron Star Merger: GW170817 and GRB 170817A*, ApJ **848** (2017) L13 [1710.05834].

[145] Abbott et al., *Multi-messenger Observations of a Binary Neutron Star Merger*, ApJ **848** (2017) L12 [1710.05833].

[146] A. von Kienlin, C. Meegan and A. Goldstein, *GRB 170817A: Fermi GBM detection.*, *GRB Coordinates Network* **21520** (2017) 1.

[147] V. Connaughton, GBM-LIGO Group, L. Blackburn, M. S. Briggs, J. Broida, E. Burns et al., *LIGO/Virgo G298048: Fermi GBM trigger 170817.529 and LIGO single IFO trigger*, *GRB Coordinates Network* **21506** (2017) 1.

[148] A. Goldstein, P. Veres, E. Burns, M. S. Briggs, R. Hamburg, D. Kocevski et al., *An ordinary short gamma-ray burst with extraordinary implications: Fermi -GBM detection of GRB 170817a*, *The Astrophysical Journal* **848** (2017) L14.

[149] V. Savchenko, C. Ferrigno, E. Kuulkers, A. Bazzano, E. Bozzo, S. Brandt et al., *INTEGRAL Detection of the First Prompt Gamma-Ray Signal Coincident with the Gravitational-wave Event GW170817*, ApJ **848** (2017) L15 [1710.05449].

[150] B. P. A. et al., *Search for gravitational waves associated with gamma-ray bursts during the first advanced LIGO observing run and implications for the origin of GRB 150906b*, *The Astrophysical Journal* **841** (2017) 89.

[151] Abbott et al., *GW170817: Observation of Gravitational Waves from a Binary Neutron Star Inspiral*, Phys. Rev. Lett. **119** (2017) 161101 [1710.05832].

[152] B. Allen, W. G. Anderson, P. R. Brady, D. A. Brown and J. D. E. Creighton, *FINDCHIRP: An algorithm for detection of gravitational waves from inspiraling compact binaries*, Phys. Rev. D **85** (2012) 122006 [gr-qc/0509116].

[153] L. S. Finn and D. F. Chernoff, *Observing binary inspiral in gravitational radiation: One interferometer*, Phys. Rev. D **47** (1993) 2198 [gr-qc/9301003].

[154] H.-Y. Chen, D. E. Holz, J. Miller, M. Evans, S. Vitale and J. Creighton, *Distance measures in gravitational-wave astrophysics and cosmology*, *Classical and Quantum Gravity* **38** (2021) 055010 [1709.08079].

[155] Abbott et al., *GW170817: Implications for the Stochastic Gravitational-Wave Background from Compact Binary Coalescences*, Phys. Rev. Lett. **120** (2018) 091101 [1710.05837].

[156] Soares-Santos et al., *The Electromagnetic Counterpart of the Binary Neutron Star Merger LIGO/Virgo GW170817. I. Discovery of the Optical Counterpart Using the Dark Energy Camera*, ApJ **848** (2017) L16 [1710.05459].

[157] Fishbach et al., *A Standard Siren Measurement of the Hubble Constant from GW170817 without the Electromagnetic Counterpart*, ApJ **871** (2019) L13 [1807.05667].

[158] Soares-Santos et al., *First Measurement of the Hubble Constant from a Dark Standard Siren using the Dark Energy Survey Galaxies and the LIGO/Virgo Binary-Black-hole Merger GW170814*, ApJ **876** (2019) L7 [1901.01540].

[159] B. F. Schutz, *Determining the Hubble constant from gravitational wave observations*, Nature **323** (1986) 310.

[160] D. E. Holz and S. A. Hughes, *Using Gravitational-Wave Standard Sirens*, ApJ **629** (2005) 15 [astro-ph/0504616].

[161] W. Del Pozzo, *Inference of cosmological parameters from gravitational waves: Applications to second generation interferometers*, *Phys. Rev. D* **86** (2012) 043011.

[162] R. Nair, S. Bose and T. D. Saini, *Measuring the hubble constant: Gravitational wave observations meet galaxy clustering*, *Phys. Rev. D* **98** (2018) 023502.

[163] H.-Y. Chen, M. Fishbach and D. E. Holz, *A two per cent Hubble constant measurement from standard sirens within five years*, Nature **562** (2018) 545 [1712.06531].

[164] R. Gray, I. M. n. Hernandez, H. Qi, A. Sur, P. R. Brady, H.-Y. Chen et al., *Cosmological inference using gravitational wave standard sirens: A mock data analysis*, *Phys. Rev. D* **101** (2020) 122001.

[165] Abbott et al., *A Gravitational-wave Measurement of the Hubble Constant Following the Second Observing Run of Advanced LIGO and Virgo*, ApJ **909** (2021) 218 [1908.06060].

[166] C. Messenger and J. Read, *Measuring a cosmological distance-redshift relationship using only gravitational wave observations of binary neutron star coalescences*, *Phys. Rev. Lett.* **108** (2012) 091101.

[167] D. F. Chernoff and L. S. Finn, *Gravitational Radiation, Inspiraling Binaries, and Cosmology*, ApJ **411** (1993) L5 [gr-qc/9304020].

[168] S. R. Taylor and J. R. Gair, *Cosmology with the lights off: Standard sirens in the einstein telescope era*, *Phys. Rev. D* **86** (2012) 023502.

[169] S. R. Taylor, J. R. Gair and I. Mandel, *Cosmology using advanced gravitational-wave detectors alone*, *Phys. Rev. D* **85** (2012) 023535.

[170] W. M. Farr, N. Sravan, A. Cantrell, L. Kreidberg, C. D. Bailyn, I. Mandel et al., *The Mass Distribution of Stellar-mass Black Holes*, ApJ **741** (2011) 103 [1011.1459].

[171] D. E. Holz, S. A. Hughes and B. F. Schutz, *Measuring cosmic distances with standard sirens*, *Physics Today* **71** (2018) 34.

[172] E. Belgacem, G. Calcagni, M. Crisostomi, C. Dalang, Y. Dirian, J. M. Ezquiaga et al., *Testing modified gravity at cosmological distances with LISA standard sirens*, J. Cosmology Astropart. Phys. **2019** (2019) 024 [1906.01593].

[173] W. L. Freedman, *Cosmology at a crossroads*, *Nature Astronomy* **1** (2017) 0121.

[174] W. L. Freedman, *Determination of the Hubble Constant*, in *Critical Dialogues in Cosmology* (N. Turok, ed.), p. 92, Jan., 1997, astro-ph/9612024.

[175] W. L. Freedman, *Measuring Cosmological Parameters*, *Proceedings of the National Academy of Science* **95** (1998) 2 [astro-ph/9706072].

[176] W. L. Freedman, *The Hubble constant and the expansion age of the Universe*, Phys. Rep. **333** (2000) 13 [astro-ph/9909076].

[177] W. L. Freedman and B. F. Madore, *The Hubble Constant*, ARA&A **48** (2010) 673 [1004.1856].

[178] L. Verde, T. Treu and A. G. Riess, *Tensions between the early and late Universe*, *Nature Astronomy* **3** (2019) 891 [1907.10625].

[179] W. L. Freedman, J. R. Mould, J. Kennicutt, R. C. and B. F. Madore, *The Hubble Space Telescope Key Project to Measure the Hubble Constant*, in *Cosmological Parameters and the Evolution of the Universe* (K. Sato, ed.), vol. 183, p. 17, Jan., 1999, astro-ph/9801080.

[180] E. M. L. Humphreys, M. J. Reid, J. M. Moran, L. J. Greenhill and A. L. Argon, *Toward a New Geometric Distance to the Active Galaxy NGC 4258. III. Final Results and the Hubble Constant*, ApJ **775** (2013) 13 [1307.6031].

[181] G. F. Benedict, B. E. McArthur, M. W. Feast, T. G. Barnes, T. E. Harrison, R. J. Patterson et al., *Hubble Space Telescope Fine Guidance Sensor Parallaxes of Galactic Cepheid Variable Stars: Period-Luminosity Relations*, AJ **133** (2007) 1810 [astro-ph/0612465].

[182] W. L. Freedman, B. F. Madore, V. Scowcroft, C. Burns, A. Monson, S. E. Persson et al., *Carnegie Hubble Program: A Mid-infrared Calibration of the Hubble Constant*, ApJ **758** (2012) 24 [1208.3281].

[183] Riess et al., *Large Magellanic Cloud Cepheid Standards Provide a 1% Foundation for the Determination of the Hubble Constant and Stronger Evidence for Physics beyond ΛCDM*, ApJ **876** (2019) 85 [1903.07603].

[184] W. L. Freedman, B. F. Madore, V. Scowcroft, A. Monson, S. E. Persson, M. Seibert et al., *The Carnegie Hubble Program*, AJ **142** (2011) 192 [1109.3802].

[185] W. L. Freedman and Carnegie Supernova Project, *The Carnegie Supernova Project*, in *Observing Dark Energy* (S. C. Wolff and T. R. Lauer, eds.), vol. 339 of *Astronomical Society of the Pacific Conference Series*, p. 50, Aug., 2005, astro-ph/0411176.

[186] C. R. Burns, E. Parent, M. M. Phillips, M. Stritzinger, K. Krisciunas, N. B. Suntzeff et al., *The Carnegie Supernova Project: Absolute Calibration and the Hubble Constant*, ApJ **869** (2018) 56 [1809.06381].

[187] M. M. Phillips, C. Contreras, E. Y. Hsiao, N. Morrell, C. R. Burns, M. Stritzinger et al., *Carnegie Supernova Project-II: Extending the Near-infrared Hubble Diagram for Type Ia Supernovae to $z \sim 0.1$*, PASP **131** (2019) 014001 [1810.09252].

[188] J. A. Rich, B. F. Madore, A. J. Monson, W. L. Freedman, R. L. Beaton, G. Clementini et al., *The Carnegie-Chicago Hubble Program: Calibration of the Near-infrared RR Lyrae Period-Luminosity Relation with HST*, ApJ **869** (2018) 82 [1812.06053].

[189] T. J. Hoyt, W. L. Freedman, B. F. Madore, D. Hatt, R. L. Beaton, I. S. Jang et al., *The Carnegie Chicago Hubble Program. VI. Tip of the Red Giant Branch Distances to M66 and M96 of the Leo I Group*, ApJ **882** (2019) 150 [1907.05891].

[190] Freedman et al., *The Carnegie-Chicago Hubble Program. VIII. An Independent Determination of the Hubble Constant Based on the Tip of the Red Giant Branch*, ApJ **882** (2019) 34 [1907.05922].

[191] R. L. Beaton, M. Seibert, D. Hatt, W. L. Freedman, T. J. Hoyt, I. S. Jang et al., *The Carnegie-Chicago Hubble Program. VII. The Distance to M101 via the Optical Tip of the Red Giant Branch Method*, ApJ **885** (2019) 141 [1908.06120].

[192] I. S. Jang, T. J. Hoyt, R. L. Beaton, W. L. Freedman, B. F. Madore, M. G. Lee et al., *The Carnegie-Chicago Hubble Program. IX. Calibration of the Tip of the Red Giant Branch Method in the Megamaser Host Galaxy, NGC 4258 (M106)*, ApJ **906** (2021) 125 [2008.04181].

[193] A. Burrow, E. Baron, C. Ashall, C. R. Burns, N. Morrell, M. D. Stritzinger et al., *Carnegie Supernova Project: Classification of Type Ia Supernovae*, ApJ **901** (2020) 154 [2008.07636].

[194] Wong et al., *H0LiCOW - XIII. A 2.4 per cent measurement of H_0 from lensed quasars: 5.3σ tension between early- and late-Universe probes*, MNRAS **498** (2020) 1420 [1907.04869].

[195] Macaulay et al., *First cosmological results using Type Ia supernovae from the Dark Energy Survey: measurement of the Hubble constant*, MNRAS **486** (2019) 2184 [1811.02376].

[196] M. Bartelmann, *TOPICAL REVIEW Gravitational lensing*, *Classical and Quantum Gravity* **27** (2010) 233001 [1010.3829].

[197] Abbott et al., *Dark Energy Survey Year 1 Results: A Precise H_0 Estimate from DES Y1, BAO, and D/H Data*, MNRAS **480** (2018) 3879 [1711.00403].

[198] S. Mukherjee and B. D. Wandelt, *Beyond the classical distance-redshift test: cross-correlating redshift-free standard candles and sirens with redshift surveys*, *arXiv e-prints* (2018) arXiv:1808.06615 [1808.06615].

[199] Di Valentino E et al., *Cosmology Intertwined I: Perspectives for the next decade*, *Astroparticle Physics* **131** (2021) 102606 [2008.11283].

[200] A. G. Riess, S. Casertano, W. Yuan, J. B. Bowers, L. Macri, J. C. Zinn et al., *Cosmic Distances Calibrated to 1% Precision with Gaia EDR3 Parallaxes and Hubble Space Telescope Photometry of 75 Milky Way Cepheids Confirm Tension with ΛCDM*, ApJ **908** (2021) L6 [2012.08534].

[201] E. Di Valentino, O. Mena, S. Pan, L. Visinelli, W. Yang, A. Melchiorri et al., *In the realm of the Hubble tension-a review of solutions*, *Classical and Quantum Gravity* **38** (2021) 153001 [2103.01183].

[202] W. L. Freedman, *Measurements of the Hubble Constant: Tensions in Perspective*, ApJ **919** (2021) 16 [2106.15656].

[203] A. G. Riess, S. Casertano, W. Yuan, L. Macri, B. Bucciarelli, M. G. Lattanzi et al., *Milky Way Cepheid Standards for Measuring Cosmic Distances and Application to Gaia DR2: Implications for the Hubble Constant*, ApJ **861** (2018) 126 [1804.10655].

[204] E. Di Valentino, D. E. Holz, A. Melchiorri and F. Renzi, *Cosmological impact of future constraints on H_0 from gravitational-wave standard sirens*, Phys. Rev. D **98** (2018) 083523 [1806.07463].

[205] K. Hotokezaka, E. Nakar, O. Gottlieb, S. Nissanke, K. Masuda, G. Hallinan et al., *A Hubble constant measurement from superluminal motion of the jet in GW170817*, *Nature Astronomy* **3** (2019) 940 [1806.10596].

[206] C. D. Huang, A. G. Riess, W. Yuan, L. M. Macri, N. L. Zakamska, S. Casertano et al., *Hubble Space Telescope Observations of Mira Variables in the SN Ia Host NGC 1559: An Alternative Candle to Measure the Hubble Constant*, ApJ **889** (2020) 5 [1908.10883].

[207] N. Khetan, L. Izzo, M. Branchesi, R. Wojtak, M. Cantiello, C. Murugeshan et al., *A new measurement of the Hubble constant using Type Ia supernovae calibrated with surface brightness fluctuations*, A&A **647** (2021) A72 [2008.07754].

[208] J. P. Blakeslee, J. B. Jensen, C.-P. Ma, P. A. Milne and J. E. Greene, *The Hubble Constant from Infrared Surface Brightness Fluctuation Distances*, ApJ **911** (2021) 65 [2101.02221].

[209] M. J. Reid, D. W. Pesce and A. G. Riess, *An Improved Distance to NGC 4258 and Its Implications for the Hubble Constant*, ApJ **886** (2019) L27 [1908.05625].

[210] Birrer S et al., *TDCOSMO. IV. Hierarchical time-delay cosmography - joint inference of the Hubble constant and galaxy density profiles*, A&A **643** (2020) A165 [2007.02941].

[211] S. Nissanke, D. E. Holz, N. Dalal, S. A. Hughes, J. L. Sievers and C. M. Hirata, *Determining the Hubble constant from gravitational wave observations of merging compact binaries*, *arXiv e-prints* (2013) arXiv:1307.2638 [1307.2638].

[212] N. Dalal, D. E. Holz, S. A. Hughes and B. Jain, *Short GRB and binary black hole standard sirens as a probe of dark energy*, Phys. Rev. D **74** (2006) 063006 [astro-ph/0601275].

[213] A. Nishizawa, *Measurement of Hubble constant with stellar-mass binary black holes*, Phys. Rev. D **96** (2017) 101303 [1612.06060].

[214] N. Seto and K. Kyutoku, *Prospects of the local Hubble parameter measurement using gravitational waves from double neutron stars*, MNRAS **475** (2018) 4133 [1710.06424].

[215] R. Nair, S. Bose and T. D. Saini, *Measuring the Hubble constant: Gravitational wave observations meet galaxy clustering*, Phys. Rev. D **98** (2018) 023502 [1804.06085].

[216] S. Vitale and H.-Y. Chen, *Measuring the Hubble Constant with Neutron Star Black Hole Mergers*, Phys. Rev. Lett. **121** (2018) 021303 [1804.07337].

[217] LIGO Scientific Collaboration and Virgo Collaboration collaboration, B. P. e. a. Abbott, *Observation of gravitational waves from a binary black hole merger*, Phys. Rev. Lett. **116** (2016) 061102.

[218] Palmese et al., *A Statistical Standard Siren Measurement of the Hubble Constant from the LIGO/Virgo Gravitational Wave Compact Object Merger GW190814 and Dark Energy Survey Galaxies*, ApJ **900** (2020) L33 [2006.14961].

[219] The LIGO Scientific Collaboration, *Constraints on the cosmic expansion history from GWTC-3*, *arXiv e-prints* (2021) arXiv:2111.03604 [2111.03604].

[220] E. J. Copeland, M. Sami and S. Tsujikawa, *Dynamics of Dark Energy*, *International Journal of Modern Physics D* **15** (2006) 1753 [hep-th/0603057].

[221] Kowalski et al., *Improved Cosmological Constraints from New, Old, and Combined Supernova Data Sets*, ApJ **686** (2008) 749 [0804.4142].

[222] Hicken et al., *CfA3: 185 Type Ia Supernova Light Curves from the CfA*, ApJ **700** (2009) 331 [0901.4787].

[223] Komatsu et al.., *Five-Year Wilkinson Microwave Anisotropy Probe Observations: Cosmological Interpretation*, ApJS **180** (2009) 330 [0803.0547].

[224] Komatsu et al., *Seven-year Wilkinson Microwave Anisotropy Probe (WMAP) Observations: Cosmological Interpretation*, ApJS **192** (2011) 18 [1001.4538].

[225] Eisenstein et al., *Detection of the Baryon Acoustic Peak in the Large-Scale Correlation Function of SDSS Luminous Red Galaxies*, ApJ **633** (2005) 560 [astro-ph/0501171].

[226] W. J. Percival, S. Cole, D. J. Eisenstein, R. C. Nichol, J. A. Peacock, A. C. Pope et al., *Measuring the Baryon Acoustic Oscillation scale using the Sloan Digital Sky Survey and 2dF Galaxy Redshift Survey*, MNRAS **381** (2007) 1053 [0705.3323].

[227] Percival et al., *Baryon acoustic oscillations in the Sloan Digital Sky Survey Data Release 7 galaxy sample*, MNRAS **401** (2010) 2148 [0907.1660].

[228] Schrabback et al., *Evidence of the accelerated expansion of the Universe from weak lensing tomography with COSMOS*, A&A **516** (2010) A63 [0911.0053].

[229] M. Kilbinger, *Cosmological parameters from weak cosmological lensing*, *arXiv e-prints* (2018) arXiv:1807.08249 [1807.08249].

[230] M. Lagos, M. Fishbach, P. Landry and D. E. Holz, *Standard sirens with a running Planck mass*, Phys. Rev. D **99** (2019) 083504 [1901.03321].

[231] D. Bertacca, A. Raccanelli, N. Bartolo and S. Matarrese, *Cosmological perturbation effects on gravitational-wave luminosity distance estimates*, *Physics of the Dark Universe* **20** (2018) 32 [1702.01750].

[232] L. F. Abbott and M. B. Wise, *Constraints on generalized inflationary cosmologies*, *Nuclear Physics B* **244** (1984) 541.

[233] L. P. Grishchuk, *REVIEWS OF TOPICAL PROBLEMS: Relic gravitational waves and cosmology*, *Physics Uspekhi* **48** (2005) 1235 [gr-qc/0504018].

[234] A. A. Starobinskiĭ, *Spectrum of relict gravitational radiation and the early state of the universe*, *Soviet Journal of Experimental and Theoretical Physics Letters* **30** (1979) 682.

[235] V. A. Rubakov, M. V. Sazhin and A. V. Veryaskin, *Graviton Creation in the Inflationary Universe and the Grand Unification Scale*, *Phys. Lett. B* **115** (1982) 189.

[236] R. Fabbri and M. d. Pollock, *The Effect of Primordially Produced Gravitons upon the Anisotropy of the Cosmological Microwave Background Radiation*, *Phys. Lett. B* **125** (1983) 445.

[237] P. D. Lasky, C. M. F. Mingarelli, T. L. Smith, J. T. Giblin, E. Thrane, D. J. Reardon et al., *Gravitational-Wave Cosmology across 29 Decades in Frequency*, *Physical Review X* **6** (2016) 011035 [1511.05994].

[238] L. P. Grishchuk, *Cosmological perturbations of quantum mechanical origin and anisotropy of the microwave background radiation*, *NATO Sci. Ser. C* **467** (1995) 205 [gr-qc/9410025].

[239] M. Chiara Guzzetti, N. Bartolo, M. Liguori and S. Matarrese, *Gravitational waves from inflation*, *arXiv e-prints* (2016) arXiv:1605.01615 [1605.01615].

[240] M. Maggiore, *Gravitational wave experiments and early universe cosmology*, Phys. Rep. **331** (2000) 283 [gr-qc/9909001].

[241] L. Martellini, *Stochastic gravitational wave background : detection methods in non-Gaussian regimes*, theses, COMUE Université Côte d'Azur (2015 - 2019), May, 2017.

[242] S. Y. Khlebnikov and I. I. Tkachev, *Classical Decay of the Inflaton*, Phys. Rev. Lett. **77** (1996) 219 [hep-ph/9603378].

[243] D. H. Lyth and A. R. Liddle, *The primordial density perturbation: Cosmology, inflation and the origin of structure*. 2009.

[244] L. Kofman, A. Linde and A. A. Starobinsky, *Towards the theory of reheating after inflation*, Phys. Rev. D **56** (1997) 3258 [hep-ph/9704452].

[245] J. H. Traschen and R. H. Brandenberger, *Particle production during out-of-equilibrium phase transitions*, *Phys. Rev. D* **42** (1990) 2491.

[246] Y. Watanabe and E. Komatsu, *Improved calculation of the primordial gravitational wave spectrum in the standard model*, Phys. Rev. D **73** (2006) 123515 [astro-ph/0604176].

[247] T. L. Smith, E. Pierpaoli and M. Kamionkowski, *New Cosmic Microwave Background Constraint to Primordial Gravitational Waves*, Phys. Rev. Lett. **97** (2006) 021301 [astro-ph/0603144].

[248] S. Bashinsky and U. Seljak, *Signatures of relativistic neutrinos in CMB anisotropy and matter clustering*, Phys. Rev. D **69** (2004) 083002 [astro-ph/0310198].

[249] A. Ota, T. Takahashi, H. Tashiro and M. Yamaguchi, *CMB μ distortion from primordial gravitational waves*, J. Cosmology Astropart. Phys. **2014** (2014) 029 [1406.0451].

[250] J. Chluba, L. Dai, D. Grin, M. A. Amin and M. Kamionkowski, *Spectral distortions from the dissipation of tensor perturbations*, MNRAS **446** (2015) 2871 [1407.3653].

[251] K. W. Masui and U.-L. Pen, *Primordial Gravity Wave Fossils and Their Use in Testing Inflation*, Phys. Rev. Lett. **105** (2010) 161302 [1006.4181].

[252] F. Schmidt and D. Jeong, *Large-scale structure with gravitational waves. II. Shear*, Phys. Rev. D **86** (2012) 083513 [1205.1514].

[253] L. Dai, D. Jeong and M. Kamionkowski, *Anisotropic imprint of long-wavelength tensor perturbations on cosmic structure*, Phys. Rev. D **88** (2013) 043507 [1306.3985].

[254] F. Schmidt, E. Pajer and M. Zaldarriaga, *Large-scale structure and gravitational waves. III. Tidal effects*, Phys. Rev. D **89** (2014) 083507 [1312.5616].

[255] S. Dodelson, E. Rozo and A. Stebbins, *Primordial Gravity Waves and Weak Lensing*, Phys. Rev. Lett. **91** (2003) 021301 [astro-ph/0301177].

[256] S. Dodelson, *Cross-correlating probes of primordial gravitational waves*, Phys. Rev. D **82** (2010) 023522 [1001.5012].

[257] D. Jeong and F. Schmidt, *Large-scale structure with gravitational waves. I. Galaxy clustering*, Phys. Rev. D **86** (2012) 083512 [1205.1512].

[258] C. J. Moore, R. H. Cole and C. P. L. Berry, *Gravitational-wave sensitivity curves*, *Classical and Quantum Gravity* **32** (2015) 015014 [1408.0740].

[259] B. C. Joshi, *Pulsar Timing Arrays*, *International Journal of Modern Physics D* **22** (2013) 1341008 [1301.5730].

[260] S. Weinberg, *Damping of tensor modes in cosmology*, Phys. Rev. D **69** (2004) 023503 [astro-ph/0306304].

[261] S. Bashinsky, *Coupled Evolution of Primordial Gravity Waves and Relic Neutrinos*, *arXiv e-prints* (2005) astro [astro-ph/0505502].

[262] D. A. Dicus and W. W. Repko, *Comment on "Damping of tensor modes in cosmology"*, Phys. Rev. D **72** (2005) 088302 [astro-ph/0509096].

[263] L. A. Boyle and P. J. Steinhardt, *Probing the early universe with inflationary gravitational waves*, Phys. Rev. D **77** (2008) 063504 [astro-ph/0512014].

[264] A. Mangilli, N. Bartolo, S. Matarrese and A. Riotto, *Impact of cosmic neutrinos on the gravitational-wave background*, Phys. Rev. D **78** (2008) 083517 [0805.3234].

[265] W. Zhao, Y. Zhang and T. Xia, *New method to constrain the relativistic free-streaming gas in the Universe*, *Physics Letters B* **677** (2009) 235 [0905.3223].

[266] R. Jinno, T. Moroi and K. Nakayama, *Probing dark radiation with inflationary gravitational waves*, Phys. Rev. D **86** (2012) 123502 [1208.0184].

[267] G. Shchedrin, *Late time evolution of the gravitational wave damping in the early Universe*, *arXiv e-prints* (2012) arXiv:1204.1384 [1204.1384].

[268] B. A. Stefanek and W. W. Repko, *Analytic description of the damping of gravitational waves by free streaming neutrinos*, Phys. Rev. D **88** (2013) 083536 [1207.7285].

[269] J. B. Dent, L. M. Krauss, S. Sabharwal and T. Vachaspati, *Damping of primordial gravitational waves from generalized sources*, Phys. Rev. D **88** (2013) 084008 [1307.7571].

[270] S. Saga, K. Ichiki and N. Sugiyama, *Impact of anisotropic stress of free-streaming particles on gravitational waves induced by cosmological density perturbations*, Phys. Rev. D **91** (2015) 024030 [1412.1081].

[271] Abbott et al., *LIGO: the Laser Interferometer Gravitational-Wave Observatory*, *Reports on Progress in Physics* **72** (2009) 076901 [0711.3041].

[272] F. Acernese, M. Alshourbagy, P. Amico, F. Antonucci, S. Aoudia, P. Astone et al., *Status of virgo*, *Classical and Quantum Gravity* **25** (2008) 114045.

[273] B. Willke, P. Ajith, B. Allen, P. Aufmuth, C. Aulbert, S. Babak et al., *The GEO-HF project*, *Classical and Quantum Gravity* **23** (2006) S207.

[274] Aasi et al., *Searching for stochastic gravitational waves using data from the two colocated LIGO Hanford detectors*, Phys. Rev. D **91** (2015) 022003 [1410.6211].

[275] F. A. Jenet, G. B. Hobbs, W. van Straten, R. N. Manchester, M. Bailes, J. P. W. Verbiest et al., *Upper Bounds on the Low-Frequency Stochastic Gravitational Wave Background from Pulsar Timing Observations: Current Limits and Future Prospects*, ApJ **653** (2006) 1571 [astro-ph/0609013].

[276] R. van Haasteren, Y. Levin, G. H. Janssen, K. Lazaridis, M. Kramer, B. W. Stappers et al., *Placing limits on the stochastic gravitational-wave background using European Pulsar Timing Array data*, *Monthly Notices of the Royal Astronomical Society* **414** (2011) 3117 [https://academic.oup.com/mnras/article-pdf/414/4/3117/18703845/mnras0414-3117.

[277] L. P. Grishchuk, *Primordial gravitons and possibility of their observation*, *Soviet Journal of Experimental and Theoretical Physics Letters* **23** (1976) 293.

[278] R. Bar-Kana, *Limits on direct detection of gravitational waves*, Phys. Rev. D **50** (1994) 1157 [astro-ph/9401050].

[279] B. Allen, *The Stochastic Gravity-Wave Background: Sources and Detection*, in *Relativistic Gravitation and Gravitational Radiation* (J.-A. Marck and J.-P. Lasota, eds.), p. 373, Jan., 1997, gr-qc/9604033.

[280] Abbott et al., *GW151226: Observation of Gravitational Waves from a 22-Solar-Mass Binary Black Hole Coalescence*, Phys. Rev. Lett. **116** (2016) 241103 [1606.04855].

[281] Abbott et al., *GW170104: Observation of a 50-Solar-Mass Binary Black Hole Coalescence at Redshift 0.2*, Phys. Rev. Lett. **118** (2017) 221101 [1706.01812].

[282] E. S. Phinney, *The Rate of Neutron Star Binary Mergers in the Universe: Minimal Predictions for Gravity Wave Detectors*, ApJ **380** (1991) L17.

[283] D. I. Kosenko and K. A. Postnov, *On the gravitational wave noise from unresolved extragalactic binaries*, *Astron. Astrophys.* **336** (1998) 786 [astro-ph/9801032].

[284] T. Regimbau and J. A. de Freitas Pacheco, *Stochastic Background from Coalescences of Neutron Star-Neutron Star Binaries*, ApJ **642** (2006) 455 [gr-qc/0512008].

[285] X.-J. Zhu, E. Howell, T. Regimbau, D. Blair and Z.-H. Zhu, *Stochastic Gravitational Wave Background from Coalescing Binary Black Holes*, ApJ **739** (2011) 86 [1104.3565].

[286] P. A. Rosado, *Gravitational wave background from binary systems*, Phys. Rev. D **84** (2011) 084004 [1106.5795].

[287] S. Marassi, R. Schneider, G. Corvino, V. Ferrari and S. Portegies Zwart, *Imprint of the merger and ring-down on the gravitational wave background from black hole binaries coalescence*, Phys. Rev. D **84** (2011) 124037 [1111.6125].

[288] C. Wu, V. Mandic and T. Regimbau, *Accessibility of the gravitational-wave background due to binary coalescences to second and third generation gravitational-wave detectors*, *Phys. Rev. D* **85** (2012) 104024.

[289] S. Kuroyanagi, T. Chiba and T. Takahashi, *Probing the universe through the stochastic gravitational wave background*, .

[290] E. F. D. Evangelista and J. C. N. de Araujo, *a New Method to Calculate the Stochastic Background of Gravitational Waves Generated by Compact Binaries*, *Modern Physics Letters A* **28** (2013) 1350174 [1504.04300].

[291] LIGO Scientific, Virgo collaboration, B. P. Abbott et al., *GW150914: Implications for the stochastic gravitational wave background from binary black holes*, *Phys. Rev. Lett.* **116** (2016) 131102 [1602.03847].

[292] K. Crocker, T. Prestegard, V. Mandic, T. Regimbau, K. Olive and E. Vangioni, *Systematic study of the stochastic gravitational-wave background due to stellar core collapse*, Phys. Rev. D **95** (2017) 063015 [1701.02638].

[293] D. M. Coward, R. R. Burman and D. G. Blair, *The stochastic background of gravitational waves from neutron star formation at cosmological distances*, MNRAS **324** (2001) 1015.

[294] T. Regimbau and J. A. de Freitas Pacheco, *Cosmic background of gravitational waves from rotating neutron stars*, A&A **376** (2001) 381 [astro-ph/0105260].

[295] B. J. Owen, L. Lindblom, C. Cutler, B. F. Schutz, A. Vecchio and N. Andersson, *Gravitational waves from hot young rapidly rotating neutron stars*, *Phys. Rev. D* **58** (1998) 084020.

[296] V. Ferrari, S. Matarrese and R. Schneider, *Stochastic background of gravitational waves generated by a cosmological population of young, rapidly rotating neutron stars*, MNRAS **303** (1999) 258 [astro-ph/9806357].

[297] J. L. Houser, J. M. Centrella and S. C. Smith, *Gravitational radiation from nonaxisymmetric instability in a rotating star*, *Phys. Rev. Lett.* **72** (1994) 1314.

[298] D. Lai and S. L. Shapiro, *Gravitational Radiation from Rapidly Rotating Nascent Neutron Stars*, ApJ **442** (1995) 259 [astro-ph/9408053].

[299] X.-J. Zhu, X.-L. Fan and Z.-H. Zhu, *Stochastic Gravitational Wave Background from Neutron Star r-mode Instability Revisited*, ApJ **729** (2011) 59 [1102.2786].

[300] S. Hod, *Stationary scalar clouds around rotating black holes*, *Phys. Rev. D* **86** (2012) 104026.

[301] V. Ferrari, *Probing the physics of neutron stars with gravitational waves*, .

[302] T. Regimbau and J. A. de Freitas Pacheco, *Gravitational wave background from magnetars*, A&A **447** (2006) 1 [astro-ph/0509880].

[303] T. Regimbau and V. Mandic, *Astrophysical sources of a stochastic gravitational-wave background*, *Classical and Quantum Gravity* **25** (2008) 184018 [0806.2794].

[304] S. Marassi, R. Schneider, G. Corvino, V. Ferrari and S. Portegies Zwart, *Imprint of the merger and ring-down on the gravitational wave background from black hole binaries coalescence*, *Phys. Rev. D* **84** (2011) 124037 [1111.6125].

[305] X.-J. Zhu, E. Howell, T. Regimbau, D. Blair and Z.-H. Zhu, *Stochastic Gravitational Wave Background from Coalescing Binary Black Holes*, *Astrophys. J.* **739** (2011) 86 [1104.3565].

[306] C.-J. Wu, V. Mandic and T. Regimbau, *Accessibility of the stochastic gravitational wave background from magnetars to the interferometric gravitational wave detectors*, *Phys. Rev. D* **87** (2013) 042002.

[307] X.-J. Zhu, E. Howell and D. Blair, *Observational upper limits on the gravitational wave production of core collapse supernovae*, MNRAS **409** (2010) L132 [1008.0472].

[308] A. Buonanno, G. Sigl, G. G. Raffelt, H.-T. Janka and E. Müller, *Stochastic gravitational-wave background from cosmological supernovae*, *Phys. Rev. D* **72** (2005) 084001.

[309] P. Sandick, K. A. Olive, F. Daigne and E. Vangioni, *Gravitational waves from the first stars*, *Phys. Rev. D* **73** (2006) 104024.

[310] M. Cavaglià and A. Modi, *Two-Dimensional Correlation Function of Binary Black Hole Coalescences*, *Universe* **6** (2020) 93 [2005.06004].

[311] P. Sandick, K. Olive, F. Daigne and E. Vangioni, *Gravitational waves from the first stars*, *Physical Review D - Particles, Fields, Gravitation and Cosmology* **73** (2006) .

[312] A. J. Farmer and E. S. Phinney, *The gravitational wave background from cosmological compact binaries*, MNRAS **346** (2003) 1197 [astro-ph/0304393].

[313] R. Brito, S. Ghosh, E. Barausse, E. Berti, V. Cardoso, I. Dvorkin et al., *Stochastic and Resolvable Gravitational Waves from Ultralight Bosons*, Phys. Rev. Lett. **119** (2017) 131101 [1706.05097].

[314] R. Brito, S. Ghosh, E. Barausse, E. Berti, V. Cardoso, I. Dvorkin et al., *Gravitational wave searches for ultralight bosons with LIGO and LISA*, Phys. Rev. D **96** (2017) 064050 [1706.06311].

[315] X.-L. Fan and Y. Chen, *Stochastic gravitational-wave background from spin loss of black holes*, Phys. Rev. D **98** (2018) 044020 [1712.00784].

[316] L. Tsukada, T. Callister, A. Matas and P. Meyers, *First search for a stochastic gravitational-wave background from ultralight bosons*, Phys. Rev. D **99** (2019) 103015 [1812.09622].

[317] C. Palomba, S. D'Antonio, P. Astone, S. Frasca, G. Intini, I. La Rosa et al., *Direct constraints on the ultralight boson mass from searches of continuous gravitational waves*, *Phys. Rev. Lett.* **123** (2019) 171101.

[318] L. Sun, R. Brito and M. Isi, *Search for ultralight bosons in cygnus x-1 with advanced ligo*, *Phys. Rev. D* **101** (2020) 063020.

[319] D. Baskaran, L. P. Grishchuk and A. G. Polnarev, *Imprints of relic gravitational waves in cosmic microwave background radiation*, Phys. Rev. D **74** (2006) 083008 [gr-qc/0605100].

[320] R. Easther, J. T. Giblin and E. A. Lim, *Gravitational wave production at the end of inflation*, *Phys. Rev. Lett.* **99** (2007) 221301.

[321] N. Barnaby, E. Pajer and M. Peloso, *Gauge field production in axion inflation: Consequences for monodromy, non-gaussianity in the cmb, and gravitational waves at interferometers*, *Phys. Rev. D* **85** (2012) 023525.

[322] J. L. Cook and L. Sorbo, *Particle production during inflation and gravitational waves detectable by ground-based interferometers*, *Phys. Rev. D* **85** (2012) 023534.

[323] A. Lopez and K. Freese, *First test of high frequency Gravity Waves from inflation using Advanced LIGO*, J. Cosmology Astropart. Phys. **2015** (2015) 037 [1305.5855].

[324] M. S. Turner, *Detectability of inflation-produced gravitational waves*, *Phys. Rev. D* **55** (1997) R435.

[325] R. Easther and E. A. Lim, *Stochastic gravitational wave production after inflation*, J. Cosmology Astropart. Phys. **2006** (2006) 010 [astro-ph/0601617].

[326] S. G. Crowder, R. Namba, V. Mandic, S. Mukohyama and M. Peloso, *Measurement of parity violation in the early universe using gravitational-wave detectors*, *Physics Letters B* **726** (2013) 66 [1212.4165].

[327] A. Kosowsky, M. S. Turner and R. Watkins, *Gravitational radiation from colliding vacuum bubbles*, *Phys. Rev. D* **45** (1992) 4514.

[328] R. Apreda, M. Maggiore, A. Nicolis and A. Riotto, *Gravitational waves from electroweak phase transitions*, *Nuclear Physics B* **631** (2002) 342 [gr-qc/0107033].

[329] B. von Harling, A. Pomarol, O. Pujolàs and F. Rompineve, *Peccei-Quinn phase transition at LIGO*, *Journal of High Energy Physics* **2020** (2020) 195 [1912.07587].

[330] P. S. B. Dev and A. Mazumdar, *Probing the scale of new physics by Advanced LIGO/VIRGO*, Phys. Rev. D **93** (2016) 104001 [1602.04203].

[331] L. Marzola, A. Racioppi and V. Vaskonen, *Phase transition and gravitational wave phenomenology of scalar conformal extensions of the Standard Model*, *European Physical Journal C* **77** (2017) 484 [1704.01034].

[332] R. R. Caldwell and B. Allen, *Cosmological constraints on cosmic-string gravitational radiation*, *Phys. Rev. D* **45** (1992) 3447.

[333] T. Damour and A. Vilenkin, *Gravitational Wave Bursts from Cosmic Strings*, Phys. Rev. Lett. **85** (2000) 3761 [gr-qc/0004075].

[334] T. Damour and A. Vilenkin, *Gravitational radiation from cosmic (super)strings: Bursts, stochastic background, and observational windows*, *Phys. Rev. D* **71** (2005) 063510.

[335] V. Mandic, S. Bird and I. Cholis, *Stochastic gravitational-wave background due to primordial binary black hole mergers*, *Phys. Rev. Lett.* **117** (2016) 201102.

[336] M. Sasaki, T. Suyama, T. Tanaka and S. Yokoyama, *Primordial black hole scenario for the gravitational-wave event gw150914*, *Phys. Rev. Lett.* **117** (2016) 061101.

[337] S. Wang, Y.-F. Wang, Q.-G. Huang and T. G. F. Li, *Constraints on the Primordial Black Hole Abundance from the First Advanced LIGO Observation Run Using the Stochastic Gravitational-Wave Background*, *arXiv e-prints* (2016) arXiv:1610.08725 [1610.08725].

[338] A. L. Miller, S. Clesse, F. De Lillo, G. Bruno, A. Depasse and A. Tanasijczuk, *Probing planetary-mass primordial black holes with continuous gravitational waves*, *Physics of the Dark Universe* **32** (2021) 100836 [2012.12983].

[339] M. Gasperini and G. Veneziano, *Pre-big-bang in string cosmology*, *Astroparticle Physics* **1** (1993) 317 [hep-th/9211021].

[340] M. Gasperini and G. Veneziano, *The pre-big bang scenario in string cosmology*, Phys. Rep. **373** (2003) 1 [hep-th/0207130].

[341] A. Buonanno, M. Maggiore and C. Ungarelli, *Spectrum of relic gravitational waves in string cosmology*, *Phys. Rev. D* **55** (1997) 3330.

[342] C. Caprini and D. G. Figueroa, *Cosmological backgrounds of gravitational waves*, *Classical and Quantum Gravity* **35** (2018) 163001 [1801.04268].

[343] B. Allen and J. D. Romano, *Detecting a stochastic background of gravitational radiation: Signal processing strategies and sensitivities*, Phys. Rev. D **59** (1999) 102001 [gr-qc/9710117].

[344] J. Kormendy and D. Richstone, *Inward Bound—The Search For Supermassive Black Holes In Galactic Nuclei*, ARA&A **33** (1995) 581.

[345] Abbott et al., *All-sky search for periodic gravitational waves in the O1 LIGO data*, Phys. Rev. D **96** (2017) 062002 [1707.02667].

[346] E. Thrane, S. Ballmer, J. D. Romano, S. Mitra, D. Talukder, S. Bose et al., *Probing the anisotropies of a stochastic gravitational-wave background using a network of ground-based laser interferometers*, Phys. Rev. D **80** (2009) 122002 [0910.0858].

[347] S. Mereghetti, J. A. Pons and A. Melatos, *Magnetars: Properties, Origin and Evolution*, Space Sci. Rev. **191** (2015) 315 [1503.06313].

[348] P. M. Woods and C. Thompson, *Soft gamma repeaters and anomalous X-ray pulsars: magnetar candidates*, vol. 39, pp. 547–586. 2006.

[349] T. Callister, L. Sammut, S. Qiu, I. Mandel and E. Thrane, *Limits of astrophysics with gravitational-wave backgrounds*, *Phys. Rev. X* **6** (2016) 031018.

[350] X. Siemens, V. Mandic and J. Creighton, *Gravitational-wave stochastic background from cosmic strings*, *Phys. Rev. Lett.* **98** (2007) 111101.

[351] M. S. Turner, *Detectability of inflation-produced gravitational waves*, Phys. Rev. D **55** (1997) R435 [astro-ph/9607066].

[352] A. A. Starobinsky, *Spectrum of relict gravitational radiation and the early state of the universe*, *JETP Lett.* **30** (1979) 682.

[353] C. Carbone, C. Baccigalupi and S. Matarrese, *Stochastic gravitational wave background from cold dark matter halos*, Phys. Rev. D **73** (2006) 063503 [astro-ph/0509680].

[354] J. Baker, T. Baker, C. Carbone, G. Congedo, C. Contaldi, I. Dvorkin et al., *High angular resolution gravitational wave astronomy*, *arXiv e-prints* (2019) arXiv:1908.11410 [1908.11410].

[355] T. Regimbau, *The astrophysical gravitational wave stochastic background*, *Research in Astronomy and Astrophysics* **11** (2011) 369 [1101.2762].

[356] M. R. Adams and N. J. Cornish, *Detecting a stochastic gravitational wave background in the presence of a galactic foreground and instrument noise*, Phys. Rev. D **89** (2014) 022001 [1307.4116].

[357] C. R. Contaldi, *Anisotropies of gravitational wave backgrounds: A line of sight approach*, *Physics Letters B* **771** (2017) 9 [1609.08168].

[358] G. Cusin, C. Pitrou and J.-P. Uzan, *Anisotropy of the astrophysical gravitational wave background: Analytic expression of the angular power spectrum and correlation with cosmological observations*, Phys. Rev. D **96** (2017) 103019 [1704.06184].

[359] G. Cusin, I. Dvorkin, C. Pitrou and J.-P. Uzan, *First Predictions of the Angular Power Spectrum of the Astrophysical Gravitational Wave Background*, Phys. Rev. Lett. **120** (2018) 231101 [1803.03236].

[360] G. Cusin, I. Dvorkin, C. Pitrou and J.-P. Uzan, *Properties of the stochastic astrophysical gravitational wave background: Astrophysical sources dependencies*, Phys. Rev. D **100** (2019) 063004 [1904.07797].

[361] K. Riles, *Gravitational waves: Sources, detectors and searches*, *Progress in Particle and Nuclear Physics* **68** (2013) 1 [1209.0667].

[362] M. Zimmermann and E. Szedenits, *Gravitational waves from rotating and precessing rigid bodies: Simple models and applications to pulsars*, *Phys. Rev. D* **20** (1979) 351.

[363] T. W. B. Kibble, *Topology of cosmic domains and strings*, *Journal of Physics A Mathematical General* **9** (1976) 1387.

[364] R. Jeannerot, J. Rocher and M. Sakellariadou, *How generic is cosmic string formation in supersymmetric grand unified theories*, Phys. Rev. D **68** (2003) 103514 [hep-ph/0308134].

[365] A. Vilenkin and E. P. S. Shellard, *Cosmic Strings and Other Topological Defects*. Cambridge University Press, 7, 2000.

[366] N. Turok, *Grand unified strings and galaxy formation*, *Nuclear Physics B* **242** (1984) 520.

[367] T. Damour and A. Vilenkin, *Gravitational wave bursts from cusps and kinks on cosmic strings*, Phys. Rev. D **64** (2001) 064008 [gr-qc/0104026].

[368] M. Sakellariadou and A. Vilenkin, *Cosmic-string evolution in flat spacetime*, *Phys. Rev. D* **42** (1990) 349.

[369] A. Vilenkin, *Cosmic strings as gravitational lenses*, ApJ **282** (1984) L51.

[370] B. Shlaer and M. Wyman, *Cosmic superstring gravitational lensing phenomena: Predictions for networks of (p,q) strings*, Phys. Rev. D **72** (2005) 123504 [hep-th/0509177].

[371] R. Brandenberger, H. Firouzjahi and J. Karouby, *Lensing and CMB anisotropies by cosmic strings at a junction*, Phys. Rev. D **77** (2008) 083502 [0710.1636].

[372] A. Vilenkin and T. Vachaspati, *Electromagnetic radiation from superconducting cosmic strings*, *Phys. Rev. Lett.* **58** (1987) 1041.

[373] N. Kaiser and A. Stebbins, *Microwave anisotropy due to cosmic strings*, Nature **310** (1984) 391.

[374] I. Gott, J. R., *Gravitational lensing effects of vacuum strings - Exact solutions*, ApJ **288** (1985) 422.

[375] T. Vachaspati and A. Vilenkin, *Gravitational radiation from cosmic strings*, *Phys. Rev. D* **31** (1985) 3052.

[376] M. Sakellariadou, *Erratum: Gravitational waves emitted from infinite strings*, *Phys. Rev. D* **43** (1991) 4150.

[377] M. Wyman, L. Pogosian and I. Wasserman, *Bounds on cosmic strings from WMAP and SDSS*, Phys. Rev. D **72** (2005) 023513 [astro-ph/0503364].

[378] N. Bevis, M. Hindmarsh, M. Kunz and J. Urrestilla, *Fitting Cosmic Microwave Background Data with Cosmic Strings and Inflation*, Phys. Rev. Lett. **100** (2008) 021301 [astro-ph/0702223].

[379] R. Battye, B. Garbrecht and A. Moss, *Tight constraints on F- and D-term hybrid inflation scenarios*, Phys. Rev. D **81** (2010) 123512 [1001.0769].

[380] A. Vilenkin and E. P. S. Shellard, *Cosmic Strings and Other Topological Defects*. 2000.

[381] Aasi, *Constraints on Cosmic Strings from the LIGO-Virgo Gravitational-Wave Detectors*, Phys. Rev. Lett. **112** (2014) 131101 [1310.2384].

[382] T. Damour and A. Vilenkin, *Gravitational radiation from cosmic (super)strings: Bursts, stochastic background, and observational windows*, *Phys. Rev. D* **71** (2005) 063510 [hep-th/0410222].

[383] S. Ölmez, V. Mandic and X. Siemens, *Gravitational-wave stochastic background from kinks and cusps on cosmic strings*, Phys. Rev. D **81** (2010) 104028 [1004.0890].

[384] A. D. Linde, *Hybrid inflation*, *Phys. Rev. D* **49** (1994) 748 [astro-ph/9307002].

[385] E. J. Copeland, A. R. Liddle, D. H. Lyth, E. D. Stewart and D. Wands, *False vacuum inflation with Einstein gravity*, Phys. Rev. D **49** (1994) 6410 [astro-ph/9401011].

[386] S. Sarangi and S. H. H. Tye, *Cosmic string production towards the end of brane inflation*, *Physics Letters B* **536** (2002) 185 [hep-th/0204074].

[387] A. Buonanno, *TASI Lectures on Gravitational Waves from the Early Universe*, *arXiv e-prints* (2003) gr [gr-qc/0303085].

[388] N. Jones, H. Stoica and S. H. H. Tye, *Brane Interaction as the Origin of Inflation*, *Journal of High Energy Physics* **2002** (2002) 051 [hep-th/0203163].

[389] Abbott et al., *Constraints on cosmic strings using data from the first Advanced LIGO observing run*, Phys. Rev. D **97** (2018) 102002 [1712.01168].

[390] Abbott, *Constraints on Cosmic Strings Using Data from the Third Advanced LIGO-Virgo Observing Run*, Phys. Rev. Lett. **126** (2021) 241102 [2101.12248].

[391] G. Boileau, A. C. Jenkins, M. Sakellariadou, R. Meyer and N. Christensen, *Ability of LISA to detect a gravitational-wave background of cosmological origin: The cosmic string case*, Phys. Rev. D **105** (2022) 023510 [2109.06552].

[392] P. Auclair, J. J. Blanco-Pillado, D. G. Figueroa, A. C. Jenkins, M. Lewicki, M. Sakellariadou et al., *Probing the gravitational wave background from cosmic strings with LISA*, *Journal of Cosmology and Astroparticle Physics* **2020** (2020) 034.

[393] T. W. B. Kibble, *Evolution of a system of cosmic strings*, *Nucl. Phys. B* **252** (1985) 227.

[394] J. J. Blanco-Pillado, K. D. Olum and B. Shlaer, *Number of cosmic string loops*, Phys. Rev. D **89** (2014) 023512 [1309.6637].

[395] C. Ringeval, M. Sakellariadou and F. R. Bouchet, *Cosmological evolution of cosmic string loops*, J. Cosmology Astropart. Phys. **2007** (2007) 023 [astro-ph/0511646].

[396] L. Lorenz, C. Ringeval and M. Sakellariadou, *Cosmic string loop distribution on all length scales and at any redshift*, J. Cosmology Astropart. Phys. **2010** (2010) 003 [1006.0931].

[397] J. J. Blanco-Pillado, K. D. Olum and X. Siemens, *New limits on cosmic strings from gravitational wave observation*, *Physics Letters B* **778** (2018) 392 [1709.02434].

[398] C. Ringeval and T. Suyama, *Stochastic gravitational waves from cosmic string loops in scaling*, J. Cosmology Astropart. Phys. **2017** (2017) 027 [1709.03845].

[399] Abbott et al., *Search for the isotropic stochastic background using data from Advanced LIGO's second observing run*, Phys. Rev. D **100** (2019) 061101 [1903.02886].

[400] T. L. Smith and R. R. Caldwell, *Lisa for cosmologists: Calculating the signal-to-noise ratio for stochastic and deterministic sources*, *Phys. Rev. D* **100** (2019) 104055.

[401] T. Robson, N. J. Cornish and C. Liu, *The construction and use of LISA sensitivity curves*, *Classical and Quantum Gravity* **36** (2019) 105011 [1803.01944].

[402] Z.-C. Chen, F. Huang and Q.-G. Huang, *Stochastic Gravitational-wave Background from Binary Black Holes and Binary Neutron Stars and Implications for LISA*, ApJ **871** (2019) 97 [1809.10360].

[403] A. C. Jenkins and M. Sakellariadou, *Anisotropies in the stochastic gravitational-wave background: Formalism and the cosmic string case*, Phys. Rev. D **98** (2018) 063509 [1802.06046].

[404] G. Cusin, C. Pitrou and J.-P. Uzan, *The signal of the gravitational wave background and the angular correlation of its energy density*, Phys. Rev. D **97** (2018) 123527 [1711.11345].

[405] G. Cusin, I. Dvorkin, C. Pitrou and J.-P. Uzan, *Stochastic gravitational wave background anisotropies in the mHz band: astrophysical dependencies*, MNRAS **493** (2020) L1 [1904.07757].

[406] N. Bartolo, D. Bertacca, S. Matarrese, M. Peloso, A. Ricciardone, A. Riotto et al., *Anisotropies and non-Gaussianity of the cosmological gravitational wave background*, Phys. Rev. D **100** (2019) 121501 [1908.00527].

[407] V. Alba and J. Maldacena, *Primordial gravity wave background anisotropies*, *Journal of High Energy Physics* **2016** (2016) 115 [1512.01531].

[408] A. C. Jenkins, R. O'Shaughnessy, M. Sakellariadou and D. Wysocki, *Anisotropies in the Astrophysical Gravitational-Wave Background: The Impact of Black Hole Distributions*, Phys. Rev. Lett. **122** (2019) 111101 [1810.13435].

[409] D. Bertacca, A. Ricciardone, N. Bellomo, A. C. Jenkins, S. Matarrese, A. Raccanelli et al., *Projection effects on the observed angular spectrum of the astrophysical stochastic gravitational wave background*, Phys. Rev. D **101** (2020) 103513 [1909.11627].

[410] I. Dvorkin, J.-P. Uzan, E. Vangioni and J. Silk, *Synthetic model of the gravitational wave background from evolving binary compact objects*, Phys. Rev. D **94** (2016) 103011 [1607.06818].

[411] C. Pitrou, G. Cusin and J.-P. Uzan, *Unified view of anisotropies in the astrophysical gravitational-wave background*, Phys. Rev. D **101** (2020) 081301 [1910.04645].

[412] N. Sugiyama, *Cosmic Background Anisotropies in Cold Dark Matter Cosmology*, ApJS **100** (1995) 281 [astro-ph/9412025].

[413] J. D. Romano and N. J. Cornish, *Detection methods for stochastic gravitational-wave backgrounds: a unified treatment*, *Living Reviews in Relativity* **20** (2017) 2 [1608.06889].

[414] P. Peter and J.-P. Uzan, *Primordial Cosmology*, Oxford Graduate Texts. Oxford University Press, 2, 2013.

[415] Bartolo N et al., *Probing Anisotropies of the Stochastic Gravitational Wave Background with LISA*, *arXiv e-prints* (2022) arXiv:2201.08782 [2201.08782].

[416] A. C. Jenkins and M. Sakellariadou, *Shot noise in the astrophysical gravitational-wave background*, Phys. Rev. D **100** (2019) 063508 [1902.07719].

[417] A. C. Jenkins, J. D. Romano and M. Sakellariadou, *Estimating the angular power spectrum of the gravitational-wave background in the presence of shot noise*, Phys. Rev. D **100** (2019) 083501 [1907.06642].

[418] S. Wang and K. Kohri, *Probing Primordial Black Holes with Angular Power Spectrum for Anisotropies in Stochastic Gravitational-Wave Background*, *arXiv e-prints* (2021) arXiv:2107.01935 [2107.01935].

[419] G. Capurri, A. Lapi, C. Baccigalupi, L. Boco, G. Scelfo and T. Ronconi, *Intensity and anisotropies of the stochastic gravitational wave background from merging compact binaries in galaxies*, J. Cosmology Astropart. Phys. **2021** (2021) 032 [2103.12037].

[420] K. M. Górski, E. Hivon, A. J. Banday, B. D. Wandelt, F. K. Hansen, M. Reinecke et al., *HEALPix: A Framework for High-Resolution Discretization and Fast Analysis of Data Distributed on the Sphere*, ApJ **622** (2005) 759 [astro-ph/0409513].

[421] L. Bethke, D. G. Figueroa and A. Rajantie, *Anisotropies in the Gravitational Wave Background from Preheating*, Phys. Rev. Lett. **111** (2013) 011301 [1304.2657].

[422] L. Bethke, D. G. Figueroa and A. Rajantie, *On the anisotropy of the gravitational wave background from massless preheating*, J. Cosmology Astropart. Phys. **2014** (2014) 047 [1309.1148].

[423] M. Geller, A. Hook, R. Sundrum and Y. Tsai, *Primordial Anisotropies in the Gravitational Wave Background from Cosmological Phase Transitions*, Phys. Rev. Lett. **121** (2018) 201303 [1803.10780].

[424] A. Ricciardone and G. Tasinato, *Anisotropic tensor power spectrum at interferometer scales induced by tensor squeezed non-Gaussianity*, J. Cosmology Astropart. Phys. **2018** (2018) 011 [1711.02635].

[425] N. Bartolo, D. Bertacca, V. De Luca, G. Franciolini, S. Matarrese, M. Peloso et al., *Gravitational wave anisotropies from primordial black holes*, J. Cosmology Astropart. Phys. **2020** (2020) 028 [1909.12619].

[426] P. Adshead, N. Afshordi, E. Dimastrogiovanni, M. Fasiello, E. A. Lim and G. Tasinato, *Multimessenger cosmology: Correlating cosmic microwave background and stochastic gravitational wave background measurements*, Phys. Rev. D **103** (2021) 023532 [2004.06619].

[427] A. Malhotra, E. Dimastrogiovanni, M. Fasiello and M. Shiraishi, *Cross-correlations as a diagnostic tool for primordial gravitational waves*, J. Cosmology Astropart. Phys. **2021** (2021) 088 [2012.03498].

[428] N. Bartolo, D. Bertacca, S. Matarrese, M. Peloso, A. Ricciardone, A. Riotto et al., *Characterizing the cosmological gravitational wave background: Anisotropies and non-Gaussianity*, Phys. Rev. D **102** (2020) 023527 [1912.09433].

[429] V. Domcke, R. Jinno and H. Rubira, *Deformation of the gravitational wave spectrum by density perturbations*, J. Cosmology Astropart. Phys. **2020** (2020) 046 [2002.11083].

[430] D. Talukder, E. Thrane, S. Bose and T. Regimbau, *Measuring neutron-star ellipticity with measurements of the stochastic gravitational-wave background*, Phys. Rev. D **89** (2014) 123008 [1404.4025].

[431] N. Mazumder, S. Mitra and S. Dhurandhar, *Astrophysical motivation for directed searches for a stochastic gravitational wave background*, Phys. Rev. D **89** (2014) 084076 [1401.5898].

[432] A. C. Jenkins, M. Sakellariadou, T. Regimbau and E. Slezak, *Anisotropies in the astrophysical gravitational-wave background: Predictions for the detection of compact binaries by LIGO and Virgo*, Phys. Rev. D **98** (2018) 063501 [1806.01718].

[433] A. C. Jenkins, R. O'Shaughnessy, M. Sakellariadou and D. Wysocki, *Anisotropies in the astrophysical gravitational-wave background: The impact of black hole distributions*, *Phys. Rev. Lett.* **122** (2019) 111101.

[434] G. Cusin, I. Dvorkin, C. Pitrou and J.-P. Uzan, *First predictions of the angular power spectrum of the astrophysical gravitational wave background*, *Phys. Rev. Lett.* **120** (2018) 231101.

[435] Zaven et al., *The NANOGrav 12.5 yr Data Set: Wideband Timing of 47 Millisecond Pulsars*, ApJS **252** (2021) 5 [2005.06495].

[436] T. Regimbau and J. A. de Freitas Pacheco, *Stochastic background from coalescences of neutron star–neutron star binaries*, *The Astrophysical Journal* **642** (2006) 455.

[437] T. Regimbau and B. Chauvineau, *A stochastic background from extra-galactic double neutron stars*, *Classical and Quantum Gravity* **24** (2007) S627.

[438] A. H. Jaffe and D. C. Backer, *Gravitational waves probe the coalescence rate of massive black hole binaries*, *The Astrophysical Journal* **583** (2003) 616.

[439] J. Blaizot, Y. Wadadekar, B. Guiderdoni, S. T. Colombi, E. Bertin, F. R. Bouchet et al., *MoMaF: the Mock Map Facility*, MNRAS **360** (2005) 159 [astro-ph/0309305].

[440] G. De Lucia and J. Blaizot, *The hierarchical formation of the brightest cluster galaxies*, MNRAS **375** (2007) 2 [astro-ph/0606519].

[441] V. Springel, S. D. M. White, A. Jenkins, C. S. Frenk, N. Yoshida, L. Gao et al., *Simulations of the formation, evolution and clustering of galaxies and quasars*, Nature **435** (2005) 629 [astro-ph/0504097].

[442] G. Lemson and t. Virgo Consortium, *Halo and Galaxy Formation Histories from the Millennium Simulation: Public release of a VO-oriented and SQL-queryable database for studying the evolution of galaxies in the LambdaCDM cosmogony*, *arXiv e-prints* (2006) astro [astro-ph/0608019].

[443] R. B. Partridge and P. J. E. Peebles, *Are Young Galaxies Visible? II. The Integrated Background*, ApJ **148** (1967) 377.

[444] J. R. Bond, B. J. Carr and C. J. Hogan, *Spectrum and Anisotropy of the Cosmic Infrared Background*, ApJ **306** (1986) 428.

[445] J. L. Puget, A. Abergel, J. P. Bernard, F. Boulanger, W. B. Burton, F. X. Desert et al., *Tentative detection of a cosmic far-infrared background with COBE.*, A&A **308** (1996) L5.

[446] B. Allen and A. C. Ottewill, *Detection of anisotropies in the gravitational-wave stochastic background*, Phys. Rev. D **56** (1997) 545 [gr-qc/9607068].

[447] N. J. Cornish, *Mapping the gravitational-wave background*, *Classical and Quantum Gravity* **18** (2001) 4277 [astro-ph/0105374].

[448] S. Mitra, S. Dhurandhar, T. Souradeep, A. Lazzarini, V. Mandic, S. Bose et al., *Gravitational wave radiometry: Mapping a stochastic gravitational wave background*, Phys. Rev. D **77** (2008) 042002 [0708.2728].

[449] J. D. Romano, S. R. Taylor, N. J. Cornish, J. Gair, C. M. F. Mingarelli and R. van Haasteren, *Phase-coherent mapping of gravitational-wave backgrounds using ground-based laser interferometers*, Phys. Rev. D **92** (2015) 042003 [1505.07179].

[450] Abbott et al., *Directional Limits on Persistent Gravitational Waves from Advanced LIGO's First Observing Run*, Phys. Rev. Lett. **118** (2017) 121102 [1612.02030].

[451] C. M. F. Mingarelli, T. Sidery, I. Mandel and A. Vecchio, *Characterizing gravitational wave stochastic background anisotropy with pulsar timing arrays*, Phys. Rev. D **88** (2013) 062005 [1306.5394].

[452] S. R. Taylor and J. R. Gair, *Searching for anisotropic gravitational-wave backgrounds using pulsar timing arrays*, Phys. Rev. D **88** (2013) 084001 [1306.5395].

[453] J. Gair, J. D. Romano, S. Taylor and C. M. F. Mingarelli, *Mapping gravitational-wave backgrounds using methods from CMB analysis: Application to pulsar timing arrays*, Phys. Rev. D **90** (2014) 082001 [1406.4664].

[454] Abbott et al., *Search for anisotropic gravitational-wave backgrounds using data from Advanced LIGO and Advanced Virgo's first three observing runs*, Phys. Rev. D **104** (2021) 022005 [2103.08520].

[455] The LIGO Scientific Collaboration, *All-sky, all-frequency directional search for persistent gravitational-waves from Advanced LIGO's and Advanced Virgo's first three observing runs*, *arXiv e-prints* (2021) arXiv:2110.09834 [2110.09834].

[456] G. Cañas-Herrera, O. Contigiani and V. Vardanyan, *Cross-correlation of the astrophysical gravitational-wave background with galaxy clustering*, Phys. Rev. D **102** (2020) 043513 [1910.08353].

[457] S. Andrianomena, C. Clarkson, P. Patel, O. Umeh and J.-P. Uzan, *Non-linear relativistic contributions to the cosmological weak-lensing convergence*, J. Cosmology Astropart. Phys. **2014** (2014) 023 [1402.4350].

[458] R. Laureijs, J. Amiaux, S. Arduini, J. L. Augueres, J. Brinchmann, R. Cole et al., *Euclid Definition Study Report*, *arXiv e-prints* (2011) arXiv:1110.3193 [1110.3193].

[459] R. E. Smith, J. A. Peacock, A. Jenkins, S. D. M. White, C. S. Frenk, F. R. Pearce et al., *Stable clustering, the halo model and non-linear cosmological power spectra*, MNRAS **341** (2003) 1311 [astro-ph/0207664].

[460] M. Fitz Axen, S. Banagiri, A. Matas, C. Caprini and V. Mandic, *Multiwavelength observations of cosmological phase transitions using LISA and Cosmic Explorer*, Phys. Rev. D **98** (2018) 103508 [1806.02500].

[461] C. Grojean and G. Servant, *Gravitational waves from phase transitions at the electroweak scale and beyond*, Phys. Rev. D **75** (2007) 043507 [hep-ph/0607107].

[462] C. Wu, V. Mandic and T. Regimbau, *Accessibility of the gravitational-wave background due to binary coalescences to second and third generation gravitational-wave detectors*, Phys. Rev. D **85** (2012) 104024 [1112.1898].

[463] S. Banagiri, M. W. Coughlin, J. Clark, P. D. Lasky, M. A. Bizouard, C. Talbot et al., *Constraining the gravitational-wave afterglow from a binary neutron star coalescence*, MNRAS **492** (2020) 4945 [1909.01934].

[464] V. Mandic, S. Bird and I. Cholis, *Stochastic Gravitational-Wave Background due to Primordial Binary Black Hole Mergers*, Phys. Rev. Lett. **117** (2016) 201102 [1608.06699].

[465] K. Crocker, V. Mandic, T. Regimbau, K. Belczynski, W. Gladysz, K. Olive et al., *Model of the stochastic gravitational-wave background due to core collapse to black holes*, Phys. Rev. D **92** (2015) 063005 [1506.02631].

[466] T. Regimbau, S. Giampanis, X. Siemens and V. Mandic, *Stochastic background from cosmic (super)strings: Popcorn-like and (Gaussian) continuous regimes*, Phys. Rev. D **85** (2012) 066001 [1111.6638].

[467] X. Siemens, V. Mandic and J. Creighton, *Gravitational-Wave Stochastic Background from Cosmic Strings*, Phys. Rev. Lett. **98** (2007) 111101 [astro-ph/0610920].

[468] V. Mandic and A. Buonanno, *Accessibility of the pre-big-bang models to LIGO*, Phys. Rev. D **73** (2006) 063008 [astro-ph/0510341].

[469] S. Banagiri, A. Criswell, T. Kuan, V. Mandic, J. D. Romano and S. R. Taylor, *Mapping the gravitational-wave sky with LISA: a Bayesian spherical harmonic approach*, MNRAS **507** (2021) 5451 [2103.00826].

[470] Abbott et al., *The basic physics of the binary black hole merger GW150914*, *Annalen der Physik* **529** (2017) 1600209 [1608.01940].

[471] LIGO Scientific Collaboration, *Advanced LIGO*, *Classical and Quantum Gravity* **32** (2015) 074001 [1411.4547].

[472] Abbott et al., *GW150914: First results from the search for binary black hole coalescence with Advanced LIGO*, Phys. Rev. D **93** (2016) 122003 [1602.03839].

[473] Abbott et al., *Binary Black Hole Mergers in the First Advanced LIGO Observing Run*, *Physical Review X* **6** (2016) 041015 [1606.04856].

[474] Acernese, *Advanced Virgo: a second-generation interferometric gravitational wave detector*, *Classical and Quantum Gravity* **32** (2015) 024001 [1408.3978].

[475] K. Somiya, *Detector configuration of KAGRA-the Japanese cryogenic gravitational-wave detector*, *Classical and Quantum Gravity* **29** (2012) 124007 [1111.7185].

[476] Y. Aso, Y. Michimura, K. Somiya, M. Ando, O. Miyakawa, T. Sekiguchi et al., *Interferometer design of the KAGRA gravitational wave detector*, Phys. Rev. D **88** (2013) 043007 [1306.6747].

[477] Akutsu et al., *Construction of KAGRA: an underground gravitational-wave observatory*, *Progress of Theoretical and Experimental Physics* **2018** (2018) 013F01 [1712.00148].

[478] F. Acernese et al., *Advanced Virgo Status*, in *14th Marcel Grossmann Meeting on Recent Developments in Theoretical and Experimental General Relativity, Astrophysics, and Relativistic Field Theories*, vol. 3, pp. 3183–3191, 2017, DOI.

[479] Abbott, *Prospects for observing and localizing gravitational-wave transients with Advanced LIGO, Advanced Virgo and KAGRA*, *Living Reviews in Relativity* **21** (2018) 3 [1304.0670].

[480] M. Punturo et al., *The Einstein Telescope: A third-generation gravitational wave observatory*, *Class. Quant. Grav.* **27** (2010) 194002.

[481] Abbott et al., *Exploring the sensitivity of next generation gravitational wave detectors*, *Classical and Quantum Gravity* **34** (2017) 044001 [1607.08697].

[482] The LIGO Scientific Collaboration et al., *GWTC-3: Compact Binary Coalescences Observed by LIGO and Virgo During the Second Part of the Third Observing Run*, *arXiv e-prints* (2021) arXiv:2111.03606 [2111.03606].

[483] F. Acernese, M. Agathos, K. Agatsuma, D. Aisa, N. Allemandou, A. Allocca et al., *Advanced virgo: a second-generation interferometric gravitational wave detector*, *Classical and Quantum Gravity* **32** (2014) 024001.

[484] The KAGRA Collaboration collaboration, Y. Aso, Y. Michimura, K. Somiya, M. Ando, O. Miyakawa, T. Sekiguchi et al., *Interferometer design of the kagra gravitational wave detector*, *Phys. Rev. D* **88** (2013) 043007.

[485] S. Anand, E. Hall and S. Nissanke, *Prospects for Multimessenger Astrophysics with Networks of Future Gravitational-Wave Detectors*, in *AAS/High Energy Astrophysics Division*, vol. 17 of *AAS/High Energy Astrophysics Division*, p. 110.02, Mar., 2019.

[486] P. S. Shawhan, LIGO Scientific Collaboration and Virgo Collaboration, *LIGO, Virgo, KAGRA and Beyond: The Future of Ground-Based Gravitational-Wave Observatories*, in *The Space Astrophysics Landscape for the 2020s and Beyond*, vol. 2135 of *LPI Contributions*, p. 5021, Apr., 2019.

[487] D. A. Brown, *Searching for Gravitational Radiation from Binary Black Hole MACHOs in the Galactic Halo*, Ph.D. thesis, -, May, 2007.

[488] Z. Carson, *Probing Fundamental Physics with Gravitational Waves*, *arXiv e-prints* (2020) arXiv:2010.04745 [2010.04745].

[489] P. R. Saulson, *Fundamentals of Interferometric Gravitational Wave Detectors*. 1994, 10.1142/2410.

[490] Abbott et al., *GW150914: The Advanced LIGO Detectors in the Era of First Discoveries*, Phys. Rev. Lett. **116** (2016) 131103 [1602.03838].

[491] D. R. Herriott and H. J. Schulte, *Folded optical delay lines*, *Appl. Opt.* **4** (1965) 883.

[492] D. Shoemaker, R. Schilling, L. Schnupp, W. Winkler, K. Maischberger and A. Rüdiger, *Noise behavior of the garching 30-meter prototype gravitational-wave detector*, *Phys. Rev. D* **38** (1988) 423.

[493] R. W. P. Drever, J. L. Hall, F. V. Kowalski, J. Hough, G. M. Ford, A. J. Munley et al., *Laser phase and frequency stabilization using an optical resonator*, *Appl. Phys. B* **31** (1983) 97.

[494] A. Abramovici, W. E. Althouse, R. W. P. Drever, Y. Gursel, S. Kawamura, F. J. Raab et al., *LIGO: The Laser Interferometer Gravitational-Wave Observatory*, *Science* **256** (1992) 325.

[495] P. Kwee, C. Bogan, K. Danzmann, M. Frede, H. Kim, P. King et al., *Stabilized high-power laser system for the gravitational wave detector advanced ligo*, *Opt. Express* **20** (2012) 10617.

[496] C. L. Mueller, M. A. Arain, G. Ciani, R. T. DeRosa, A. Effler, D. Feldbaum et al., *The advanced LIGO input optics*, *Review of Scientific Instruments* **87** (2016) 014502 [1601.05442].

[497] T. T. Fricke, N. D. Smith-Lefebvre, R. Abbott, R. Adhikari, K. L. Dooley, M. Evans et al., *DC readout experiment in Enhanced LIGO*, *Classical and Quantum Gravity* **29** (2012) 065005 [1110.2815].

[498] J. Aasi, J. Abadie, B. P. Abbott, R. Abbott, T. Abbott, M. R. Abernathy et al., *Characterization of the LIGO detectors during their sixth science run*, *Classical and Quantum Gravity* **32** (2015) 115012.

[499] N. Christensen, *Measuring the stochastic gravitational-radiation background with laser-interferometric antennas*, *Phys. Rev. D* **46** (1992) 5250.

[500] E. E. Flanagan, *Sensitivity of the laser interferometer gravitational wave observatory to a stochastic background, and its dependence on the detector orientations*, *Phys. Rev. D* **48** (1993) 2389.

[501] B. Allen and J. D. Romano, *Detecting a stochastic background of gravitational radiation: Signal processing strategies and sensitivities*, *Phys. Rev. D* **59** (1999) 102001.

[502] Abbott et al., *Open data from the first and second observing runs of Advanced LIGO and Advanced Virgo*, *SoftwareX* **13** (2021) 100658 [1912.11716].

[503] M. Fishbach and D. E. Holz, *Where Are LIGO's Big Black Holes?*, ApJ **851** (2017) L25 [1709.08584].

[504] B. P. Abbott, R. Abbott, R. Adhikari, P. Ajith, B. Allen, G. Allen et al., *LIGO: the laser interferometer gravitational-wave observatory*, *Reports on Progress in Physics* **72** (2009) 076901.

[505] Abadie et al., *TOPICAL REVIEW: Predictions for the rates of compact binary coalescences observable by ground-based gravitational-wave detectors*, *Classical and Quantum Gravity* **27** (2010) 173001 [1003.2480].

[506] C. S. Unnikrishnan, *IndIGO and Ligo-India Scope and Plans for Gravitational Wave Research and Precision Metrology in India*, *International Journal of Modern Physics D* **22** (2013) 1341010 [1510.06059].

[507] B. J. Meers, *Recycling in laser-interferometric gravitational-wave detectors*, *Phys. Rev. D* **38** (1988) 2317.

[508] Walker et al., *Effects of transients in LIGO suspensions on searches for gravitational waves*, *Review of Scientific Instruments* **88** (2017) 124501 [1702.04701].

[509] Buikema et al., *Sensitivity and performance of the Advanced LIGO detectors in the third observing run*, Phys. Rev. D **102** (2020) 062003 [2008.01301].

[510] A. Buonanno and Y. Chen, *Quantum noise in second generation, signal-recycled laser interferometric gravitational-wave detectors*, *Phys. Rev. D* **64** (2001) 042006.

[511] F. Acernese, P. Amico, M. Al-Shourbagy, S. Aoudia, S. Avino, D. Babusci et al., *Status of Virgo*, *Classical and Quantum Gravity* **22** (2005) S869 [gr-qc/0406123].

[512] Abbott et al., *Search for Tensor, Vector, and Scalar Polarizations in the Stochastic Gravitational-Wave Background*, Phys. Rev. Lett. **120** (2018) 201102 [1802.10194].

[513] T. Callister, A. S. Biscoveanu, N. Christensen, M. Isi, A. Matas, O. Minazzoli et al., *Polarization-based tests of gravity with the stochastic gravitational-wave background*, *Phys. Rev. X* **7** (2017) 041058.

[514] D. R. Lorimer, *Binary and Millisecond Pulsars*, *Living Reviews in Relativity* **11** (2008) 8 [0811.0762].

[515] K. Riles, *Recent searches for continuous gravitational waves*, *Modern Physics Letters A* **32** (2017) 1730035 [1712.05897].

[516] Abbott et al., *Search for gravitational waves from Scorpius X-1 in the second Advanced LIGO observing run with an improved hidden Markov model*, Phys. Rev. D **100** (2019) 122002 [1906.12040].

[517] Y. Zhang, M. A. Papa, B. Krishnan and A. L. Watts, *Search for Continuous Gravitational Waves from Scorpius X-1 in LIGO O2 Data*, ApJ **906** (2021) L14 [2011.04414].

[518] C. M. Espinoza, A. G. Lyne, B. W. Stappers and M. Kramer, *A study of 315 glitches in the rotation of 102 pulsars*, MNRAS **414** (2011) 1679 [1102.1743].

[519] G. Ashton, R. Prix and D. I. Jones, *Statistical characterization of pulsar glitches and their potential impact on searches for continuous gravitational waves*, *Phys. Rev. D* **96** (2017) 063004.

[520] S. Dhurandhar, B. Krishnan, H. Mukhopadhyay and J. T. Whelan, *Cross-correlation search for periodic gravitational waves*, *Phys. Rev. D* **77** (2008) 082001.

[521] L. Sun, A. Melatos, P. D. Lasky, C. T. Y. Chung and N. S. Darman, *Cross-correlation search for continuous gravitational waves from a compact object in snr 1987a in ligo science run 5*, *Phys. Rev. D* **94** (2016) 082004.

[522] K. Wette, B. J. Owen, B. Allen, M. Ashley, J. Betzwieser, N. Christensen et al., *Searching for gravitational waves from Cassiopeia A with LIGO*, *Classical and Quantum Gravity* **25** (2008) 235011 [0802.3332].

[523] V. Dergachev, M. A. Papa, B. Steltner and H.-B. Eggenstein, *Loosely coherent search in ligo o1 data for continuous gravitational waves from terzan 5 and the galactic center*, *Phys. Rev. D* **99** (2019) 084048.

[524] O. J. Piccinni, P. Astone, S. D'Antonio, S. Frasca, G. Intini, I. La Rosa et al., *Directed search for continuous gravitational-wave signals from the galactic center in the advanced ligo second observing run*, *Phys. Rev. D* **101** (2020) 082004.

[525] Abbott et al., *Optically targeted search for gravitational waves emitted by core-collapse supernovae during the first and second observing runs of advanced LIGO and advanced Virgo*, Phys. Rev. D **101** (2020) 084002 [1908.03584].

[526] The LIGO Scientific Collaboration, *All-sky search for short gravitational-wave bursts in the third Advanced LIGO and Advanced Virgo run*, *arXiv e-prints* (2021) arXiv:2107.03701 [2107.03701].

[527] The LIGO Scientific Collaboration, *All-sky search for long-duration gravitational-wave bursts in the third Advanced LIGO and Advanced Virgo run*, *arXiv e-prints* (2021) arXiv:2107.13796 [2107.13796].

[528] Abbott et al., *Upper limits on the isotropic gravitational-wave background from Advanced LIGO and Advanced Virgo's third observing run*, Phys. Rev. D **104** (2021) 022004 [2101.12130].

[529] H. Grote, *The GEO 600 status*, *Classical and Quantum Gravity* **27** (2010) 84003.

[530] *Gravitational Wave Experiments - Proceedings of the First Edoardo Amaldi Conference*, July, 1995. 10.1142/2529.

[531] B. Willke, P. Aufmuth, C. Aulbert, S. Babak, R. Balasubramanian, B. W. Barr et al., *The GEO 600 gravitational wave detector*, *Classical and Quantum Gravity* **19** (2002) 1377.

[532] M. Ando, K. Arai, R. Takahashi, G. Heinzel, S. Kawamura, D. Tatsumi et al., *Stable Operation of a 300-m Laser Interferometer with Sufficient Sensitivity to Detect Gravitational-Wave Events within Our Galaxy*, Phys. Rev. Lett. **86** (2001) 3950 [astro-ph/0105473].

[533] K. Tsubono, *300-m laser interferometer gravitational wave detector (TAMA300) in Japan.*, in *First Edoardo Amaldi Conference on Gravitational Wave Experiments* (E. Coccia, G. Pizzella and F. Ronga, eds.), p. 112, Jan., 1995.

[534] M. Maggiore, C. Van Den Broeck, N. Bartolo, E. Belgacem, D. Bertacca, M. A. Bizouard et al., *Science case for the Einstein telescope*, J. Cosmology Astropart. Phys. **2020** (2020) 050 [1912.02622].

[535] S. Kawamura et al., *The Japanese space gravitational wave antenna DECIGO*, *Class. Quant. Grav.* **23** (2006) S125.

[536] D. Reitze, R. X. Adhikari, S. Ballmer, B. Barish, L. Barsotti, G. Billingsley et al., *Cosmic Explorer: The U.S. Contribution to Gravitational-Wave Astronomy beyond LIGO*, in *Bulletin of the American Astronomical Society*, vol. 51, p. 35, Sept., 2019, 1907.04833.

[537] M. Evans, R. X. Adhikari, C. Afle, S. W. Ballmer, S. Biscoveanu, S. Borhanian et al., *A Horizon Study for Cosmic Explorer: Science, Observatories, and Community*, *arXiv e-prints* (2021) arXiv:2109.09882 [2109.09882].

[538] Amaro-Seoane et al., *Laser Interferometer Space Antenna*, *arXiv e-prints* (2017) arXiv:1702.00786 [1702.00786].

[539] A. Klein, E. Barausse, A. Sesana, A. Petiteau, E. Berti, S. Babak et al., *Science with the space-based interferometer eLISA: Supermassive black hole binaries*, Phys. Rev. D **93** (2016) 024003 [1511.05581].

[540] N. Christensen, *Stochastic gravitational wave backgrounds*, *Reports on Progress in Physics* **82** (2019) 016903 [1811.08797].

[541] A. Lamberts, S. Blunt, T. B. Littenberg, S. Garrison-Kimmel, T. Kupfer and R. E. Sanderson, *Predicting the LISA white dwarf binary population in the Milky Way with cosmological simulations*, *Monthly Notices of the Royal Astronomical Society* **490** (2019) 5888 [https://academic.oup.com/mnras/article-pdf/490/4/5888/30995029/stz2834.pdf].

[542] M. R. Adams and N. J. Cornish, *Detecting a stochastic gravitational wave background in the presence of a galactic foreground and instrument noise*, *Phys. Rev. D* **89** (2014) 022001.

[543] E. Barausse, R. Brito, V. Cardoso, I. Dvorkin and P. Pani, *The stochastic gravitational-wave background in the absence of horizons*, *Classical and Quantum Gravity* **35** (2018) 20LT01 [1805.08229].

[544] P. Auclair, J. J. Blanco-Pillado, D. G. Figueroa, A. C. Jenkins, M. Lewicki, M. Sakellariadou et al., *Probing the gravitational wave background from cosmic strings with LISA*, J. Cosmology Astropart. Phys. **2020** (2020) 034 [1909.00819].

[545] eLISA Consortium et al., *The Gravitational Universe*, *arXiv e-prints* (2013) arXiv:1305.5720 [1305.5720].

[546] M. e. a. Armano, *Sub-femto-g free fall for space-based gravitational wave observatories: Lisa pathfinder results*, *Phys. Rev. Lett.* **116** (2016) 231101.

[547] N. Tamanini, C. Caprini, E. Barausse, A. Sesana, A. Klein and A. Petiteau, *Science with the space-based interferometer eLISA. III: probing the expansion of the universe using gravitational wave standard sirens*, J. Cosmology Astropart. Phys. **2016** (2016) 002 [1601.07112].

[548] C. Caprini and N. Tamanini, *Constraining early and interacting dark energy with gravitational wave standard sirens: the potential of the eLISA mission*, J. Cosmology Astropart. Phys. **2016** (2016) 006 [1607.08755].

[549] J. Crowder and N. J. Cornish, *Beyond LISA: Exploring future gravitational wave missions*, Phys. Rev. D **72** (2005) 083005 [gr-qc/0506015].

[550] Kagra Collaboration, *KAGRA: 2.5 generation interferometric gravitational wave detector*, *Nature Astronomy* **3** (2019) 35 [1811.08079].

[551] Abbott et al., *GWTC-2: Compact Binary Coalescences Observed by LIGO and Virgo during the First Half of the Third Observing Run*, *Physical Review X* **11** (2021) 021053 [2010.14527].

[552] M. Kramer and D. J. Champion, *The european pulsar timing array and the large european array for pulsars*, *Classical and Quantum Gravity* **30** (2013) 224009.

[553] M. A. McLaughlin, *The North American Nanohertz Observatory for Gravitational Waves*, *Classical and Quantum Gravity* **30** (2013) 224008 [1310.0758].

[554] G. Hobbs, *The Parkes Pulsar Timing Array*, *Classical and Quantum Gravity* **30** (2013) 224007 [1307.2629].

[555] R. N. Manchester and IPTA, *The International Pulsar Timing Array*, *Classical and Quantum Gravity* **30** (2013) 224010 [1309.7392].

[556] T. Regimbau, M. Evans, N. Christensen, E. Katsavounidis, B. Sathyaprakash and S. Vitale, *Digging Deeper: Observing Primordial Gravitational Waves below the Binary-Black-Hole-Produced Stochastic Background*, Phys. Rev. Lett. **118** (2017) 151105 [1611.08943].

[557] C. Cutler and J. Harms, *Big Bang Observer and the neutron-star-binary subtraction problem*, Phys. Rev. D **73** (2006) 042001 [gr-qc/0511092].

[558] J. Harms, C. Mahrdt, M. Otto and M. Prieß, *Subtraction-noise projection in gravitational-wave detector networks*, *Phys. Rev. D* **77** (2008) 123010.

[559] N. Bartolo, C. Caprini, V. Domcke, D. G. Figueroa, J. Garcia-Bellido, M. Chiara Guzzetti et al., *Science with the space-based interferometer LISA. IV: probing inflation with gravitational waves*, J. Cosmology Astropart. Phys. **2016** (2016) 026 [1610.06481].

[560] R. M. Shannon, V. Ravi, W. A. Coles, G. Hobbs, M. J. Keith, R. N. Manchester et al., *Gravitational-wave limits from pulsar timing constrain supermassive black hole evolution.*, *Science* **342** (2013) 334 [1310.4569].

[561] D. Blas and A. C. Jenkins, *Bridging the μHz gap in the gravitational-wave landscape with binary resonance*, *arXiv e-prints* (2021) arXiv:2107.04601 [2107.04601].

[562] G. Janssen, G. Hobbs, M. McLaughlin, C. Bassa, A. Deller, M. Kramer et al., *Gravitational Wave Astronomy with the SKA*, in *Advancing Astrophysics with the Square Kilometre Array (AASKA14)*, p. 37, Apr., 2015, 1501.00127.

[563] Badurina L. et al, *AION: an atom interferometer observatory and network*, J. Cosmology Astropart. Phys. **2020** (2020) 011 [1911.11755].

[564] Abe et al., *Matter-wave Atomic Gradiometer Interferometric Sensor (MAGIS-100)*, *Quantum Science and Technology* **6** (2021) 044003 [2104.02835].

[565] B. Goncharov, R. M. Shannon, D. J. Reardon, G. Hobbs, A. Zic, M. Bailes et al., *On the Evidence for a Common-spectrum Process in the Search for the Nanohertz Gravitational-wave Background with the Parkes Pulsar Timing Array*, ApJ **917** (2021) L19 [2107.12112].

[566] J. P. W. Verbiest, S. Oslowski and S. Burke-Spolaor, *Pulsar Timing Array Experiments*, *arXiv e-prints* (2021) arXiv:2101.10081 [2101.10081].

[567] W. Baade and F. Zwicky, *Cosmic Rays from Super-novae*, *Proceedings of the National Academy of Science* **20** (1934) 259.

[568] T. Gold, *Rotating Neutron Stars as the Origin of the Pulsating Radio Sources*, Nature **218** (1968) 731.

[569] F. Pacini, *Rotating Neutron Stars, Pulsars and Supernova Remnants*, Nature **219** (1968) 145.

[570] R. S. Lynch, *Pulsar Timing Arrays*, *J. Phys. Conf. Ser.* **610** (2015) 012017.

[571] M. Maiorano, F. De Paolis and A. A. Nucita, *Principles of Gravitational-Wave Detection with Pulsar Timing Arrays*, *Symmetry* **13** (2021) 2418 [2112.08064].

[572] D. R. Lorimer and M. Kramer, *Handbook of Pulsar Astronomy*, vol. 4. 2004.

[573] M. McLaughlin, *Pulsar Timing Arrays*, *IAU Focus Meeting* **29B** (2016) 321.

[574] S. Detweiler, *Pulsar timing measurements and the search for gravitational waves*, ApJ **234** (1979) 1100.

[575] A. Sesana and A. Vecchio, *Measuring the parameters of massive black hole binary systems with pulsar timing array observations of gravitational waves*, Phys. Rev. D **81** (2010) 104008 [1003.0677].

[576] R. W. Hellings and G. S. Downs, *Upper limits on the isotropic gravitational radiation background from pulsar timing analysis.*, ApJ **265** (1983) L39.

[577] A. Sesana, F. Haardt, P. Madau and M. Volonteri, *Low-Frequency Gravitational Radiation from Coalescing Massive Black Hole Binaries in Hierarchical Cosmologies*, ApJ **611** (2004) 623 [astro-ph/0401543].

[578] P. A. Rosado, A. Sesana and J. Gair, *Expected properties of the first gravitational wave signal detected with pulsar timing arrays*, MNRAS **451** (2015) 2417 [1503.04803].

[579] C. M. F. Mingarelli, T. J. W. Lazio, A. Sesana, J. E. Greene, J. A. Ellis, C.-P. Ma et al., *The local nanohertz gravitational-wave landscape from supermassive black hole binaries*, *Nature Astronomy* **1** (2017) 886 [1708.03491].

[580] S. Burke-Spolaor, S. R. Taylor, M. Charisi, T. Dolch, J. S. Hazboun, A. M. Holgado et al., *The astrophysics of nanohertz gravitational waves*, A&A Rev. **27** (2019) 5 [1811.08826].

[581] M. Favata, *Nonlinear Gravitational-Wave Memory from Binary Black Hole Mergers*, ApJ **696** (2009) L159 [0902.3660].

[582] T. Damour and A. Vilenkin, *Gravitational radiation from cosmic (super)strings: Bursts, stochastic background, and observational windows*, Phys. Rev. D **71** (2005) 063510 [hep-th/0410222].

[583] C. Caprini, R. Durrer and X. Siemens, *Detection of gravitational waves from the QCD phase transition with pulsar timing arrays*, Phys. Rev. D **82** (2010) 063511 [1007.1218].

[584] A. Kobakhidze, C. Lagger, A. Manning and J. Yue, *Gravitational waves from a supercooled electroweak phase transition and their detection with pulsar timing arrays*, *European Physical Journal C* **77** (2017) 570 [1703.06552].

[585] L. P. Grishchuk, *Relic Gravitational Waves and Their Detection*, in *Gyros, Clocks, Interferometers ...: Testing Relativistic Gravity in Space* (C. Lämmerzahl, C. W. F. Everitt and F. W. Hehl, eds.), vol. 562, p. 167. 2001. DOI.

[586] W. Buchmuller, V. Domcke and K. Schmitz, *From NANOGrav to LIGO with metastable cosmic strings*, *Physics Letters B* **811** (2020) 135914 [2009.10649].

[587] X. Siemens, J. S. Hazboun, P. T. Baker, S. Burke-Spolaor, D. Madison, C. Mingarelli et al., *Physics Beyond the Standard Model With Pulsar Timing Arrays*, *arXiv e-prints* (2019) arXiv:1907.04960 [1907.04960].

[588] P. B. Demorest, R. D. Ferdman, M. E. Gonzalez, D. Nice, S. Ransom, I. H. Stairs et al., *Limits on the Stochastic Gravitational Wave Background from the North American Nanohertz Observatory for Gravitational Waves*, ApJ **762** (2013) 94 [1201.6641].

[589] R. van Haasteren, Y. Levin, G. H. Janssen, K. Lazaridis, M. Kramer, B. W. Stappers et al., *Placing limits on the stochastic gravitational-wave background using European Pulsar Timing Array data*, MNRAS **414** (2011) 3117 [1103.0576].

[590] M. Kramer and D. J. Champion, *The European Pulsar Timing Array and the Large European Array for Pulsars*, *Classical and Quantum Gravity* **30** (2013) 224009.

[591] R. N. Manchester, G. Hobbs, M. Bailes, W. A. Coles, W. van Straten, M. J. Keith et al., *The Parkes Pulsar Timing Array Project*, PASA **30** (2013) e017 [1210.6130].

[592] Arzoumanian Z et al., *The NANOGrav 12.5 yr Data Set: Search for an Isotropic Stochastic Gravitational-wave Background*, ApJ **905** (2020) L34 [2009.04496].

[593] Pol N. et al., *Astrophysics Milestones for Pulsar Timing Array Gravitational-wave Detection*, ApJ **911** (2021) L34 [2010.11950].

[594] D. N. Spergel, L. Verde, H. V. Peiris, E. Komatsu, M. R. Nolta, C. L. Bennett et al., *First-Year Wilkinson Microwave Anisotropy Probe (WMAP) Observations: Determination of Cosmological Parameters*, ApJS **148** (2003) 175 [astro-ph/0302209].

[595] S. Mukherjee, B. D. Wandelt and J. Silk, *Multimessenger tests of gravity with weakly lensed gravitational waves*, Phys. Rev. D **101** (2020) 103509 [1908.08950].